PTB bericht
Wissenschaftliche Veröffentlichungen

Diss-30
April 2026

Dissertation

Mohanad Dawood Hasan Al-Dabbagh

Advanced Measurement Techniques and Testbeds for the Characterization of Sub-THz Channel Sounding Systems

ISSN 2941-1297
ISBN 978-3-944659-62-6

DOI 10.7795/110.20260421

Mohanad Dawood Hasan Al-Dabbagh

Advanced Measurement Techniques and Testbeds for the Characterization of Sub-THz Channel Sounding Systems

Dissertation

PTB-Diss- 30

Braunschweig, 20. April 2026

ISSN 2751-6598
ISBN 978-3-944659-62-6

DOI 10.7795/110.20260421

Empfohlene Zitierweise/recommended citation

Al-Dabbagh, M.D.H., 2026. *Advanced Measurement Techniques and Testbeds for the Characterization of Sub-THz Channel Sounding Systems*,
Technische Universität Carolo-Wilhelmina zu Braunschweig.
Braunschweig: Physikalisch-Technische Bundesanstalt.
PTB-Bericht Diss-30. ISBN 978-3-944659-62-6.
Verfügbar unter: https://doi.org/10.7795/110.20260421

Herausgeber:
Physikalisch-Technische Bundesanstalt
ISNI: 0000 0001 2186 1887

Presse und Öffentlichkeitsarbeit

Bundesallee 100
38116 Braunschweig

Telefon: (05 31) 592-93 21
Telefax: (05 31) 592-92 92
www.ptb.de

Advanced Measurement Techniques and Testbeds for the Characterization of Sub-THz Channel Sounding Systems

Von der Fakultät für Elektrotechnik, Informationstechnik, Physik
der Technischen Universität Carolo-Wilhelmina zu Braunschweig

zur Erlangung des Grades eines Doktors
der Ingenieurwissenschaften (Dr.-Ing.)

genehmigte Dissertation

von: Mohanad Dawood Hasan Al-Dabbagh
aus: Bagdad - Irak

1. Referent: Prof. Dr.-Ing. Thomas Kleine-Ostmann
2. Referent: Prof. Dr. rer. nat. Thomas Schneider
3. Referent: Dr. David A. Humphreys

eingereicht am: 18.08.2025
mündliche Prüfung am: 20.01.2026

Druckjahr: 2026

https://doi.org/10.7795/110.20260421

https://doi.org/10.7795/110.20260421

Abstract

The increasing demand for ultra-high data rate wireless communication is pushing research toward the Terahertz (THz) frequency range, where large amounts of unused spectrum are available. This band has been actively studied as a promising candidate for enabling next-generation applications such as sixth-generation (6G), high-speed wireless backhaul, and ultra-fast radar systems in recent years. Despite its potential, accurately characterizing THz channels remains challenging due to higher free-space path loss (FSPL), hardware non-linearities, and unreliable calibration and validation methods. This thesis addresses these challenges by developing advanced measurement approaches and experimental testbeds aimed at precisely characterizing THz channel sounder (CS) systems, with a strong focus on metrological principles to reduce measurement uncertainty. The testbeds are designed to evaluate system performance under both guided and over-the-air (OTA) conditions, enabling a consistent evaluation of channel behavior across different frequency bands, propagation scenarios, and system architectures. These combined efforts aim to establish a robust framework that reduces measurement uncertainty and provides reliable data for the modeling and optimization of future THz communication systems.

The work begins by establishing the role and importance of metrology in THz communication systems. This research's motivation, aim, and objectives are introduced, followed by an overview of fundamental measurement principles. This includes the system architectures used in our hardware setup and an explanation of metrological traceability. Various sources of error in the system are identified, and different calibration techniques are discussed for correcting these errors and improving measurement accuracy.

We then investigate metrology for THz communication in more depth, focusing on the calibration procedures used to correct systematic measurement errors for both the vector network analyzer (VNA) and correlation-based CS systems, where these error term corrections can significantly enhance measurement accuracy and reliability. Both waveguide and OTA measurement setups are explored using a VNA with frequency extension modules and custom-designed CS systems. We investigate in detailed characterization the horn antennas to extract gain and phase center. Calibration procedures are compared and analyzed across different scenarios, including both line-of-sight (LoS) and non-line-of-sight (NLoS) environments, to evaluate how measurement conditions affect accuracy.

https://doi.org/10.7795/110.20260421

Next, we examine time-varying channel behavior using a VNA in controlled environments. This part of the work helps to understand the propagation behavior in dynamic conditions better and assess how VNA sweep time and segmented waveform capture influence the measurements. A dedicated experimental setup is used to simulate and study time-varying transmission scenarios. The results showed variations in time intervals from the VNA at different intermediate frequency bandwidth (IFBW)s, as well as differences between continuous wave (CW) and linear sweep (LS) segments. We analyze the sweep duration and evaluate different waveform types, conducting experimental verification to establish a measurement scenario. This scenario improves the understanding of time-varying measurements and enables their application to more dynamic CS systems, allowing for estimating associated measurement uncertainties.

Finally, we demonstrate a setup for measuring a sub-THz wireless link using a hybrid transmission system based on standard optical communication hardware. The signal was transmitted over a 6-meter distance. A positive-intrinsic-negative photodiode (PIN-PD) was used on the transmitter side, propagating the sub-THz signal, while the receiver employed a subharmonic down-converter. The system was tested across the 240 GHz to 300 GHz frequency range. Several key factors were adjusted to characterize performance, including the optical carrier frequency, frequency hopping, the direct current (DC) bias applied, equalizer configuration, and digital signal processing (DSP). A 25.6 Gbit/s quasi-error-free QPSK signal was achieved. Further tests with 16-QAM focused on how the power split between two optical paths affected the signal quality, particularly the error vector magnitude, linearity of the in-phase and quadrature (IQ) amplitude, and signal distribution. The setup was validated through successful error-free transmission of actual data, demonstrated by sending an image.

https://doi.org/10.7795/110.20260421

Kurzfassung

Die steigende Nachfrage nach drahtloser Kommunikation mit extrem hohen Datenraten treibt die Forschung in Richtung des THz-Frequenzbereichs, in dem große Bereiche ungenutzten Spektrums zur Verfügung stehen. In den letzten Jahren wurde dieses Frequenzband intensiv als vielversprechender Kandidat für die Realisierung zukünftiger Anwendungen wie 6G, Hochgeschwindigkeits-Wireless-Backhaul und ultraschnelle Sensorsysteme untersucht. Trotz seines Potenzials bleibt die präzise Charakterisierung von THz-Kanälen eine Herausforderung, bedingt durch höhere Funkfelddämpfung, nichtlineares Verhalten von Komponenten und unzuverlässige Kalibrierungs- und Validierungsmethoden. Diese Arbeit adressiert diese Herausforderungen durch die Entwicklung fortschrittlicher Messmethoden und experimenteller Testumgebungen, mit dem Ziel, THz-Channel-Sounding-Systeme präzise zu charakterisieren. Dabei liegt ein besonderer Fokus auf metrologischen Prinzipien zur Reduktion von Messunsicherheiten.

Zu Beginn der Arbeit wird die Rolle und Bedeutung der Metrologie in THz-Kommunikationssystemen erläutert. Die Motivation, Zielsetzung und Forschungsfragen werden vorgestellt, gefolgt von einer Einführung in grundlegende Messprinzipien. Dies umfasst die Systemarchitekturen der verwendeten Hardware sowie eine Darstellung der metrologischen Rückführbarkeit. Verschiedene Fehlerquellen im Messsystem werden identifiziert und unterschiedliche Kalibrierverfahren zur Korrektur dieser Fehler und zur Erhöhung der Messgenauigkeit diskutiert.

Im weiteren Verlauf wird die Metrologie für THz-Kommunikation vertieft untersucht, mit Fokus auf die Kalibrierungsverfahren zur Korrektur systematischer Messfehler sowohl beim VNA als auch bei korrelationsbasierten Channel-Sounding-Systeme. Die Korrektur dieser Fehlerterme kann die Messgenauigkeit und -zuverlässigkeit erheblich verbessern. Es werden sowohl Wellleiter- als auch over-the-air-Messaufbauten analysiert, wobei ein VNA mit Frequenzverlängerungsmodulen und eigens entwickelte Channel-Sounding-Systeme zum Einsatz kommen. Die Hornantennen werden detailliert charakterisiert, um Parameter wie Gewinn und Phasenzentrum zu bestimmen. Die Kalibrierungsverfahren werden in unterschiedlichen Szenarien – einschließlich Line-of-Sight- und Non-Line-of-Sight-Umgebungen – verglichen und analysiert, um den Einfluss der jeweiligen Messbedingungen auf die Genauigkeit zu bewerten.

Anschließend wird das zeitvariable Kanalverhalten mithilfe eines VNA unter kontrollierten Bedingungen untersucht. Dieser Teil der Arbeit dient dem besseren Verständnis des Aus-

https://doi.org/10.7795/110.20260421

breitungsverhaltens unter dynamischen Bedingungen und der Bewertung des Einflusses von VNA-Sweep-Zeiten und segmentierter Wellenformen auf die Messergebnisse. Ein dedizierter Versuchsaufbau wird genutzt, um zeitvariable Übertragungsszenarien zu simulieren und zu analysieren. Die Ergebnisse zeigen Variationen der Zeitintervalle des VNA bei unterschiedlichen Zwischenfrequenzbandbereite-Einstellungen sowie Unterschiede zwischen Segmenten des kontinuierlichen Wellenmodus und der linearen Frequenzdurchläufe. Die Sweep-Dauer wird analysiert und verschiedene Wellenformtypen werden bewertet. Durch experimentelle Verifikation wird ein Messszenario etabliert, das das Verständnis zeitvariabler Messungen verbessert und deren Anwendung auf dynamischere Channel-Sounding-Systeme ermöglicht, wodurch die Abschätzung zugehöriger Messunsicherheiten unterstützt wird.

Abschließend wird ein Messaufbau für einen over-the-air-Sub-THz-Link demonstriert, der ein hybrides Übertragungssystem nutzt, bestehend aus Standardkomponenten der optischen Kommunikation, wobei das Signal über eine Strecke von 6 Metern übertragen wird. Der Sender war eine PIN-Fotodiode, der Empfänger ein subharmonischer Down-Converter. Der Übertragungsteststand für Frequenzen zwischen 240 GHz und 300 GHz wurde umfassend charakterisiert. Wichtige Parameter wie optische Frequenz, Frequenzsprungverfahren, DC-Vorspannung des Senders, Equalization-Taps und die Phasen der digitalen Signalverarbeitung wurden zur Leistungsoptimierung untersucht. Ein fehlerfreies 25,6 Gbit/s quadrature phase shift keying (QPSK)-Signal konnte realisiert werden. Eine 16QAM (quadrature amplitude modulation) Charakterisierung untersuchte die Leistungsverteilung der beiden optischen Zweige, die der Fotodiode zugeführt wurden, sowie deren Einfluss auf die EVM (error vector magnitude) der IQ-Amplitudenlinearität und die Abschätzung Der Datenübertragungsexperiment wurde durch die erfolgreiche Übertragung realer Daten validiert, in diesem Fall anhand eines übertragenen Bildes.

https://doi.org/10.7795/110.20260421

Acknowledgment of AI Assistance

Parts of the grammar revision of this thesis and the translation of the abstract into German were supported by the AI language model ChatGPT-4o (OpenAI). The use of this tool was limited to linguistic refinement and translation. All substantive content, analysis, and conclusions remain the work of the author.

https://doi.org/10.7795/110.20260421

https://doi.org/10.7795/110.20260421

Acknowledgments

I am honored to mark this important milestone in my academic journey with the completion of this doctoral thesis. This work represents several years of research, perseverance, and personal growth, made possible through the guidance of mentors, the collaboration of colleagues, and the steadfast support of family and friends.

I would like to express my sincere gratitude to my supervisors, Prof. Dr.-Ing. Thomas Kleine-Ostmann and Dr. David A. Humphreys, for their guidance, expertise, and encouragement throughout my doctoral studies. Their insight, constructive feedback, and continuous support were essential to the development and completion of this work. I also thank the members of my examination committee, chaired by Prof. Dr.-Ing. Thomas Kürner, as well as Prof. Dr. rer. nat. Thomas Schneider, for their careful evaluation and valuable comments. I would also like to extend my thanks to my first supervisor from the University of Magdeburg, Prof. Dr.-Ing. Abbas Omar, for his great support during the early stages of my PhD work.

My special thanks go to my colleagues at the Physikalisch-Technische Bundesanstalt (PTB) for creating a stimulating research environment and providing access to high-accuracy measurement facilities. I would particularly like to thank the head of my working group, Dr. Kai Baaske, for his support and leadership. I am also grateful to my working group colleagues, especially Mr. David Ulm, for the fruitful discussions and assistance in building different measurement scenarios.

I further thank my research partners in the Meteracom project, coordinated by Prof. Dr.-Ing. Thomas Kürner, for their collaboration and insightful discussions. I am grateful to colleagues at the University of Marburg, TU Ilmenau, and TU Braunschweig for the productive exchanges during this work. My sincere appreciation also goes to my colleagues at the National Physical Laboratory (NPL), particularly Dr. Mira Naftaly, Dr. Irshaad Fataden, and Dr. Jessica Smith, for their warm welcome and generous support during my research visit.

I gratefully acknowledge the financial support of the Deutsche Forschungsgemeinschaft (DFG), which made this research possible.

Finally, I wish to thank my family for their constant encouragement and support. To my mother, sister, and brother, thank you for supporting me during this journey. I remember with deep gratitude my late father, whose guidance continue to inspire me; this work and all my achievements in life are dedicated to him. To my wife, thank you for your support throughout this journey and for sharing both its challenges and its joys. As we welcome our child, this moment has been a meaningful source of motivation during the final stages of this work.

https://doi.org/10.7795/110.20260421

https://doi.org/10.7795/110.20260421

Contents

1 Introduction **1**

1.1 Need for Metrology in Terahertz Communications 1

1.2 Aims and Objectives: Advancing Measurement Techniques for Sub-THz Propagation 5

1.3 Structure of the Thesis 7

2 General Principles of Measurement Systems and Channel Assessments **11**

2.1 System Architecture 11

2.1.1 VNA Architecture 11

2.1.2 Correlational-Based Channel Sounder Architecture 14

2.1.3 Photonic-Assisted Channel Sounder Architecture 15

2.2 Metrology Fundamentals to Traceability 17

2.2.1 Evaluation of Vector Network Analyzers 17

2.2.2 Evaluation of Time-Domain Channel Sounders 24

2.3 THz Signal Propagation 27

2.3.1 Guided Signal Propagation 27

2.3.2 Over-the-Air Signal Propagation 30

2.4 Signal Processing Techniques 35

2.4.1 Power Delay Profile Analysis for Understanding Signal Propagation in Communication Scenarios 35

2.4.2 Interpolation and Windowing Techniques 36

3 System Error Correction and Calibration Procedures **41**

3.1 VNA Calibration and Error Modeling 41

3.1.1 Calibration Standards 42

3.1.2 Noise Floor and Trace Noise 44

3.1.3 Drift of Transmission Tracking 45

3.1.4 Non-Linearity and Cable Movement 47

3.2 Horn Antenna Calibration for Precise OTA Measurements 49

3.2.1 Distance Measurement 51

3.2.2 Rotational Measurement 54

https://doi.org/10.7795/110.20260421

3.3 Correlational-Based Channel Sounder Calibration . . . 58
3.3.1 Time-Zero Measurement using Reference Transmitter . . . 58
3.3.2 Back-to-Back Frequency Response Measurement . . . 58
3.3.3 IQ Imbalance . . . 60
3.3.4 DC Offset . . . 61

4 Characterization of Sub-THz Channel Sounding Systems in OTA Measurement Scenarios 65
4.1 Line-of-Sight Distance Measurement . . . 65
4.1.1 Measurement Setup . . . 65
4.1.2 Channel Sounder Frequency Step Size . . . 66
4.1.3 Spectrum Boundaries . . . 68
4.1.4 Bandwidth Feasibility . . . 69
4.1.5 Reference Measurement Selection . . . 71
4.2 Combined VNA and CS Measurement Uncertainties . . . 72
4.3 Multipath Measurements . . . 73
4.3.1 Plane Reflector . . . 73
4.3.2 Single Reflector Analysis . . . 78
4.3.3 Multiple Reflectors Analysis . . . 82

5 Characterizing OTA Time-Varying Measurements Using a VNA 85
5.1 Fundamentals of Time-Varying Transmissions . . . 86
5.2 Traceability Challenges in Time-Varying Transmissions . . . 87
5.3 Measurement Setup and Scenario Simulation . . . 88
5.3.1 Selected Waveforms . . . 89
5.3.2 Measurement Setup . . . 89
5.3.3 Simulated Waveform . . . 91
5.4 Measurement Results and Discussion . . . 93
5.4.1 Linear Stage Velocity . . . 93
5.4.2 Continuous Wave Signal Analysis . . . 94
5.4.3 Linear Sweep Signal Analysis . . . 96

6 Characterizing the Photonic-Assisted Coherent Free-Space Link for Sub-THz Data Transmission 101
6.1 Introduction into Photonic-Assisted Sub-THz Data Transmission . . . 102
6.2 Measurement Setup . . . 104
6.3 Digital Signal Processing Techniques . . . 106
6.4 Beam Profile Analysis . . . 109
6.5 Results and Discussion . . . 111
6.5.1 QPSK Measurement . . . 111
6.5.2 16-QAM Measurement . . . 115
6.5.3 Image transmission . . . 118

https://doi.org/10.7795/110.20260421

7 Summary and Perspectives **121**
7.1 Main Achievements 121
7.2 Implications and Future Directions 124

List of Publications **125**

List of Acronyms **127**

Bibliography **131**

https://doi.org/10.7795/110.20260421

https://doi.org/10.7795/110.20260421

1 Introduction

This chapter introduces this work, emphasizing the need for metrology in THz communications. A general overview of sub-THz communication principles is presented and discussed the reasons for selecting this frequency band for future mobile communication systems. A brief update on the state of the art is provided, highlighting the advancements achieved so far in the field of THz communications and the challenges related to signal propagation. It also discusses the investigations required to ensure reliable and repeatable measurements.

Subsequently, the metrological concepts in this work are introduced to establish measurement uncertainties and ensure consistency across all measuring devices.

Following this, the aims and objectives, evaluating the effectiveness of CS techniques and measurement procedures used to characterize the THz channel advancing measurement techniques for sub-THz propagation are discussed.

Five objectives are outlined, each of which will be discussed and supported by measurement results in the subsequent chapters of this work. Finally, the structure of this thesis is presented.

1.1 Need for Metrology in Terahertz Communications

The sub-THz band is being used for the next generation of wireless communications, referring to wireless systems operating at frequencies above 100 GHz to 10 THz. Interest in this band, specifically around 300 GHz, is not accidental. However, an inevitable result of the ever-increasing demand for higher data rates and more extensive data volumes, which double every 18 months [1]. Most of our wireless communications applications are currently in the range of frequencies below 95 GHz. This has driven the need to explore frequencies beyond the overcrowded bands, where most wireless communication development has occurred. Fig. 1.1 illustrates the frequency allocation of the radio spectrum including the possible sub-THz band for 6G.

The increasing demand for bandwidth, driven by the rapid growth of new mobile communication applications, has pushed research toward exploring advanced bandwidth management techniques such as frequency and time multiplexing [3, 4], spatial multiplexing [5], spectrum allocation [6], and combinations of these methods (Fig.1.2). Time and frequency division protocols and spatial multiplexing through beamforming techniques have significantly enhanced

https://doi.org/10.7795/110.20260421

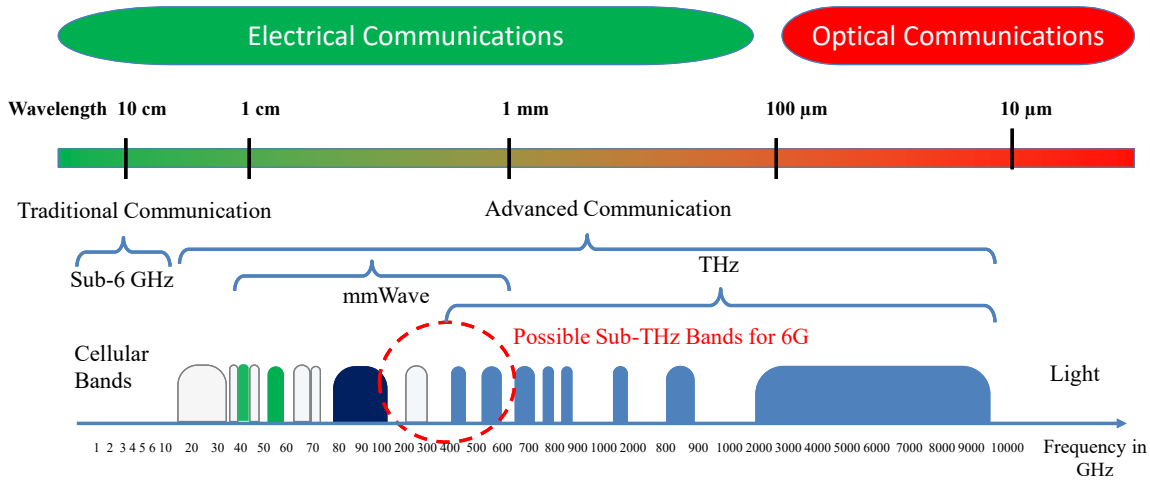

Figure 1.1: Frequency allocation of the radio spectrum. (Adopted from [2]).

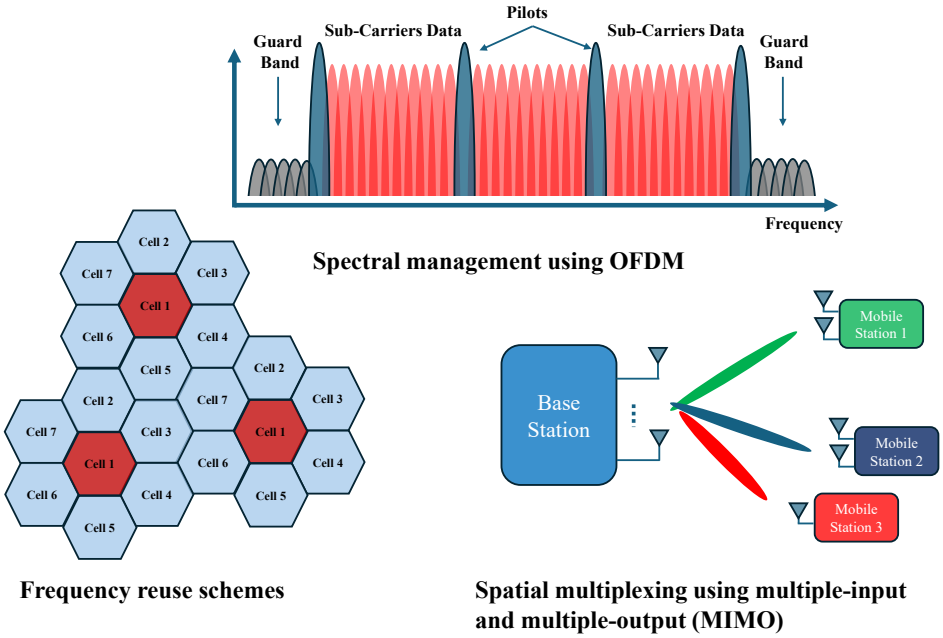

Figure 1.2: State-of-the-art examples of bandwidth management techniques.

user capacity and adaptive data rate allocation. Notable examples include IEEE 802.11ax [7], which improves performance in crowded environments by dynamically switching between two frequency bands and incorporating spatial multiplexing, as well as fourth-generation (4G) long term evolution (LTE), which employs a similar approach to optimize mobile communication [8].

While these techniques can improve bandwidth efficiency, they alone are insufficient to keep up with the accelerating demand for higher data rates unless an appropriate spectrum is allocated to each wireless spatial link in the order of tens of GHz. A wider bandwidth is essential to meet these growing needs.

The introduction of fifth-generation (5G) standards, together with the IEEE 802.11ad stan-

https://doi.org/10.7795/110.20260421

dard at 60 GHz, has extended wireless operating frequencies beyond the sub-6 GHz range that had been the norm for many years [9, 10]. This advancement has encouraged further research into even higher frequency regions exceeding 100 GHz to meet the growing demand for faster and more efficient wireless communication. This has resulted more significantly, with the IEEE802.15.3d standard explicitly targeting sub-THz frequencies, identifying them as key candidates for 6G communication [11, 12].

This frequency band has historically been overlooked due to hardware limitations, propagation losses, and measurement uncertainty and traceability challenges at such high frequencies. However, it presents a promising solution by offering the bandwidth for next-generation communication systems. Spectrum allocation in the THz communication region provides the high bandwidth required for future mobile applications, supported by advanced signal processing techniques for modulation and spatial multiplexing.

Remarkable progress in wireless communications, enabled by harmonic mixers and signal amplifiers, has made THz frequency exploration possible through radio or optical fibers. Advances in radio frequency technology have raised base-band signals through multi-stage mixers, producing cost-effective components that operate up to 500 GHz [13, 14]. At this range, waveguides play a crucial role. Their design, based on coupling electrical waves into hollow forms (e.g., rectangular, square, or circular waveguides), enables bandwidth extension of up to 40 % of the center frequency. For instance, the WR03 rectangular waveguide, ranging from 220–330 GHz and centered at 275 GHz, provides a 40 % bandwidth of 110 GHz [15, 16]. However, challenges such as increased costs, misalignment, and miniaturization persist as frequencies exceed 500 GHz. Expertise gained from lower frequencies has been instrumental in addressing these challenges, and compact antenna designs like that from the project TERAPAN at the WR03 band have demonstrated promising beamforming performance [17, 18].

Simultaneously, optical technologies have advanced quasi-optical coupling, using techniques such as lenses, mirrors, and free-space propagation, and optical mixers, were initially developed for wired communications. Optical fibers became the backbone of long-range data transmission, offering high efficiency and low error vector magnitude (EVM) at high data rates. Optical mixers, such as Mach-Zehnder-Modulator (MZM)s [19], electro-absorption modulators (EAM)s, and cross-absorption modulation (XAM) in photo mixers like uni-traveling carrier photodiode (UTC-PD)s and PIN-PDs, have expanded bandwidths up to 3 THz [20]. These systems address limitations in electrical technologies, although challenges in cost and compact design for user equipment remain [21].

Hybrid systems combining electrical and optical technologies can potentially harmonize data transmission across frequencies from 100 GHz to 500 GHz [22, 23]. Such systems could transform wide bandwidths, available in optical systems, into versatile access points, enabling simultaneous communication between in frequency bands and paving the way for THz communication applications, including wireless backhaul, indoor data transmission, near-field communication, and chip-to-chip communication [11].

Although THz frequencies are promising, their practical applications face new challenges that are not significant at lower frequencies. Many of these challenges are related to the

https://doi.org/10.7795/110.20260421

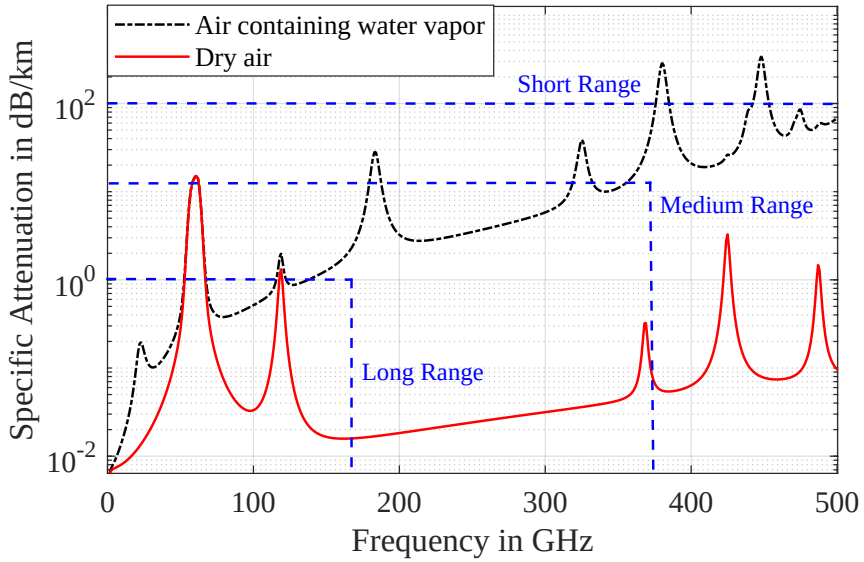

Figure 1.3: Specific attenuation due to atmospheric gases as a function of frequency, calculated using MATLAB ITU-R P.676-10 model for sea-level reference conditions (dry air pressure $p = 1013.25\,\mathrm{hPa}$ and temperature $T = 15°\mathrm{C}$). The curve labelled "Air containing water vapor" assumes a water-vapour density $\rho = 7.5\,\mathrm{g\,m^{-3}}$, while "Dry air" assumes $\rho = 0\,\mathrm{g\,m^{-3}}$. The plotted quantity is the specific attenuation γ in $\mathrm{dB\,km^{-1}}$. The total gaseous attenuation over a propagation path of length L (km) is $A = \gamma L$ (dB) [24].

fundamental properties of THz waves, such as atmospheric absorption, attenuation, limited propagation distances, and the difficulty of generating and detecting THz signals. This makes the sub-THz band mostly suitable for medium- to short-range applications, as presented in the atmospheric absorption graph shown in Fig.1.3 [24].

To address these limitations and make sub-THz communications practical, signal propagation at these frequencies is investigated with metrology, the science of measurement, which is crucial to understanding how these waveforms propagate. Accurate signal generation and measurement form the foundation of any wireless communication system. Precise frequency control is critical for high-frequency communication systems to operate reliably and harmoniously with other systems. When such high-frequency bands are generated, they pass through various signal processing stages of mixing and amplification components that can add noise and disturbances to the signal and uncertainty to its measurement, some of which are not critical. In contrast, others can destroy the signal reception. This requires in-depth investigation to understand and analyze the source of measurement errors, correct them, and determine the additional uncertainty contributions to the measurements. Therefore, measuring THz frequencies involves establishing robust frequency standards and ensuring traceability to international references, such as those provided by the International System of Units (SI) or national metrology institutes (NMIs).

Measurement traceability is a fundamental concept in metrology, ensuring that measurement results can be linked to stated references—typically national or international standards—through an unbroken chain of comparisons with known uncertainties [25]. To achieve traceability, well-characterized measuring equipment can serve as reference measurement de-

https://doi.org/10.7795/110.20260421

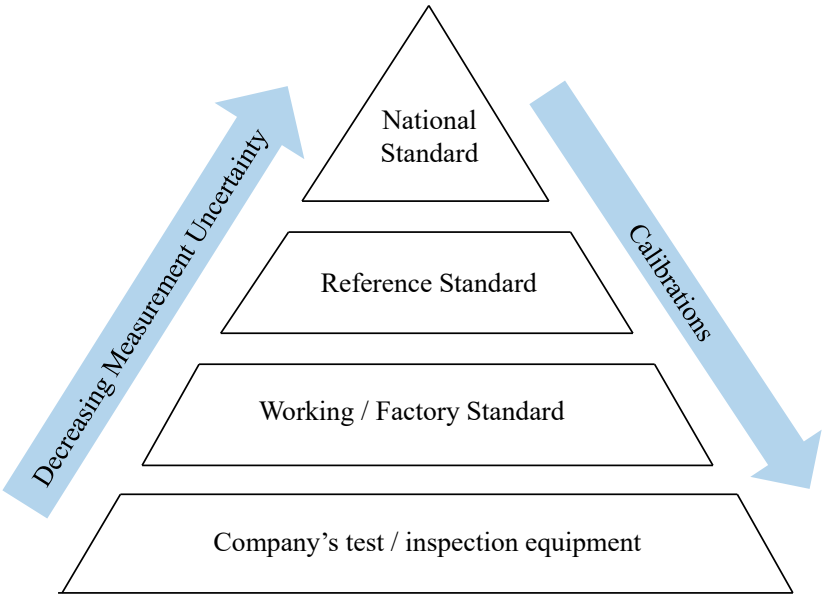

Figure 1.4: Measurement Traceability Steps.

vices by applying calibration standards. Additionally, comparisons with a reference device help mitigate environmental influences such as multipath effects and absorptions, which could otherwise impact measurement accuracy. Furthermore, theoretical calculations can be employed as a reference to verify the measured values, providing an additional layer of validation. The target would be achieved by decreasing the measurement uncertainties with increased calibration procedures until reaching reliable and traceable measurements as shown in Fig.1.4.

The measurement and signal integrity challenges described here are addressed through detailed system architecture definitions in Chapter 2, where hardware and propagation models are introduced for later analysis.

1.2 Aims and Objectives: Advancing Measurement Techniques for Sub-THz Propagation

This thesis aims to thoroughly investigate the metrology principles and practices essential for the effective measurement and analysis of sub-THz communication systems. With the rapid advancement in THz technology for next-generation communication systems, it is important to understand the challenges posed by signal propagation at these frequencies, as well as the calibration and characterization of the hardware involved. This thesis seeks to address the current gaps in measurement practices by evaluating the signal propagation characteristics of THz systems and exploring the various meteorological tools and techniques required to support the design and deployment of these systems.

Specifically, this research aims to evaluate the effectiveness of CS techniques and measurement procedures used to characterize THz communication channels. It will also investigate the calibration methodologies necessary for ensuring accuracy in THz communication

https://doi.org/10.7795/110.20260421

measurements, using a variety of state-of-the-art measurement equipment such as VNA and correlation-based CS. A key focus will be on OTA signal propagation under controlled conditions to cover LoS and NLoS measurement scenarios. Another aspect will be the investigation of time-varying signal propagation, which can have significant signal degradation in the channel performance of dynamic THz communication links. Finally, this thesis aims to develop and test a measurement testbed involving optical-based transmitters and radio frequency (RF) receivers to enable real-data transmission and evaluate the performance of quadrature amplitude modulation (QAM) signals at the sub-THz band.

Objectives of the Work

1. **Investigation of Metrology Principles in THz Communications:** The primary objective is to explore the metrological principles and challenges specific to THz communications. This includes a deep dive into the fundamental aspects of signal propagation at THz frequencies, where traditional microwave metrology techniques may not be directly applicable. The objective is to understand how THz waves propagate through the atmosphere, and behave in controlled environments. The research will focus on developing measurement standards and calibration procedures that ensure accurate characterization of the THz communication channels.

2. **Characterization of CS Systems:** One of the key challenges in THz communications is accurately characterizing the communication channel itself. This objective evaluates different CS systems, both guided-wave and OTA, under controlled experimental conditions. By analyzing the performance of these systems in terms of channel estimation, delay spread, path loss, and other parameters, the work will provide insights into their suitability for THz channel modeling. This will involve the testing of various hardware setups and measurement configurations to identify the most reliable and accurate systems for THz communication channel characterization.

3. **Calibration Procedures Using VNAs and Correlation-Based CSs:** Accurate calibration of measurement instruments is essential to ensure that the readings taken during experimental setups are precise and consistent. This objective focuses on testing and evaluating calibration procedures for VNAs and correlation-based channel sounders at WR05 and WR03 frequency bands. The work will investigate the methodologies used to calibrate these instruments for THz frequencies and evaluate their performance in a controlled testbed environment. By doing so, this objective aims to establish best practices for instrument calibration in THz communications.

4. **Exploring Time-Varying Signal Propagation in THz Communications:** The dynamic nature of THz communication channels, particularly in mobile or rapidly changing environments, requires a thorough understanding of time-varying signal propagation. This objective investigates how THz signals behave over time, considering factors such as mobility, atmospheric conditions, and interference. By using a VNA, the research will analyze how these time-varying conditions impact the communication performance, including signal stability, bandwidth availability, and error rates. This will help in developing accurate models for dynamic THz channels and provide insights into optimizing THz communication systems for

https://doi.org/10.7795/110.20260421

real-world conditions.

5. **Measurement Testbed Using Optical-Based Transmitters and RF Receivers:** A final objective of this research is to create a measurement testbed for real data transmission in the sub-THz band. This involves using an optical-based transmitter, which is often employed in high-frequency communications, alongside an RF receiver to propagate QAM modulated signals. By testing this system, the research will evaluate the feasibility of real data transmission, examining factors such as processing techniques, beam profile, frequency hopping and the voltage biasing effect on the transmitted signal. The objective is to investigate the optical and RF components to enable efficient and reliable data transmission in the sub-THz band, a key challenge for future THz communication systems.

The findings will serve as a foundation for improving measurement standards, developing more reliable testing methods, and advancing the practical deployment of THz communication systems in real-world applications.

Each objective corresponds to a specific part of the thesis: Investigation of Metrology Principles are covered in Chapter 2, Characterization of CS Systems is addressed in Chapter 3, Calibration Procedures Using VNAs and Correlation-Based CSs is detailed in Chapter 4, Exploring Time-Varying Signal Propagation in THz Communications are explored in Chapter 5, and the Measurement Testbed Using Optical-Based Transmitters and RF Receivers is presented in Chapter 6.

1.3 Structure of the Thesis

The thesis is organized as the following:

Chapter 2 defines the fundamental principles related to this work. It begins by introducing the system architecture of the VNA, CS systems based on correlation techniques, and optical-based CS operating at sub-THz frequencies. Next, the metrological principles required to achieve traceability for both the VNA and CS systems are presented. This outlines key calibration procedures and measurement techniques to ensure accuracy and consistency. Following this, the fundamentals of signal propagation in both guided and OTA environments are discussed. This includes essential calibration considerations and theoretical calculations related to path loss and antenna characterization. Additionally, signal processing techniques relevant to channel impulse response and frequency response analysis are explored. A visual representations of propagation characteristics in both the time and frequency domains and discuss the challenges associated with filtering and signal processing techniques to ensure reliable and repeatable measurements across different measuring devices are provided. Also a theoretical background on the use of interpolation and windowing techniques and their influence on the received signals is presented.

Chapter 3 investigates the calibration procedures related to the VNA and CS systems. It includes the VNA system error corrections applied to correct the VNA systematic errors

https://doi.org/10.7795/110.20260421

to enhance measurement precision.

It investigates two well-known VNA calibration procedures to ensure repeatability in sub-THz measurements. Various calibration techniques, including unknown through, offset short, short, match (UOSM) and through, reflect, line (TRL) calibrations are explored, evaluating their effectiveness at sub-THz frequency bands. Additionally, transmission tracking drift, which arises from instability in the measurement system over time are examined. The magnitude and phase drift influence on the VNA's transmission S-parameters are evaluated. Another VNA characterization involves the impact of noise floor and trace noise on system performance. High-frequency measurements are susceptible to external interference and instrument noise, so the VNA is characterized to monitor the noise influence on the measurement uncertainties. Lastly, the theoretical Friis path loss model to characterize the VNA's non-linearity and cable movements is used.

In this chapter, the antenna characterization regarding their radiation pattern, gain, and phase center characterization over different frequencies covering the spectrum under test is presented.

It explores CS systems and their calibration procedures. CS system performance is often affected by systematic errors and calibration challenges. The first aspect involves the time-zero measurement, essential for establishing accurate reference points in time-domain measurements using a reference transmitter. It also examines the back-to-back frequency response, which helps evaluate the frequency-dependent behavior of the CS system and ensures a flat response across the measurement bandwidth. Then, the in-phase and quadrature imbalance, which affects the CS spectrum in magnitude and phase, distorting the complex-valued received signal measurements is investigated. Lastly, the analysis of the DC offset, which arises due to imperfections in CS design is examined. This includes the DC offset's influence on the received signal, which can negatively affect system linearity.

Chapter 4 presents different OTA measurement scenarios to compare the VNA and the CS equipment at different frequency bands, around 200 GHz and 300 GHz. First, it explores LoS measurement scenarios, which are fundamental for characterizing direct-path propagation. The CS's frequency step size, bandwidth feasibility, spectrum boundaries, and reference measurement selection are key aspects. It also presents multipath propagation, where signals reflect off various surfaces, causing interference patterns. It examined three key scenarios represented by: plane reflector analysis, which models single-surface reflections and their impact on signal strength, and single-reflector and multiple-reflector cases, the signal propagation reflected from small reflective objects in terms of their power delay profile (PDP) path gain and delay at different rotations is analyzed. These controlled measurement scenarios help to characterize the different equipment and to understand the effect of having complex propagation environments.

Chapter 5 investigates the THz signal transmission in a time-varying measurement scenario

https://doi.org/10.7795/110.20260421

using a VNA; it focuses on understanding time-dependent changes in channel characteristics and their influence on how the VNA captures the signal. It investigates the traceability challenges of measuring time-varying waveforms to understand the measurement uncertainties and the benefit of using a combination of CW and LS segments to obtain accurate velocity and positioning information. A measurement setup to create a time-varying scenario, including VNA-based segmented waveform analysis to capture variations over time was built. The study combines CW and LS signals under different waveform segments using different IFBW, which controls the total sweep duration. The propagation scenario to validate the experimental results and quantify the measurement uncertainties in our error computations for both CW and LS waveform segments was simulated.

Chapter 6 presents a practical implementation of sub-THz data transmission, evaluating its feasibility through an optical-based testbed. DSP techniques to improve transmission efficiency are explored, including Resampling and normalization, constant-modulus algorithm (CMA) equalization, Frequency offset estimation, and Carrier phase recovery. It investigates the propagating beam characteristics using four parabolic mirrors, evaluating factors such as beam divergence, side lobes, and polarization effects at different sub-THz center frequencies at different locations of the measurement testbed. Finally, it conducts data transmission experiments, including QPSK modulation tests, 16-QAM measurements, and Image transmission trials, demonstrating data transfer over 6 meters.

Chapter 7 summarizes key findings, highlighting our contributions to THz metrology, channel modeling, and system characterization. It also discusses future research directions.

This logical structure ensures that calibration and theory feed directly into experimental procedures and that each chapter builds on the previous findings to support a complete, end-to-end characterization approach.

In Fig.1.5 a block diagram of the experimental investigations carried out in this thesis is presented.

https://doi.org/10.7795/110.20260421

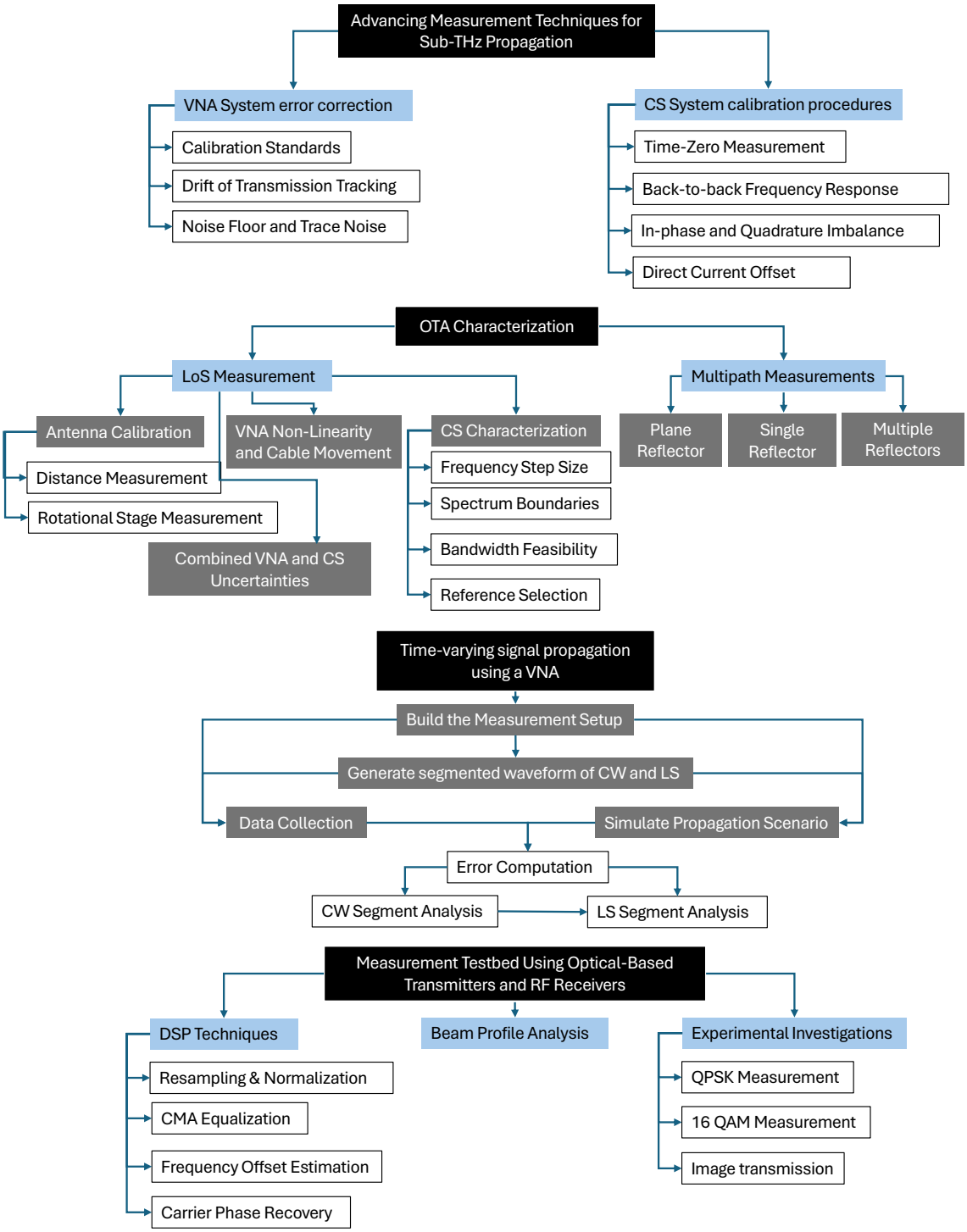

Figure 1.5: A block diagram of thesis structure.

https://doi.org/10.7795/110.20260421

2

General Principles of Measurement Systems and Channel Assessments

In this chapter, the fundamental principles related to the work presented in this thesis are defined. It begins with an introduction to the system architecture of the VNA, correlational-based CS systems, and the photonic-assisted CS systems operating at sub-THz frequencies. Next, it presents the metrological principles required to achieve traceability for the VNA and CS systems, where the calibration procedures and measurement techniques used to correct for systematic errors and the recommended procedures before performing measurements are presented. After this, the fundamentals of signal propagation using waveguide-based and OTA scenarios are discussed, including essential calibration considerations, theoretical path loss, and antenna characterization calculations. Additionally, signal processing techniques relevant to channel impulse response and frequency response analysis are explored. This chapter investigates the propagation characteristics in both the time and frequency domains. It also discusses the challenges associated with IQ imbalance and signal processing techniques to ensure reliable and repeatable measurements across different measuring devices. It also presents the basic principles of guided and OTA signal propagation, and the theoretical background on interpolation and windowing and their influence on the received signals in terms of the received time-domain and frequency domain responses.

2.1 System Architecture

2.1.1 VNA Architecture

The VNA is a fundamental measurement device used to characterize and emulate measurement networks, including static wireless channels [26, 27]. This makes the VNA essential for calibrating and validating the scattering parameters of other CS systems. VNAs offer flexibility regarding frequency range selection, frequency step size, and range resolution. The VNA provides accuracy by detecting slight variations in the measurement environment, thanks to their low noise floor and trace noise, which are controlled by setting a suitable IFBW, dwell time, and averaging control [28]. The VNA's IFBW can be as low as a few hertz, allowing the VNA to elevate the investigated signal above the noise and enhance confidence in the

https://doi.org/10.7795/110.20260421

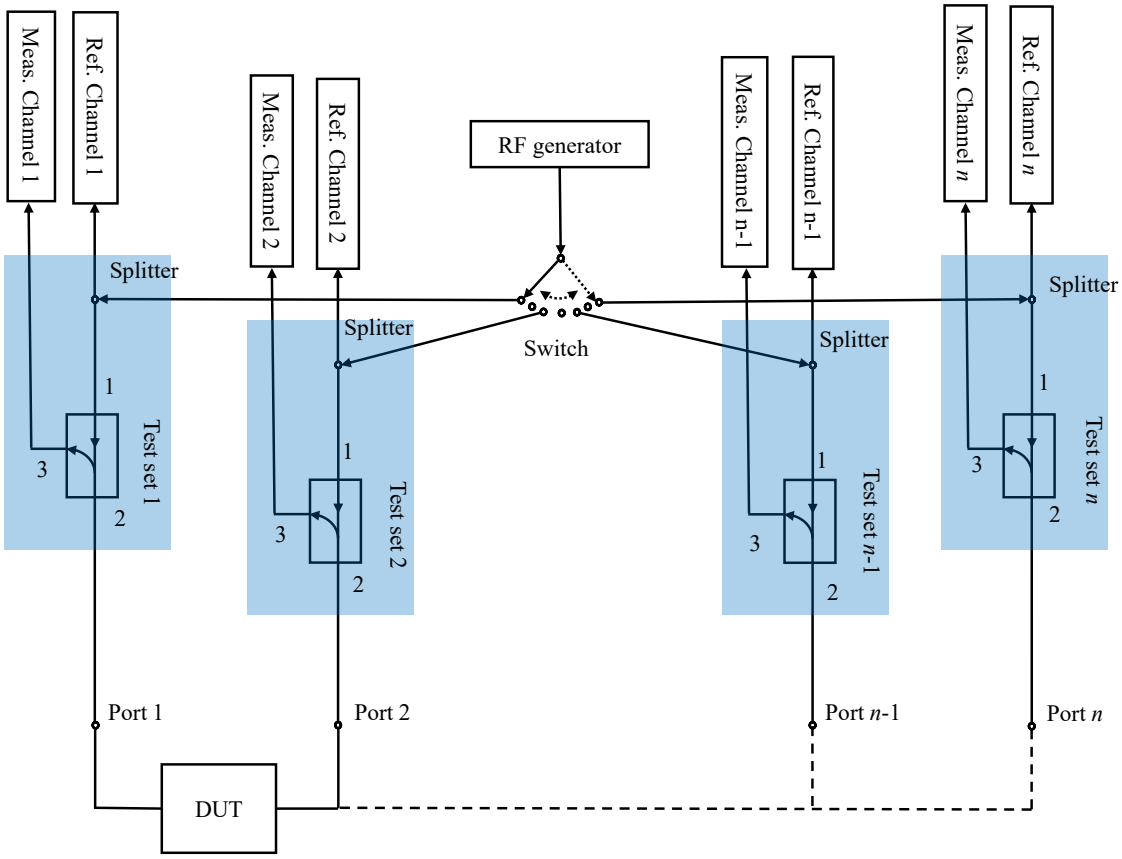

Figure 2.1: n-port network analyzer architecture. The signal from an RF generator is distributed to active ports, which are switched on consecutively. Measurement and reference channel receivers serve to measure the wave quantities.

measured values. Throughout this thesis, the IFBW settings are used extensively in Chapter 3 for calibration validation and in Chapter 5 to manage time-varying signal detection.

The VNA also allows flexibility in investigating specific frequency ranges with customized frequency step size, making it a suitable reference measuring device to perform comparisons with other CS systems [29].

Compared to other CS systems, VNAs have well-established calibration procedures that resolve systematic errors using linear equations via mechanically characterized calibration standards [30]. The calibrations ensure that measurements are repeatable with known uncertainty contributions for each investigated error term, establishing traceability in the measured values. The VNA's architecture, measuring the frequencies in sequential steps, makes it unsuitable for characterizing rapidly changing channels.

The architecture of a VNA is designed to measure the S-parameters of a device under test (DUT) across a wide range of frequencies, providing information about the transmission and reflection properties of RF and microwave networks. The VNA consists of several key components that work together to perform these measurements accurately. Fig. 2.1 shows the architecture of an n-port network analyzer [31, 32].

The signal source is one of the main components of the VNA, which generates a stable, CW

https://doi.org/10.7795/110.20260421

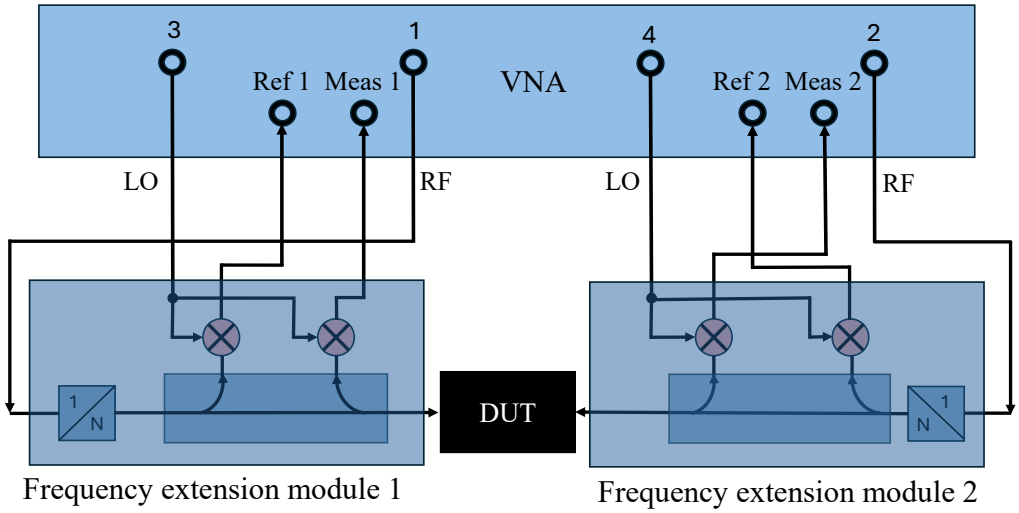

Figure 2.2: External frequency extension modules for waveguide bands. To operate the extension modules, a 4-port VNA with access to reference and measurement channels at two ports is necessary.

signal over a specified frequency range. This signal is directed towards the DUT through a series of switches and couplers, which allow the VNA to control and direct the signal as needed. The splitters and couplers are used to separate signals propagating forward and backward from the DUT, referred to as test sets.

Directional couplers are essential in the VNA's architecture, as they split the incident and reflected signals at each port of the DUT. The incident signal is the one that is sent towards the DUT, while the reflected signal is the portion that is bounced back from the DUT. The VNA measures the incident and reflected signals to determine the reflection and transmission coefficients [33].

The signal is then digitized by an analogue-to-digital converter (ADC) to allow the VNA's DSP to apply the data analyses. The digital amplitude and phase information are extracted through the DSP process, and the S-parameters of the DUT are calculated.

The VNA's calibration process involves accounting for systematic errors such as cable losses, impedance mismatches, and signal leakage, which can affect the accuracy of the S-parameter measurements. Calibration routines measure known standards (e.g., open, short, match, and through) to characterize the VNA's internal error terms. Generally, the upper-frequency limits of the coaxial connector system used, e.g., N (18 GHz), 2.92 mm (40 GHz), 2.4 mm (50 GHz), 1.85 mm (67 GHz), or 1.0 mm (110 GHz), define the operation frequency range of the VNA. However, the range can be extended to distinct waveguide frequency bands using external frequency extension modules as shown in Fig. 2.2. Usually, they are operated with a 4-port VNA, which has access to reference and measurement channels at two of the ports [31, 32].

Finally, the VNA's user interface allows the operator to control the measurement process, set parameters such as frequency range and power level, and view the results.

https://doi.org/10.7795/110.20260421

2.1.2 Correlational-Based Channel Sounder Architecture

An alternative to sinusoid frequency steps used by the VNAs, a time-domain CS is a broadband measuring device based on the principle of generating a periodic signal. The correlation is performed by processing the received signal with a copy of the transmitted one to obtain the complex channel impulse response (CIR) and improve the dynamic range. The excitation signal is usually a pseudorandom binary sequence (PRBS) [34, 35] or a different type of periodic multicarrier signal like orthogonal frequency-division multiplexing (OFDM) [36].

The ultra-wideband (UWB) waveforms employed by the CSs will provide the extended measurement bandwidth across several GHz within the microwave frequency range needed to emulate real-data propagation. This broad frequency range means the RF components cannot be finely tuned to a single frequency. This makes the CSs tolerant to non-ideal behaviors, such as frequency response ripples and limited port match [37]. Calibration procedures are essential to reduce these systematic errors, ensuring that the measured data reflects only the test scenario's characteristics rather than the measurement device's properties.

The received signal is down-converted and directly digitized at a high sampling rate. A correlation of the received signal with the ideal transmitted signal is performed in post-processing. A fast Fourier transform (FFT) is later applied in the subsequent steps. A matching filter is then applied to match the frequency response of the received signal with the reference transmitted one. Band-pass filtering is sometimes applied to limit the spectrum boundaries or to correct for hardware non-idealities. An inverse fast Fourier transform (IFFT) is then performed on the filtered response to obtain the time-domain CIR. The direct correlation FFT method is viable because of the signal's periodic nature, enabling circular convolution through frequency-domain multiplication. Compared to performing correlation in the time domain, this approach significantly lowers computational complexity [34, 38].

This thesis tested two correlation-based channel sounding systems, each with a base central unit generating a 12-bit PRBS, at center frequencies of 187.5 GHz and 304 GHz. Both systems use multistage up-and-down conversion processes. The received waveforms are divided into the in-phase (I) and quadrature (Q) components, forming a double-sided band received spectrum. Each received waveform contained several recorded PRBS sequences, ranging from 40 to 256 waveforms, using the WR05 and WR03 rectangular waveguide standards, which support frequency ranges of 140 GHz – 220 GHz and 220 GHz – 325 GHz, respectively. It should be noted that while the waveguide standards cover these full frequency ranges, the CS itself may not operate across the entire band.

These waveforms are then averaged to obtain the mean complex received impulse response:

$$h_{\text{mean}} = \frac{1}{K} \sum_{k=1}^{K} h_k, \tag{2.1}$$

where K represents the number of recorded sequences, and h_k is the kth recorded complex sequence. Figure 2.3 illustrates a schematic of the up- and down-conversion principle for the extended UWB.

These system blocks form the basis of Chapter 3, where Correlational-Based Channel

https://doi.org/10.7795/110.20260421

Sounder Calibration is further investigated in Section 3.3..

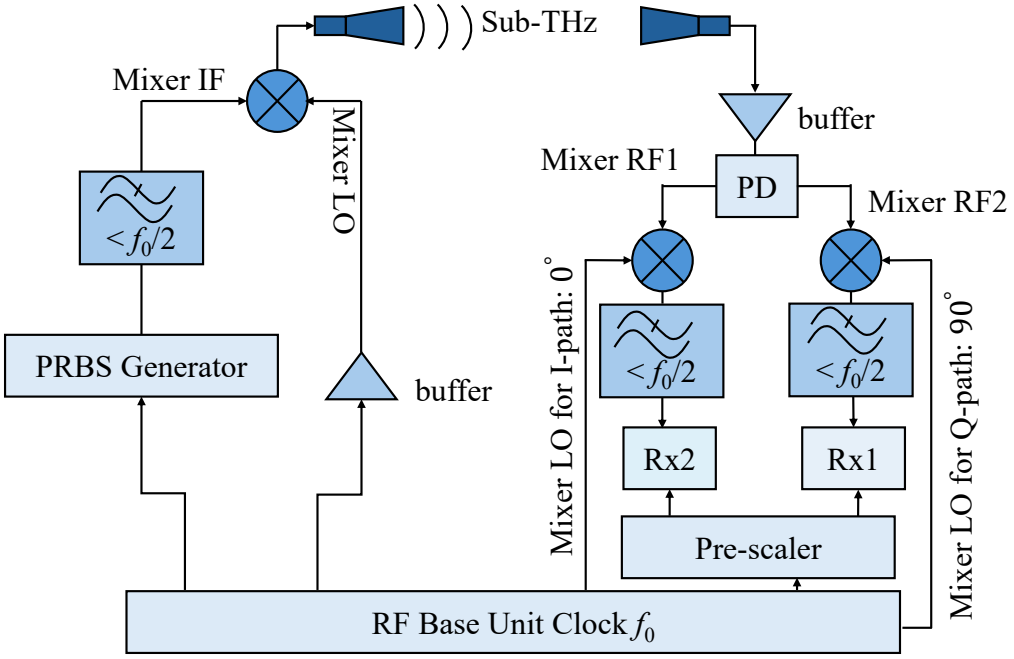

Figure 2.3: Up- and down-conversion principles in extended UWB-band CS systems. The RF base unit provides a common clock reference for phase-locking between the transmitter and the receiver. (Adopted from [39]).

2.1.3 Photonic-Assisted Channel Sounder Architecture

Since the sub-THz range lies between the RF and optical frequencies, the research investigated the possible system designs to cover the sub-THz band from both directions. Optical-based CSs employ high-performance optical components to achieve ultra-wideband and high-resolution. Compared to conventional RF systems, optical systems downconvert two optical frequencies to the targeted sub-THz range. This method provides low-loss signal generation and makes it easier to reach the higher bands of the spectrum without using the limited band waveguides, allowing for much higher tunability [40].

The optical-based systems enable precise characterization of high-frequency wireless channels, particularly for future millimeter-wave and THz communications. This section discusses the main optical-based transmitter system architecture, including laser sources, MZMs, arbitrary waveform generator (AWG)s, optical modulators, PIN-PDs, and erbium-doped fibre amplifier (EDFA)s.

Laser sources play a dual role in the architecture of optical-based channel sounders. One laser acts as the primary optical carrier, while a second laser can be used for modulation. The primary laser source provides a stable and coherent optical carrier operating mainly in the C-band (1550 nm) due to its low attenuation and high stability in optical fibers and the availability of components, as this is the main fiber communication wavelength. The carrier lasers used in communication systems have a narrow linewidth of 100 kHz or even less and high coherence, which minimizes phase noise and ensures frequency stability [41]. The two lasers are

https://doi.org/10.7795/110.20260421

combined, and their frequency offset is carefully controlled to generate a heterodyne signal. The dual-laser approach enhances the system's flexibility by allowing different modulation schemes and improving spectral efficiency [40].

To compensate for optical losses during modulation and transmission, EDFAs are employed. EDFAs boost the optical signal power, ensuring that the transmitted signal maintains a high signal-to-noise ratio (SNR). They are instrumental when the optical signal travels through long fiber links or experiences significant attenuation due to modulator insertion loss. By amplifying the modulated optical carrier before transmission, EDFAs enable high-fidelity signal propagation, which is critical for accurate channel sounding [42].

MZMs use the electro-optic effect to encode the RF baseband signal onto the optical carrier. Based on the input electrical signal, the modulator splits the light into two paths, applying a phase shift in one arm or both. When the paths recombine, the intensity-modulated light will produce the output of the MZM. Proper biasing ensures linearity, which is crucial for reliable channel characterization. Dual-drive MZMs, that enables driving the two phase modulators independently, are preferred for their broad modulation bandwidth and improved linearity, are ideal for wideband applications. By modulating the laser output, the MZM creates an optical signal ready for transmission [19].

The AWG produces precise baseband signals required for CS. Its flexibility allows the generation of various waveforms such as PRBS, chirps, and multitone signals. High-speed AWGs can output signals with bandwidths of tens of GHz, ensuring broad spectral coverage. Custom waveform generation tailored to specific measurement needs enhances the sounder's adaptability. The baseband signal from the AWG is fed into the MZM for modulation.

Next, the carrier and the modulated optical signals are coupled and fed into a photodiode (PD), where the photomixing takes place. The UTC-PD [43] and PIN-PD [44], are the two well-known, intensively used photodiodes due to their nonlinear current response. Using these photomixers can achieve an extended wide bandwidth reaching up to 3 THz, which electrical systems have problems providing. This technology is still expensive, and the design for compact-size systems that fit the user's equipment is far from being applied regularly. However, they can be used in hybrid systems as access points, turning their wide bandwidth into a possibility to communicate with different electrical-based communication systems operating at different frequencies from 100 GHz to 500 GHz simultaneously.

The PD converts the modulated optical signal into an electrical signal prior to transmission through an antenna. The PD's performance significantly impacts the transmitted signal's accuracy. It generates a photocurrent proportional to the incident optical power, and a reverse bias enhances carrier collection speed, ensuring high-frequency response. High-speed PIN-PDs with bandwidths exceeding tens of GHz is essential for wideband applications.

The signal is then propagated and received to be down-converted to an intermediate frequency (IF) for easier post-processing operations. Advanced signal processing techniques analyze the received signal. These include deconvolution to extract the channel impulse response, Fourier analysis to estimate frequency response, and noise filtering to improve channel estimation accuracy. An example of a hybrid system architecture using a sub-harmonic mixer (SHM) on the

https://doi.org/10.7795/110.20260421

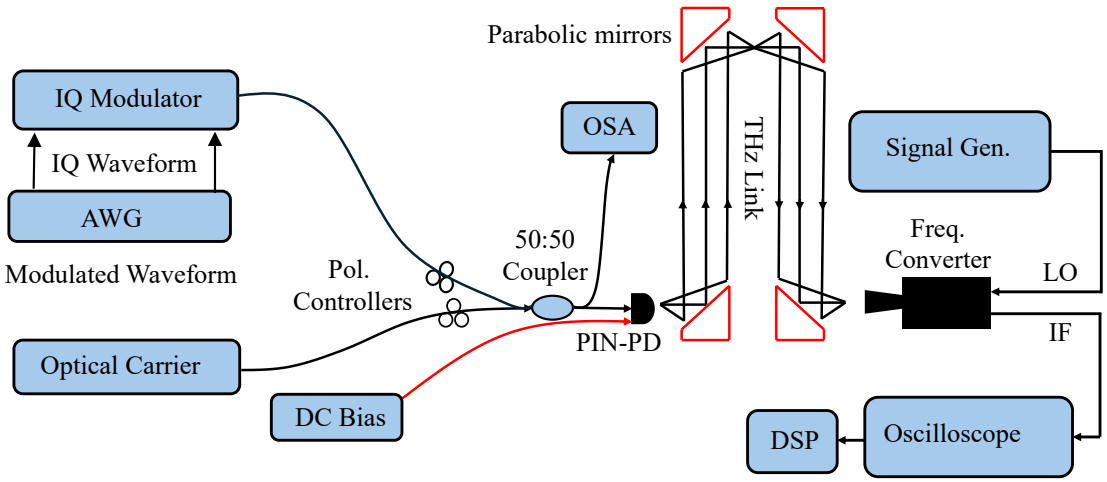

Figure 2.4: Photonic-assisted free-Space data transmission architecture showing the measurement setup of a sub-THz OTA transmission path.

receiver size is shown in Fig. 2.4. This architecture is used in the system design and evaluation presented in Chapter 6, where photonic-assisted data transmission is experimentally validated.

2.2 Metrology Fundamentals to Traceability

2.2.1 Evaluation of Vector Network Analyzers

The VNA measures the S-parameters, which have been developed in the context of microwave measurements but have a clear connection to voltages and currents that are the standard reference for most electrical engineering applications [45].

For an n-port network, the scattering parameters are described by an $n \times n$ matrix $\mathbf{S}$, where each element S_{ij} represents the ratio of the wave exiting port i to the wave incident at port j, assuming all other ports are terminated with matched loads to prevent reflections. The scattering matrix $\mathbf{S}$ establishes the relationship between the incident wave vector $\mathbf{a}$ and the reflected wave vector $\mathbf{b}$, and can be expressed as [32]:

$$\mathbf{b} = \begin{bmatrix} b_1 \\ b_2 \\ \vdots \\ b_n \end{bmatrix} = \mathbf{S} \cdot \mathbf{a} = \begin{bmatrix} S_{11} & S_{12} & S_{13} & \dots & S_{1n} \\ S_{21} & S_{22} & S_{23} & \dots & S_{2n} \\ \vdots & \vdots & \vdots & \ddots & \vdots \\ S_{n1} & S_{n2} & S_{n3} & \dots & S_{nn} \end{bmatrix} \cdot \begin{bmatrix} a_1 \\ a_2 \\ \vdots \\ a_n \end{bmatrix} \tag{2.2}$$

For example, the parameter S_{11} quantifies the reflection at port 1, indicating the fraction of the incident wave at port 1 that is reflected. The term S_{21} represents the forward transmission coefficient, describing how much of the signal applied at port one propagates to port 2. Likewise, S_{12} characterizes the reverse transmission from port 2 to port 1. At the same time, S_{22} defines the reflection coefficient at port 2, representing the portion of the incident wave at port 2 that is reflected. A visual depiction of a two-port network with its associated wave quantities is provided in Fig. 2.5.

https://doi.org/10.7795/110.20260421

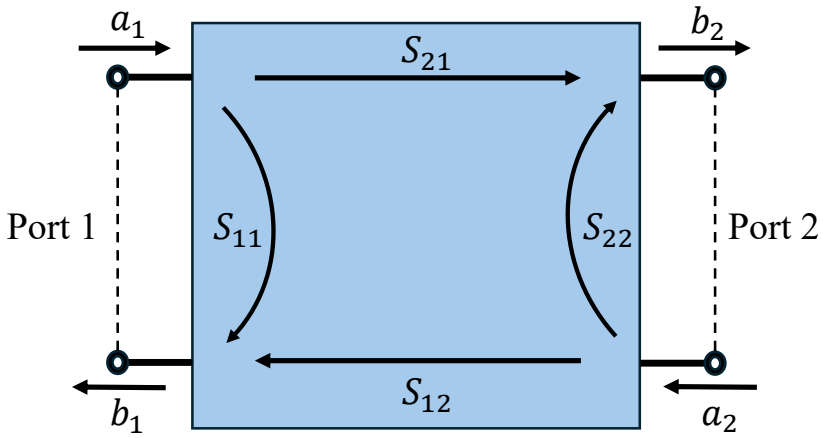

Figure 2.5: Representation of a 2-port network with wave quantities.

S-parameters are dimensionless complex numbers and can be represented either as amplitude and phase or as real and imaginary parts. Often, the amplitude is given on a logarithmic scale as $|S_{ij}|_{\mathrm{dB}} = 20 \cdot \log |S_{ij}|$. Depending on the measured S-parameter, the magnitude represents the signal strength being reflected from or transmitted through the DUT network, and the phase represents the amount of phase change of the incident signal to the received one. The magnitude and phase provide essential information on signal path loss and delay caused when the measured frequency passes through the DUT network. The VNA allows measuring in different sweep variations but typically over a wide range of frequencies, where each frequency point can provide a different response inside the measured network. This makes the S-parameters frequency dependent. These VNA measurements are performed by sending a known signal to the network and measuring the resulting signals at various ports.

Measurement errors in VNAs can be classified into random and systematic. Random errors arise from factors such as receiver noise, mechanical inconsistencies (e.g., connector repeatability and cable movements), and environmental influences like fluctuations in temperature. While these errors cannot be eliminated, they can be characterized via controlled environmental conditions and careful measurement handling. Our work incorporates extended error terms caused by environmental and hardware influences on the measured values, such as noise floor, trace noise, drift, non-linearity, and cable movement, to ensure a comprehensive and reliable calibration process [30].

On the other hand, systematic errors are predictable and can be mathematically characterized and removed from VNA measurements, particularly for linear devices. Systematic errors are traditionally grouped into three categories: *Frequency Response Errors*, which result from variations in magnitude and phase over frequency; *Mismatch Errors*, caused by impedance discontinuities leading to reflections; and *Leakage Errors*, arising from coupling between signal paths [45]. The systematic error coefficients considered during the VNA calibration process include directivity, reflection tracking, source match, and switch terms. These terms are corrected using mechanically characterized calibration standards, represented by shims of varying lengths, short standards, and match standards. By identifying, quantifying, and applying proper calibration techniques, systematic errors can be corrected, which, as a

https://doi.org/10.7795/110.20260421

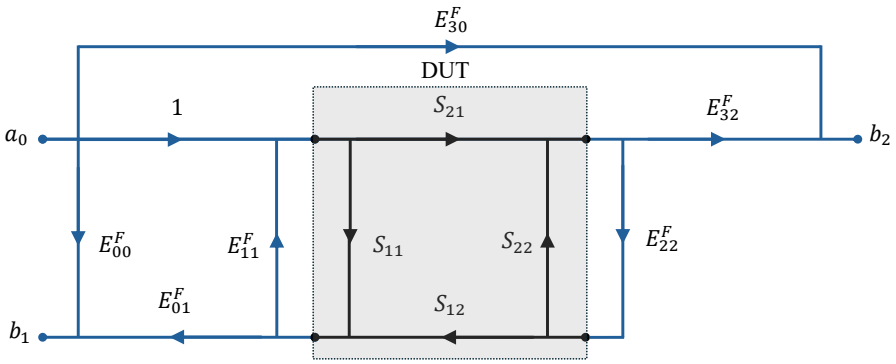

Figure 2.6: A signal flow graph representing the 12-term forward VNA error model, which includes the isolation term, is employed in two-port measurements. This model defines the relationship between the measured forward S-parameters, $S_{m11} = \frac{b_1}{a_0}$ and $S_{m21} = \frac{b_2}{a_0}$, and the actual S-parameters, S_{11} and S_{21}. (Adopted from [46]).

result, can significantly improve the precision of VNA measurements, taking into account the residual uncertainties originating from random errors [46].

Two different error models are commonly used for two-port VNA measurements: the seven-term error model and the 12-term error model. These models correspond to different VNA architectures—namely, the four-receiver VNA (or dual reflectometer VNA), in which each reflectometer has its own reference channel, and the three-receiver VNA, which employs a single reference channel.

The 12-term error model is the most widely adopted method for systematic error modeling. For a two-port VNA performing measurements in both directions, the model consists of six error terms in the forward direction and six in the reverse. Table 2.1 summarizes the error coefficients of the 12-term model. A signal flow graph illustrating the forward-direction error terms is shown in Fig. 2.6, while the reverse-direction model is depicted in Fig. 2.7 [46].

Symbol		**Error Coefficient**
Forward	**Reverse**	
E_{00}^F	E_{33}^R	Directivity
E_{01}^F	E_{32}^R	Reflection Tracking
E_{11}^F	E_{22}^R	Source Match
E_{22}^F	E_{11}^R	Load Match
E_{32}^F	E_{01}^R	Transmission Tracking
E_{30}^F	E_{03}^R	Isolation

Table 2.1: Forward and Reverse Symbols with Corresponding Error Coefficients of the 12-term error model. (Adopted from [46]).

In contrast, the seven-term error model, shown in Table 2.2, defines seven independent error coefficients, or nine when the isolation terms are included, along with two switch terms accounting for the signal path direction. This model is occasionally referred to as the eight-term error model; however, this designation overlooks the fact that one of the tracking terms is

https://doi.org/10.7795/110.20260421

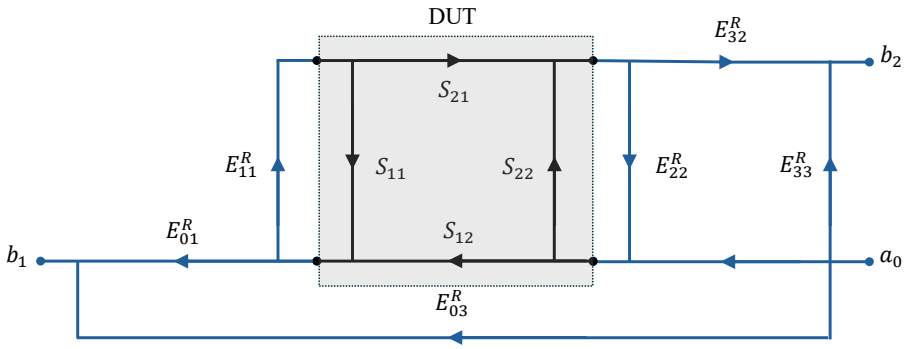

Figure 2.7: A signal flow graph representing the 12-term reverse VNA error model, which incorporates the isolation term, is utilized for two-port measurements. This model characterizes the relationship between the measured reverse S-parameters, $S_{m22} = \frac{b_2}{a_0}$ and $S_{m12} = \frac{b_1}{a_0}$, and the corresponding actual S-parameters, S_{22} and S_{12}. (Adopted from [46]).

conventionally normalized to unity, thereby reducing the number of independent parameters.

Calibration methods based on the seven-term error model have been extensively developed, employing suitable combinations of one-port and two-port calibration standards [46]. The signal flow representation of this model is illustrated in Fig. 2.8.

Symbol		**Error Coefficient**
Forward	**Reverse**	
E_{00}	E_{33}	Directivity
E_{01}	$E_{32}E_{23}$	Reflection tracking
E_{11}	E_{22}	Source match
E_{30}	E_{03}	Isolation
W_{00}	W_{33}	Switch terms

Table 2.2: Systematic Error Coefficients of the Seven-Term Error Model in VNA Measurements. (Adopted from [46]).

To include the random error terms into consideration, the flow graph can be extended to account for the random error terms listed in Table 2.3, which can be presented in terms of a flow graph illustration as shown in Fig. 2.9 [46].

The VNA calibration procedure may appear time-consuming, and calculating uncertainties for each error term requires significant effort. However, specialized software, such as VNA Tools, simplifies this process by facilitating the creation of uncertainty budgets through a calibration workflow. The software also allows the investigation of the same calibration standards with different calibration procedures and supports the determination of over-determined error terms. This is especially necessary at THz frequencies, where connection repeatability and non-linearity investigations pose challenges [47].

Using VNAs for radio channel investigations requires careful metrological considerations, particularly when the measurement range exceeds a few meters. Signal attenuation, cable movements, and reflections from unaccounted paths can impact the studied frequencies. Due

https://doi.org/10.7795/110.20260421

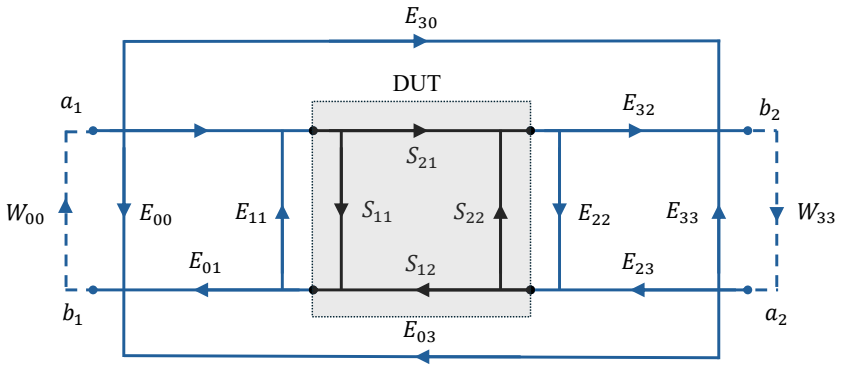

Figure 2.8: The signal flow graph illustrates the seven-term VNA error model, including the isolation terms, as applied to two-port measurements. The associated error coefficients and switch terms are summarized in Table 2.2. This model establishes the relationship between the measured S-parameters—$S_{m11} = \frac{b_1}{a_1}$, $S_{m21} = \frac{b_2}{a_1}$, $S_{m22} = \frac{b_2}{a_2}$, and $S_{m12} = \frac{b_1}{a_2}$—and the corresponding actual S-parameters: S_{11}, S_{21}, S_{22}, and S_{12}. (Adopted from [46]).

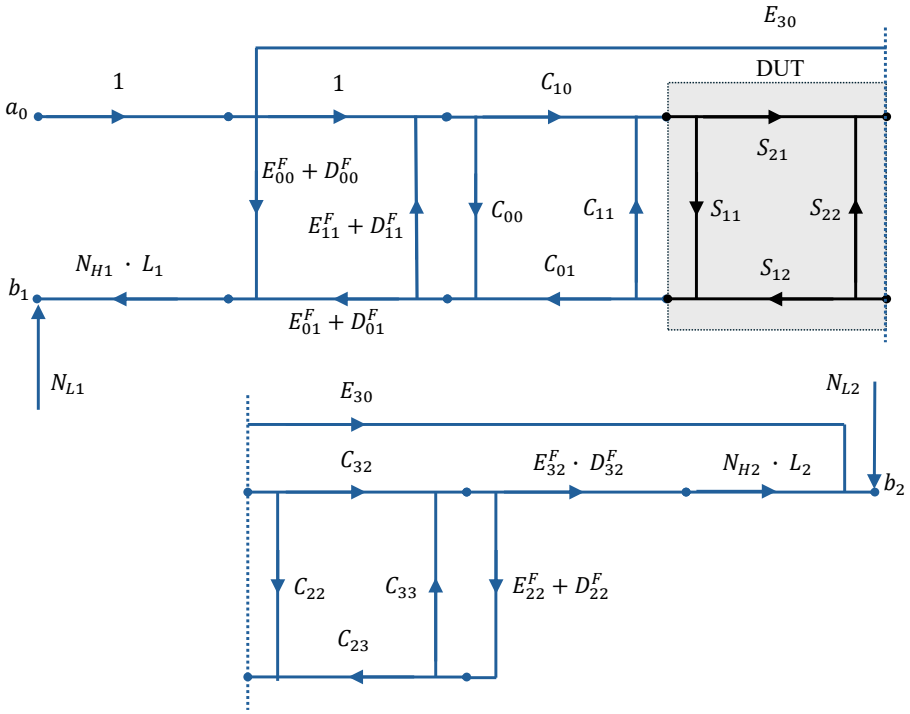

Figure 2.9: The signal flow graph represents a two-port VNA measurement model, extending the conventional 12-term forward VNA error model by incorporating additional terms that influence the measurement results. The complete diagram is presented in two separate sections, connected by dashed lines to indicate continuity. The corresponding measurement model for the reverse direction follows the same structure and is based on the ten-term reverse VNA error model. (Adopted from [46]).

https://doi.org/10.7795/110.20260421

Symbol	Description
N_L	Noise Floor
N_H	Trace Noise
L	Non-Linearity
D_{00}	Drift of Directivity
D_{01}	Drift of Reflection Tracking
D_{11}	Drift of Source Match
$C_{00}C_{11}$	Reflection of Cable and Connector
$C_{01}C_{10}$	Transmission of Cable and Connector

Table 2.3: Uncertainty Contributions of the extended error terms in VNA Measurements. (Adopted from [46]).

to their sensitivity to small changes, VNAs require accurate positioning and alignment to ensure reliable measurements. This makes VNAs more suitable for controlled measurement conditions, while outdoor measurements are generally impractical. For extended distances, one solution is to use optical-based interfaces [48], which replace long VNA cables. While effective, this approach increases complexity and cost and may introduce signal-to-noise ratio challenges due to active components in the signal path. Additionally, RF-to-optical converters are often limited to specific frequency ranges, requiring multiple assemblies to cover the entire range of interest. Another solution involves signal amplification to compensate for cable losses. Both optics-based and amplification-based solutions have unique advantages and challenges, as discussed in [49].

The systematic errors caused by directivity, reflection tracking, source match, and potentially switch terms are thoroughly accounted for in calibration procedures that characterize the quality of the test sets. Switch terms refer to errors introduced by imperfect isolation and mismatches in the internal switches of a VNA, particularly relevant when reversing signal paths during full two-port calibration. Systematic error correction can address these error terms, often denoted as the VNA calibration.

Evaluating the performance of a calibrated VNA system requires the production of uncertainty budgets, which provide insights into the expected magnitude of individual uncertainty contributions attributed to systematic errors within the measurement system [46, 50]. The VNA error model serves as the fundamental framework, enabling the translation of raw measurements into accurate and meaningful data. The error correction procedures depend on the VNA receivers configuration, aiming to define and solve the linear equations representing these error terms with high accuracy and minimal uncertainties.

This thesis uses a four-receiver VNA, which allows us to calibrate our two-port system using well-known calibration procedures. The error coefficients characterized for each port include directivity, reflection tracking, source match, and switch terms. These procedures are designed to correct these error terms by characterizing the calibration standards. Additionally, other error terms such as noise floor and trace noise, drift, non-linearity, connection repeata-

https://doi.org/10.7795/110.20260421

bility, isolation, and cable movement are considered, ensuring a comprehensive and reliable calibration.

Using the four-receiver VNA allows us to apply the calibration using the seven-term or the classical 12-term error correction model. In principle, calibration using frequency extenders and waveguides is the same as the one applied using coaxial connectors. Nevertheless, one of the critical challenges in dealing with waveguide ports is the requirement of specialized calibration standards, represented by well-characterized shims, to achieve optimal results. For this thesis calibration using two shims of $\frac{1}{4}$ and $\frac{3}{4}$ wavelength of the converter central operating range and a 180° phase shift of the reflecting coefficient is applied to ensure stability across the frequency band. Another difference is that waveguide calibration standards do not have an open standard, as an open waveguide circuit does not have a well-defined reflection [45].

Two well-established calibration procedures are used for error correction: TRL, and UOSM calibrations. These techniques are renowned for their precision, providing confidence in the accuracy of our research.

TRL calibration offers simplified and efficient methodologies for waveguide systems, further enhancing measurement accuracy and repeatability. It requires mainly four different connections to encompass seven independent error terms. Two additional switch terms ($\Gamma_F = \frac{a_1}{b_1}$ and $\Gamma_R = \frac{a_2}{b_2}$) are needed, totaling the number of unknowns to nine terms, which is the minimum number of independent equations to solve the TRL calibration problem effectively.

On the other hand, the UOSM calibration method, a classical 12-term error model, offers its unique advantages. Similar to TRL calibration, this method requires the computation of switch terms. However, unlike TRL, UOSM calibration employs the same set of calibration standards used in 12-term calibration, while offering distinct degrees of freedom in the calibration process [45].

The UOSM calibration method is straightforward. It requires a single transmission measurement under reciprocity between the two transmission S-parameters; hence, their product S_{21}^2 presumes reciprocity. The insertion loss should be well above the noise floor, and the distance between the ports should be below 90° of electrical length between the subsequent frequency steps. This is why sufficient frequency points for wider unknowns through calibration distance are necessary to obtain the correct phase values. Similar to TRL calibration, the values for Γ_F and Γ_R are measured during the unknown through calibration step. Six more connections are required to finalize the calibration process. These provide two independent equations for each tested standard, totaling 12 independent equations obtained to solve the error terms. The solution is rather complex but has been presented in several forums and is available in the literature.

The advancement in the VNA measurement process and modeling achieves measurement traceability across all fundamental RF/microwave parameters, including impedance, power, attenuation, frequency, and noise. The identified VNA-specific errors, such as calibration procedures, drift, noise, and non-linearity are discussed in Section 3.1 through VNA calibration and error modeling.

At sub-THz frequencies, establishing the traceability chain is increasingly challenging due

https://doi.org/10.7795/110.20260421

to the sensitivity of measurements at such high frequencies. The uncertainties associated with these standards are typically low, yet they become more pronounced at higher frequencies [51, 52]. The complexity of propagating calibration standard uncertainties through the calibration process, error correction, and, ultimately, the device measurement process intensifies with frequency. This would lead to measurement uncertainties in the range of 1 dB when no specialized calibrations are performed to quantify the error terms more accurately.

2.2.2 Evaluation of Time-Domain Channel Sounders

The correlational-based CS technique involves transmitting a predefined PRBS sequence through the channel and correlating the received signal with the original sequence to extract the CIR. Let the transmitted sequence be denoted by $s(t)$ and the received signal by $r(t)$. Assuming a linear time-invariant channel, the received signal can be expressed as [53]:

$$r(t) = s(t) * h(t) + n(t), \tag{2.3}$$

where $h(t)$ represents the channel impulse response and $n(t)$ is additive noise. The CIR is obtained by correlating $r(t)$ with $s(t)$, yielding [53]:

$$\hat{h}(\tau) = \int r(t)s(t-\tau)dt. \tag{2.4}$$

This correlation operation effectively deconvolves the transmitted PRBS sequence from the received signal, revealing multipath components characterized by distinct delays and amplitudes.

Traceability in CS necessitates strict calibration of the entire measurement setup, including carrier signal and data generators, modulators, and receivers. Each component must be carefully calibrated to ensure it operates within specified tolerances. For the transmitted PRBS sequence, it is essential to verify its autocorrelation properties to ensure accurate channel sounding. The PRBS sequence should have an autocorrelation function $\phi_{ss}(\tau)$ that closely approximates a delta function:

$$\phi_{ss}(\tau) \approx \delta(\tau), \tag{2.5}$$

so that the correlation output produces distinguishable peaks corresponding to actual multipath components without significant sidelobe interference.

Several parameters must be considered to ensure traceability in sub-THz CS. These include:

1. Time synchronization: Precise synchronization between the transmitter and receiver is critical, as any timing errors directly affect the accuracy of delay measurements. This can be accounted for using the Time-Zero measurement to a reference transmitter, correcting the phase deviations when the CS sensor nodes randomly initiate after every system's restart [54].

2. Phase noise: Phase stability of the local oscillators at both the transmitter and receiver sides is essential to ensure consistent Doppler shift and coherence bandwidth measurements, as when the physical channel is considered deterministic, phase noise disrupts its stability

https://doi.org/10.7795/110.20260421

by introducing a randomizing effect. This leads to fading and contributes to capacity errors, especially in multiple-input and multiple-output (MIMO) systems [55].

3. Noise floor: The receiver's noise floor must be well-characterized to distinguish weak multipath components from noise. CSs can be characterized using different well-characterized attenuation DUTs, with measurement repeatability, this can provide a good indication of the actual noise floor levels where the CIR will suffer an increased amount of uncertainties [56].

4. Bandwidth: The bandwidth of the transmitted signal determines the time resolution of the CIR. Wider bandwidths enable finer resolution, allowing closely spaced multipath components to be distinguished [57]. For sub-THz frequencies, UWB signals are often feasible due to the availability of large spectral bandwidths. The bandwidth characterization involves investigating the total spectrum represented by calculating the frequency step size with the total number of frequency points, and also the characterization of the feasible spectrum boundaries where the signal is properly received.

In addition to calibration and uncertainty analysis, verification of the correlation process is vital. This involves comparing the measured CIR with a known reference channel or simulated ground truth to assess the accuracy of the CS.

The correlational-based CSs were purpose-designed, with no possibility of calibrating each component individually. This makes measurement artifacts essential to perform comparable measurements with a reference measuring device as the VNA, and with theoretical calculations for signal propagation in guided or OTA channels.

The back-to-back (B2B) calibration combined with the Time-Zero measurements using a reference transmitter are the main steps to achieve a system calibration before performing any measurements in the system. Measurement repeatability at different time intervals is helpful to understand the system's behavior towards the drift, especially when the measurement duration requires an extended time before the re-calibration process.

The B2B calibration used artifacts need to be well characterized to be able to distinguish their influence on the measurement, as it will act as the reference that all the subsequent measurements will depend upon when evaluating the frequency and impulse response.

CS systems need to be evaluated towards their basic parametric measurements, as minor deviations can lead to extended measurement errors in terms of phase and magnitude.

An example is the IQ imbalance. CS hardware can be affected by impairments caused by the mismatch between the analog components of I and Q paths in the RF chain, which is known as the IQ imbalance. The IQ imbalance can be due to a gain imbalance, which is the amount of amplifier and filter gain imbalance between I and Q signals. Alternatively, a Timing skew originating from the difference in sampling instances of I and Q signals or both can contribute to the phase mismatch between I and Q signals as shown in Fig. 2.10.

$$I'(t) = A[I(t) - Q(t-\tau)]\sin\varphi, \tag{2.6}$$

$$Q'(t) = Q(t-\tau)\cos\varphi, \tag{2.7}$$

https://doi.org/10.7795/110.20260421

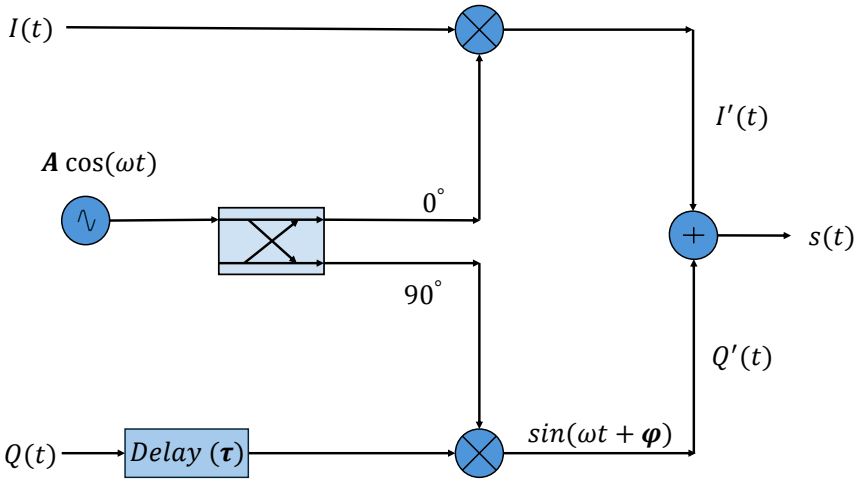

Figure 2.10: IQ impairment of a CS system representing the possibilities of gain and timing imbalance.

where

$$G = 10^{\frac{\text{IQ Gain Imbalance}}{20}},$$

ϕ is the quadrature skew, τ is the timing skew,

A is the magnitude of the signal,

$I'(t)$ is the impaired in-phase component of the signal,

$Q'(t)$ is the impaired quadrature-phase component of the signal,

$I(t)$ is the ideal in-phase component of the signal,

and $Q(t)$ is the ideal quadrature-phase component of the signal.

Another example is the DC offset, where the local oscillator (LO) may suffer from frequency leakage, which combines with DC offsets introduced by the sampling circuits and ADCs. These offsets arise from inherent mismatches in analog components, such as bias currents, voltage offsets, and clock feedthrough in the sampling circuitry, as well as quantization and reference voltage errors in the ADCs. The combination of these effects can introduce strong unwanted components at or near DC, resulting in unreliable information that must be carefully filtered out during signal processing [58].

Using different hardware components will influence the CS's spectrum boundaries, which need to be investigated carefully to avoid including extra noise in the measurement analysis; the frequency step size can be very effective in having the correct delay accuracy, and this takes into account characterizing the antenna elements knowing their reference plane to achieve precise delay calculations.

The B2B measurement calibration serves as the reference for all subsequent measurements. Therefore, it is recommended to perform it multiple times and compare different B2B measurements in order to establish the measurement uncertainty associated with evaluating the same artifact using different calibration references. This will be very helpful in selecting different delays and attenuations and providing valuable information on the equipment noise floor and the range resolution.

The calibration aspects introduced here are considered in Chapter 3 when applying the B2B

https://doi.org/10.7795/110.20260421

calibration and matching the reference plane with the VNA is applied. This work will compare system performance by investigating further on IQ imbalance and DC offset in Sections 3.3.3 and 3.3.4, respectively.

2.3 THz Signal Propagation

2.3.1 Guided Signal Propagation

At sub-THz frequencies, hollow waveguides are often the preferred transmission medium due to their low loss and high power-handling capabilities [59]. Hollow waveguides are easier to handle and fabricate than other transmission lines, such as gap waveguides, and provide a minimal loss compared to microstrip and substrate-integrated waveguides. Their advantages originate from a large single-mode bandwidth, ease of integration, and well-established fabrication techniques, making them particularly relevant for emerging applications such as 6G communications, high-resolution radar, and terahertz imaging.

Rectangular metallic waveguides, in particular, are widely used in this frequency range and are well-standardized. IEEE standards define waveguide dimensions, frequency bands, and measurement uncertainties, providing a framework for accurate and repeatable measurements [60–62].

NMIs rely on these standardized waveguides to establish traceability at these frequencies [63]. A prerequisite for such traceability is the availability of reference standards for calibrating measurement instruments such as VNAs. VNAs are commonly used for sub-THz measurements, characterizing DUTs through scattering parameters. To ensure reliable results, these instruments must be calibrated using well-characterized reference standards [64, 65]. The accuracy of these measurements depends on selecting the correct waveguide interfaces and following proper operating procedures [15].

Standard rectangular waveguides are typically designed so that each frequency band starts where the previous one ends, with some overlap to ensure smooth transitions [66]. The lower frequency edge is generally set about 25 % above the waveguide's cut-off frequency, while the upper edge is around 5 % below the cut-off of the next higher-order mode. The waveguide height is usually half its width, a proportion that optimizes both mechanical stability and electromagnetic performance. Hollow waveguides, being entirely metallic, provide fully shielded transmission with minimal radiation and dielectric losses since no substrate is required. However, due to complex transitions and packaging constraints, their non-planar structure makes integration with other transmission lines challenging.

Additionally, their performance is sensitive to manufacturing and assembly tolerances, particularly in multi-layer structures like antenna arrays, where good electrical contact between adjacent waveguide layers is critical. The fabrication of hollow waveguides typically involves etching multi-layer metallic structures and bonding them using diffusion bonding [67]. A waveguide schematic of a WR03 waveguide is shown in Fig. 2.11.

The characterization of attenuators and line waveguides is crucial for calculating the signal propagation delay inside the waveguide, defining the CS reference plane, and investigating the

https://doi.org/10.7795/110.20260421

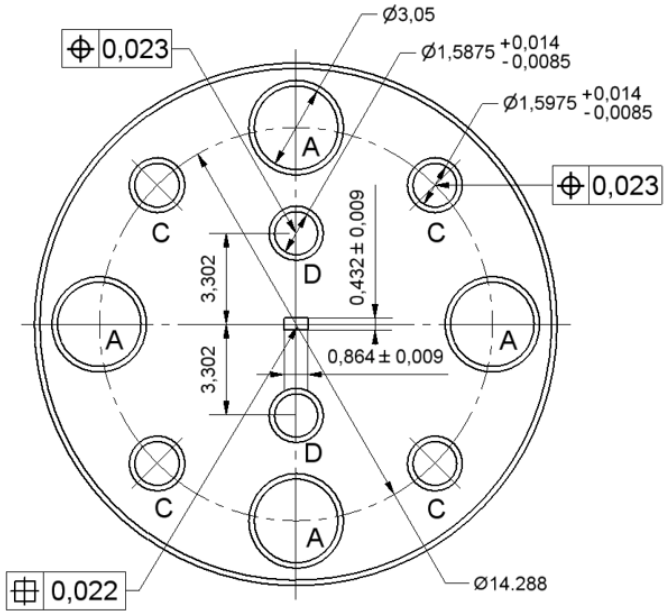

Figure 2.11: Drawing of shim of the R&S ZV-WR03 with mechanical tolerances [68].

CS's linearity for LoS and multipath reflections.

It also acts as a standard where metrological principles can be easily applied, and the measurement uncertainties can be calculated. It is still the preferable transmission line in VNA and CSs as both kinds of equipment use it as an output for their up- and down-converted connections with standard horn antennas, for instance.

This work mainly deals with the WR05 and WR03 waveguide standards to cover the sub-THz frequencies under test. Their specific dimensions influence cut-off frequency, signal propagation characteristics, and signal loss. The cut-off frequency f_c of the dominant TE_{10} mode for a rectangular waveguide is given by [15, 60]:

$$f_{\mathrm{c}} = \frac{c}{2a}, \tag{2.8}$$

where c is the speed of light, and a is the more significant inner dimension of the waveguide. For WR05 ($a = 1.27\,\mathrm{mm}$) and WR03 ($a = 0.864\,\mathrm{mm}$), the cut-off frequencies are approximately 118 GHz and 174 GHz, respectively, allowing WR05 to operate up to 220 GHz and WR03 up to 330 GHz. These dimensions enable WR05 and WR03 waveguides to support higher frequencies and increase susceptibility to conduction loss as the frequency approaches the cut-off.

The attenuation constant, α, is calculated using the following formula [60]:

$$\alpha = 0.023273 \times \sqrt{\frac{\rho}{\rho_0}} \times \frac{1}{b\sqrt{a}} \times \frac{\left(\frac{f}{f_{\mathrm{c}}}\right)^2 + \frac{2b}{a}}{\sqrt{\frac{f}{f_{\mathrm{c}}}} \times \sqrt{\left(\frac{f}{f_{\mathrm{c}}}\right)^2 - 1}} \quad \mathrm{dB/cm}, \tag{2.9}$$

where:

https://doi.org/10.7795/110.20260421

- ρ = resistivity of the waveguide conductor
- ρ_0 = reference resistivity = 17.241 nΩ·m
- a = waveguide width (mm)
- b = waveguide height (mm)
- f_c = cut-off frequency (GHz)
- f = frequency at which attenuation constant is calculated (GHz)

Electrical length L_e is critical for phase-sensitive applications and depends on the effective guided wavelength λ_g, which is [69]:

$$\lambda_g = \frac{\lambda_0}{\sqrt{1-(f_c/f)^2}}, \tag{2.10}$$

where λ_0 is the free-space wavelength. For a waveguide of physical length L, the electrical length L_e is:

$$L_e = \frac{L}{\lambda_g}. \tag{2.11}$$

Small mechanical changes in WR05 and WR03, such as flange misalignment, introduce phase and magnitude errors, which become more relevant to smaller waveguide dimensions.

Ensuring precise and consistent waveguide connections requires accounting for flange quality, appropriate torque application, and any additional alignment tools used during setup, as these factors can impact the adequate torque at the interface [45]. Meanwhile, misalignment or inconsistent torque can lead to reflection losses and insertion loss variability, which can be mitigated by multiple calibrated reconnections at varying azimuthal orientations. These values can be statistically measured and included within the measurement uncertainty budget [63].

A cascade of waveguide components made of attenuators and lines is typically used to set a reference phase and magnitude for a CS reference measurement. This helps to specify the calibrated delay and path loss for other measurements, as shown in Fig. 2.12(a).

A waveguide line in the WR05 band has been simulated and fabricated in the Scientific Instrumentation Department at Physikalisch-Technische Bundesanstalt (PTB), as shown in Fig. 2.12(b).

Our tests involved the WR03 waveguide cascade and the fabricated WR05 waveguide line, focusing on measurement repeatability under different orientations and reconnections to determine the associated measurement uncertainties. Figure 2.13(a) and (b) show the extended uncertainties of the repeated waveguide measurements for reconnection, flipping, and rotation, specifically for the scattering magnitude S_{21} at 180 GHz – 200 GHz and 290 GHz – 310 GHz, respectively.

An example of the PDP measurement of a WR03 waveguide cascade consisting of two lines and two attenuators characterized using the VNA and the correlational-based CS systems is presented in Fig. 2.14.

https://doi.org/10.7795/110.20260421

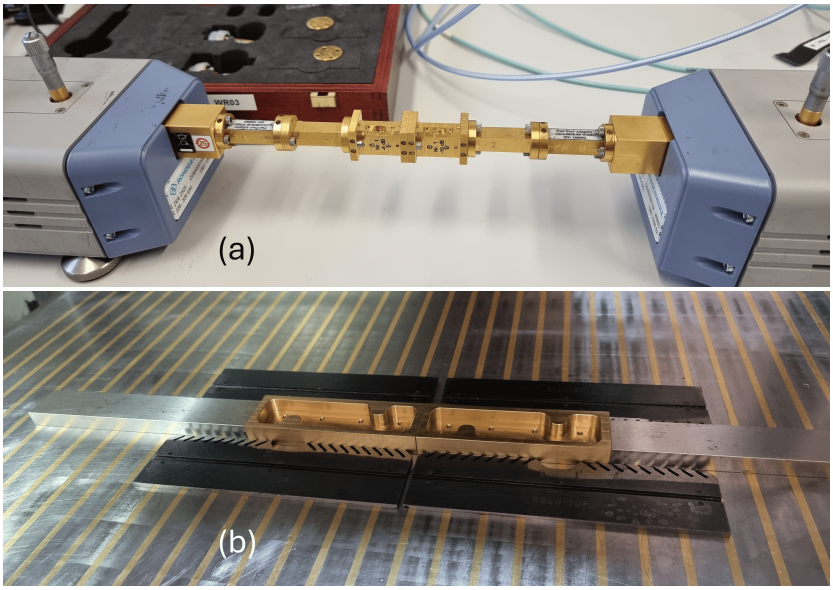

Figure 2.12: Component characterization, (a) Attenuators and lines cascaded in the WR03 band. (b) Waveguide artifact fabrication in the WR05 band.

2.3.2 Over-the-Air Signal Propagation

To investigate the full range of OTA signal propagation at sub-THz frequencies, it is essential to examine various factors that impact the quality of communication and measurement systems. These aspects include the underlying physics of propagation, antenna characteristics, calibration procedures, channel impairments, and the specific challenges posed by sub-THz frequencies [39, 70].

Characterizing CS systems is essential for ensuring reliable sub-THz radio channel measurements and managing uncertainties. Controlled conditions are essential to isolate hardware imperfections, such as non-linearities and sampling noise, which standard calibrations cannot fully resolve. These imperfections can distort the actual channel properties, emphasizing the importance of comprehensive characterization to enhance precision, as highlighted in prior millimeter wave studies [71, 72]. Sub-THz systems face challenges due to increased susceptibility to hardware instability and environmental factors, requiring repeatable testing under controlled conditions. Accurate measurements at these frequencies are essential for developing reliable channel models, as impairments like hardware noise and external disruptions significantly impact parameters such as PDP, delay spread, and path gain [39]. These issues can introduce artifacts during postprocessing, compromising model accuracy. While early studies on sub-THz propagation for indoor, outdoor, and industrial scenarios are available [73–75], further work is needed to refine methods for analyzing errors, ensuring accurate propagation models.

Channel modeling is essential in developing wireless technology. It accounts for different conditions, such as LoS and multipath propagation. It helps analyze the measurement system's reliability and characterize the measurement parameters.

Traditionally used for free-space propagation, the Friis path loss equation remains a cor-

https://doi.org/10.7795/110.20260421

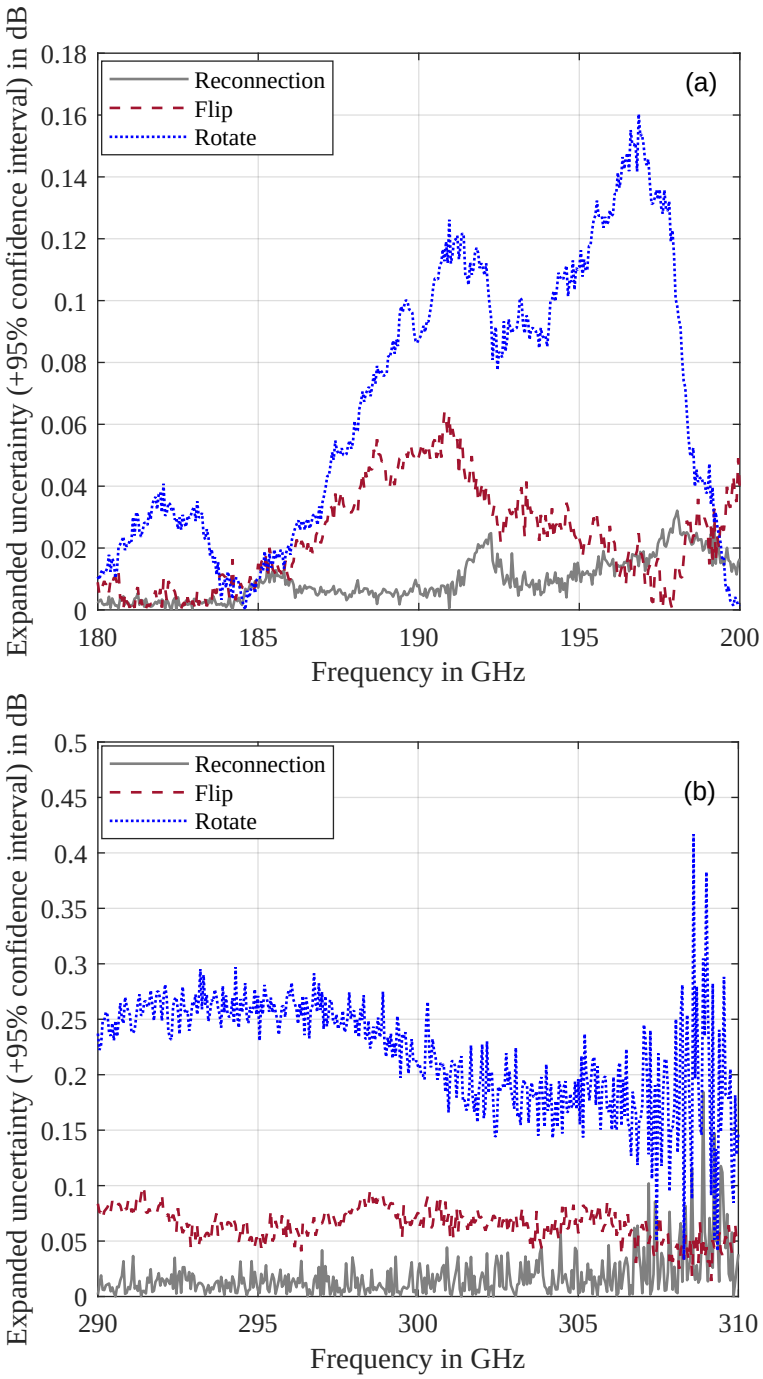

Figure 2.13: Magnitude of the expanded measurement uncertainty at the +95 % confidence interval ($k = 2$), expressed in dB, for the waveguide components following reconnection, flipping, and waveguide artifact rotation by 180° measured using (a) WR05 and (b) WR03 waveguides.

nerstone for OTA propagation analysis. However, at sub-THz frequencies, its application must be extended to incorporate the effects of antenna gains, environmental conditions, and atmospheric absorption, which significantly impact these high frequencies [76, 77].

Absolute gain measurements are based on the Friis transmission formula, which states that for a two-antenna system, the power received at a matched load connected to the receiving antenna can be calculated as [78].

https://doi.org/10.7795/110.20260421

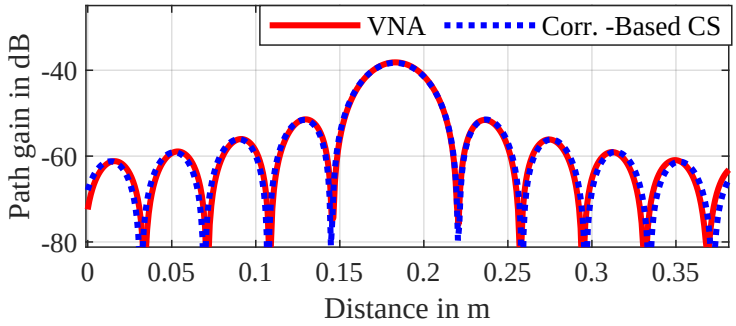

Figure 2.14: Reference waveguide PDP measurement result consisting of two attenuators and two lines. The measurement used the VNA and the CS devices at the WR03 band.

$$L_{\text{path}} = \left(\frac{4\pi df}{c}\right)^2 \cdot \frac{1}{G_{\text{T}} G_{\text{R}}}, \tag{2.12}$$

where:

- d is the distance between the transmitter and receiver,
- f is the frequency of the signal,
- c is the speed of light,
- G_{T} and G_{R} are the gains of the transmitting and receiving antennas, respectively.

This transmission formula assumes that the antennas are aligned correctly in terms of polarization and that the separation distance satisfies the far-field condition. For directive antennas such as horn antennas, the far-field region is generally considered to begin at a distance of $d_{\text{FF}} \geq 2D_{\text{ph}}^2/\lambda_0$, where D_{ph} is the largest physical dimension of the antenna aperture. Meeting this condition ensures that the phase front is locally planar, minimizing near-field effects and validating the use of the Friis transmission equation [79]. Other variations may include additional factors to account for mismatches at the antenna terminals and polarization discrepancies [79]. To measure the antenna gain, two well-known measurement techniques are used:

- **Two-Antenna Method:** When antennas A and B are identical or one of them with known gain, their gains can be determined by measuring the separation distance, the power received, and the power transmitted. Since this method involves only two antennas, it is referred to as the two-antenna method [80].
- **Three-Antenna Method:** If antennas A and B are different, a third antenna, C, with a known gain, is used. The received power is measured for each antenna pair, and the gains of all three antennas are calculated by solving a set of linear equations. In this setup, antenna A is used only for transmission, antenna C only for reception, and antenna B operates in both modes, meaning it must be reciprocal. Measurements are

https://doi.org/10.7795/110.20260421

taken for all three antenna combinations, leading to Equations the following equations [80].

$$(G_A)dB + (G_B)dB = 20\log_{10}\left(\frac{4\pi R}{\lambda}\right) - 10\log_{10}\left(\frac{P_{in}}{P_r}\right)_{AB}, \tag{2.13}$$

$$(G_A)dB + (G_C)dB = 20\log_{10}\left(\frac{4\pi R}{\lambda}\right) - 10\log_{10}\left(\frac{P_{in}}{P_r}\right)_{AC}, \tag{2.14}$$

$$(G_B)dB + (G_C)dB = 20\log_{10}\left(\frac{4\pi R}{\lambda}\right) - 10\log_{10}\left(\frac{P_{in}}{P_r}\right)_{BC}, \tag{2.15}$$

where G_A, G_B, and G_C represent the antenna gains of antennas A, B, and C, respectively. P_{in} and P_r denote the input power to the transmitting antenna and the received power at the receiving antenna, respectively. R is the separation distance between the antennas' phase centers, though it is often generalized to the aperture-to-aperture distance, as the exact value is typically not critical when operating in the far-field. λ is the wavelength of the transmitted signal.

Another factor to consider with the antennas for successful OTA transmission at sub-THz frequencies to be able to characterize the metrological principles using OTA measurements, is the necessity to consider the radiation pattern at different frequencies and the changes related to the phase center (PC) calculations.

The antenna's PC, is where the electromagnetic waves appear to originate. Accurate knowledge of the PC is essential for minimizing measurement errors in OTA testing, especially at high frequencies. The phase center location can shift with frequency and the antenna's design, which could lead to discrepancies in the received signal strength and phase measurements if not adequately accounted for [26].

Understanding the precise location of the actual phase center for an antenna is often an important system integration need. Knowledge of the accurate antenna phase center position and phase center variation factors are critical in precise positioning, especially in the sub-THz range [78]. For metrological applications and to achieve a high directivity to compensate for the path loss at the sub-THz band, horn antennas are widely used for that purpose, and their gain, radiation pattern, and PC were under investigation. The horn antenna PC was mathematically calculated based on their dimensions. A graphical representation illustrating these dimensions in relation to their phase center calculations is shown in Fig. 2.15 [81].

The PC of a horn antenna is determined using Fresnel integrals, incorporating wave propagation characteristics and antenna dimensions to estimate the PC offset. The calculation begins with the Fresnel parameter v_m, which is derived from the antenna length and wavelength. Two normalized parameters, U_1 and W_1, are then introduced to frame the problem in terms of Fresnel integrals.

The Fresnel integrals include the cosine Fresnel integral $C(x)$ and the sine Fresnel integral $S(x)$, which are defined as [81]:

https://doi.org/10.7795/110.20260421

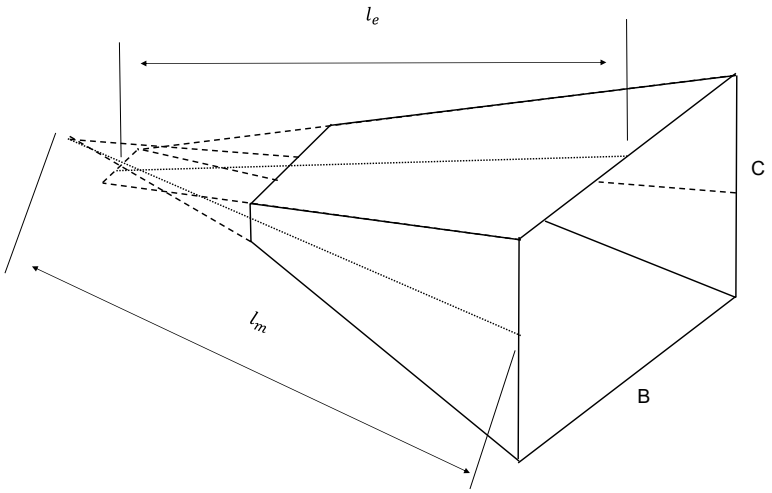

Figure 2.15: Horn antenna parameters for PC claculations, I_e represents the length of the horn along the x-axis, which is perpendicular to the electric field, while I_m denotes the length of the wall parallel to the electric field. (Adopted from [81]).

$$C(x) = \int_0^x \cos\left(\frac{\pi}{2}t^2\right) dt, \quad S(x) = \int_0^x \sin\left(\frac{\pi}{2}t^2\right) dt. \tag{2.16}$$

The values of these integrals at U_1 and W_1, denoted as $C_{U1}, C_{W1}, S_{U1}, S_{W1}$, are used in computing the PC offset. The final expression for the phase center offset Δ is [81]:

$$\begin{aligned}\Delta = l_m\Bigg(1 + &\frac{\left(W_1 \cos\left(\frac{\pi}{2}U_1^2\right) - U_1 \cos\left(\frac{\pi}{2}W_1^2\right)\right)(C_{U1} - C_{W1})}{(C_{U1} - C_{W1})^2 + (-S_{U1} + S_{W1})^2} \\ &+ \frac{\left(U_1 \sin\left(\frac{\pi}{2}W_1^2\right) - W_1 \sin\left(\frac{\pi}{2}U_1^2\right)\right)(-S_{U1} + S_{W1})}{(C_{U1} - C_{W1})^2 + (-S_{U1} + S_{W1})^2}\Bigg).\end{aligned} \tag{2.17}$$

Even though that ray-tracing techniques are valid to characterize measurement scenarios at sub-THz as with the lower frequency ranges, there is less possibility of getting a strong influence of multipath reflections, as the LoS measurement scenarios are more dominant. This will raise the need for more focused signal propagation, which will require the employment of beamforming and beam tracking techniques. While THz applications are viable for both indoor and outdoor environments, indoor scenarios are expected to be more realistic [82].

The theoretical background developed here is applied in the antenna calibration procedure presented in Section 3.2 and in Chapter 4 during experimental LoS and multipath characterization.

https://doi.org/10.7795/110.20260421

2.4 Signal Processing Techniques

2.4.1 Power Delay Profile Analysis for Understanding Signal Propagation in Communication Scenarios

The PDP is an essential tool to characterize communication systems, especially for CS measurements. It converts the received power into a function of time where multipath elements can be separated into time delays, each represented by a specific received power.

The PDP acts as a spatial filter by isolating multipath components based on their delays. This property is advantageous in distinguishing LoS and NLoS paths in complex measurement scenarios by analyzing the time delays and corresponding power levels.

The PDP captures these multipath components, enabling detailed channel characterization essential for advanced applications such as beamforming, massive multiple-input and multiple-output (MIMO), and UWB communication.

Using a VNA, the raw PDP data is obtained by taking the inverse Fourier transform (IFT) of the measured frequency response, typically represented by the complex $S_{xy}(f)$ parameter from a VNA, or the received time-domain response $h(\tau)$ for a correlational-based CS, where both hold the amplitude and phase information of the received signal over time, with the PDP derived as $|h(\tau)|^2$ [83].

$$PDP(\tau) = |h(\tau)|^2. \tag{2.18}$$

One of the key characteristics of the raw PDP data is the time resolution, which determines the ability to distinguish closely spaced multipath components. The time delay is often converted to a spatial delay in meters. The PDP is derived by taking the IFT of the frequency response $H(f)$, obtained through measurements or simulations:

$$P(\tau) = \left|\mathcal{F}^{-1}\{H(f)\}\right|^2, \tag{2.19}$$

where $\mathcal{F}^{-1}$ denotes the inverse Fourier transform, $P(\tau)$ is the power as a function of delay τ, and $H(f)$ is the complex channel frequency response.

The resulting PDP provides insights into the delay and strength of multipath components. However, the time resolution of the PDP is determined by the bandwidth B of the measurement:

$$\Delta\tau = \frac{1}{B}. \tag{2.20}$$

A larger bandwidth improves resolution but may increase noise sensitivity. This highlights the importance of bandwidth in determining the close multipath components of the PDP.

In addition to time resolution, the total measurable delay range $\tau_{\max}$ depends on the number of frequency points N used in the measurement and the frequency step size Δf:

$$\tau_{\max} = \frac{1}{\Delta f}. \tag{2.21}$$

https://doi.org/10.7795/110.20260421

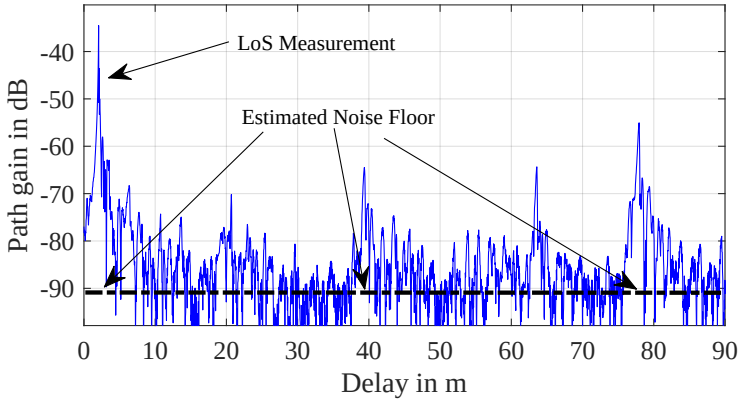

Figure 2.16: Example of an instantaneous uncalibrated PDP taken from a LoS measurement at 304 GHz with 8 GHz of bandwidth showing an estimate of the noise floor level.

This equation indicates that with the number of points being increased, it can extend the observable delay range. However, increasing N also increases the measurement time, which can introduce system stability and drift challenges, especially when dealing with VNA sweeps along. Using the cyclic property of the total PDP range might also be beneficial to avoid extending the number of measured points [84]. This property arises from the periodic nature of the discrete Fourier transform (DFT), which causes the channel impulse response to repeat cyclically over the observation window. As a result, excess delay components outside the window may alias into the measured range, allowing efficient analysis without increasing the measurement length.

The noise floor of the PDP is another critical factor, as it determines the minimum detectable signal level and influences the identification of weaker multipath components. The noise floor is primarily affected by the VNA settings, including the IF and the averaging factor. A lower IFBW reduces the noise level but increases the sweep time while averaging multiple measurements, which improves the SNR at the cost of longer measurement durations.

An effective way to estimate noise level is to recognize that the measured impulse response would lose energy at extensive delays, due to the increased path loss, or by performing a linearity test setting incremental attenuation amounts between the test ports and examining the received impulse response or PDP and identifying the tail end where no detectable signal is present. Based on this, a SNR threshold, sometimes referred to as a "noise threshold", can be set relative to the average noise floor [46, 85]. In Fig. 2.16, it shows an example of the PDP for an OTA LoS measurement using the correlational-based CS and an estimate of the noise floor.

2.4.2 Interpolation and Windowing Techniques

A network is mathematically characterized by its transfer function, which is typically presented in time or frequency domain. The Fourier analysis is ideally suited for that regard and provides helpful network analysis to distinguish between these representations. However, practical measurement systems, such as VNAs and time domain CSs, operate over finite bandwidths

https://doi.org/10.7795/110.20260421

and discrete frequency and time points, requiring careful interpretation of results [45].

Since VNA measurements are typically performed in the frequency domain, converting this data into the time domain involves applying the IFT, and the inverse discrete Fourier transform (IDFT) is used when working with discrete frequency data, defined as:

$$f(\tau) = \sum_{n=0}^{N-1} F(\nu) e^{j2\pi(\nu/N)\Delta\tau}, \tag{2.22}$$

where ν/N represents frequency in samples per cycle, $\Delta\tau$ is the discrete-time increment, and $F(\nu)$ is the discrete frequency data set [45].

The IFFT is commonly employed for computational efficiency in generating the time-domain response. However, applying the IFFT directly to measured frequency-domain data introduces constraints. The fixed time resolution and uniform spacing between time samples may obscure important effects between sampled points. VNAs and CSs also apply advanced signal processing to enhance accuracy beyond basic FFT or IFFT transformations.

In contrast to frequency-swept VNAs, correlation-based CSs estimate the time-domain CIR by transmitting a known broadband signal, such as a PRBS or chirp, and correlating the received signal with the known transmitted waveform:

$$h(\tau) = \mathcal{F}^{-1}\{H(f)\} = \int_{-\infty}^{\infty} H(f) e^{j2\pi f\tau} df, \tag{2.23}$$

where $h(\tau)$ is the CIR, and $H(f)$ represents the frequency response of the system. These sounders inherently perform the IFFT in hardware by exploiting the correlation properties of wideband signals.

The FFT is an efficient algorithm for computing the DFT, significantly reducing computational complexity. However, when working with finite-length signals, spectral leakage can occur due to discontinuities at window edges, leading to energy spreading across adjacent frequency bins.

Windowing is particularly important when transforming frequency-domain measurements into time-domain impulse responses and vice versa, as it affects delay spread characterization in channel sounding and time-gating accuracy in network analysis. Applying windowing to the measured frequency response $H(f)$ before performing the inverse Fourier transform reduces distortions in the time-domain response:

$$H_{\mathrm{w}}(f_n) = H(f_n) \cdot w(n), \tag{2.24}$$

where $H_{\mathrm{w}}(f_n)$ represents the windowed frequency response and n denotes the sample index. It is important to point out that windowing does not improve the resolution, which is linked to bandwidth [86].

The choice of windows impacts the balance between noise suppression and spatial resolution. Different windowing techniques provide trade-offs between resolution and leakage suppression [87]:

- Rectangular Window: No tapering, highest resolution, but substantial leakage.

https://doi.org/10.7795/110.20260421

- Hann-Window: Balanced resolution and leakage reduction.
- Hamming Window: Lower nearest side lobes with moderate resolution. - Blackman
- Harris Window: Strong side lobe suppression at the cost of a broader main lobe.
- Flat Top Window: Best for amplitude accuracy but with the broadest main lobe.

This work explored the Tukey window, which can be adjusted between the rectangular and Hann windows. However, comparisons showed no significant improvement in selection when transitioning toward the Hann window was applied offering flexibility in tapering [88]:

$$w(n) = \begin{cases} \frac{1}{2}\left[1 + \cos\left(\frac{2\pi n}{\alpha N} - \pi\right)\right] & 0 \leq n < \frac{\alpha N}{2} \\ 1 & \frac{\alpha N}{2} \leq n \leq N - \frac{\alpha N}{2} \\ \frac{1}{2}\left[1 + \cos\left(\frac{2\pi n}{\alpha N} + \pi\right)\right] & N - \frac{\alpha N}{2} < n \leq N, \end{cases} \tag{2.25}$$

where N is the total number of samples and α controls the transition between a rectangular ($\alpha = 0$) and Hann window ($\alpha = 1$). Proper window selection enhances accuracy in VNAs, time-domain channel sounders, and time-domain CSs.

In Fig. 2.17, it illustrates the effects of different windowing functions on a LoS measurement at a distance of 2.6 m. The measurement was performed using a VNA operating in the 300–310 GHz frequency range. The impact of windowing is clearly observed in the magnitude of the received signal, the transmission coefficient of the real component of the S-parameter (S_{21}), and the resulting PDP.

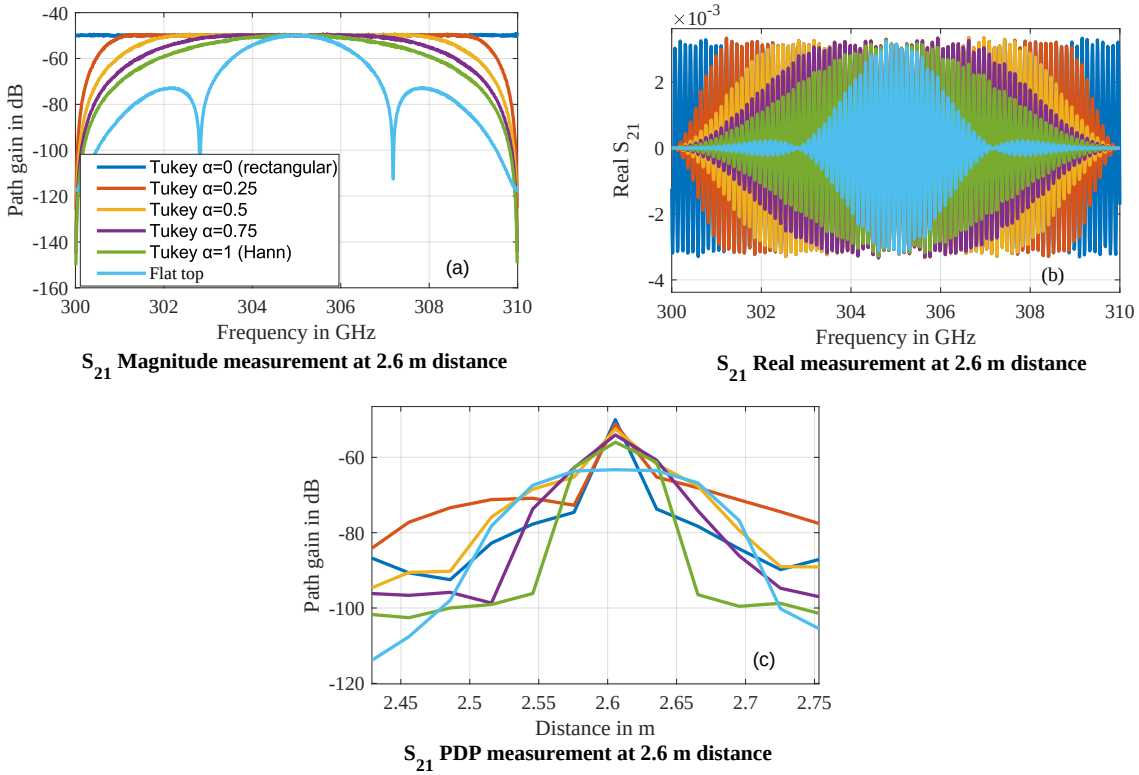

Figure 2.17: Windowing influence on the VNA transmission parameters for a distance measurement at 2.6 m LoS distance (a) Magnitude (b) Real component (b) PDP.

https://doi.org/10.7795/110.20260421

On the other hand, interpolation is widely used to improve the perceived resolution of the PDP by increasing the density of data points in the frequency response. In practical measurement systems, the resolution of the PDP is constrained by the available bandwidth, as the time resolution is inversely proportional to the measurement bandwidth [89]. Since the peaks in the PDP may not align precisely with the spatial grid points set by the measurement bandwidth, interpolation techniques are employed to refine the resolution and accurately estimate multipath components.

Standard interpolation methods include linear and cubic spline interpolation. Cubic spline interpolation utilizes piecewise cubic polynomials to achieve smooth transitions between data points:

$$S_i(x) = a_i + b_i(x - x_i) + c_i(x - x_i)^2 + d_i(x - x_i)^3, \tag{2.26}$$

where the coefficients a_i, b_i, c_i, d_i are determined by solving continuity and smoothness conditions across adjacent intervals [90]. Compared to linear interpolation, cubic splines provide better accuracy by ensuring second-order continuity, making them well-suited for estimating missing or non-uniformly spaced data in frequency-domain measurements.

Another practical approach to improving PDP resolution is zero-padding, which extends the maximum frequency of the measurement data set before applying an IFT [91]. Zero-padding does not add new information but increases the density of computed time-domain samples, effectively reducing the grid-spacing of the PDP peak location. This method is computationally efficient and helps refine delay estimation, especially in high-resolution CS applications. Interpolation and zero-padding are essential for post-processing frequency-domain data to enhance time-domain resolution. Their proper application is crucial in accurate multipath analysis, radar signal processing, and high-frequency communication systems requiring acceptable delay resolution.

Fig. 2.18 illustrates the effect of zero-padding interpolation on a measured PDP at a distance of 1 m. The measurement was conducted using a VNA operating at 300 GHz with a measurement bandwidth of 10 GHz, which results in a time resolution of 100 ps, corresponding to a spatial resolution of 2.99 cm. Since the peaks in the PDP may not align precisely with the spatial grid points defined by the measurement bandwidth, interpolation improves resolution by increasing the density of computed time-domain samples [27].

A simulated PDP for distance measurements ranging from 0.1 m to 10 m is shown in Fig. 2.19. This figure compares the Hann window's and zero-padding interpolation's effects against the expected free-space path loss. Zero-padding interpolation provides a better representation of the power decay, improving the accuracy of the measured path loss trend. The expected FSPL follows an inverse square law, resulting in a decay of 20 dB per decade of distance, which is captured more accurately with only windowing techniques.

Throughout this thesis, interpolated and windowed PDP was extensively applied to calibrate the horn atennas in Chapter 3, and to establish OTA comparable measurements among different measurement equipment, in Chapter 4. The interpolated PDP was also presented shortly in Chapter 5 in LS segments analysis.

https://doi.org/10.7795/110.20260421

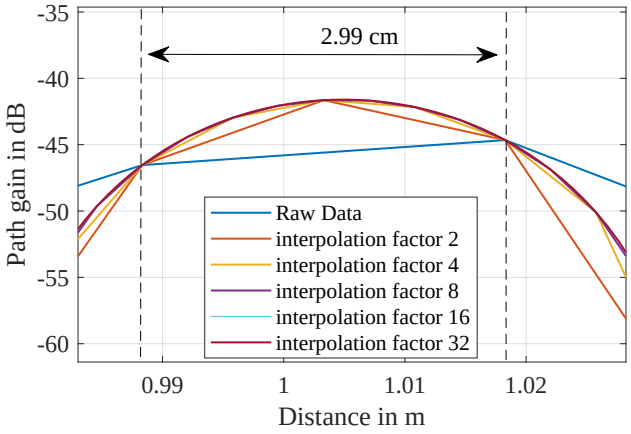

Figure 2.18: Raw data measurement and zero-padding grid-spacing for 1 m PDP.

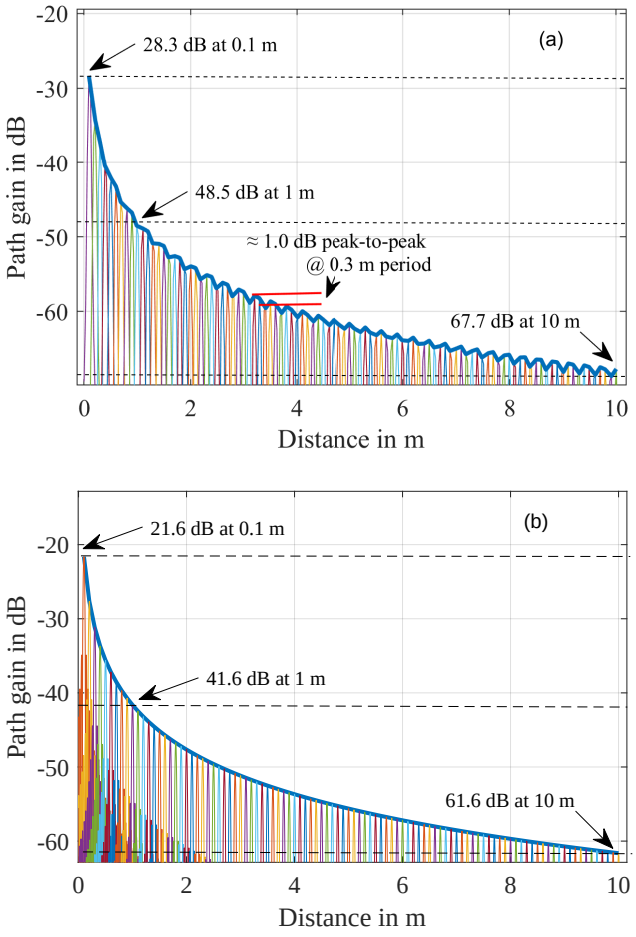

Figure 2.19: PDP simulation of an OTA path gain for distances between 0.1 m–10 m with (a) Hann window and (b) interpolation factor of 40. In (a), the ripple is ≈1.0 dB peak-to-peak (max 1.53 dB) with a period of ≈0.30 m (as indicated).

https://doi.org/10.7795/110.20260421

3

System Error Correction and Calibration Procedures

This chapter describes the calibration procedures used to correct systematic measurement errors for both the VNA and correlation-based CS systems. Correcting these error terms significantly enhances measurement accuracy and reliability, enabling precise wireless channel characterization and the development of accurate channel models.

These calibration procedures ensure that measurements are comparable across different setups and scenarios. To ensure that calibration and error correction are directly applicable to actual operating conditions, these procedures must be conducted within the measurement environment. This approach results in more accurate and relevant measurement results.

3.1 VNA Calibration and Error Modeling

As discussed in Chapter 2, the VNA error model serves as a fundamental framework, enabling the translation of raw measurements into accurate and meaningful data. The error coefficients characterized for each port, including directivity, reflection tracking, source match, and switch terms, are carefully accounted for in the calibration procedures. These procedures are designed to correct for these error terms by characterizing the known calibration standards. Additionally, it considers other error terms such as noise floor and trace noise, drift, non-linearity, and cable movement, ensuring a comprehensive and reliable calibration process [30].

To handle the calibration process, METAS VNA Tools software is used by providing straightforward interfaces for calibration setup, data acquisition, and error correction [47].

VNA calibration is essential for achieving measurement accuracy and serves as a foundational process to identify and mitigate systematic measurement errors, commonly referred to as error coefficients or terms. These errors significantly influence the accuracy and reliability of VNA measurements which establishes a relationship between the VNA's readings, often referred to as raw S-parameters, and the true S-parameters of the DUT connected to the VNA's test port.

A central element of the VNA calibration process is the determination of error coefficients, which are integral components of the VNA error model. These coefficients combine these systematic errors and are derived by measuring a set of known calibration standards. By quantifying and characterizing these error coefficients, calibration corrects raw S-parameter

https://doi.org/10.7795/110.20260421

measurements, improving the accuracy and reliability of subsequent measurements conducted on the DUT.

An essential aspect of VNA calibration is its dependence on calibration standards, which serve as reference points for the construction of the error model. These standards include components such as open circuits, short circuits, and precision loads, each of them is characterized with regard to the SI units under controlled conditions to implement traceability.

Challenges arise when calibrating waveguide ports, which require specialized procedures for optimal results. Unlike coaxial ports, waveguide ports have unique characteristics that necessitate tailored calibration techniques. For example, standard calibration kits for waveguide ports often include specialized components, such as quarter-wave shims, designed to address the absence of well-defined reflections in open waveguides [64].

Calibration for waveguide ports typically involves the use of quarter-wave shims in conjunction with standard calibration procedures. These shims introduce a 90° phase shift across the waveguide band, enabling accurate calibration of waveguide-based devices. Advanced techniques, such as TRL calibration, further enhance accuracy and repeatability, offering simplified and efficient methodologies for waveguide systems. For short offset calibration, the phase shift of the quarter-wave shim is approximately 50° to 120° over the nominal waveguide band. To achieve accurate calibration, the phase shift at each frequency must be precisely calculated using the waveguide dispersion formula [45]:

$$\phi_f = \frac{360f}{c}\sqrt{1-\left(\frac{f_c}{f}\right)^2} \quad \text{in } ^\circ/\text{m}. \tag{3.1}$$

This section outlines the calibration procedures used to correct systematic measurement errors in both the VNA frequency bands corresponding to the system definitions in Chapter 2 and are later used in OTA analysis in Chapter 4 to enable consistent results across measurements. These steps ensure that measurements remain comparable. Furthermore, the calibration must be conducted within the specific measurement scenario to guarantee that error correction is directly applicable to actual operating conditions, leading to more accurate results.

3.1.1 Calibration Standards

Using a four-receiver VNA enables calibration through the seven-term or the classical 12-term error correction model. Generally, the calibration process for frequency extenders and waveguides follows the same principles as coaxial connectors. However, a key challenge when working with waveguide ports is the need for specialized calibration standards, typically represented by well-characterized shims, to achieve optimal accuracy.

For both frequency bands investigated using the VNA in this and the following chapters, calibration was carried out using two shims with lengths corresponding to 1/4 and 3/4 of the center wavelength of the converter's operating range. A 180° phase shift in the reflection coefficient was introduced to ensure measurement stability across the frequency band. One significant difference in waveguide calibration is the absence of an open standard, as an open

https://doi.org/10.7795/110.20260421

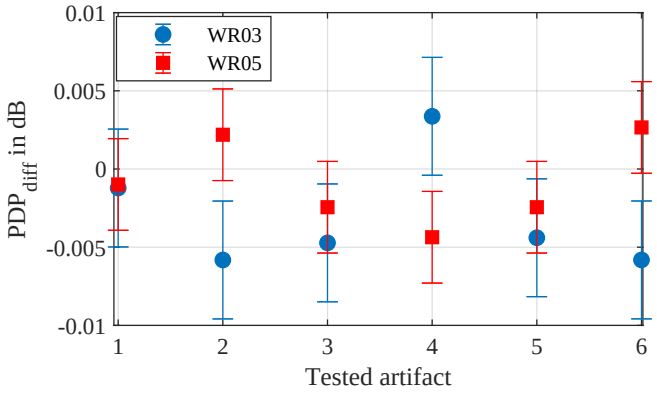

Figure 3.1: WR05 and WR03 waveguide bands PDP peak magnitude difference between TRL and UOSM calibration procedures, showing 95 % confidence intervals at k=2. (Adopted from [39]).

waveguide circuit lacks a well-defined reflection [92]. This chapter applied two widely used calibration methods to correct systematic errors: TRL and UOSM.

TRL calibration is a well-established approach for waveguide systems, offering simplified implementation and improved measurement repeatability. It requires four different connections to determine seven independent error terms. UOSM, has its distinct advantages. Like TRL, it requires switch term measurements but simplifies transmission measurements by assuming reciprocity between the two transmission S-parameters, meaning $S_{21} = S_{12}$ [30, 45].

Each calibration method has its specific advantages:

- **TRL calibration** ensures high accuracy, making it well-suited for precision laboratory setups, where well-characterized line standards can be used to refine propagation delay measurements.
- **UOSM calibration** offers more flexibility in environments where direct port coupling is not feasible, tolerating alignment errors and imperfections in calibration standards.

While TRL provides superior accuracy, UOSM offers greater flexibility when measuring OTA scenarios. Combining both methods helps balance TRL's precision and UOSM's adaptability, making them practical for sub-THz measurement applications.

One of the key advantages of using METAS VNA Tools in this study is the ability to perform measurements on the same DUT across multiple calibration schemes. This approach provides valuable insights into how different calibration techniques influence measurement accuracy.

The PDP was measured across 180–200 GHz and 290–310 GHz using seven different measurement artifacts, including attenuators, lines, and through connections. The calibration differences for each artifact were computed and normalized to the initial measurement. This approach allowed us to evaluate the extended uncertainties associated with each calibration method while accounting for linear variations in magnitude and phase. The interpolated PDP peaks were compared across different calibrations for various measurement artifacts, capturing differences in both magnitude and delay. The magnitude difference between the two calibration procedures was calculated using [39]:

https://doi.org/10.7795/110.20260421

$$\mathrm{PDP}_{\mathrm{diff},i} = (P_{i,\mathrm{UOSM}} - P_{i,\mathrm{TRL}}) - (P_{1,\mathrm{UOSM}} - P_{1,\mathrm{TRL}})\,, \tag{3.2}$$

where $\mathrm{PDP}_{\mathrm{diff},i}$ represents the difference in PDP peak magnitude between the first and the subsequent measurement artifacts, while $P_{i,\mathrm{UOSM}}$ and $P_{i,\mathrm{TRL}}$ denote the interpolated PDP peaks obtained using UOSM and TRL calibrations, respectively.

The 95 % confidence interval in Fig. 3.1 indicates a 0.01 dB difference between the two calibrations at WR05 and 0.02 dB at WR03. No significant timing differences were observed across calibrations, given the 0.24 ps time resolution of the interpolated peaks.

3.1.2 Noise Floor and Trace Noise

The VNA's noise floor and trace noise measurements vary depending on measurement parameters, mainly depending on the IFBW. To ensure consistency, the measurement frequency steps were fixed at 50 MHz and the IFBW at 10 Hz, matching the values used in subsequent measurements. An appropriate IFBW is crucial for achieving the necessary range resolution in OTA measurement scenarios and accurately characterizing the VNA noise performance.

Noise characterization was conducted using VNA Tools, with short terminations applied to both waveguide ports. the noise floor was estimated by averaging the power level of the fluctuations over the measurement bandwidth. The measured noise floor remained below -80 dB across both frequency bands, ensuring that it does not interfere with actual measurements. Fig. 3.2 shows the noise floor measurements for the frequency ranges under test over 20 GHz of measurement bandwidth at WR05 and WR03 waveguide bands [39].

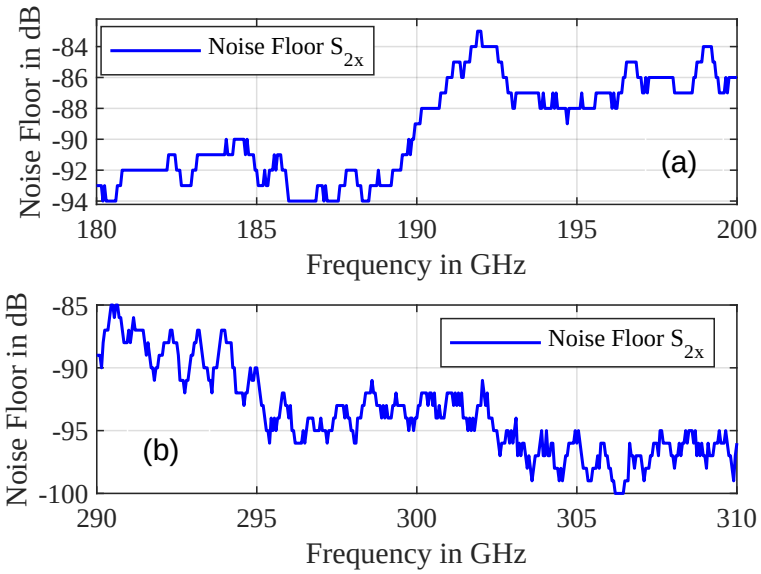

Figure 3.2: Noise floor characterization using VNA with 20 GHz of bandwidth and 50 MHz frequency steps. The results show quantized changes caused by measurement resolution. (a) WR05. (b) WR03.

In contrast, trace noise accounts for random fluctuations in magnitude and phase during S-parameter measurements. These fluctuations arise due to internal noise sources and system imperfections and become particularly significant at sub-THz frequencies, impacting measure-

https://doi.org/10.7795/110.20260421

ment accuracy and system reliability [39]. Understanding trace noise behavior is essential for high-precision applications, as it allows for VNA stability assessment and enables uncertainty incorporation into the overall measurement model. Repeated S-parameter measurements were performed using short terminations on both waveguide ports to quantify trace noise. The standard deviation of the measured values was computed for each frequency point, and the root mean square (RMS) of these deviations across the frequency range provided a scalar representation of trace noise [30].

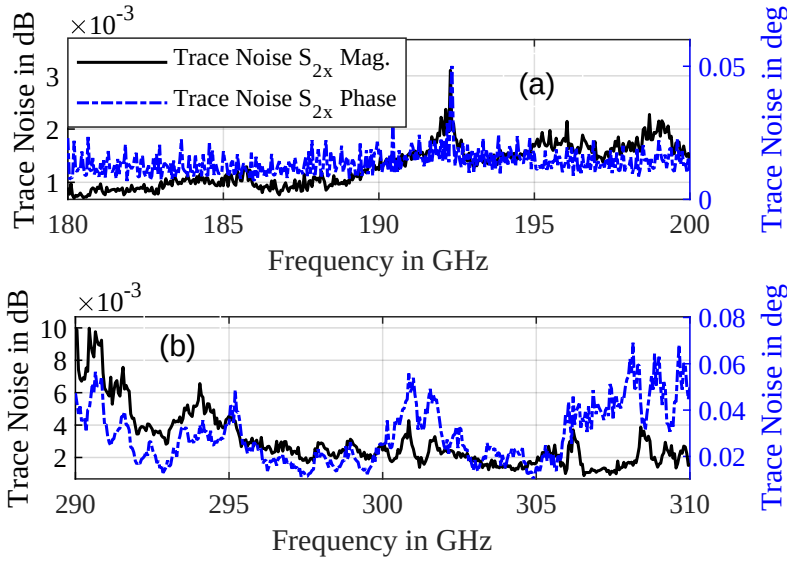

Figure 3.3: VNA S_{2x} magnitude and phase trace noise for both VNA frequency bands under test at (a) WR05 and (b) WR03. (Adopted from [39]).

Figure 3.3 presents the trace noise levels obtained across both frequency bands. Each measurement was conducted using 100 data points per frequency step. The highest observed trace noise magnitude was 3.2×10^{-3} dB, with a trace noise phase deviation of 0.04° at WR05. For the WR03 band, the peak trace noise magnitude was 10×10^{-3} dB, while the peak phase deviation reached 0.08°.

3.1.3 Drift of Transmission Tracking

The surrounding environment significantly influences the stability of a test system. VNA measurement drift occurs due to temperature-induced variations affecting signal path lengths and component performance. In this work, measurements were performed several hours before recalibration, and the drift was evaluated over a 12-hour period, which is longer than the interval between recalibrations. Data was recorded every 15 minutes. Drift measurements were performed in an OTA LoS setup with a 1-meter separation between the two VNA extension modules to evaluate environmental influences. Horn antennas with gains of 20 dBi and 26 dBi were used at WR05 and WR03 bands, respectively. The drift in S_{21} was calculated relative to the initial measurement at $t = 0$, with 95 % confidence intervals for expanded uncertainties in magnitude and phase for each jth frequency step:

https://doi.org/10.7795/110.20260421

$$\Delta S_{21}(t) = \frac{S_{21,j,t}}{S_{21,j,0}}. \tag{3.3}$$

The maximum deviations in magnitude and phase were then computed as [30]:

$$\max(|\Delta S_{21}(t)|) - 1, \quad \max(|\arg[\Delta S_{21}(t)]|). \tag{3.4}$$

For all tested frequencies, the maximum drift in magnitude was 0.24 dB for the WR05 band and 0.41 dB for the WR03 band. The peak-to-peak phase drift reached 21° for WR05 and 60° for WR03.

Figure 3.4 illustrates the impact of drift on PDP path gain and delay, showing raw data, interpolated results, Hann-windowed data, and a combination of both. The interpolation factor was set to 40. The raw data, recorded with a 20 GHz bandwidth, provided a time resolution of 15 mm. After interpolation, the resolution improved to 0.37 mm. Figure 3.4(a) illustrates the PDP peak delay deviations over time. Notably, PDP delay drift became apparent only after applying interpolation. At WR05, the peak delay shifted by 1.5 mm when interpolation was applied, with a similar shift when combined with a Hann window. At WR03, the PDP delay deviation was 0.8 mm with interpolation alone, increasing to 2.3 mm when both interpolation and the Hann window were applied. Figure 3.4(b) presents the drift effects on PDP peaks before and after applying interpolation and windowing. At WR05, the maximum PDP peak magnitude drift was 0.2 dB when both interpolation and the Hann window were applied, compared to 0.1 dB in the raw PDP peak measurements. At WR03, drift had a more significant effect on path gain, with a maximum PDP path gain drift of 0.8 dB for the raw PDP peak, which was reduced to 0.45 dB after applying both interpolation and the Hann window. Phase drift influences the PDP delay measurements.

An alternative approach to analyzing drift measurements is to examine the variation at each frequency step for the transmission S-parameters. Figure 3.5 depicts the drift of S_{21} relative to the initial measurement at $t = 0$, with 95 % confidence intervals representing the extended uncertainties in magnitude and phase for each frequency step. The drift uncertainty $u(D)$ is determined using:

$$u\left(D\right) = k \cdot \frac{\sqrt{\frac{1}{n-1}\sum_{i=1}^{n}\left(D_{j,i} - \hat{D}_{\text{mean}}\right)^2}}{\sqrt{n}}, \tag{3.5}$$

where $\hat{D}_{\text{mean}}$ is the mean vector of $S_{21,j,t}$, and $D_{j,t} = S_{21,j,t} - S_{21,j,0}$. The maximum peak-to-peak drift magnitude across all measured frequencies was 0.24 dB for the WR05 band and 0.41 dB for the WR03 band. The peak-to-peak drift phase reached 21° for WR05 and 60° for WR03.

Both approaches deliver consistent results; however, since the goal is to compare the results with the CS system, the PDP measurement approach is adopted for inclusion in the uncertainty analysis.

https://doi.org/10.7795/110.20260421

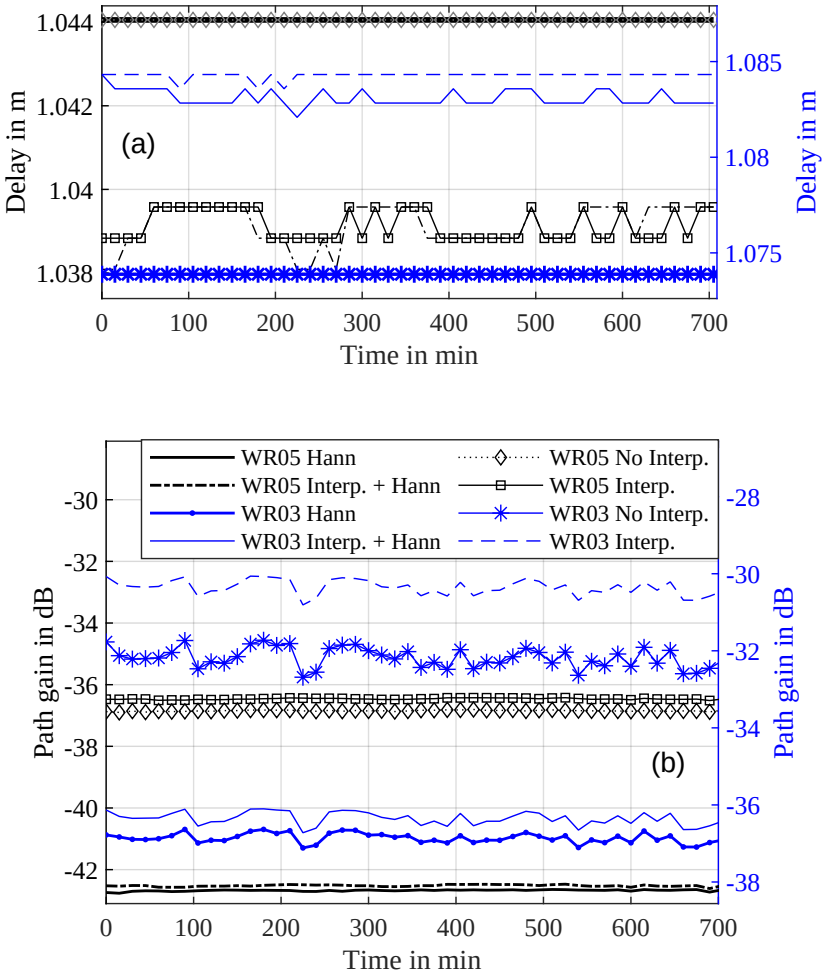

Figure 3.4: VNA S_{21} PDP peak drift for WR05 and WR03 in terms of (a) delay and (b) path gain. in blue: WR03, in black: WR05 (Adopted from [39]).

3.1.4 Non-Linearity and Cable Movement

The VNA operates as a linear network, maintaining a direct relationship between the forward and backward waves detected by its receivers. Any deviation from this linear behavior is referred to as non-linearity, which depends on the VNA source power level. Since access to individual VNA components is limited, non-linearity is evaluated at the receiver signal ratio level, explicitly using S-parameters. At higher frequencies, non-linearity is typically assessed using a characterized fixed attenuation device [30]. However, due to the absence of characterized attenuators at sub-THz frequencies, the evaluation is performed by comparing measurements against the expected Friis path loss [39]. The examination involves measuring across the test frequency range, applying VNA error correction, and estimating the S-parameters, specifically S_{21}. Incremental attenuations for the error-corrected measurements are calculated at different attenuation states $y = 1, 2, 3, \ldots$. The maximum deviation between measured and reference incremental attenuations is determined as follows [30]:

https://doi.org/10.7795/110.20260421

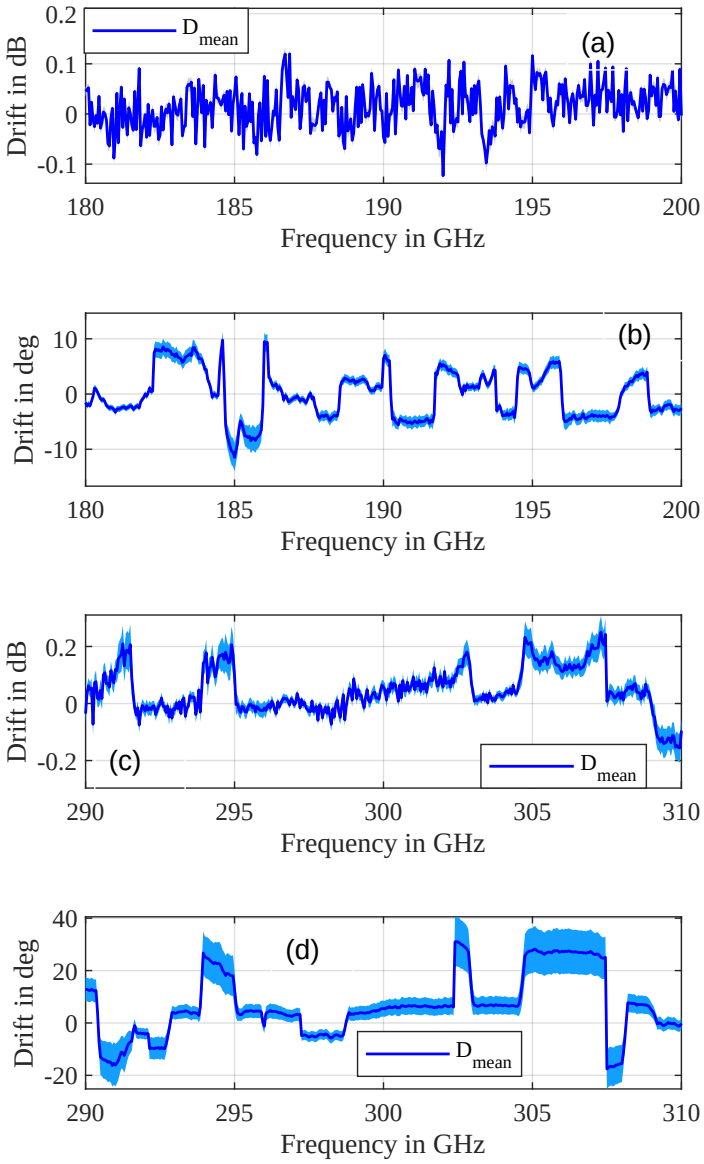

Figure 3.5: The S_{21} magnitude and phase differences due to drift are shown. Magnitude measurements are presented for (a) WR05 and (c) WR03, while phase measurements are shown for (b) WR05 and (d) WR03. The shaded regions indicate the 95 % uncertainty (k=2) intervals.

$$L_y = \max\left(|S_{21}(y)| - |S_{21,\mathrm{ref}}(y)|\right). \tag{3.6}$$

These deviations are then enclosed within an envelope over the entire attenuation range. The values are converted to linear units and incorporated as uncertainties in the analysis. Another factor influencing measurement uncertainty is the use of frequency extenders, which are connected to the VNA via four coaxial cables, including RF and LO connections [30].

Cable movement can introduce additional uncertainty in the measurements. As a result, the total measurement uncertainty accounts for system non-linearity and cable-induced variations. The difference between the measured $|S_{21}|_{\mathrm{Meas}}$ and the theoretical Friis loss $|S_{21}|_{\mathrm{theor}}$ showed

https://doi.org/10.7795/110.20260421

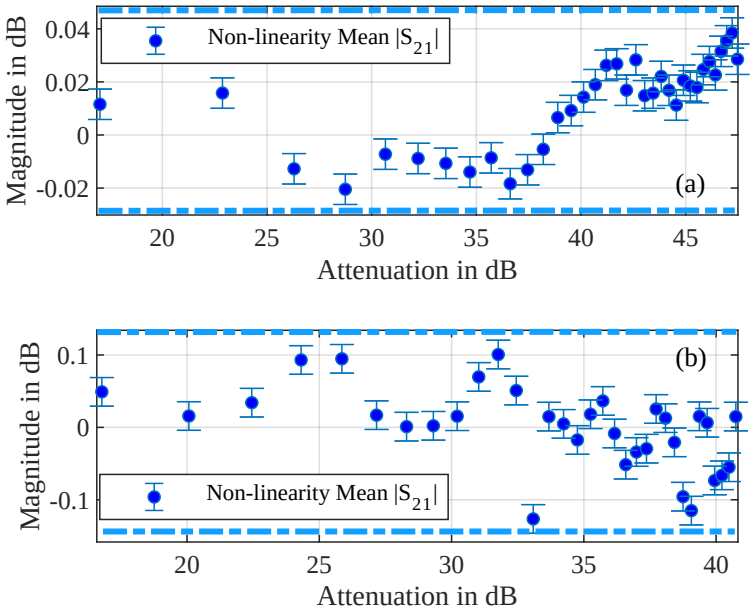

Figure 3.6: VNA Non-linearity difference between the measured and theoretical Friis-loss at (a) WR05 and (b) WR03 bands. The dashed blue lines represent the possible envelope covering the non-linear region. The error bars indicate the 95 % uncertainty (k=2.78) intervals derived from five repeated measurements.

a peak-to-peak variation of 0.07 dB for WR05 and 0.24 dB for WR03 when using a 20 GHz measurement bandwidth. Measurement uncertainties are considered to be a combination of system non-linearity and the effects of cable movement.

Fig. 3.6 shows the non-linearity combined with the cable movement difference between the measured $|S_{21}|_{\text{Meas}}$ and the theoretical Friis-loss $|S_{21}|_{\text{theor}}$ for the WR05 and WR03 bands [39].

Fig. 3.7 presents the non-linearity and cable movement influence in terms of the interpolated PDP peaks obtained at the same frequency range, and the peak-to-peak deviations showed similar results to the magnitude measurements with 0.06 and 0.22 dB for the WR05 and WR03 bands, respectively. Both approaches in this case showed consistency in the measurement results indicating a minimal influence of any unwanted multipath reflections for this measurement scenario.

3.2 Horn Antenna Calibration for Precise OTA Measurements

Horn antennas are well-known for providing high gain, which is why they are being used extensively as reference antennas to investigate signal propagation at such high frequencies. The knowledge of PC is essential for precise measurements at sub-THz frequency bands. The wavelength at this band is very short, making the distance between the antenna aperture and the actual PC easily exceed several wavelengths and significantly affecting the propagating signal's phase measurement, linearity, and increasing the measurement uncertainties. The theoretical background related to calculating the horn antenna PC was presented in the context of OTA signal propagation in the previous chapter, in Section 2.3.2

This section investigates measurements using a calibrated VNA with frequency extension

https://doi.org/10.7795/110.20260421

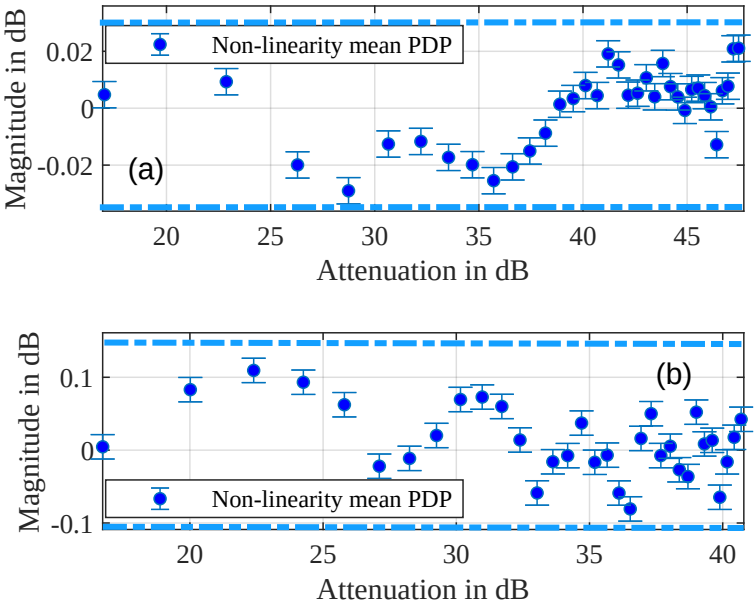

Figure 3.7: VNA nonlinearity and cable movement S_{21} PDP peak deviation based on distance measurement separations. The dashed blue lines represent the possible envelope covering the nonlinear region. (a) WR05. (b) WR03. The error bars indicate the 95 % uncertainty (k=2.78) intervals derived from five repeated measurements. (Adopted from [39]).

modules and Standard Gain Horn Antennas of 25 dBi and 20 dBi covering frequencies at WR03 and WR05 frequency bands, respectively. The objective here is to compare the PC calculation methods based on the antenna's physical dimensions, their combined gain for different measurement separations, and antenna rotation around its aperture. It will address challenges related to multipath reflections that become dominant at short-range measurements and their influence on PC calculations. It will investigate Friis path-loss and molecular absorption and whether they affect the PC calculation. Finally, since the PC is changing non-linearly with frequency, It will investigate the influence of measurement bandwidth on PC position and its related uncertainties.

Antenna calibration is critical and must be accurately considered and applied across all OTA measurement setups. In relation to the next chapters, the consideration of the antenna PC will play a key role in characterizing the CS's phase and magnitude in Chapter 4. In Chapter 5, a proper match between the measured and simulated parameters cannot be achieved unless the PC is carefully taken into account. Additionally, in Chapter 6, the information derived from the PC calculation facilitates the correct positioning of the antenna PC at the focal point of the parabolic mirrors, leading to improved beam collimation in the sub-THz measurement testbed. In the next subsections two methods to characterize our antennas under test will be presented, with the help of using the PDP's magnitude and delay.

Two horn antennas at WR03 and WR05 waveguide standards were tested, with identical antennas placed on each frequency extension module waveguide output, representing the two ports of the VNA with extended frequency range. The antenna dimensions are provided in Table 3.1, corresponding to the labeled dimensions A-F in Figure 3.8. Measurements were

https://doi.org/10.7795/110.20260421

conducted using a Rohde & Schwarz ZVA24™ VNA along with ZVA-Z220™ and ZVA-Z325™ frequency extension modules.

Dimensions (mm)	WR05	WR03
Total Length (A)	17.6	37.7
Aperture Width (B)	6.7	7.9
Aperture Height (C)	4.6	5.9
Waveguide Width (D)	2.217	0.864
Waveguide Height (E)	1.469	0.432
Flare Length (F)	12.5	34.7

Table 3.1: Horn antenna dimensions. (Adopted from [26, 39]).

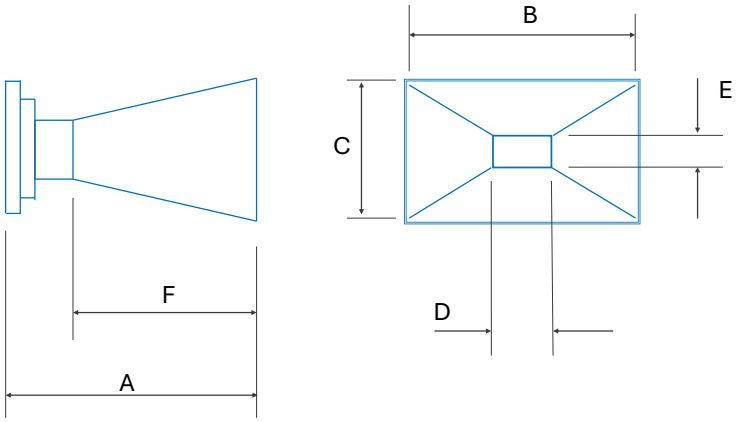

Figure 3.8: Horn antenna dimensions. (Adopted from [26, 39]).

The UOSM calibration was performed at a 10 Hz IFBW, achieving an 80 dB dynamic range for the OTA measurement setup. A 50 MHz step-size linear frequency sweep was used across the measured spectrum. The measurements were conducted in the far-field using a spherical antenna scanner with an angular precision of 0.01 degrees. Using a linear stage, the scanner also facilitated variable separation distances, allowing for measurements up to 3.5 m [26].

The test environment was temperature- and humidity-controlled; the antennas were aligned using a leveling laser. Distance readings were recorded using a laser-based measurement system fixed on the transmitter side and aligned with a fixed reference at the receiver side. Two measurement setups were implemented to analyze the PC of the horn antennas.

3.2.1 Distance Measurement

The first setup involved distance measurement, where the PDP magnitude was used to estimate the PC by calculating the RMS difference between the measured values and the shifted Friis path loss model. The goal was to identify the optimal separation distance, minimizing the difference between measured values and Friis path loss calculations, following a similar approach used in [93].

https://doi.org/10.7795/110.20260421

The PDP approach also allowed for an investigation into the impact of bandwidth on PC estimation, offering insights into each measurement's frequency and time resolution. The resolution achieved using PDP alone spans multiple wavelengths, even when testing the entire waveguide bandwidth. Therefore, an interpolation factor of 40 was applied to improve the estimation of PDP peak position and magnitude. The interpolation principle was presented in Section 2.4.2. Measurements were performed by varying the separation distance between antennas in steps of 10 cm, ranging from 10 cm to 340 cm. The PDP for the forward transmission parameter S_{21} is derived from [56] with an additional frequency-domain windowing function:

$$\mathrm{PDP} = \left|\mathrm{IFFT}(S_{21}(f)w(f))\right|^2, \tag{3.7}$$

where $w(f)$ is a frequency-domain window function. Since the antenna gain remains constant in the far field, the combined antenna gain $G(f)_{\mathrm{dBi}}$ is estimated as an average value from the Friis equation [26, 39]:

$$G(f)_{\mathrm{dBi}} = \frac{1}{n}\sum_{x=1}^{n}\left(S_{21}(f,P_x)_{\mathrm{dB}} - PL_{\mathrm{corr}}(f,P_x-\Delta P)_{\mathrm{dB}}\right), \tag{3.8}$$

where $S_{21}(f,P_x)_{\mathrm{dB}}$ and $PL_{\mathrm{corr}}(f,P_x-\Delta P)_{\mathrm{dB}}$ represent the measured VNA transmission results and the calculated path loss at each antenna separation P_x, respectively, corrected for the reference plane offset ΔP.

Figure 3.9 presents a schematic of the measurement configuration. The parameter D_x represents the measured separation between the antenna apertures for a given separation distance reading x. The parameter d_x corresponds to the calculated optimal separation distance, representing the PC separation of the two antennas that aligns with the path loss calculations. The parameter R_x denotes the PDP delay, which includes both the signal propagation delay within the antenna's waveguide and the OTA signal delay at separation distance x. The delay R_x at each measured distance accounts for both the OTA propagation and the electrical length of the signal traveling inside the antennas. Notably, R_x differs from the reference plane of the waveguide, which is established after performing VNA calibration.

The PC is influenced by antenna dimensions, exhibiting a nonlinear increase with frequency [81]. Figure 3.10 illustrates the expected PC positions based on antenna dimensions defined in Table 3.1. The plot highlights how uncertainties in antenna dimensions, particularly width, can significantly alter the PC values. The blue and red curves represent a deviation of 0.5 mm in antenna width and length, respectively.

The PDP approach effectively solves the multipath reflections at short measurement distances where antenna surface reflections can be significant without absorbers.

Figure 3.11 illustrates the PDP delay difference across various frequencies, along with the averaged delay for different separation distances. A 20 GHz bandwidth was tested for center frequencies ranging from 180–200 GHz and 290–310 GHz, with intervals of 5 GHz. The blue region represents the 95 % confidence interval for the measurement distances between 10 cm and 340 cm, showing the PDP delay difference from the antenna apertures in free space and

https://doi.org/10.7795/110.20260421

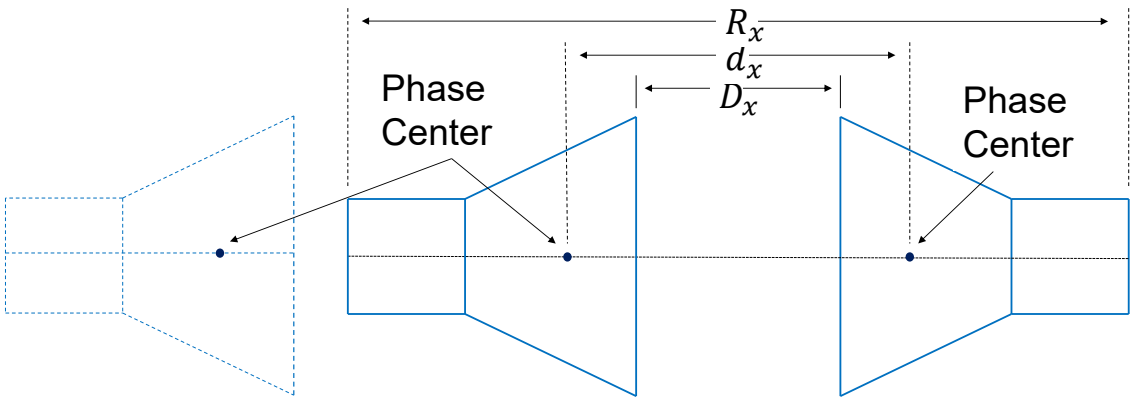

Figure 3.9: Sketch of the far-field antenna distance measurement setup. (Adopted from [26, 39]).

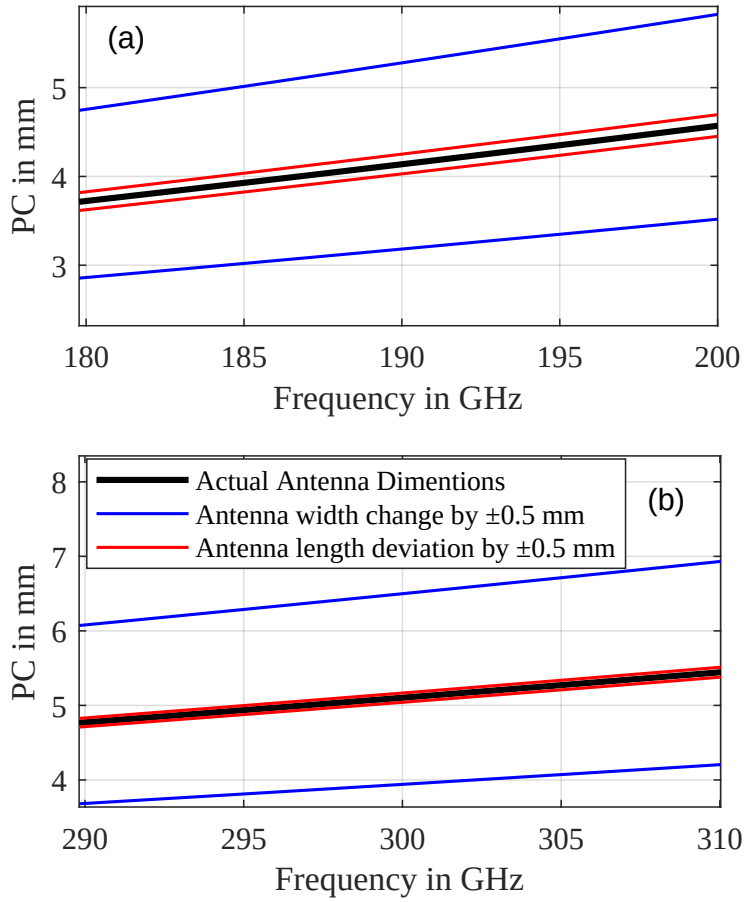

Figure 3.10: Horn antenna phase center calculation at (a) WR05 and (b) WR03 bands. (Adopted from [26]).

how this delay varies across different frequencies.

The mean PDP delay exhibited a shift of approximately 0.8 mm for both waveguide bands across the tested frequency range, with variations primarily resulting from different separation distances.

Analyzing the total measured distances and calculating the antenna gains as a common variable at each distance step provides an estimation of the antenna gain behavior across the

https://doi.org/10.7795/110.20260421

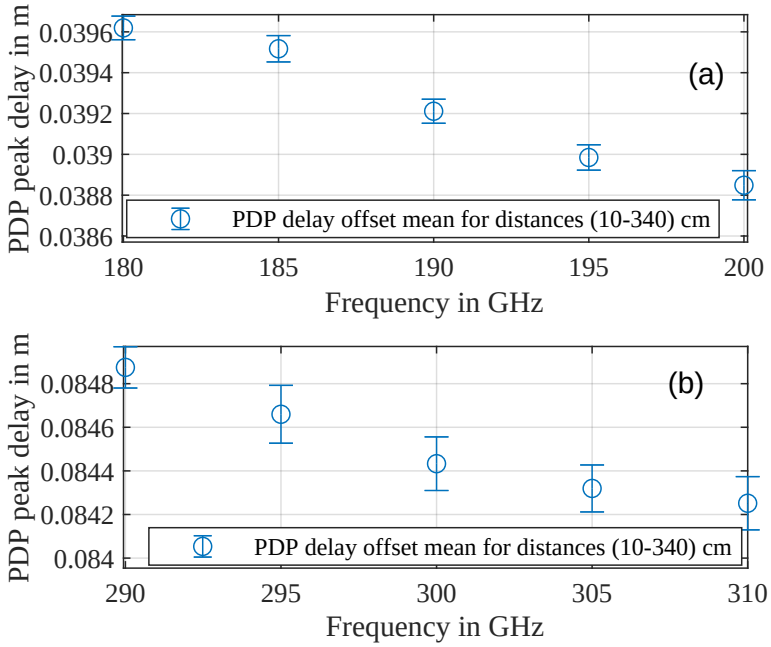

Figure 3.11: PDP delay offset vs. frequency using 20 GHz measurment bandwidth and 5 GHz step with 95 % confidence intervals (k=2). (a) WR05 Horn (b) WR03 Horn. (Adopted from [26, 39]).

entire measured bandwidth. The mid-frequency combined antenna gain, derived from this dataset, was found to be 41.47 ± 0.05 dB for the WR05 horn antenna and 52.25 ± 0.09 dB for the WR03 horn antenna, both at a 95 % confidence level.

Figure 3.12 presents the combined antenna gain achieved across different measurement distances, ranging from 40 cm to 340 cm, for both horn antennas. Three main factors influence the gain measurements and help explain the deviations observed in both measurement cases: drift effects, cable movement, and the alignment accuracy of the antennas at varying separation distances. The higher deviations observed in the WR03 band are likely caused primarily by increased drift originating from the frequency extenders. To increase confidence in the results, uncertainties related to antenna gain were also included in the overall uncertainty budget.

Figure 3.13 presents the RMS difference between the measured and calculated path gain based on the PDP peak calculation for both waveguide bands and antennas under test at the same measurement distances. The measurements were conducted over a 20 GHz spectrum, centered around 190 GHz and 300 GHz.

The combined PC calculations reveal a lower RMS difference of 0.02 dB at 8.7 mm for the WR05 antennas and 0.06 dB at 12.6 mm for the WR03 antennas. This corresponds to a PC of 4.35 mm per antenna for WR05 and 6.3 mm for WR03. A comparison of different measurement techniques for antenna PC estimation is discussed in [26].

3.2.2 Rotational Measurement

The second measurement setup focused on antenna rotation with a fixed separation between the antenna apertures. Rotating a single antenna introduces a delay shift, altering the effective distance between phase centers, which can be calculated using the interpolated PDP.

https://doi.org/10.7795/110.20260421

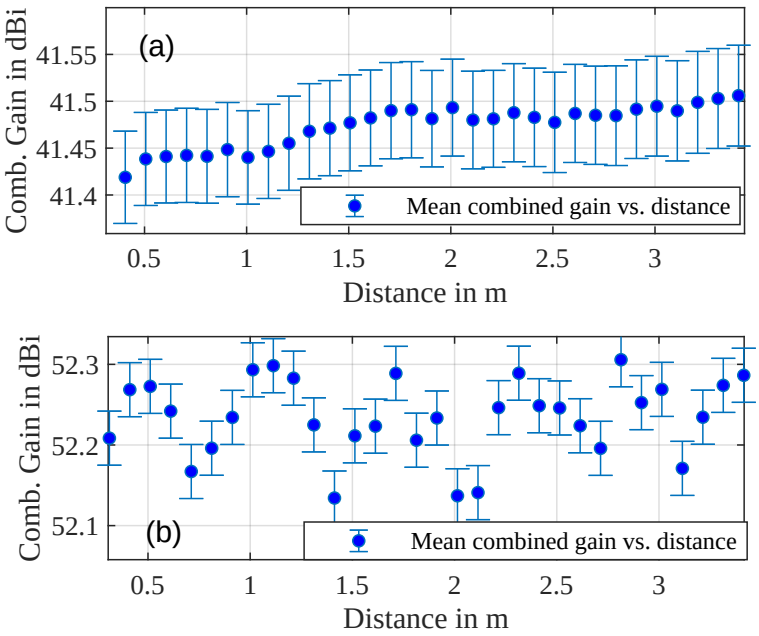

Figure 3.12: Combined antenna gain versus separation distances, shown with 95 % confidence intervals (k=2). (a) WR05. (b) WR03. (Adopted from [26, 39]).

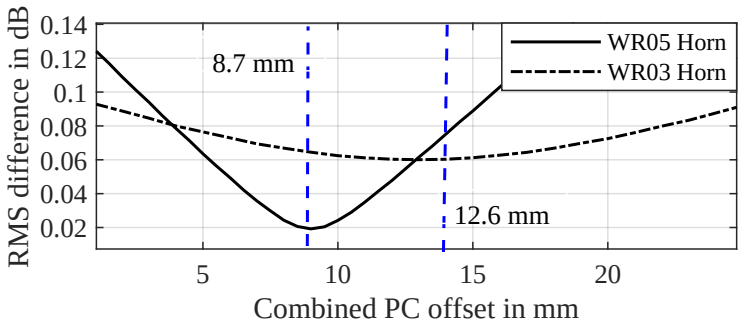

Figure 3.13: RMS difference in decibels between the PDP and measurement distance versus successive combined PC offset comparison for WR05 and WR03 horn antennas. (Adopted from [39]).

The spherical rotation of the PC creates a cosine-shaped delay pattern in the PDP as the longitudinal separation between the phase centers decreases.

Figure 3.14 illustrates the measurement setup. Here, D represents the physical separation between the antennas' apertures, d denotes the distance between phase centers at a rotational angle $\alpha = 0°$, and β signifies the targeted phase center distance from the antenna's aperture.

The relative PDP delay variation as a function of α is described by:

$$\Delta_p = \beta \cos(\pi\alpha) + R. \tag{3.9}$$

The PDP delay changes across different rotational angles due to the shift of the rotating antenna's phase center. R represents the measured PDP delay values, combining both the fixed delay contribution from the electrical distance traveled inside the antenna and the OTA separation between the antennas.

https://doi.org/10.7795/110.20260421

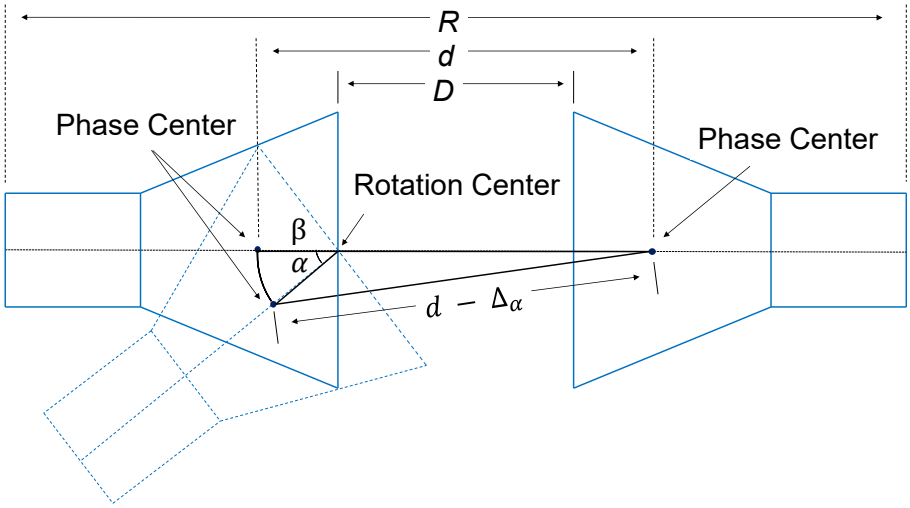

Figure 3.14: Measurement setup for antenna rotation, where D is the physical separation between the antenna apertures, d is the phase center separation at 0°, and β is the targeted phase center distance from the aperture. (Adopted from [26]).

Fig. 3.15, presents the PC calculation using angular rotation for WR05 and WR03 horn antennas across frequency ranges of 190–200 GHz and 300–310 GHz, respectively. The PDP delay shifts in response to antenna rotation, with delays decreasing as the antenna rotates away from 0°, reflecting the change in distance between the rotating antenna's phase center and the receiver. Fig. 3.15 displays the PDP delay shift across rotational angles from 0° to 50°, where signal strength enabled accurate PDP peak estimation above the noise floor. From the fitted curves, $\beta = 3.5$ mm for the WR05 horn and $\beta = 6.5$ mm for the WR03 horn antennas were determined.

This PC estimation method highlights the influence of radiation pattern null regions, especially those located away from the main lobe, where signal strength is reduced. The results show that for the WR05 horn, the estimated phase center delay is 3.5 mm, with a PDP delay uncertainty of ±1.7 mm before and ±0.5 mm after removing pattern nulls. A similar analysis for the WR03 horn yielded a phase center delay of 6.5 mm, with an uncertainty of approximately ±5 mm before and ±0.92 mm after pattern null removal.

Compared to distance-based phase center estimation methods, this approach shows some discrepancy. This deviation is largely attributed to the stronger impact of pattern nulls and higher angular sensitivity in the sub-THz regime, which can bias delay-based estimations. Additionally, mechanical alignment tolerances and the finite angular resolution of the measurement setup can introduce further discrepancies when using distance-based methods. Despite these differences, both approaches agree within the reported uncertainty bounds after pattern null removal, indicating consistency in identifying the effective phase center location.

The antenna radiation pattern was measured using the three-antenna method discussed in Chapter 2. Fig. 3.16 presents the angle-dependent antenna gain characteristics in the H-plane for both horn antennas, based on their S-parameter measurements. At 190 GHz, the WR05 horn exhibited a gain of 20.75 dB at 0°, while the WR03 horn, measured at 300 GHz, showed

https://doi.org/10.7795/110.20260421

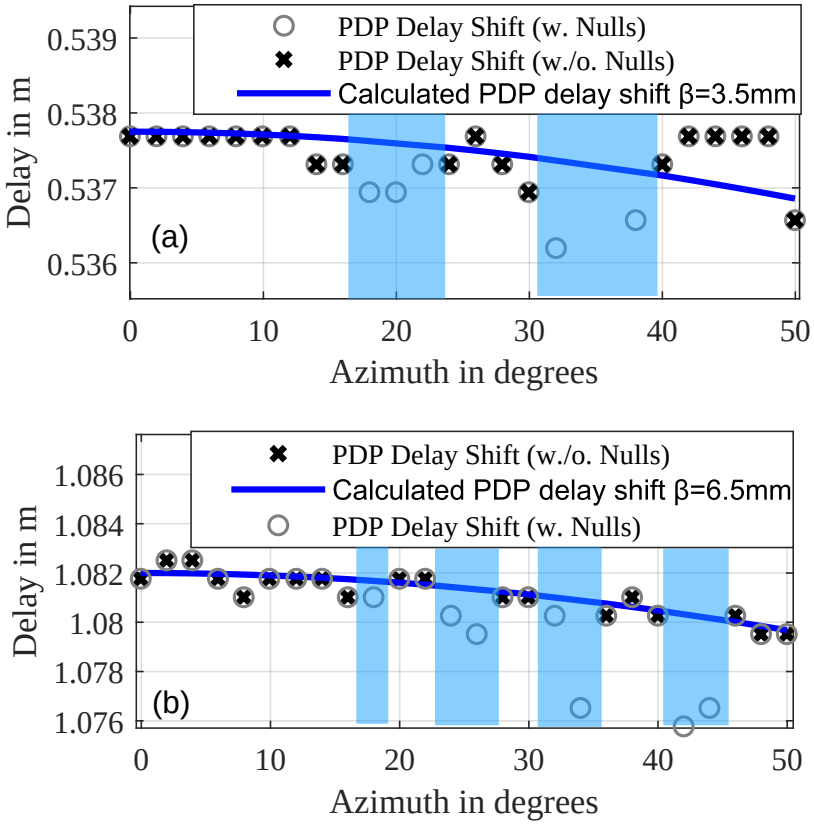

Figure 3.15: Phase center (PC) delay shift for WR05 and WR03 horn antennas across rotational angles from 0° to 50°. (a) WR05 horn delay shift; (b) WR03 horn delay shift. Fitted curves estimate phase centers at 3.5 mm and 6.5 mm, respectively. (Adopted from [26]).

a gain of 26.2 dB at 0°. The half-power beamwidth (HPBW) was 24° for the WR05 and 10° for the WR03 horn.

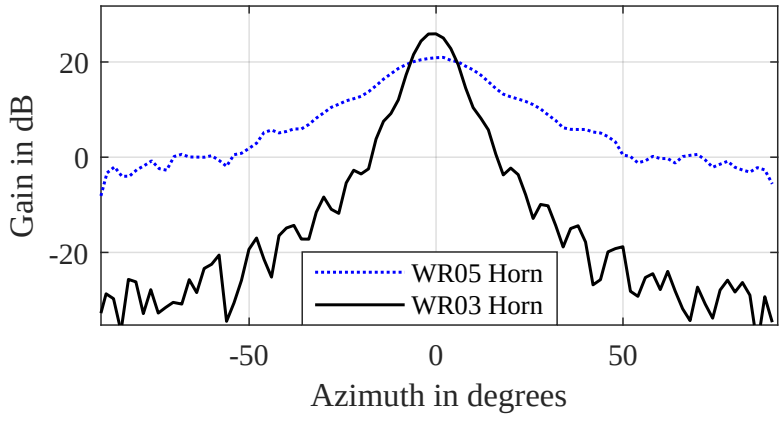

Figure 3.16: Angle-dependent gain in the H-plane for WR05 and WR03 horn antennas based on measured S-parameters. The WR05 horn exhibited a gain of 20.75 dB at 0° with an HPBW of 24°, while the WR03 horn achieved a gain of 26.2 dB at 0° with an HPBW of 10°. (Adopted from [26, 39].

https://doi.org/10.7795/110.20260421

3.3 Correlational-Based Channel Sounder Calibration

3.3.1 Time-Zero Measurement using Reference Transmitter

Each CS sensor node is equipped with both UWB transmitters and receivers to maintain consistent and fixed time alignment within each node. However, when the system is activated, an unknown time offset, a multiple of the sampling time, emerges between the transmitting and receiving nodes. These offsets vary with each system startup and must be measured to accurately determine the channel delays between nodes. Therefore, an onsite measurement is necessary before conducting any additional measurements [94].

The relative time offset is determined through a time-zero measurement, using a reference transmitter located in the base unit. This transmitter can be directly connected to the receiver via multifunction cables. By recording the impulse responses of the reference signal and identifying the sample positions corresponding to the reference pulse, the time offsets between transmitting and receiving nodes can be measured and subsequently corrected in the actual measurement data.

The time offset T_{offset} can be computed using the following equation:

$$T_{\text{offset}} = \left(\arg\max_{s} \left(m_{\text{cal}}(s \cdot t_s) \right) - \Delta s \right) \cdot t_s, \tag{3.10}$$

where $s \in [0, \ldots, 2^m - 2]$,

$$\Delta s = \arg\max_{s} \left(m_{\text{ref}}(s \cdot t_s) \right),$$

$m_{\text{cal}}(s \cdot t_s)$ represents the measured received signal at the receiver node, and $m_{\text{ref}}(s \cdot t_s)$ denotes the reference transmitted signal [39].

3.3.2 Back-to-Back Frequency Response Measurement

The instantaneous bandwidth of the CS spans several GHz, which can result in measurement shifts across different frequency ranges, introducing a frequency-dependent transfer function. To mitigate this, a well-characterized waveguide artifact or a precisely defined separation distance is employed. This allows for the equalization of the frequency response transfer function through deconvolution, ensuring accurate measurements across a wide range of frequencies [17, 39].

Characterizing the VNA using selected B2B measurements is critical for aligning magnitude and phase variations, as well as adjusting the reference plane between the VNA and the CS. This alignment guarantees measurement consistency. The frequency response of the CS, $H_{\text{deconv}}(f)$, is calculated using:

$$H_{\text{deconv}}(f) = A e^{-2\pi f d/c} \frac{H_{\text{mean}}(f)}{H_{\text{B2B}}(f)}, \tag{3.11}$$

where f denotes the down-converted frequency, A represents the magnitude of the characterized artifact, d is the electrical length of the measured waveguide or the actual delay from a LoS measurement, and c is the speed of light. Here, $H_{\text{mean}}(f) = \mathcal{F}(h_{\text{mean}})$, and $H_{\text{B2B}}(f)$

https://doi.org/10.7795/110.20260421

corresponds to the frequency response from the B2B measurement.

In addition to the waveguide cascade between transmitting and receiving ports, a LoS measurement was applied for B2B calibration, which will be further elaborated on in Chapter 4. The delay and path loss data acquired from the VNA were transferred to the channel sounding system, based on the common reference measurement, to ensure consistency between the two equipment.

Figure 3.17 presents the PDP reference plane and path gain corrections obtained using a B2B connection with a reference waveguide cascade. The setup included a WR03 waveguide, two short lines, and two attenuators (10 dB and 20 dB), measured using both the CS and the VNA across the 300–305 GHz range. This configuration enabled both phase and magnitude calibration from the VNA, revealing a shifted reference plane and a total path loss corresponding to an electrical length of 18.29 cm and a loss of 38.26 dB [95].

A notable observation in the figure is the large variation of path gain along the distance axis. This variation arises from the combination of the limited frequency span (only 5 GHz) and the time-domain resolution, which causes energy spreading and delay uncertainty. As discussed in Chapter 2, the presence or absence of windowing significantly impacts the apparent gain levels. When no window is applied (i.e., using a rectangular window), the frequency components are preserved in full magnitude, but this leads to increased sidelobe levels in the time domain due to spectral leakage. These sidelobes can interfere constructively or destructively with the main lobe, leading to greater fluctuations in observed gain across delay bins.

In contrast, applying a Hann window suppresses these sidelobes by tapering the frequency content at the edges of the bandwidth. However, this comes at the cost of reducing the overall magnitude of the signal in the time domain, including the main path component. The reduction is not a correction of physical gain but a consequence of the window's envelope, which effectively reduces the energy of all frequency components. This explains the significant difference in path gain values with and without the Hann window and highlights the importance of consistent windowing when comparing calibrated measurements or estimating gain from the PDP. [95].

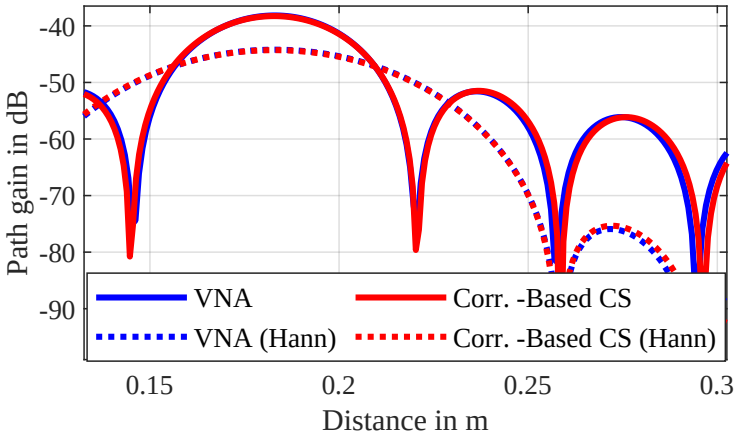

Figure 3.17: Reference waveguide PDP measurement using VNA and CS at the WR03 band. (Adopted from [95]).

https://doi.org/10.7795/110.20260421

3.3.3 IQ Imbalance

At sub-THz frequencies, manufacturing imperfections often cause discrepancies between I and Q channels, leading to amplitude and phase imbalances. This IQ imbalance can significantly degrade signal quality and increase measurement uncertainties [96]. These issues may arise from slight deviations in the ideal LO phase shift for the I and Q paths, with CSs higher frequencies and broader bandwidths being more susceptible to thermal and phase noise.

The WR03 CS exhibited significant IQ spectral distortion, which varied between measurements, making it difficult to apply a consistent correction across all cases. This distortion affects both the amplitude and phase balance between the in-phase (I) and quadrature (Q) components, leading to an inaccurate reconstruction of the complex baseband signal. To compensate for these imbalances, phase and magnitude corrections were applied using the following transformation matrix [97]:

$$\begin{pmatrix} \hat{h}_I(t) \\ \hat{h}_Q(t) \end{pmatrix} = \begin{bmatrix} \frac{1}{\alpha} & 0 \\ -\frac{\tan(\phi)}{\alpha} & \frac{1}{\cos(\phi)} \end{bmatrix} \begin{pmatrix} h_{\mathrm{mean}_I}(t) \\ h_{\mathrm{mean}_Q}(t) \end{pmatrix}, \tag{3.12}$$

where ϕ and α denote the phase and magnitude imbalance correction parameters, respectively. $h_{\mathrm{mean}_I}(t)$ and $h_{\mathrm{mean}_Q}(t)$ represent the uncorrected averaged I and Q components of the received impulse response, while $\hat{h}_I(t)$ and $\hat{h}_Q(t)$ are the corrected components. This correction matrix accounts for gain mismatches and quadrature errors between the I and Q channels, improving the fidelity of the complex-valued signal representation.

Figure 3.18 shows the spectrum distortion due to IQ imbalance for distances of 240 cm, 250 cm, and 260 cm, using a 10 cm measurement as a reference. The distortion primarily affects the higher sideband, but it also introduces some impact on the lower sideband, increasing uncertainty.

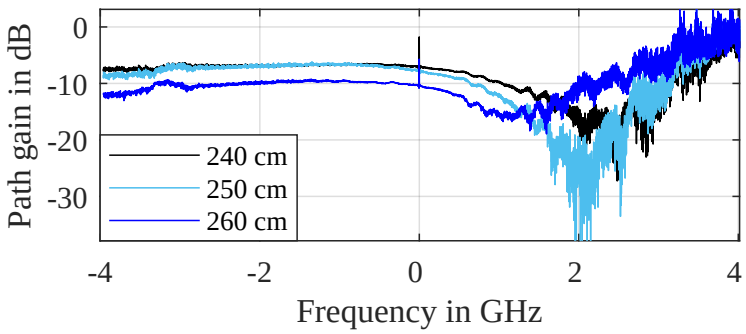

Figure 3.18: WR03 CS B2B calibrated frequency response of LoS for subsequent measurement distances of 240 cm, 250 cm, and 260 cm. (Adopted from [39]).

To evaluate the uncertainty influence on the lower part of the spectrum, a 60 cm measurement was used as an example. Figure 3.19 shows the received spectrum before B2B calibration. To assess the impact of IQ imbalance, phase corrections were applied with ϕ ranging from 0 to 0.2 radians (in 0.02 increments), and magnitude corrections with α ranging from 1 to 2 (in 0.1 increments). The resulting variations in the corrected spectra are also illustrated in Figure 3.19, highlighting the sensitivity of the system response to small IQ mismatches.

https://doi.org/10.7795/110.20260421

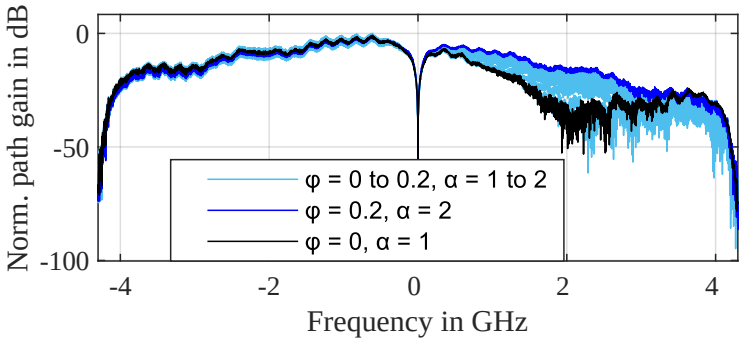

Figure 3.19: WR03 CS received spectrum at a 60 cm distance with different IQ corrections applied. (Adopted from [39]).

The variation significantly affects the sideband spectrum, with deviations of several dB. The interpolated PDP for the lower spectrum, shown in Figure 3.20, highlights a peak deviation of 2.4 dB for a 5 GHz bandwidth between 300 GHz and 305 GHz. While no universal correction was found, manual adjustments allowed for better alignment with the VNA frequency response. In contrast, the WR05 CS showed no observable IQ imbalance effects.

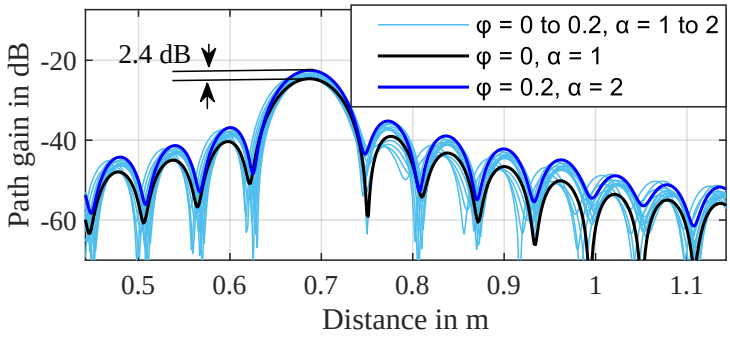

Figure 3.20: WR03 CS PDP for a 5 GHz bandwidth at a 60 cm distance under various IQ corrections. (Adopted from [39]).

3.3.4 DC Offset

After up-conversion at the transmitted, or the down-conversion at the received PRBS signal, the LO frequency f_{LO} would fall near the DC region of the baseband spectrum. In practice, the system can experience LO leakage due to finite isolation in the mixer or imperfections in the LO distribution network. This leakage is translated as a spectral spike at or near DC and becomes particularly problematic when combined with DC offsets introduced by the sampling circuits and ADC. The combination of these effects can introduce spurious low-frequency components into the signal, degrading the accuracy of the measurement. These artifacts must be filtered out or mitigated through calibration to ensure reliable results.

Figure 3.21 illustrates the transmitter-side schematic of the CS, highlighting how LO leakage can arise in the system. Although the figure focuses on the transmitter, similar mechanisms apply to the receiver path, where LO leakage also contributes to unwanted energy near DC in the down-converted signal.

https://doi.org/10.7795/110.20260421

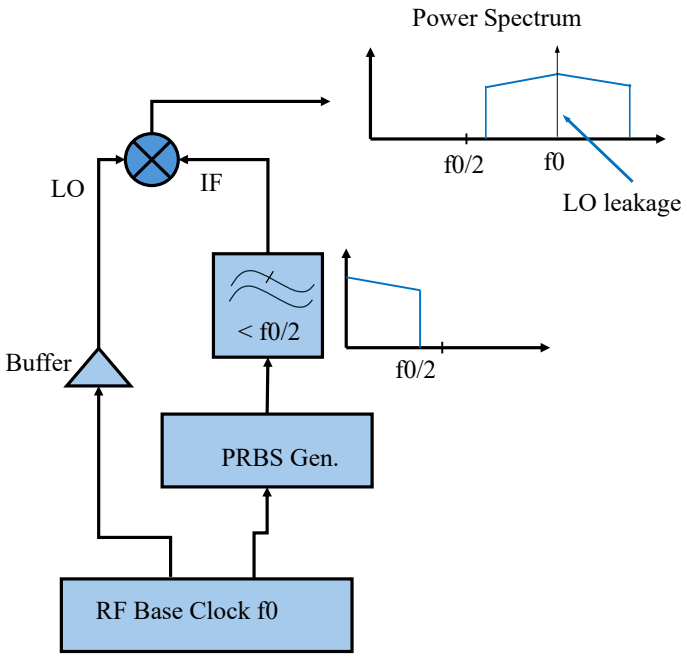

Figure 3.21: LO leakage and DC offset in the CS transmitter. (Adopted from [39]).

Following B2B calibration, the magnitude of the residual DC offset in the calibrated measurement can vary due to differences in the reference measurement's delay and attenuation. Since the B2B reference is used to normalize the measurement under test, any DC-related distortion present in the reference, such as frequency-dependent leakage or reflections, will be transferred onto the calibration and subsequently influence the final result. This effect is particularly noticeable in the lower-frequency portion of the spectrum, where even small DC mismatches can shift the spectral baseline higher or lower depending on the characteristics of the reference measurement. This shift often aligns toward the reference measurement, causing nonlinear changes in the measured magnitude. These nonlinearities can significantly impact PDP measurements and their associated uncertainties. Figure 3.22 presents the frequency spectrum around the DC component for two measurement artifacts using the WR05 CS, where LO leakage extends approximately 50 MHz around the DC.

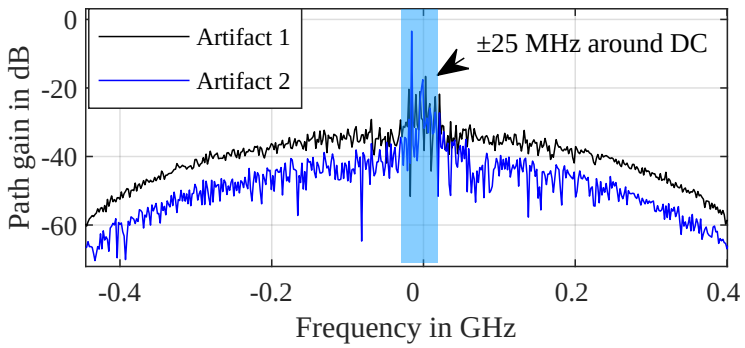

Figure 3.22: WR05 CS DC offset influence on two measurement artifacts. (Adopted from [39]).

https://doi.org/10.7795/110.20260421

Figure 3.23 shows the PDP results for two measurements taken at 90 cm and 240 cm, both before and after applying DC offset filtering. The results demonstrate that the DC offset nonlinearly varies between measurements, depending on the path loss relative to the reference measurement at 100 cm. The observed peak differences between the filtered and unfiltered magnitudes were 0.26 dB and 0.94 dB for the 90 cm and 240 cm measurements, respectively.

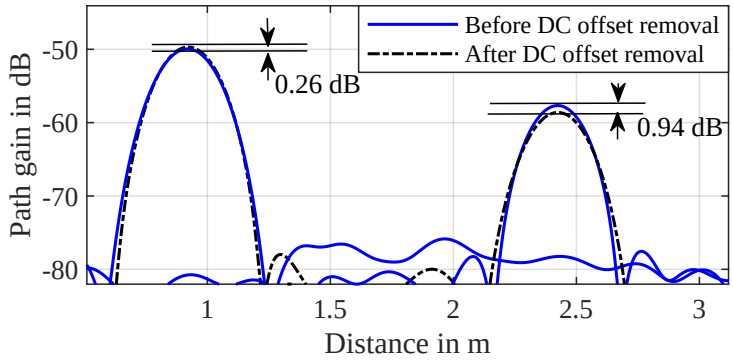

Figure 3.23: PDP of two measurement artifacts before and after DC removal. (Adopted from [39]).

To mitigate this distortion in the spectrum, a digital band-reject filter (BRF) with a bandwidth of 50 MHz was applied:

$$H_{\text{Filter}}(f) = H_{\text{mean}}(f) \cdot \text{BRF}(f), \tag{3.13}$$

where $\text{BRF}(f)$ is a band-reject filter designed to suppress frequencies within a ± 25 MHz range around the DC component [39].

These characterizations are applied in Chapter 4 to establish the full investigation to the CS systems under test.

https://doi.org/10.7795/110.20260421

https://doi.org/10.7795/110.20260421

4

Characterization of Sub-THz Channel Sounding Systems in OTA Measurement Scenarios

In this chapter, the CS systems using controlled OTA measurement conditions are characterized. This includes a LoS measurement at different separation distances, which will help investigating the systems' non-linearity, and other system parameters, which represent a challenging investigation at Sub-THz band. The distance measurement will help identifying the exact frequency step size of the CSs by matching the obtained delays with the actual separations and considering the antenna calibration which was discussed in Chapter 3. Different measurement separations can be used to investigate the feasible bandwidth used for the CS and the spectrum boundaries; it helps identify the noise floor influence on the measurements as extended distances can characterize attenuation. Different separations can help to investigate the B2B calibration using different references and to understand the influence of the DC offset and IQ imbalance that was discussed in the previous chapter in Sections 3.3.4 and 3.3.3, respectively.

On the other hand, the multi-path measurement acts as a realistic application for our characterized CSs. It will help to understand a more complex measurement scenario and the ability of the measurement equipment to distinguish multi-path components. This involved different scenarios, including a plane reflector and small reflectors of various dimensions as single and multiple rotational reflectors at different angles. It consists of the investigation where the accurate delays obtained from different multi-paths will be essential to monitor the changing positions of the reflectors and the difference in resolution when windowing is applied.

Reflected component delays correspond to the theoretical models in Section 2.3.2. Their separation is enhanced by applying the interpolation and Hann windowing procedures introduced in Section 2.4.2 and used the earlier VNA calibration procedures in Section 3.1.

4.1 Line-of-Sight Distance Measurement

4.1.1 Measurement Setup

An automated control system was employed to vary the separation distance between the transmitter and receiver from 10 cm to 340 cm in increments of 10 cm. The initial separation

https://doi.org/10.7795/110.20260421

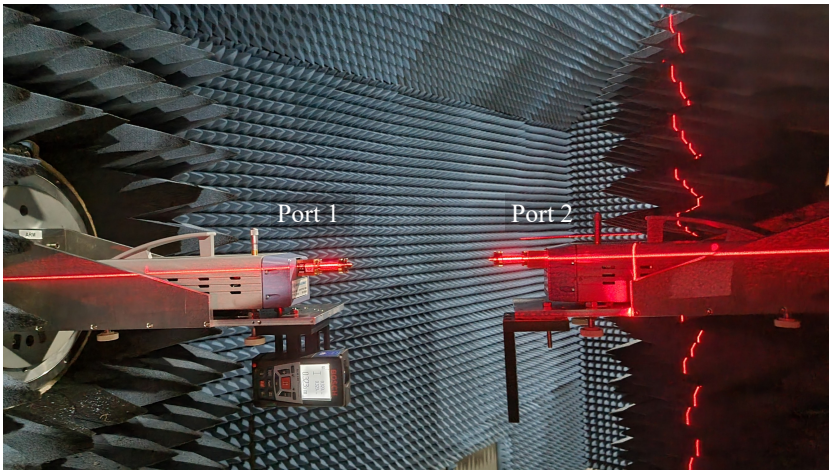

Figure 4.1: Far field measurement setup showing the VNAfrequency converters positioned on motorized mounts. Port 2 moved successive steps of 10 cm away from port 1 to cover the total range between 10 cm – 340 cm. The same setup was repeated for the CS systems.

was measured using a calibrated laser distance meter, with a measurement uncertainty of ±1 mm. Subsequent distances were verified using both the automated instrumentation and the laser distance meter.

All measurements were conducted in a temperature-controlled anechoic chamber at PTB. The relative humidity (RH) and temperature were maintained between % and 41.6 %, and 22.8° C to 23.5° C, respectively [27]. Given the short propagation path length and the sub-THz frequencies under test, humidity was considered to have a negligible influence on the results. Figure 4.1 shows a photograph of the far-field measurement setup. The separation distances were determined based on the antenna PC calculations discussed in Section 3.2.

The VNA measurement system consisted of a Rohde & Schwarz ZVA24™ VNA, calibrated using the UOSM method, with ZVA-Z220™ and ZVA-Z325™ frequency converters for WR05 and WR03 bands, respectively. A linear frequency sweep of 401 points was performed over a 20 GHz bandwidth, covering the frequency ranges of 180–200 GHz for WR05 and 290–310 GHz for WR03. Both measurements employed an IFBW of 10 Hz.

The CS systems included a base unit that generated a 12-bit PRBS. The clock signal was distributed via SMA cables to the transmitting and receiving sensor nodes, with an IF of 9.22 GHz. These nodes were connected to RF transmitting and receiving heads, operating at center frequencies of 187.5 GHz and 304 GHz for the WR05 and WR03 CS systems, respectively [26]. The architecture of the CS systems was presented in Section 2.1.2.

4.1.2 Channel Sounder Frequency Step Size

Both CS systems transmit a PRBS waveform consisting of 4096 symbols. A main objective of this investigation is to determine the frequency step size with high accuracy. Distance measurements are used to validate this by analyzing the resulting PDP delay. Verifying the delay across varying distances ensures that the frequency step size is correctly set. Any deviation in the frequency step would lead to a corresponding shift in the delay value, either increasing or

https://doi.org/10.7795/110.20260421

decreasing relative to the reference distance used in the B2B calibration [39].

The results for the frequency step size characterization are presented in Figure 4.2. Specifically, Figure 4.2(a) displays the delay differences for the WR05 system, while Figure 4.2(b) illustrates the corresponding results for WR03. The figures show how the measured delays compare with the VNA reference delay at various separation distances. The interpolation factor of 40 was used to achieve a better estimate for the PDP delay peaks [39].

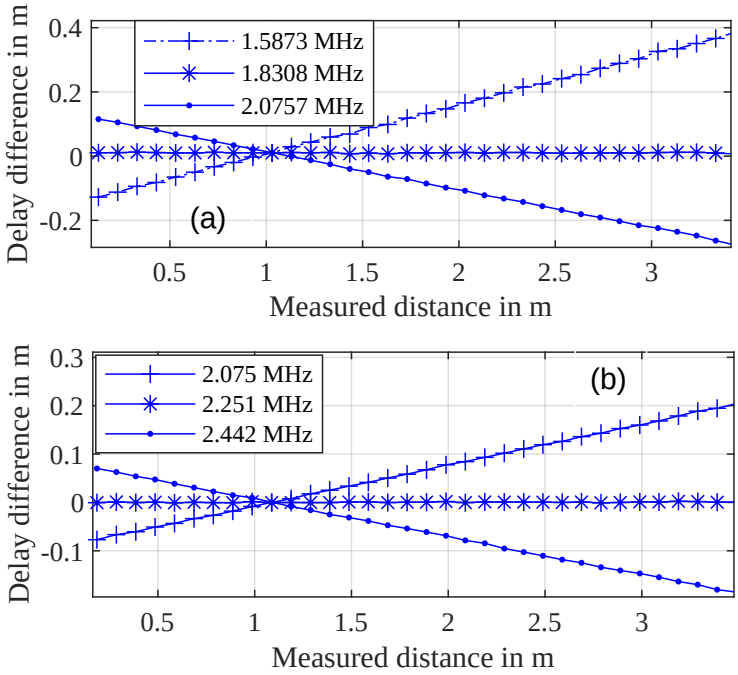

Figure 4.2: Characterization of the frequency step size based on distance separations and delay differences from the VNA reference delay. (Adopted from [39]).

The comparison between the CS PDP-based delay measurements, the VNA-based delays, and the physical distances confirms that delay estimation accuracy in CS systems is highly sensitive to the frequency step size used during the measurement. The best agreement was observed for a step size of 1.83 MHz for the WR05 CS and 2.25 MHz for the WR03 CS, indicating that these configurations minimize interpolation errors and spectral leakage effects.

To further evaluate the stability of the delay estimates, the peak-to-peak delay deviations across all measured distances were evaluated. Figure 4.3(a) shows the WR05 system results, where the delay deviation remained below 6 mm across a 7.52 GHz bandwidth (±5 MHz). Similarly, Figure 4.3(b) illustrates that the WR03 system maintained a peak-to-peak delay variation under 4 mm across a bandwidth of 9.224 GHz (±5 MHz). These findings confirm that with carefully selected frequency step sizes, the CS system can achieve consistent and accurate delay estimation across wide sub-THz frequency bands, making it well suited for high-resolution time-domain channel characterization [39]..

https://doi.org/10.7795/110.20260421

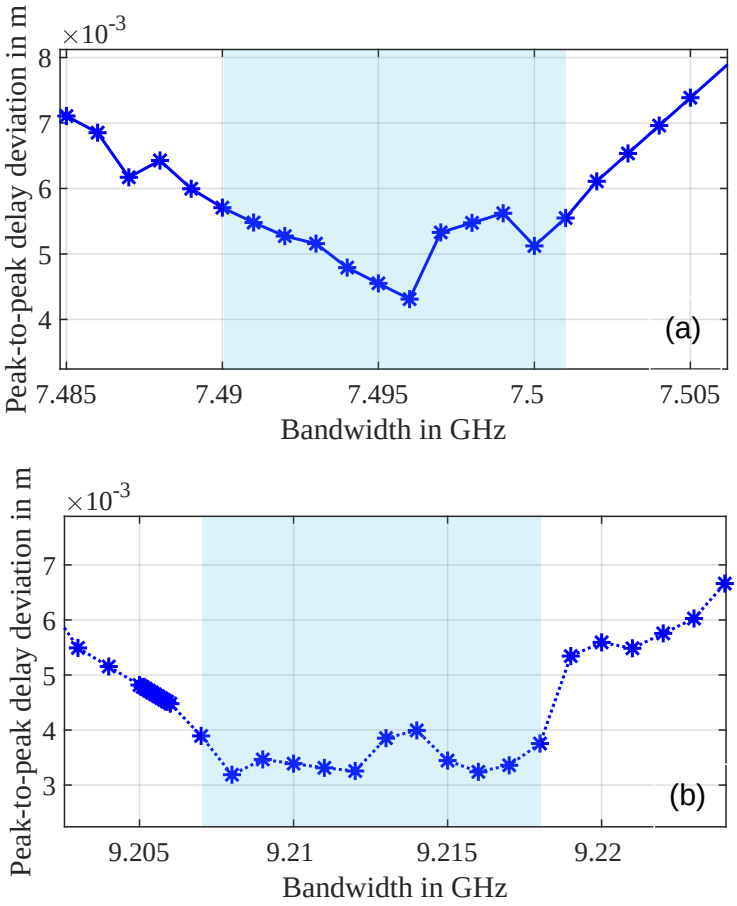

Figure 4.3: Total CS spectrum showing the combined peak-to-peak delay deviation across all measured distances (a) WR05. (b) WR03. (Adopted from [39]).

4.1.3 Spectrum Boundaries

The spectrum boundaries refer to the frequency range where the signal is not fully recovered, often exhibiting weaker strength due to the effects of finite bandwidth filtering. Bandpass filters limit the signal within a defined frequency range; however, their roll-off region near the edges of the passband gradually attenuates signal strength, leading to reduced amplitude at the spectrum boundaries. Furthermore, applying windowing functions to minimize spectral leakage can further suppress signal amplitude, particularly near the edges [39].

Noise and interference also contribute significantly to weakening the signals at the spectrum boundaries. The SNR tends to decrease at the edges due to the combined effects of filtering, windowing, and hardware imperfections, which reduces the clarity of correlation peaks and increases sensitivity to noise.

This chapter uses the PDP delay characterization method to identify the spectrum boundaries for both CS systems under investigation. By aligning the measured PDP delays with reference values obtained from the VNA and theoretical calculations, it can evaluate the effectiveness of the bandpass filtering and confirm the signal's integrity within the defined frequency range.

https://doi.org/10.7795/110.20260421

In Fig. 4.4 A 500 MHz spectral window was swept across the complete spectrum of both CS systems in 100 MHz increments. While the 500 MHz bandwidth does not provide high resolution, it effectively identifies the spectral boundaries where the signal is accurately received. Delay values were computed for all measured distances and compared with reference measurements. Fig. 4.4(a) illustrate the measurement results for the WR05 band, the spectral boundaries ranged from 1.16 GHz to 5.66 GHz, while Fig. 4.4(b) shows the WR03 CS boundaries, where they extended from 0.59 GHz to 8.57 GHz [39].

As shown in the figure, this technique highlights the influence of DC offset on the WR05 system and the impact of IQ imbalance on the WR03 CS. These affected spectral regions exhibit phase deviations, which become evident when compared to the corresponding VNA measurements.

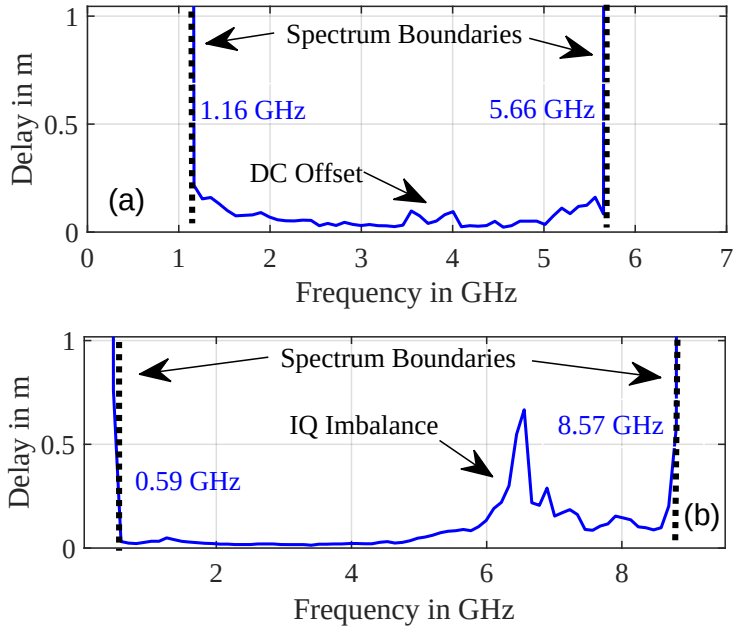

Figure 4.4: CS spectrum boundaries investigation using a 500 MHz spectral window swept across the complete spectrum of both CS systems in 100 MHz increments. (a) WR05. (b) WR03. (Adopted from [39]).

4.1.4 Bandwidth Feasibility

After determining the total bandwidth and identifying the spectral boundaries, the next step is to identify the feasible measurement bandwidth that each CS system can support to ensure optimal linearity and resolution. To achieve this, the remaining bandwidth of both CS systems is evaluated by analyzing the PDP path gain and delay. The interpolated peaks were compared against the theoretical Friis path loss and the VNA-measured path gain. Additionally, this work calculated the combined delay deviation with respect to the VNA and laser distance meter measurements for each CS system using 500 MHz step increments. The path loss was evaluated both before and after applying a Hann window [39].

The results of the peak-to-peak magnitude deviations across different measurement bandwidths are shown in Figure 4.5. Figure 4.5(a) presents the results for the WR05 sounder, while

https://doi.org/10.7795/110.20260421

Figure 4.5(b) illustrates those for the WR03 sounder.

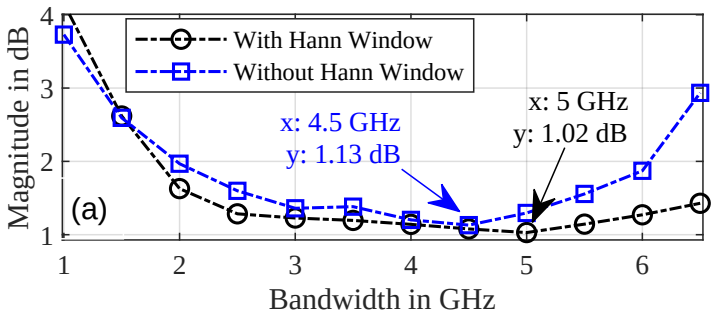

(a) WR05

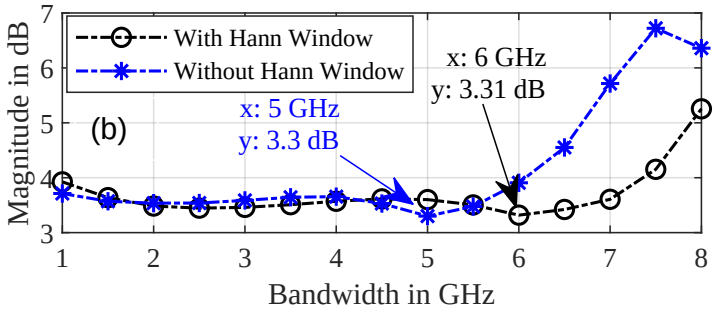

(b) WR03

Figure 4.5: CS peak-to-peak magnitude deviation across different measurement bandwidths. (a) WR05. (b) WR03. (Adopted from [39]).

For the WR05 sounder, the smallest path loss deviation was observed at a 4.5 GHz bandwidth, with a difference of 1.13 dB. When applying a Hann window, this minimum shifted to a 5 GHz bandwidth, reducing the deviation to 1.02 dB of the combined distances. In the case of the WR03 sounder, the smallest magnitude deviation occurred at a 5 GHz bandwidth, with a combined peak-to-peak path loss difference of 3.3 dB. Applying the Hann window extended the feasible bandwidth to 6 GHz, reducing the deviation slightly to 3.31 dB.

To investigate the feasible bandwidth in terms of delay, the same procedure was repeated to monitor the PDP peak shift in time across the bandwidths increments. Those results are presented in Figure 4.6. For the WR05 sounder, the lowest delay deviation was recorded at a 4.5 GHz bandwidth, corresponding to a deviation of 4.66 mm. Similarly, for the WR03 sounder, the lowest combined delay deviation was observed at a 5 GHz bandwidth, with a deviation of 3.18 mm.

These results demonstrate that the feasible bandwidth for each CS system is not solely determined by the total available spectrum but also by how well the system maintains consistency in both magnitude and delay across the measurement range. The optimal bandwidth points—4.5 GHz for WR05 and 5 GHz for WR03—represent the best trade-offs between minimizing path loss variation and preserving time-domain alignment with reference measurements. The slight improvements introduced by applying a Hann window suggest that spectral smoothing can help reduce ripple effects, although the improvements are marginal. Overall, the analysis confirms that careful selection of the measurement bandwidth is critical to

https://doi.org/10.7795/110.20260421

ensuring reliable calibration and accurate delay estimation in sub-THz CS systems.

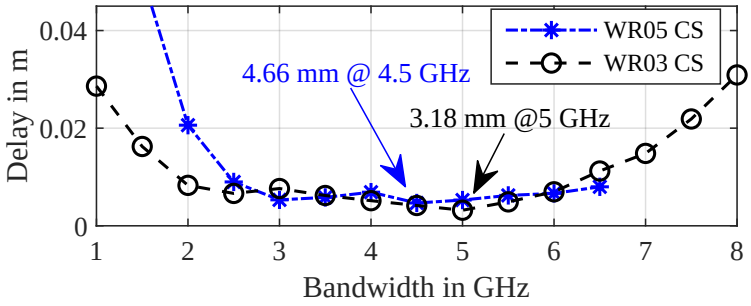

Figure 4.6: WR05 and WR03 CS peak-to-peak delay deviation across different measurement bandwidths. (Adopted from [39]).

4.1.5 Reference Measurement Selection

One of the most important analysis that affects the reliability of the CS systems is the selection of the reference measurement. These are essential as they are used in the CSs B2B calibration process, where any deviations in their magnitude and phase will affect all subsequent measurements and increase the measurement uncertainties. The CS evaluation using the B2B calibration and other procedures were presented in Section 2.2.2 and Section 3.3.2.

All measurement distances are characterized using a reference VNA measurement and the OTA distance between the antenna elements and their corresponding PC values. This measurement scenario is beneficial for this investigation, as it allows any measurement to be selected as a reference for performing B2B deconvolution. It is essential to thoroughly assess the reference measurement to account for uncertainties that may arise from choosing different references. It ensures that the selected reference does not introduce significant path gain deviations when compared to others, thereby increasing confidence in the accuracy of the measurements and identifying potential inconsistencies.

Figure 4.7 illustrates the path gain differences across measurement distances ranging from 10 cm to 90 cm, comparing deviations from a 100 cm calibration reference. To ensure consistency, the 10 cm measurement distance was normalized to zero for all comparisons.

For the WR05 CS, Figure 4.7(a) shows that selecting different references leads to increasing PDP path gain deviations as measurement distances grow. Deviations begin at 0.06 dB for distances under 1 m and increase to 0.09 dB by 1.3 m. Beyond this range, the deviation continues to rise, reaching 0.14 dB between 2.3 m and 2.7 m, and ultimately peaks at 0.2 dB for distances beyond 3 m.

In contrast, the WR03 CS displays greater stability across various distances, as seen in Figure 4.7(b). The peak-to-peak path gain deviation remains within 0.06 dB, indicating more consistent performance across different reference selections. The blue-shaded region in both figures represents the 95 % confidence interval calculated from the combined reference measurements at each distance.

The CS uncertainty analysis builds on the Friis model from Section 2.3.2 and uses the

https://doi.org/10.7795/110.20260421

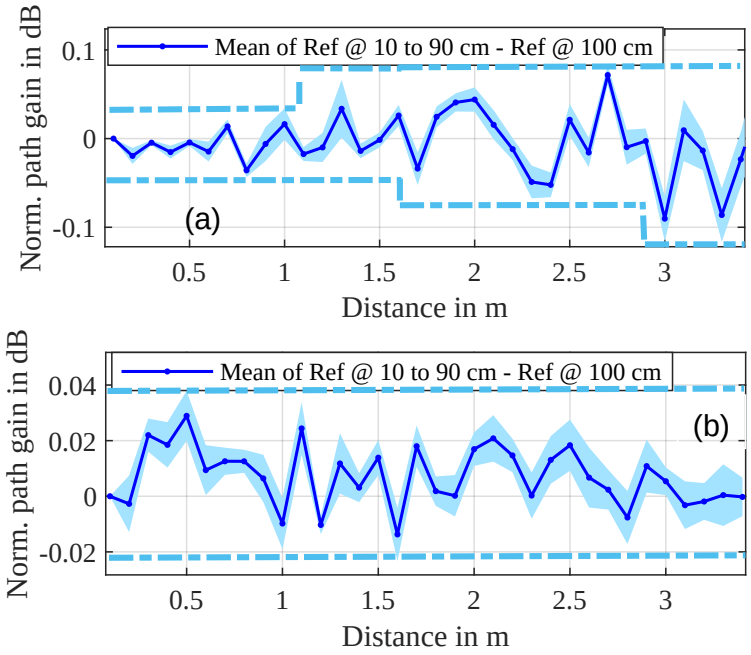

Figure 4.7: PDP path gain differences using measurement distances between 10 cm and 90 cm as reference measurements, compared to a 100 cm reference for the CS systems at (a) WR05 and (b) WR03. (Adopted from [39]).

antenna calibration measurements established in Section 3.2.1.

4.2 Combined VNA and CS Measurement Uncertainties

As discussed in Section 2.4.2 the PDP is the central focus across various measurement devices, it aims to analyze the interpolated PDP peaks across different measurement distances, comparing the results obtained from our DUTs with the theoretical Friis loss. The VNA measurements discussed previously revealed several sources of uncertainty, including drift (u_{drift}), calibration effects (u_{cal}), trace noise (u_{noise}), antenna gain (u_{ant}), and non-linearity ($u_{\text{n-linear}}$).

The combined extended uncertainty for each frequency band was determined using a simplified model where individual error contributions are combined through the root-sum-square method:

$$u_{\text{Combin}} = \sqrt{u_{\text{cal}}^2 + u_{\text{noise}}^2 + u_{\text{drift}}^2 + u_{\text{ant}}^2 + u_{\text{n-linear}}^2} \tag{4.1}$$

Table 4.1 summarizes the parameters and their corresponding PDP magnitude uncertainties for the WR05 and WR03 VNA measurements.

Figure 4.8(a) displays the path gain deviations for the WR05 band, comparing VNA and CS measurements against theoretical Friis loss values across the frequency range of 185 GHz to 190 GHz. The VNA measurements exhibited a standard deviation of 0.01 dB with a combined uncertainty of ±0.22 dB. For the CS system, after removing the DC offset, the standard deviation reached 0.4 dB, with values of 0.34 dB recorded both before and after applying the Hann window [39].

https://doi.org/10.7795/110.20260421

Parameter	WR05 (dB)	WR03 (dB)
Calibration	0.01	0.02
Trace Noise	3.2×10^{-3}	10×10^{-3}
Drift	0.2	0.45
Antenna Gain	0.05	0.1
Non-Linearity	0.06	0.22

Table 4.1: VNA PDP magnitude uncertainties at WR05 and WR03 bands [39].

For the WR03 band, Figure 4.8(b) presents the path gain deviations between VNA and CS measurements relative to the theoretical Friis loss within the 300 GHz to 305 GHz frequency range. The VNA measurements exhibited a standard deviation of 0.04 dB with a combined uncertainty of ± 0.51 dB. For the WR03 CS system with a 5 GHz bandwidth, the standard deviations were 1.4 dB before applying the Hann window and 1 dB after applying it [39]. The figure also shows the uncertainties related to the extended CS spectrum ranging between 300 and 308 GHz after applying the IQ corrections which provided a similar performance to the Hann-windowed 5 GHz CS bandwidth.

The uncertainty analysis reveals that the CS system can approach the precision of VNA measurements when appropriate signal processing techniques and corrections are applied. While the VNA maintains low deviation and tight uncertainty bounds across both bands, the CS results show greater sensitivity, particularly in the WR03 band. Nevertheless, applying a Hann window and extending the measurement bandwidth with IQ correction significantly reduces path gain variability, bringing the CS performance within an acceptable uncertainty range for sub-THz channel characterization.

4.3 Multipath Measurements

4.3.1 Plane Reflector

The LoS distance measurements presented in the previous section provided the essential characterization of the measurement systems, and now it is needed to evaluate their performance in a more complicated scenario by having a combined LoS and a NLoS measurement paths. Measurements were carried out in the same temperature controlled anechoic chamber at PTB, that was previously presented, with a stainless steel sheet reflector positioned at a distance between the antennas, as shown in Fig. 4.9(a), where an illustration of the measurement setup is shown. Fig 4.9(b) shows a photograph of the measurement setup. An automated control system adjusted the rotational angle of the transmitting antenna around the aperture edge of the high-gain transmitting horn antenna [95]. The separation distance between the transmitting and receiving antennas was 2 m.

The setup included two different antennas at the transmitter and receiver ports. A high-gain horn antenna with a 26.01 dBi gain and a narrow beam was placed at the transmitting end, while a wide-beam horn antenna with a 14.85 dBi gain and a short waveguide was used at the receiving end. Antenna gains were measured across the 300 to 305 GHz frequency range

https://doi.org/10.7795/110.20260421

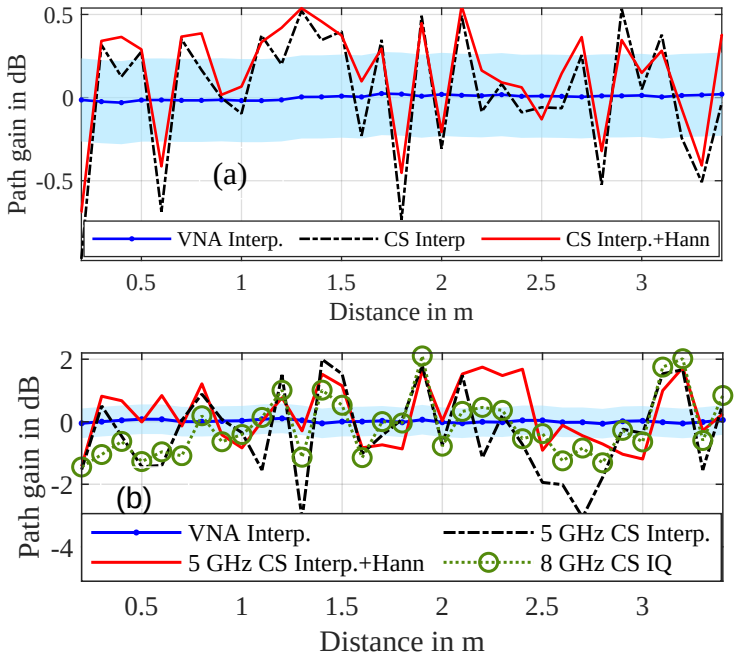

Figure 4.8: Distance measurement deviations from the theoretical path gain for (a) WR05 and (b) WR03 CS systems. The shaded blue region indicate the VNA measurement uncertainty expressed as expanded uncertainty with 95 % confidence (coverage factor k=2). (Adopted from [39]).

using a VNA with 100 MHz frequency steps. The direct LoS distance between the antenna apertures was 2 meters, while the reflected path, caused by a metallic surface, measured 2.644 meters, as illustrated in Figure 4.9 [95].

The antennas' radiation E-plane RMS gain is shown in Figure 4.10. The antenna separation and center of rotation were measured using a calibrated laser device. Measurements were performed for both instruments at rotational angles between 0° and 90°. Since this measurement depends on antenna radiation patterns, using the same antennas for both measuring devices was essential for consistency between the CS and VNA setups [95].

The VNA used for the measurements was a UOSM-calibrated Rohde & Schwarz ZVA24™ VNA with ZVA-Z325™ frequency converters and WR03 waveguides. S-parameter measurements were performed using a linear sweep of 100 MHz frequency steps covering 256 GHz – 320 GHz, with an IF bandwidth of 10 Hz. This wide VNA bandwidth enabled testing of multipath conditions with high delay resolution, examining the impact of center frequency shifts, and ensuring alignment with the CS frequency range before and after filtering. This setup with extended frequency investigation was presented in [95].

To ensure consistency between measurements, the reference plane and path gain for the CS were aligned with calibrated values from the VNA. These adjustments were based on a B2B setup that included a reference waveguide arrangement made up of two short sections and two attenuators rated at 10 dB and 20 dB. Measurements were taken using both the CS and the VNA. The results of this B2B calibration, along with the reference plane shift, are shown in Fig. 3.17 and detailed in [95] and in Section 3.3.2. This configuration was used to define the reference point for the CS, with the VNA providing known phase and amplitude

https://doi.org/10.7795/110.20260421

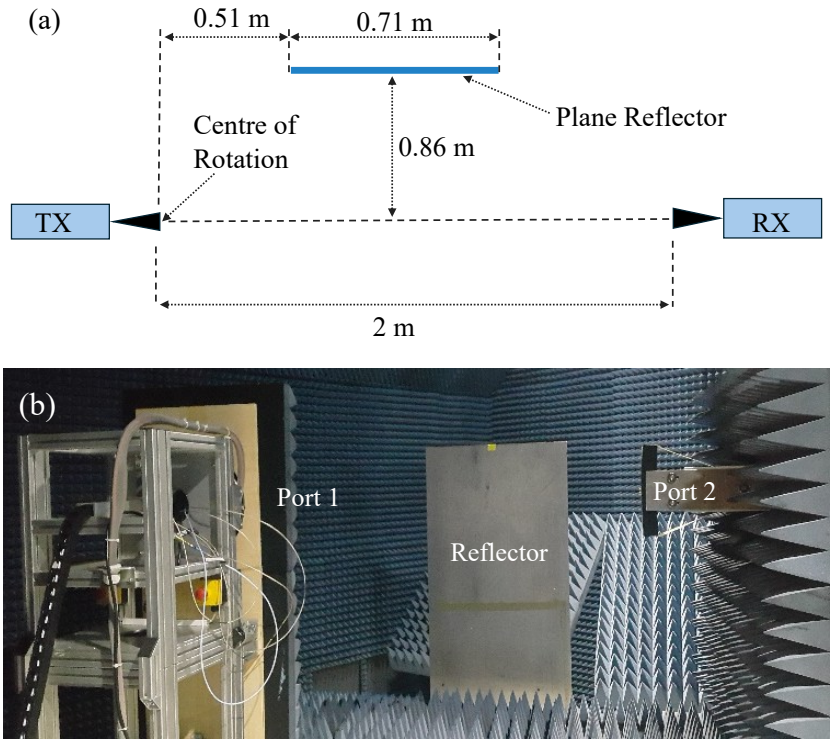

Figure 4.9: Plane reflector measurement setup. (a) Schematic of the measurement configuration. (b) Photograph of the experimental setup. The transmitting antenna is rotated around the aperture edge of the high-gain transmitting horn antenna. The phase center and the center of rotation are not coincident.

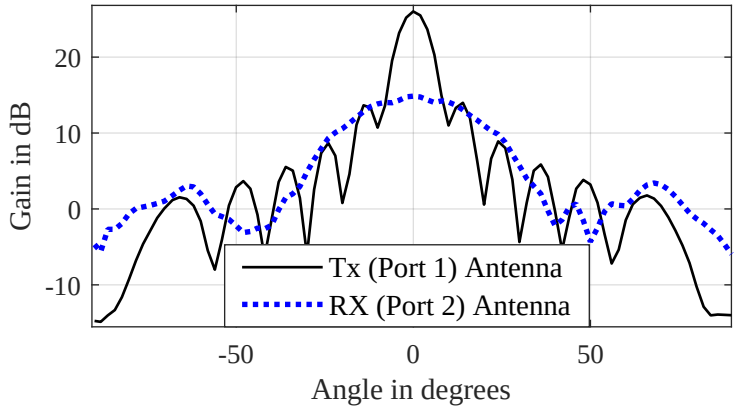

Figure 4.10: Transmitting and receiving antennas' RMS gain measured using the three-antenna method. (Adopted from [95])

characteristics. To improve distance resolution, both data sets were interpolated by a factor of 40.

The Hann window was applied, which flattened the measured peaks while showing no delay or path gain deviations between the VNA and CS. A measurement bandwidth of 5 GHz was used for both the VNA and CS, resulting in distance deviations of ±2.2 mm and ±6.6 mm, respectively. The LoS and reflected paths at different rotational angles concerning distance and path gain were measured using both VNA and CS, as shown in Figure 4.11.

https://doi.org/10.7795/110.20260421

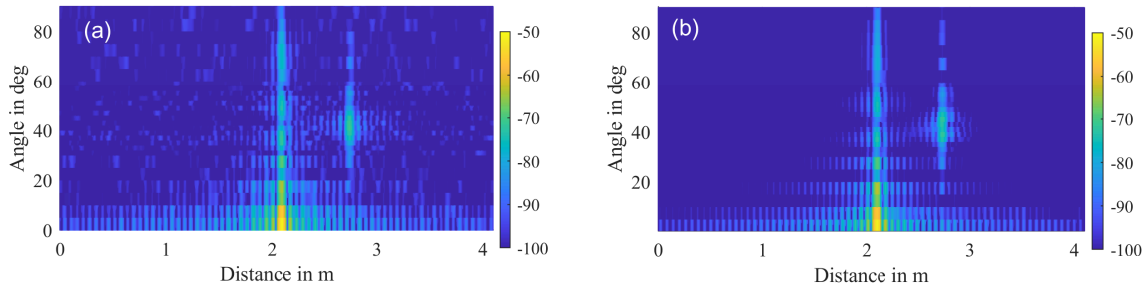

Figure 4.11: Measured LoS and reflection at different rotational angles concerning distance and path gain.(a) VNA (b) CS. (Adopted from [95]).

The measured path gain at different rotation angles demonstrates that the VNA and CS results are comparable in terms of signal loss for LoS and reflected PDP impulse responses. The interpolated peaks from both measurement systems were analyzed, and the RMS difference between the VNA and CS measurements was found to be 1.72 dB for the LoS path and 2.02 dB with the Hann window. The difference increased for the reflected path due to the more significant noise influence, with RMS deviations of 2.35 dB and 2.55 dB before and after applying the Hann window, respectively, as shown in Figure 4.12(a).

Different antennas and waveguides shift the reference plane based on their physical dimensions. As mentioned in earlier, This work used the same set of antennas for both VNA and CS experiments to maintain consistent radiation patterns, gain, and reference plane shift for the VNA and CS. Both LoS and reflected path measurements showed the reference plane shift. For improved resolution, the VNA was set to a center frequency of 302.5 GHz, and the measurement bandwidth was extended to 20 GHz, followed by interpolation. The RMS shift in the reference plane for both antennas was calculated to be 9.60 cm, with a variation of ± 0.5 mm observed across different rotation angles for both the direct LoS and reflected signal paths, as reported in [95]. The deviation between the measured and actual distances between the antenna apertures is shown in Figure 4.12(b).

The CS system demonstrated comparable performance to the VNA in both WR05 and WR03 bands under combined LoS and NLoS conditions. While the VNA maintained lower delay and path gain deviations, the CS system achieved acceptable accuracy, with RMS differences in path gain and distance measurements . These results confirm the suitability of the CS system for high-resolution sub-THz multipath characterization when proper calibration and signal processing are applied.

https://doi.org/10.7795/110.20260421

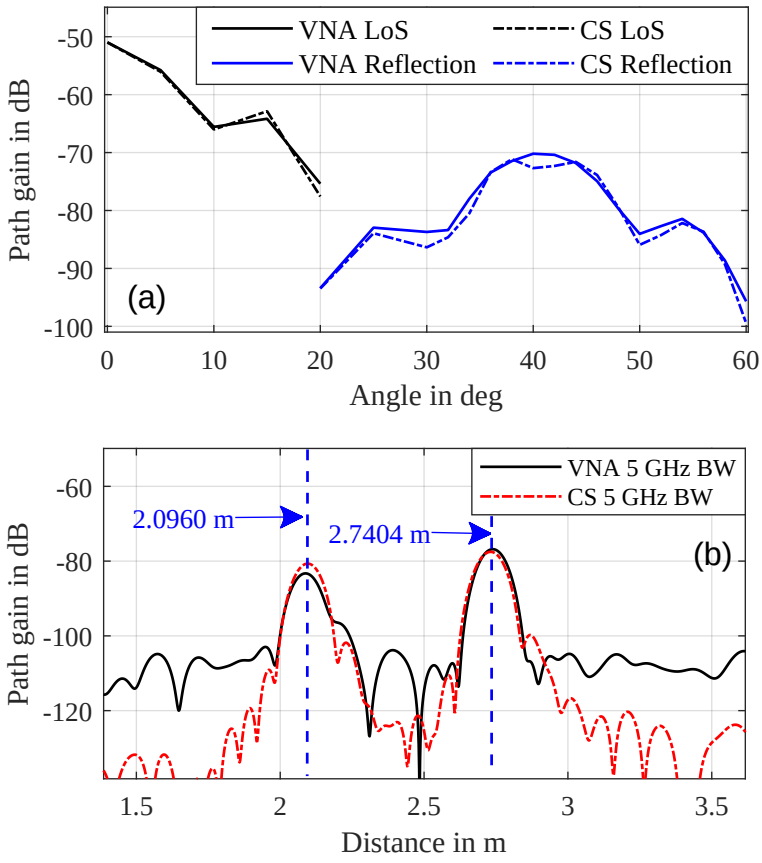

Figure 4.12: Measured PDP at different rotation angles. (a) PDP at 40° rotational angle showing LoS and reflection peaks (b) VNA and CS measured path gain based on PDP LoS and reflection peaks. (Adopted from [95]).

https://doi.org/10.7795/110.20260421

4.3.2 Single Reflector Analysis

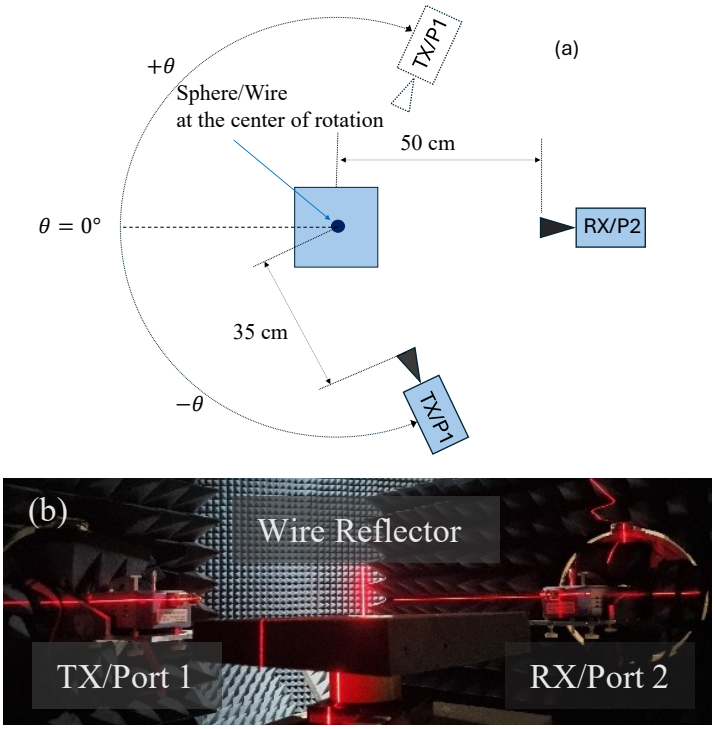

Figure 4.13: Far-field single reflector measurement setup. (a) Sketch of the measurement setup. (b) Measurement setup showing the frequency converters placed on motorized mounts. Port 1 rotates in 10° steps around the wire at the rotation's center. (Adopted from [39]).

Another NLoS measurement scenario is investigating the signal propagation of small reflectors. Our DUTs are analyzed for their reflection characteristics using various reference objects to study propagation effects in multipath scenarios, including both LoS and reflected components. In this experimental setup, a stainless-steel reflector, spheres of varying diameters, and an 8 cm long wire with a diameter of 1.5 mm were placed at the center of rotation. The transmitting and receiving antennas are aligned with the reflector's center to maintain symmetry in the measurements. The transmitting antenna is positioned 35 cm from the center of rotation and rotates around the reflector in steps of θ degrees. The receiving antenna remains stationary 50 cm away from the center of rotation, fixed at $\theta = 180°$. PDP measurements are performed for each reflection angle in increments of $\Delta\theta = 10°$, with the LoS path becoming more dominant as the transmitter moves toward $\theta = 0°$. For the WR05 band, the VNA and CS were tested between 185 GHz and 190 GHz, while the WR03 band was examined from 300 GHz to 305 GHz. Laser guides were used to position the antennas relative to the reflector and maintain the rotation axis to ensure accurate alignment. The reflector reflectors were placed on a microwave absorber foam stage, which rotated in sync with the movements of the transmitter. The foam was used to elevate the spheres above the table absorber while keeping the antennas aligned with the center point of the spheres. The thin foam stick was tested before placing the reflectors, and it showed a weak reflectivity near the noise floor of the measuring devices. The foam support extended 15 mm above the absorber table. The wire reflector, on the other

https://doi.org/10.7795/110.20260421

hand, was placed vertically on the table absorber with a visible length of 80 mm. Figure 4.13 illustrates the experimental setup.

Reference measurements used for calibration purposes were recorded over LoS measurements were taken at 0.85 m for WR05 and 1 m for WR03 CSs. The reflectors were tested over different rotational angles ranging from $-110°$ to $20°$ for WR05 and $0°$ to $115°$ for WR03 [39].

To achieve finer resolution, VNA measurements were conducted over a 20 GHz bandwidth, spanning 180 GHz to 200 GHz for WR05 and 290 GHz to 310 GHz for WR03 [39].

The reflectors were tested at different rotational angles, including a wire of 1.5 mm diameter, 10 mm, and 6 mm spheres.

Figures 4.14, Figures 4.15 and 4.16 show the resulting channel impulse responses for the respective sphere sizes using four different measurement equipment. This configuration enabled a systematic study of different reflectors and their effect on signal propagation. The reflections at different angles show a dominant LoS path as the transmitter nears $\theta = 0°$ [39].

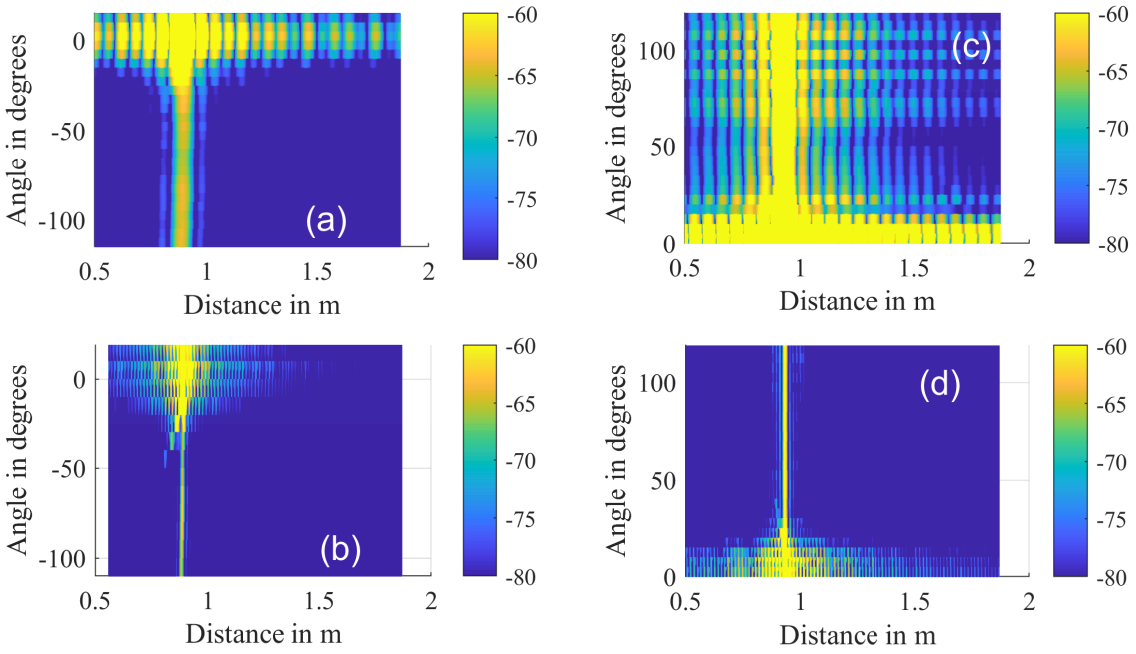

Figure 4.14: Channel impulse response of a 1.5 mm diameter metallic wire with 8 cm long reflector placed at the center of rotation of the rotational stage. (a) WR05 CS. (b) WR05 VNA. (c) WR03 CS. (d) WR03 VNA. (Adopted from [39]).

https://doi.org/10.7795/110.20260421

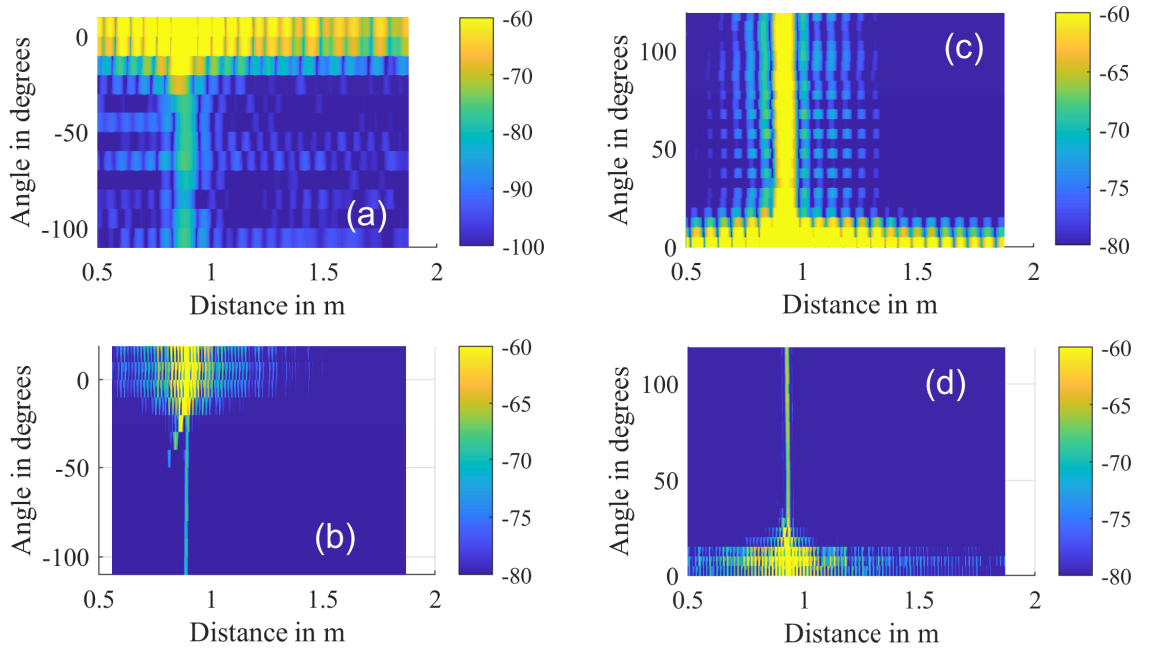

Figure 4.15: Channel impulse response of a 10 mm diameter metallic sphere reflector placed at the center of rotation of the rotational stage. (a) WR05 CS. (b) WR05 VNA. (c) WR03 CS. (d) WR03 VNA. (Adopted from [39]).

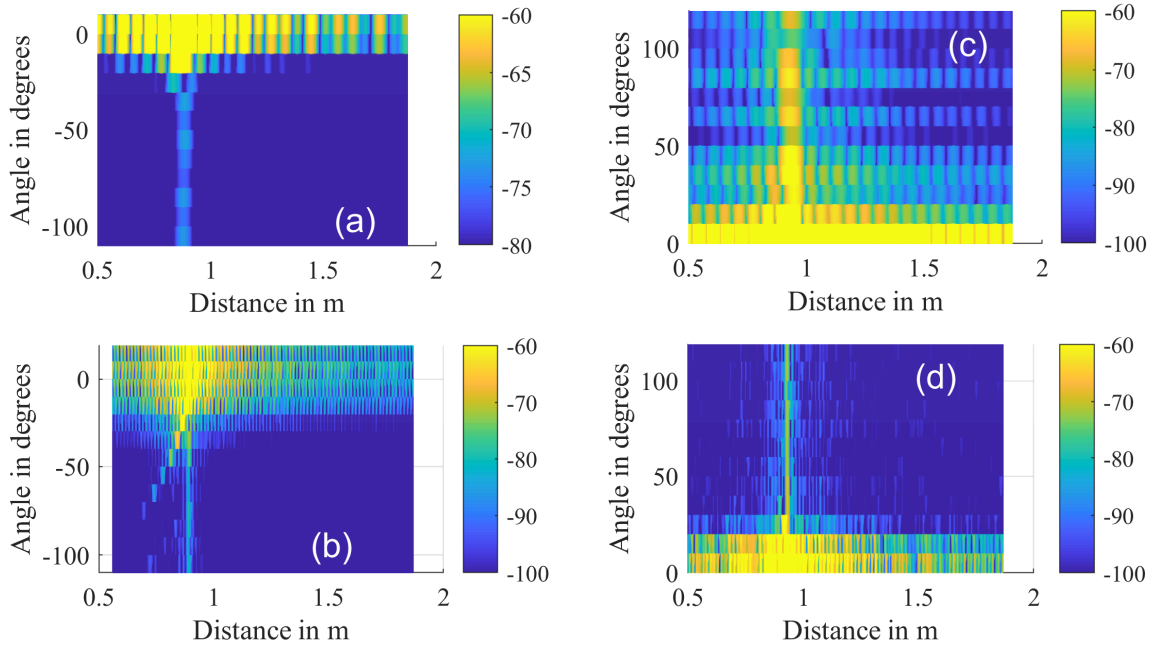

Figure 4.16: Channel impulse response of a 6 mm diameter metallic sphere reflector placed at the center of rotation of the rotational stage. (a) WR05 CS. (b) WR05 VNA. (c) WR03 CS. (d) WR03 VNA. (Adopted from [39]).

Figure 4.17 presents the PDP for reflectors tested at rotational angles between $-110°$ and $-70°$ for WR05 and $110°$ to $70°$ for WR03. The CSs were set to a 5 GHz bandwidth, with center frequencies of 187.5 GHz for WR05 and 302.5 GHz for WR03. An interpolation factor

https://doi.org/10.7795/110.20260421

of 40 and a Hann window were applied to improve resolution. The shadowed regions indicate the uncertainty in PDP measurements at different rotational angles. Ideally, similar delay and path gain values would be observed across measurements, but variations arise due to noise affecting weaker reflections. The wire produced the strongest reflection among the reflectors, with a mean path gain of -70.5 dB for WR05 and -62.8 dB for WR03. The noise impact differed across reflectors, with WR05 CS exhibiting greater path gain uncertainties. Path gain decreases as the reflector's cross-section reduced, with the 10 mm sphere less reflective than the wire. Additionally, smaller spheres exhibited lower reflection magnitudes [39].

Fig. 4.17 shows the PDP delay difference between the two frequency bands under test, which is originated from using different antennas with varying combined PC on the transmitting and receiving ports.

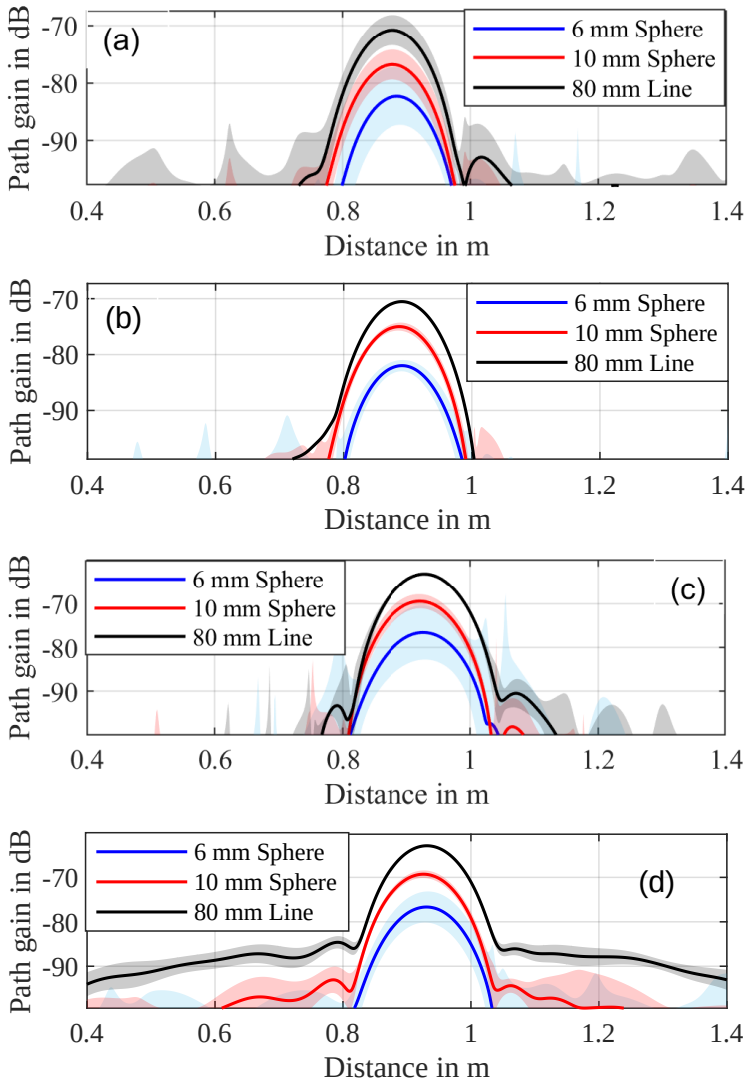

Figure 4.17: 5 GHz measurement bandwidth PDP of the different reflectors at rotational angles of $-110°$ to $-70°$ for the WR05 band and $110°$ to $70°$ for the WR03 band placed at the center of the rotational stage. (a) WR05 CS. (b) WR05 VNA. (c) WR03 CS. (d) WR03 VNA. (Adopted from [39]).

https://doi.org/10.7795/110.20260421

4.3.3 Multiple Reflectors Analysis

For the multiple reflector setup, two reflectors were positioned on the rotating stage with a known separation across the center of rotation. This setup allows us to examine multiple reflection characteristics and their effect on signal propagation [39].

Controlled PDP delays can be observed using two reflectors as they vary with rotational angles. The schematic of the measurement setup and a photograph of the measurement scenario are shown in Fig. 4.18(a) and 4.18(b), respectively [39].

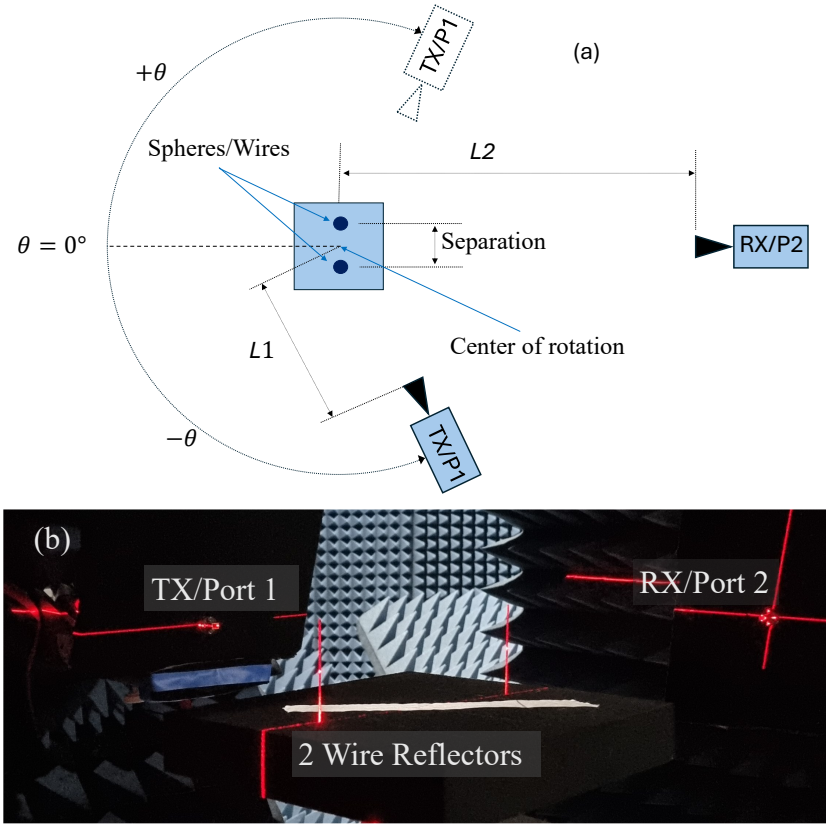

Figure 4.18: Far-field multi-reflector measurement setup. (a) Schematic representation of the measurement setup. (b) Measurement setup showing the frequency converters placed on motorized mounts, where Port 1 rotates in 10° steps around the center of rotation. (Adopted from [39]).

The antenna radiation pattern is critical in aligning path gain measurements across different DUTs. Therefore, a direct comparison of path gain between the WR05 CS and WR05 VNA, or with WR03 horn antennas, is inappropriate. Instead, measurement consistency is ensured by focusing on delay characterization.

Two 80 mm long wires with a fixed separation were mounted vertically on the rotational stage table. The transmitting and receiving antennas were placed at distances L_1 and L_2 from the center of rotation. This measurement serves as a range resolution assessment, where the circular motion of the reflectors introduces shifted reflector positions ranging from approximately 0.05 mm to 1.7 mm per measurement, depending on the rotational angle. Additionally, the resolution of combined paths is evaluated, aiding in selecting the optimal windowing function, interpolation factors, and bandwidth to enhance measurement accuracy.

https://doi.org/10.7795/110.20260421

Multipath artifact measurements for WR05 CS and VNA are illustrated in Figure 4.19. Figure 4.19(a) presents results for the wires separated by 20 cm around the center of rotation, with the rotational stage moving between $-110°$ and $110°$. The antennas were positioned at $L_1 = 0.35$ m and $L_2 = 0.5$ m from the center of rotation. The LoS component is evident at $\theta = 0°$.

Figure 4.19(b) shows the same measurement of a 20 GHz bandwidth using the WR05 VNA, showing the measurement with a PDP higher peak resolution.

Figures 4.20(a) and 4.20(b) display the WR03 CS and VNA under similar conditions, but with a fixed position of the transmitting and receiving antenna, The transmitter antenna was fixed at $-110°$, with the LoS blocked between the antennas. In this case, only the stage was rotated between $0°$ and $350°$. The measurements were at $L_1 = 0.42$ m and $L_2 = 1$ from the rotational center for both the transmitter and receiver apertures, respectively.

A second experiment used wires separated by 30 cm and tested with all measuring devices at different angles. The measurement distance was adjusted to $L_1 = 0.42$ m and $L_2 = 1$ m to ensure the antennas' radiation patterns fully covered the reflectors. Here, the transmitter was fixed at $-110°$, while the stage was rotated between $0°$ and $180°$. Figure 4.21(a) shows the WR05 CS response with Hann windowing applied, while Figure 4.21(b) presents the corresponding 20 GHz VNA response.

The WR03 frequency band was also examined. Figure 4.21(c) illustrates the CS response for a 30 cm wire separation with Hann window applied, while Figure 4.21(d) shows the VNA measurement under similar conditions with 20 GHz bandwidth. Figures 4.21(c) and 4.21(d).

The Hann window was applied to separate the signal from noise, and a 20 GHz bandwidth was used for VNA measurements to achieve higher resolution.

In conclusion, the multi-reflector measurements demonstrate the capability of both the CS and VNA systems to resolve closely spaced multipath components with high temporal resolution. By varying the reflector positions and using controlled delays, these measurements provide valuable information about the time-domain resolution accuracy and limits of each system. The results can be used to evaluate the effectiveness of different processing techniques, such as windowing and interpolation, and support the validation of CS systems in complex propagation environments involving dense multipath or closely spaced reflectors.

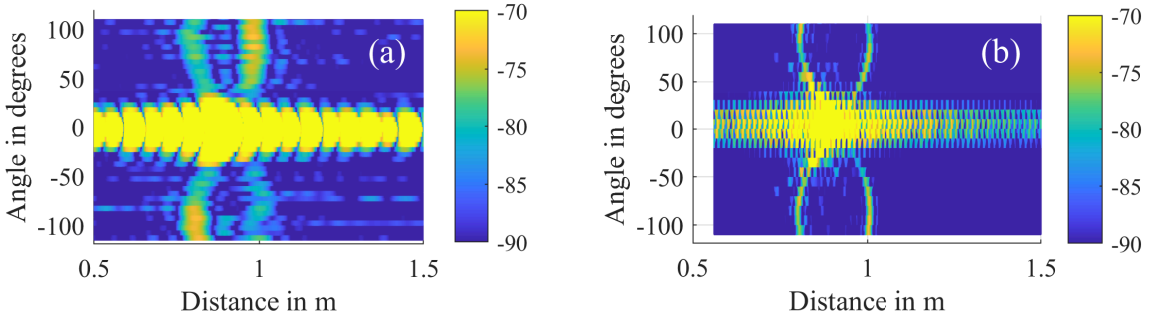

Figure 4.19: CIR of a two-wire artifact with 200 mm separation: (a) WR05 CS at 5 GHz bandwidth and (b) WR05 VNA at 20 GHz bandwidth. (Adopted from [39]).

https://doi.org/10.7795/110.20260421

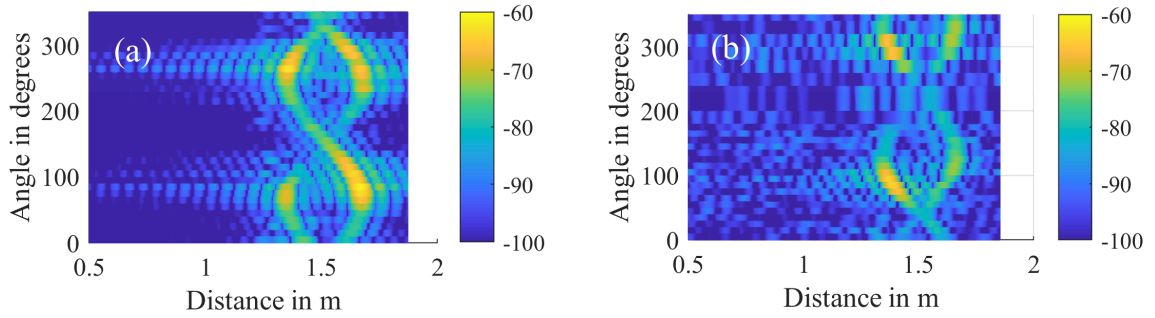

Figure 4.20: CIR of a two-wire artifact with 200 mm separation: (a) WR03 CS at 5 GHz bandwidth and (b) WR03 VNA at 5 GHz bandwidth. (Adopted from [39]).

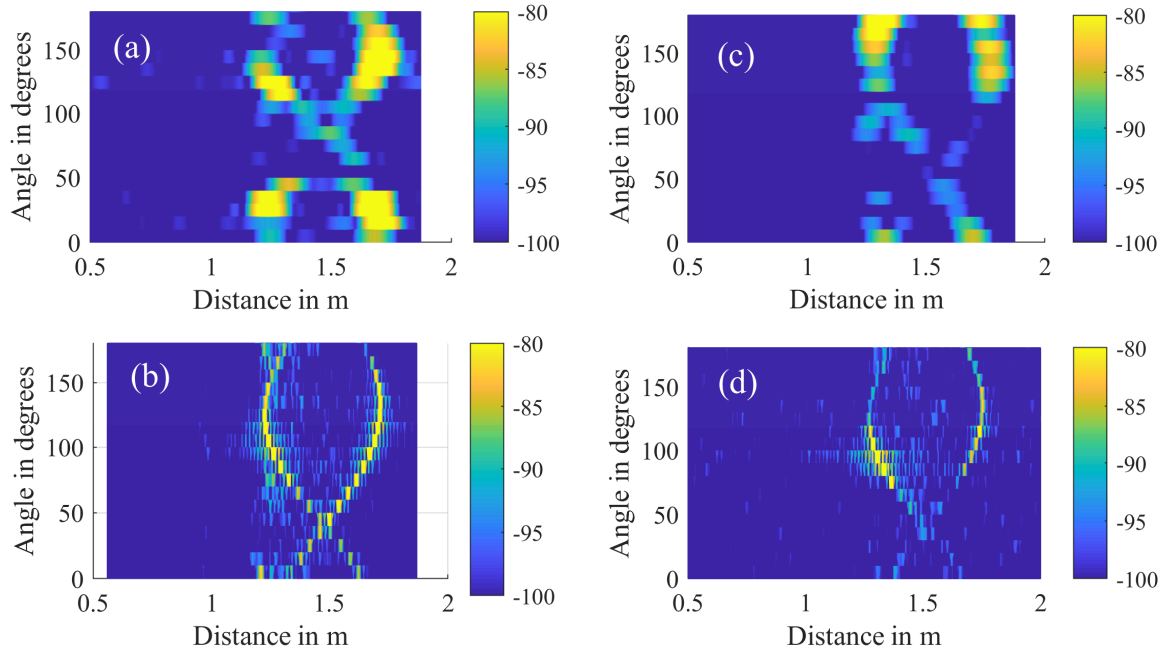

Figure 4.21: CIR of a two-wire artifact with 300 mm separation: (a) WR05 CS at 5 GHz bandwidth with Hann window applied. (b) WR05 VNA at 20 GHz bandwidth. (c) WR03 CS at 5 GHz bandwidth with Hann window applied. (d) WR03 VNA at 20 GHz bandwidth. (Adopted from [39]).

https://doi.org/10.7795/110.20260421

5

Characterizing OTA Time-Varying Measurements Using a VNA

This chapter extends the investigation at sub-THz frequencies by applying movements into the measurement setup. As in realistic communications channels, a time-varying signal is a common case even for short or medium range applications. This charactrization is using a VNA with its frequency extenders operating at the WR03 frequency range .

Segmented waveforms are applied for this investigation, which consist of a sequence of discrete frequency steps, offering a balanced approach to achieving both temporal resolution and frequency coverage. These waveforms are mainly useful in scenarios requiring concurrent velocity and position information. By characterizing frequency steps and segment durations, segmented waveforms can capture detailed motion information while maintaining high accuracy across the frequency spectrum.

A compact-scale measurement scenario was designed to investigate time-varying signal propagation using a VNA. This proof-of-concept testbed provides a valuable tool for characterizing channel sounder equipment operating at sub-THz frequencies. Comparable measurements enhance understanding of system responses to movement within the measurement environment.

VNAs are primarily designed to measure time-invariant networks by capturing the complex voltage response at discrete frequency points within a sample window defined by the IFBW. The interval between frequency steps, influenced by parameters such as the selected IFBW and sweep type in combination with the total frequency points, determines the overall measurement duration. This conventional approach presents challenges when measuring time-varying transmissions, as waveform changes must be considered throughout the measurement period. To address this, methods to adapt signal acquisition for time-varying signals are investigated, evaluating the feasibility and limitations of using VNAs for this purpose.

The measurement scenario presented in this chapter improves the understanding of time-varying measurements and enables their application to more dynamic CS systems, allowing for estimating associated measurement uncertainties. The measurement setup, mathematical analysis to simulate the scenario, and time intervals obtained for each measured segment at varying velocities are considered, optimizing position with frequency step selection.

The segmented sweep architecture builds on the VNA system architecture, that was presented in Section 2.1.1. This dynamic measurement scenario extends the OTA scenarios ex-

https://doi.org/10.7795/110.20260421

amined in Chapter 3 and Chapter 4 under static conditions.

5.1 Fundamentals of Time-Varying Transmissions

Time invariance in a system implies that its response remains constant over time. For example, if an input signal is delayed, the system output will simply be a delayed version of the original, taking into consideration the changes happening due to the drift and noise influence on the received signal. This concept is straightforward when applied to static systems. However, in time-varying systems, the response characteristics change over time, introducing variability in the output. This variability can significantly impact signal measurement and analysis, especially in dynamic environments where conditions are continuously changing.

A straightforward and physically meaningful way to characterize time-varying channels is through delays and Doppler shifts. Delays arise from multipath propagation and time dispersion, while Doppler shifts occur due to mobility, carrier frequency offsets, and oscillator drift, as these shifts resembles Doppler effects, especially in time-varying channel analysis [98]. In practical wireless communication systems, mobility is inherent, leading to time-variant signals influenced by the motion of transmitters, receivers, or reflecting objects. This rapid channel variation poses challenges for accurate signal measurement and analysis, particularly in dynamic environments where conditions continuously fluctuate [99, 100].

As millimeter-wave communication systems and future mobile networks explore higher frequencies, addressing these challenges becomes critical. Dynamic scenarios introduce additional complexities as moving objects further impact signal behavior through Doppler effects and variations in path length. Properly managing these influences is essential to ensure precise data collection and reliable measurements. Accurately accounting for these dynamic factors allows for a better understanding of signal behavior, which is crucial for efficient operation at high frequencies and under rapidly changing conditions [101, 102].

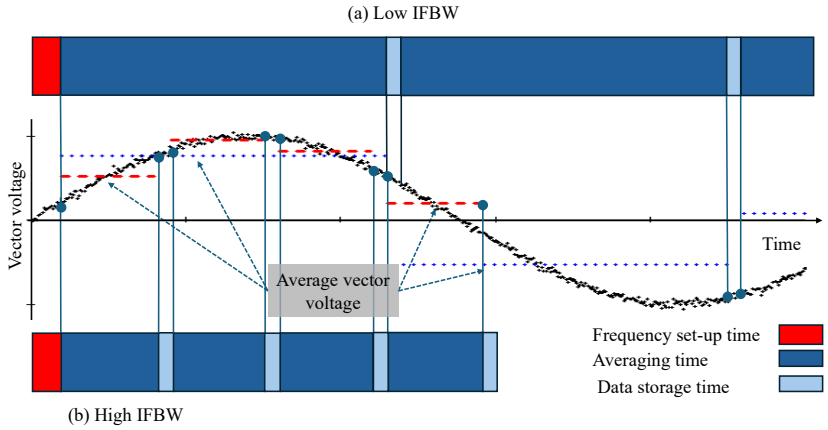

Figure 5.1: Reflection from a moving object will cause a rotation of the vector voltage phase. This phase rotation can be captured using a higher VNA IFBW.

The VNA sequentially measures frequency points, and the receiver averages the vector voltage over a period defined by the IFBW. However, CS involving moving targets results

https://doi.org/10.7795/110.20260421

in Doppler-shifted signals, causing the vector-voltage phase to fluctuate within the averaging period. Higher IFBW measurements enable tracking faster phase changes, corresponding to higher velocities. Additionally, the VNA hardware requires time to store measurements and adjust synthesizer frequencies. This limits the highest practical IFBW since storage and acquisition times become comparable, as illustrated in Fig. 5.1.

5.2 Traceability Challenges in Time-Varying Transmissions

Achieving traceability in time-varying measurements is challenging, especially at sub-THz frequencies. It ensures that measurements remain reliable and comparable by linking results to national or international standards through certified calibrations. Measurement uncertainty is a key factor, providing a statistical confidence level in the obtained values. Recent advancements have extended VNA traceability up to 1.1 THz, using precise waveguide measurements and electromagnetic simulations to reduce uncertainties [63].

VNAs are essential for characterizing reflection and transmission properties across RF, microwave, millimeter-wave, and THz bands. However, high-frequency measurements introduce challenges, particularly above 100 GHz, where small waveguide dimensions increase alignment uncertainties. To address this, calibration procedures developed by NMIs account for errors such as directivity, reflection tracking, source match, noise, drift, and non-linearity. Proper calibration ensures accurate measurements under different conditions. These calibration procedures were addressed in Chapter 2 and in Chapter 3.

Operating at millimeter-wave and sub-THz frequencies also introduces strong wave attenuation, complicating OTA measurements. Reference devices such as flush short circuits, short waveguide sections, and cross-connected waveguides help maintain calibration accuracy despite these difficulties.

Repeatability in time-varying measurements adds further complexity. Small variations in velocity, position, and setup parameters can affect magnitude and phase measurements. Controlled test scenarios are necessary to ensure consistent results.

Traceability in time-varying measurements is also important for channel-sounding systems in wireless communications. Sounders operating at sub-THz frequencies rely on accurate measurements to evaluate system performance in dynamic conditions. Establishing traceability aligns results across different systems, ensuring reliable performance in networks with moving transmitters, receivers, or reflectors. This supports the development of next-generation communication standards.

In this chapter, time-varying signals are analyzed by examining reflections from a moving reflector at different velocities. Since the VNA measures frequencies sequentially, reflections from moving objects differ from those in conventional channel sounders. A segmented waveform combining CW and LS signals estimates object velocity and position. Measurements were taken from 220 GHz to 325 GHz WR03 at two IFBWs, demonstrating the ability of VNAs to capture time-varying signals at sub-THz frequencies.

Figure 5.2 outlines the measurement model used for time-varying analysis. A segmented

https://doi.org/10.7795/110.20260421

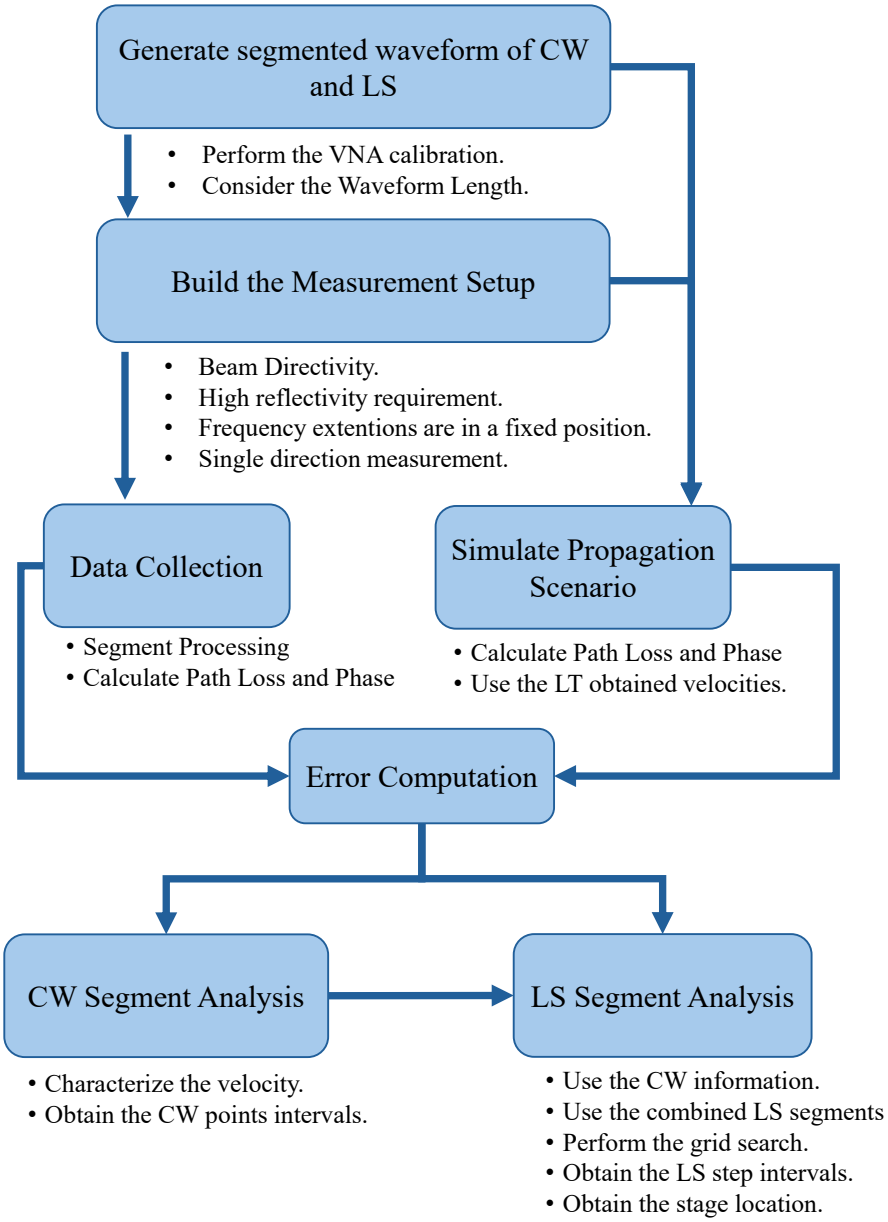

Figure 5.2: Measurement model applied to investigate the time-varying signal propagation using a VNA.

waveform combining CW and LS segments is generated and calibrated. The setup is adjusted for reflectivity, beam directivity, and stable frequency extenders. Data collection captures path loss and phase. A simulated propagation scenario mirrors real conditions, and error computation identifies deviations between measured and simulated data. Finally, separate analyses of CW and LS signals provide insights into propagation effects.

5.3 Measurement Setup and Scenario Simulation

After performing the TRL calibration to our segmented waveform, the collected measurements of S_{21} are analyzed and compared with simulated results to evaluate the accuracy and reliability of the experimental setup [103].

https://doi.org/10.7795/110.20260421

5.3.1 Selected Waveforms

The choice of waveforms is crucial for analyzing time-varying signals. Different waveform types, of CW and LS, are used depending on the measurement requirements.

CW signals are essential for velocity estimation, as their constant frequency allows continuous tracking of movement. This makes them effective in Doppler-based applications and radar systems [104], while their high temporal resolution enables accurate detection of velocity changes.

LS signals, on the other hand, are designed for precise position estimation. When the frequency sweeps over time, the LS segments can provide accurate distance measurements, estimating the possible velocity of the moving object as well based on the position acquired for each frequency set. This makes LS waveforms valuable in range-finding and imaging applications. LS waveforms can also capture reflections from multiple objects, allowing for a more detailed analysis of the environment. However, prior knowledge of the object's velocity is often necessary for proper interpretation of the measurements.

In this investigation, a segmented VNA sweep combining both CW and LS segments are presented, a different combination of waveforms is presented in [103]. In Table 5.1, the waveform configuration used in our measurements is showing the selected frequency steps and total points per segment optimize tuning flexibility across different frequency ranges. The segmentation of CW and LS waveforms is illustrated in Fig. 5.3, showing how they were structured to improve motion tracking and maintain measurement accuracy.

This waveform was tested with IFBWs of 1 kHz and 10 kHz. The frequency range spanned between 270 GHz and 325 GHz with 333 points. These configurations support flexible tuning across wide and narrow frequency ranges, optimizing both precision and coverage in high-frequency measurements.

Start (GHz)	Stop (GHz)	Step (MHz)	Points
270	275	50	101
277	277	-	100
280	290	100	101
295	325	1000	31
		Total Points	**333**

Table 5.1: Segmented waveform configuration with selected frequency steps and points.

5.3.2 Measurement Setup

The measurement setup was designed to accurately capture time-varying signals using a VNA and associated equipment. A Rohde & Schwarz ZVA50™ VNA with VDI-WR3.4 VNAX™ frequency extension modules was used, covering the 220 GHz to 325 GHz range. Standard gain horn antennas with 20 dBi gain were employed to ensure consistent radiation patterns. The antennas were aligned toward a flat metallic reflector mounted on a Newport™ motorized linear stage, which moved at velocities ranging from 10 mm/s to 200 mm/s. This setup allowed

https://doi.org/10.7795/110.20260421

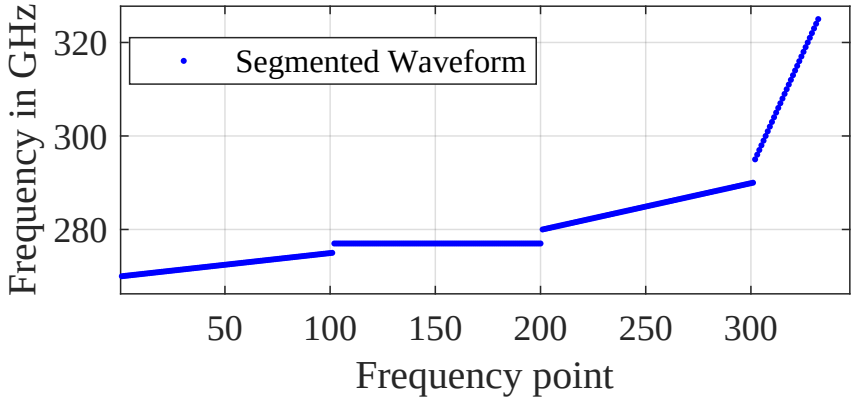

Figure 5.3: CW and LS segments of the measured waveform.

for the investigation of how time-varying signals influence the stability of S-parameters at different velocities. Considering the antenna PC at various frequency points improved phase measurement accuracy, which is essential for system characterization. The fixed initial and final reflector positions served as reference points for these measurements [26, 27, 105]. Further details related to antenna PC characterization with antenna calibration procedures is presented in Section 3.2.

The calibration was performed using the TRL method to correct systematic errors and ensure accurate representation of the DUT. Calibration accuracy is particularly critical at high frequencies, where small errors can lead to significant deviations. Regular verification was necessary, especially near the upper frequency limits of the equipment, where non-linearities and imperfections become more pronounced. To maintain consistency, all measurements were conducted in a temperature-controlled lab at PTB, minimizing the impact of environmental factors such as temperature and humidity variations.

Continuous measurement sweeps were recorded using the METAS VNA Tools software [106] while the reflector moved along a 300 mm travel range. The motion was directed toward the antennas, with the initial and final positions set at 680 mm and 380 mm from the antennas reference plane, respectively. Sweeps were captured before and after the reflector's movement to analyze the dynamic impact on the signal. A schematic of the setup is presented in Fig. 5.4(a), while a photograph of the actual measurement setup is shown in Fig. 5.4(b).

https://doi.org/10.7795/110.20260421

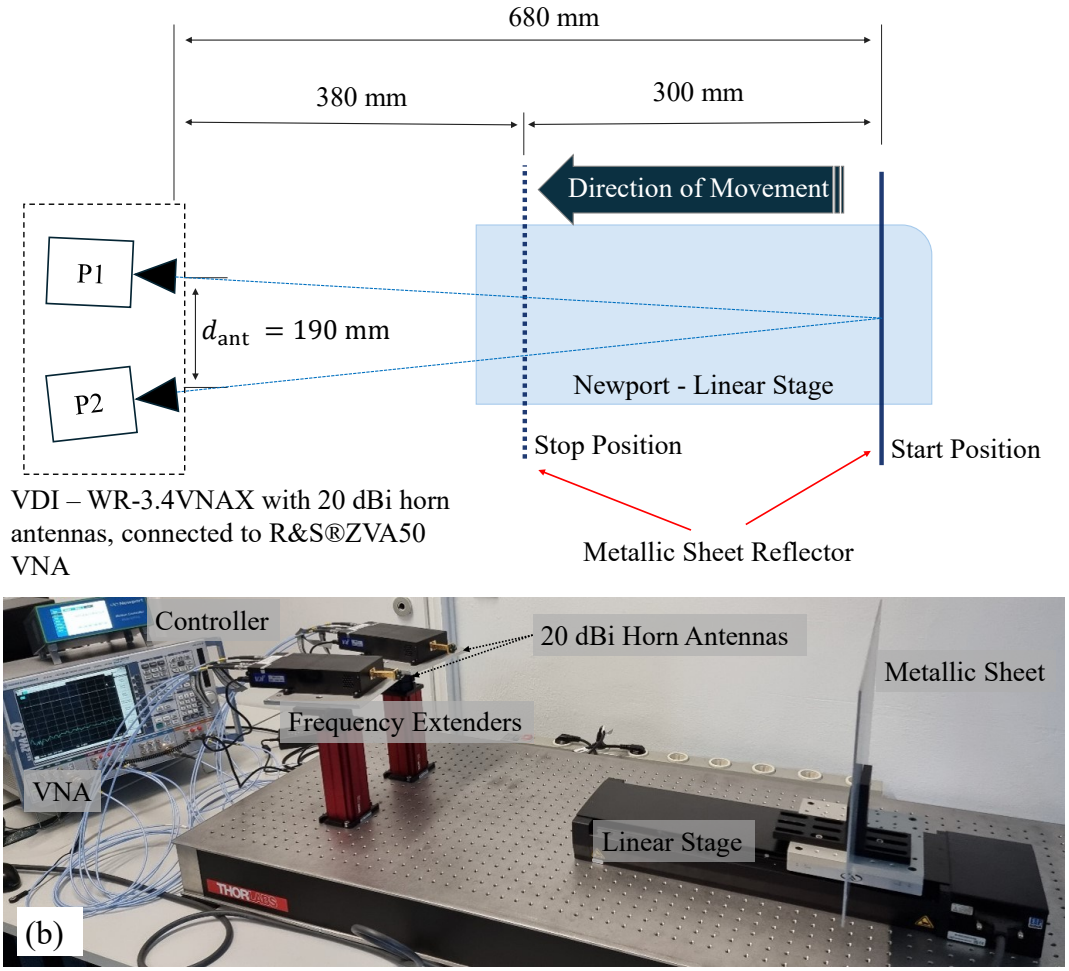

Figure 5.4: Investigating the time-varying measurement scenario using a VNA (a) Illustration of the measurement setup. (b) Photograph of the measurement scenario.

5.3.3 Simulated Waveform

To adapt VNA measurements for moving objects, the object's position must be tracked over time. This requires calculating the duration of each frequency step and its effect on measurement accuracy. Adjusting the path length for each measurement point ensures precise frequency response data even in dynamic scenarios.

For CW segments, the CW step duration δt_{CW} is varied from 0.1 ms to 15 ms in 0.1 ms increments. The capturing time for each frequency point is given by:

$$t_{\mathrm{Capture,CW}} = [0, \delta t_{\mathrm{CW}}, 2\delta t_{\mathrm{CW}}, \ldots, (p-1)\delta t_{\mathrm{CW}}], \tag{5.1}$$

where p is the number of CW points at a given frequency. The initial capturing distance d_0, measured from the horn antennas' plane to the metallic reflector, is optimized within 380 mm to 680 mm at 0.1 mm steps. The capturing distances are computed as:

$$d_{\mathrm{capture}} = d_0 - v \cdot t_{\mathrm{Capture,CW}}, \tag{5.2}$$

https://doi.org/10.7795/110.20260421

where v is the velocity of the object, fixed using linear stage readings between 0 mm/s and 200 mm/s. The path length for each measurement is adjusted using:

$$Path = 2 \cdot \sqrt{\left(\frac{d_{\text{ant}}}{2}\right)^2 + d_{\text{capture}}^2}, \tag{5.3}$$

where d_{ant} is the fixed 190 mm direct distance between the horn antennas. The phase and unwrapped phase are theoretically determined based on path length and frequency:

$$\phi = -2\pi \frac{Path \cdot f}{c} + \phi_0, \tag{5.4}$$

where ϕ and ϕ_0 are the simulated phase and initial phase point, respectively, with c being the speed of light and f the frequency. The unwrapped phase in degrees is computed as:

$$\phi_{\text{Uphase}} = \text{unwrap}(\phi) \cdot \frac{180^\circ}{\pi}. \tag{5.5}$$

To examine phase shifts over time, the phase difference between the CW start i and end j points is given by:

$$\delta\phi_{\text{Uphase,CW}} = \phi_{\text{Uphase}}(i) - \phi_{\text{Uphase}}(j). \tag{5.6}$$

The agreement between measured and theoretical phase shifts in CW measurements is evaluated as:

$$\phi_{\text{CW}} = \delta\phi_{\text{Uphase,CW,meas}} - \delta\phi_{\text{Uphase,CW,theor}}. \tag{5.7}$$

For LS optimization, the goal is to minimize the error between measured and theoretical unwrapped phases. This involves computing the unwrapped phase while optimizing the initial capture distance d_0 and LS frequency step duration δt_{LS}.

The unwrapped phase is computed across the LS segment, with δt_{LS} varying from 0.1 ms to 15 ms at 0.1 ms increments. The initial capture distance d_0 is adjusted from 380 mm to 680 mm in 0.1 mm steps. The velocity v is typically fixed (0 mm/s to 200 mm/s), though it is also tested in 1 mm/s steps for its impact.

Total capture time is divided into segments of LS and CW steps. These segments are represented as $t_{\text{Capture},x}$, where x denotes the segment number.

The first segment is an LS segment, with capture times given by:

$$t_{\text{Capture,1}} = [0, \delta t_{\text{LS}}, 2\delta t_{\text{LS}}, \ldots, (p_1 - 1)\delta t_{\text{LS}}], \tag{5.8}$$

where p_1 is the number of points in the segment. The second segment is a CW, with capture times computed as:

$$t_{\text{Capture,2}} = t_{\text{Capture,1}}^{\text{end}} + [\delta t_{\text{CW}}, 2\delta t_{\text{CW}}, \ldots, p_2\delta t_{\text{CW}}]. \tag{5.9}$$

Here, $t_{\text{Capture,1}}^{\text{end}}$ is the last time point of the first segment, and p_2 is the number of points in

https://doi.org/10.7795/110.20260421

the second segment.

This process continues for the third and fourth segments, both LS segments:

$$t_{\text{Capture},3} = t^{\text{end}}_{\text{Capture},2} + [\delta t_{\text{LS}}, 2\delta t_{\text{LS}}, \ldots, p_3 \delta t_{\text{LS}}], \tag{5.10}$$

$$t_{\text{Capture},4} = t^{\text{end}}_{\text{Capture},3} + [\delta t_{\text{LS}}, 2\delta t_{\text{LS}}, \ldots, p_4 \delta t_{\text{LS}}]. \tag{5.11}$$

The final capture time array includes all four segments:

$$t_{\text{Capture}} = [t_{\text{Capture},1}, t_{\text{Capture},2}, t_{\text{Capture},3}, t_{\text{Capture},4}]. \tag{5.12}$$

To optimize the LS segment, a grid search is conducted across d_0, δt_{LS}, and v, while keeping δt_{CW} fixed based on prior CW segment optimization.

The optimization minimizes the error between measured and theoretical unwrapped phases:

$$\text{err} = \sum_f \left(\phi_{\text{Uphase,LS,meas}}(f) - \phi_{\text{Uphase,LS,theor}}(f)\right)^2, \tag{5.13}$$

where $\phi_{\text{Uphase,LS,meas}}(f)$ is the measured unwrapped phase and $\phi_{\text{Uphase,LS,theor}}(f)$ is the theoretical unwrapped phase at frequency point f.

The grid search identifies the optimal values of d_0, δt_{LS}, and potentially v, yielding the best agreement between measured and theoretical unwrapped phases.

5.4 Measurement Results and Discussion

5.4.1 Linear Stage Velocity

To confirm the velocity of the linear stage, a laser tracker (LT) continuously recorded its position over time, providing sequential measurements. The recorded positions at time instances $(t_1,\ t_2,\ \ldots,\ \ t_i)$ are expressed as:

$$(x_1,\ y_1, z_1)\,,\ \ (x_2,\ y_2, z_2)\,,\ \ldots,\ (x_i,\ y_i, z_i)\,.$$

The velocity v at any time interval i is determined by calculating the positional change over the corresponding time interval. The instantaneous velocity is computed using the Euclidean distance between consecutive position points in three-dimensional space:

$$v_i = \frac{\sqrt{(x_{i+1} - x_i)^2 + (y_{i+1} - y_i)^2 + (z_{i+1} - z_i)^2}}{t_{i+1} - t_i}. \tag{5.14}$$

Velocity calculations were performed across multiple intervals and compared to the target values to verify the stage's expected motion. Six different velocities, ranging from 10 mm/s to 200 mm/s, were tested. The results showed high stability, with mean velocities closely matching the nominal values provided by the stage. Deviations from the target velocities were minimal, ranging between 0.0009 mm/s and 0.01388 mm/s.

https://doi.org/10.7795/110.20260421

Figure 5.5 presents the recorded velocities within the tested range of 10 mm/s to 200 mm/s, measured using the LT device. The uncertainties, computed with a 95 % confidence interval, remained low across all speeds. A slight increase in uncertainty was observed at higher velocities, starting at ±0.00220 mm/s for 10 mm/s and reaching ±0.01771 mm/s at 200 mm/s. This increase results from fewer measurements recorded at higher speeds within the fixed time interval of 0.1 seconds. However, the uncertainty remains within an acceptable range, which confirms the reliability of the system for velocity verification. Taking into consideration that the laser tracker is providing the exact position at each time interval.

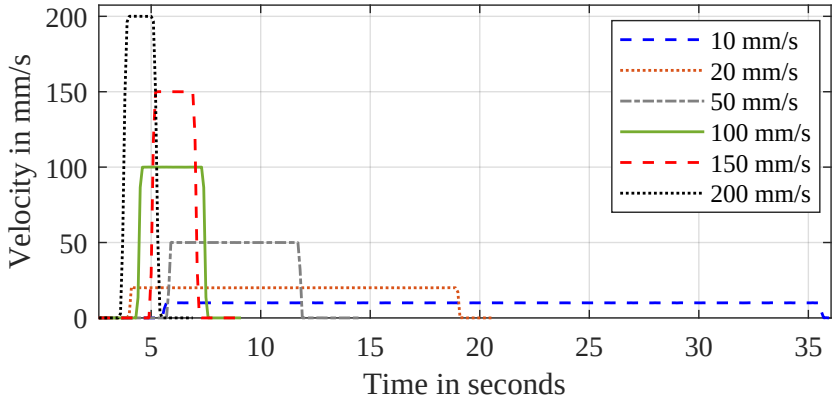

Figure 5.5: Recorded velocities from 10 mm/s to 200 mm/s using the laser tracker (LT) device with 95% confidence intervals.

5.4.2 Continuous Wave Signal Analysis

After confirming the stage velocity using the LT, the VNA optimization process begins by analyzing the CW segment of 100 frequency points at 277 GHz.

Measurements were conducted at various velocities, and φ_{CW} was calculated based on the optimized δt_{CW} and d_0. The CW segment provides direct velocity information about the reflector. Considering the 190 mm separation between the horn antennas, a nonlinear path change occurs along the track length. This path change can be compensated by optimizing d_0, ensuring better alignment with the reflector's actual movement.

Fig. 5.6 and Fig. 5.7 present the mean $\delta\varphi_{\mathrm{Uphase\_CW,meas}}$ of three repeated measurements with a 95 % confidence interval, compared to the simulated $\delta\varphi_{\mathrm{Uphase\_CW,Theor}}$ at CW frequency time intervals of 2.07 ms and 0.42 ms for 1 kHz and 10 kHz IFBW, respectively. The figures illustrate results for velocities of 10 mm/s, 20 mm/s, 50 mm/s, and 100 mm/s for both IFBWs under test. The difference between the measured and simulated values is represented by φ_{CW}.

Fig. 5.8(a) displays results for segmented CW at velocities ranging from 10 mm/s to 100 mm/s, repeated three times for each velocity. φ_{CW} was optimized at different δt_{CW} values, ranging from 1.5 ms to 2.5 ms in 0.01 ms intervals for an IFBW of 1 kHz.

The φ_{CW} optimization was repeated for the 10 kHz IFBW measurement, as shown in Fig. 5.8(b), at velocities of 10 mm/s, 20 mm/s, 50 mm/s, 100 mm/s, 150 mm/s, and 200 mm/s, with three repetitions for each measured velocity. The δt_{CW} optimization was performed for

https://doi.org/10.7795/110.20260421

values ranging from 0.2 ms to 0.6 ms in 0.01 ms intervals. The best fit for φ_{CW} across all measured velocities in the 1 kHz IFBW tests indicates a mean optimized δt_{CW} of (2.073 ± 0.002) ms with 95 % confidence. For the 10 kHz IFBW measurement, the faster sweep rates enabled investigating higher velocities up to 200 mm/s. The best fit for φ_{CW} across all measured velocities indicates a mean optimized δt_{CW} of (0.402 ± 0.002) ms with 95 % confidence.

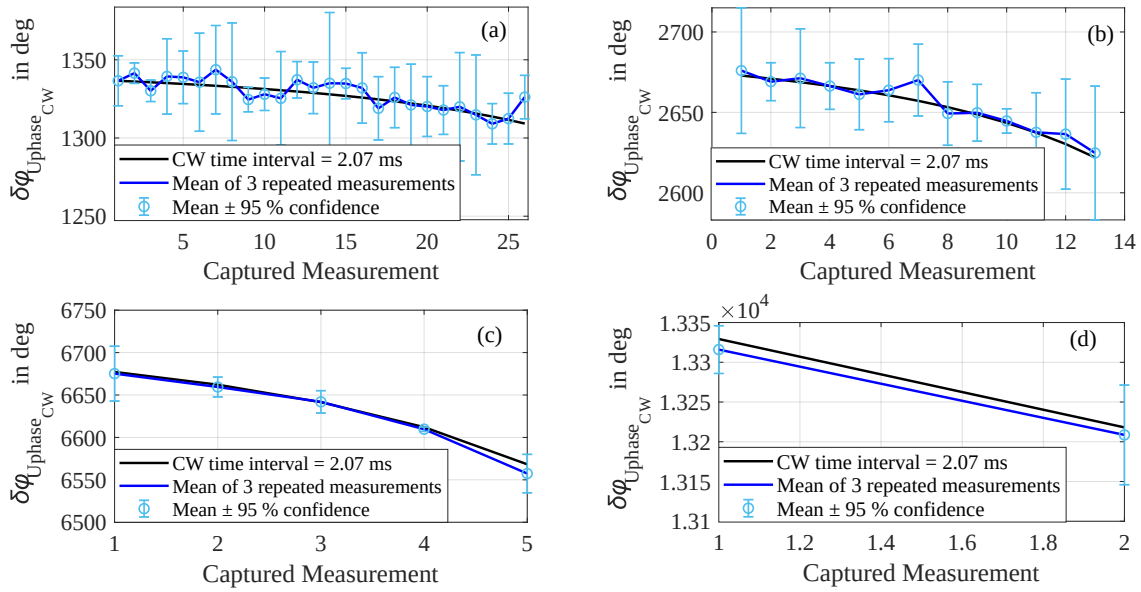

Figure 5.6: Mean phase deviation $\delta\varphi_{\mathbf{Uphase_{CW},meas}}$ of three repeated measurements with 95 % confidence, compared to the simulated phase deviation $\delta\varphi_{\mathbf{Uphase_{CW},Theor}}$ at different velocities and IFBW of 1 kHz (a) 10 mm/s (b) 20 mm/s (c) 50 mm/s (d) 100 mm/s.

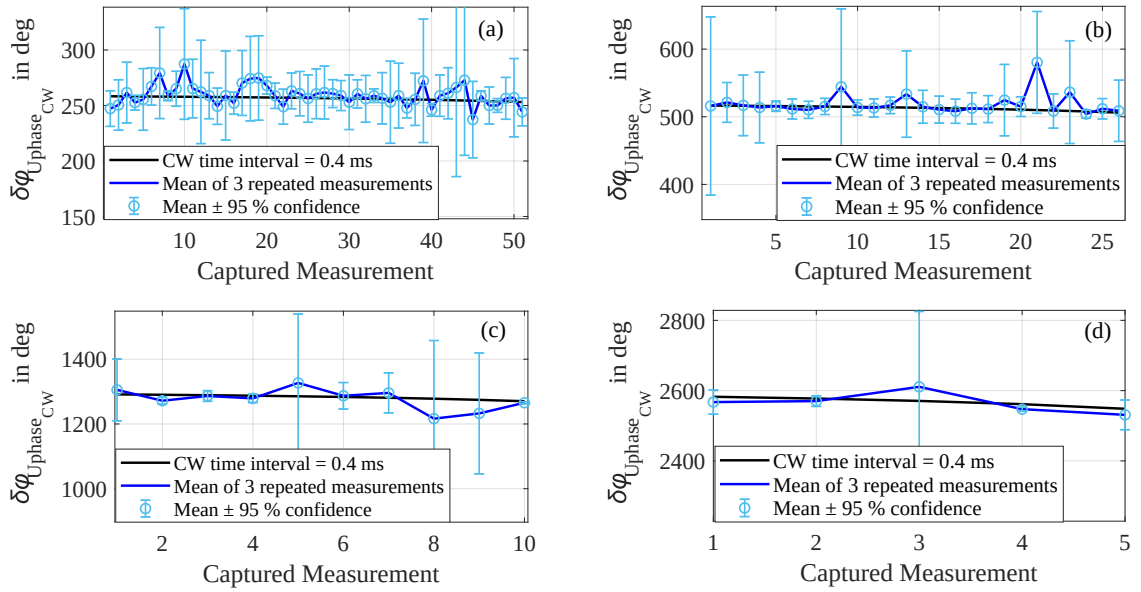

Figure 5.7: Mean phase deviation $\delta\varphi_{\mathbf{Uphase_{CW},meas}}$ of three repeated measurements with 95 % confidence, compared to the simulated phase deviation $\delta\varphi_{\mathbf{Uphase_{CW},Theor}}$ at different velocities and IFBW of 10 kHz (a) 10 mm/s (b) 20 mm/s (c) 50 mm/s (d) 100 mm/s

https://doi.org/10.7795/110.20260421

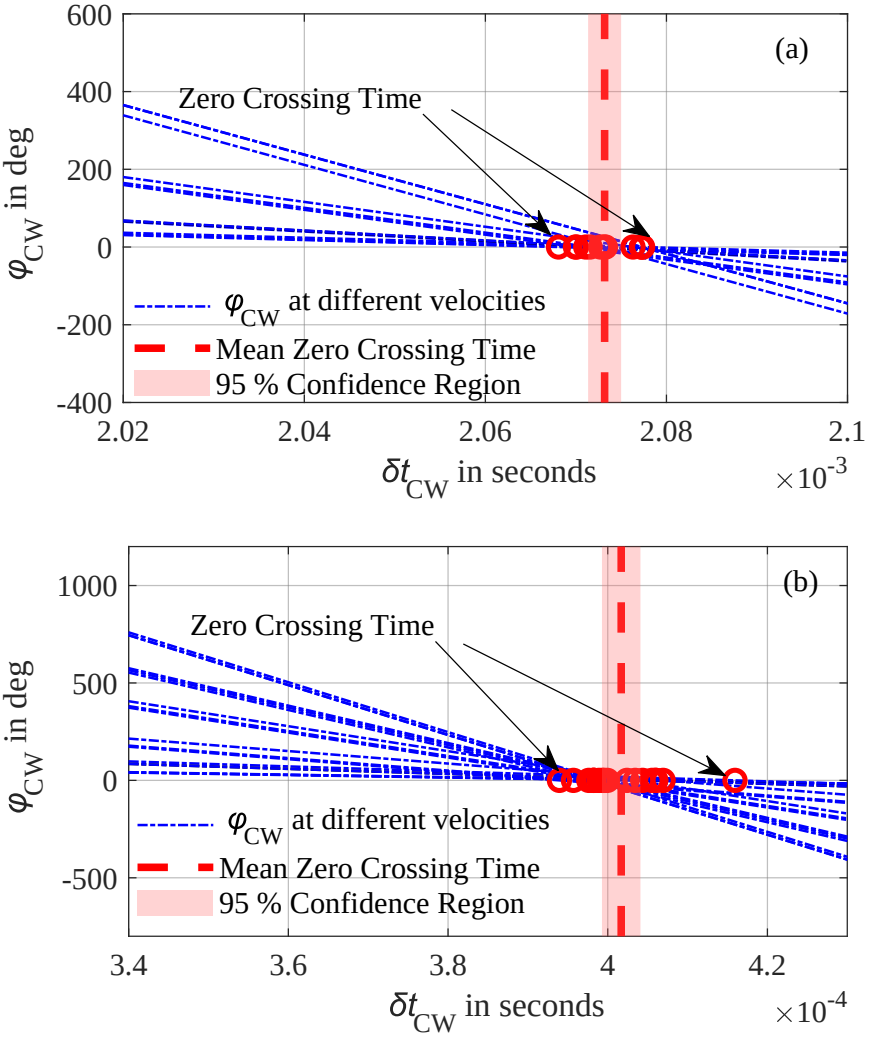

Figure 5.8: Unwrapped phase agreement between the measured and simulated time-varying positions represented by $\varphi_{\mathbf{CW}}$ vs. different CW step durations $\delta \mathbf{t_{CW}}$ at different velocities.

The consistent estimation of the optimized time intervals δt_{CW} across different measurement repetitions and velocities, matching well with theoretical analysis, demonstrates the feasibility of using the VNA CW mode for reliable velocity measurements.

5.4.3 Linear Sweep Signal Analysis

To characterize LS segments, it requires estimate of the phase error difference by considering the combined capturing time of the CW and LS segments. The goal is to minimize the error between the measured LS phases and the theoretical calculations of the unwrapped LS phases. Fig. 5.9 presents an example of the unwrapped phases for the three LS segments under test at different velocities. The captured sweeps are measured during the mid-range of the reflector movement, with d_0 varying between 520 mm and 480 mm. Due to the nature of the movement in this investigation, having a repeatable position at different velocities was challenging. Fig. 5.9(a) displays the unwrapped phases to varying velocities along with their corresponding theoretical unwrapped phases for a 1 kHz IFBW, while Fig. 5.9(b) illustrates

https://doi.org/10.7795/110.20260421

the same results for a 10 kHz IFBW.

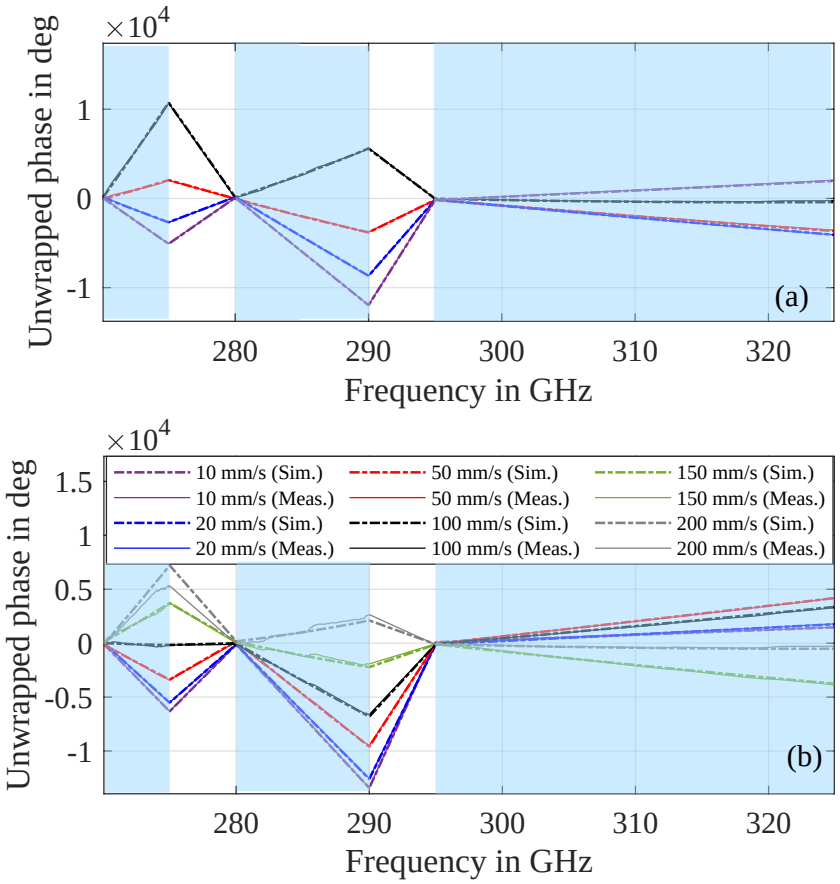

Figure 5.9: Unwrapped phase agreement between the measured and simulated time-varying positions of the LS segments.

To apply the grid optimization, δt_{LS} and d_0 at different measurement velocities will be characterized, using both IFBWs. Figure 5.10 presents the optimization results for measurements taken at a 1 kHz IFBW, with velocities of 10 mm/s, 20 mm/s, 50 mm/s, and 100 mm/s. The optimized δt_{LS} ranged between 2.7 ms and 3 ms, while d_0 showed the expected decreasing distance for each subsequent captured segment, ranging from 680 mm to 380 mm. A similar analysis is presented in [103].

The measurements were repeated at a 10 kHz IFBW, as shown in Figure 5.11, with the optimization results yielding δt_{LS} values stable at 1.1 ms with slight deviation reaching 1.2 ms at 10 mm/s. δt_{LS} demonstrated better stability for higher velocities, remaining at 1.1 ms. This improved stability at higher velocities is due to the reduced likelihood of multiple fits. The figure also shows a decreasing d_0 for the subsequently captured segments, indicating a consistent trend in distance reduction until reaching the final position.

The analysis of the LS segment enables the estimation of the reflector's position at each frequency point, which can also be represented in terms of the PDP. Figure 5.12 shows an example of the PDP for the time-varying signal, demonstrating agreement between the measured and simulated data when the reflector was moving at a velocity of 50 mm/s, with a VNA IFBW set to 10 kHz.

https://doi.org/10.7795/110.20260421

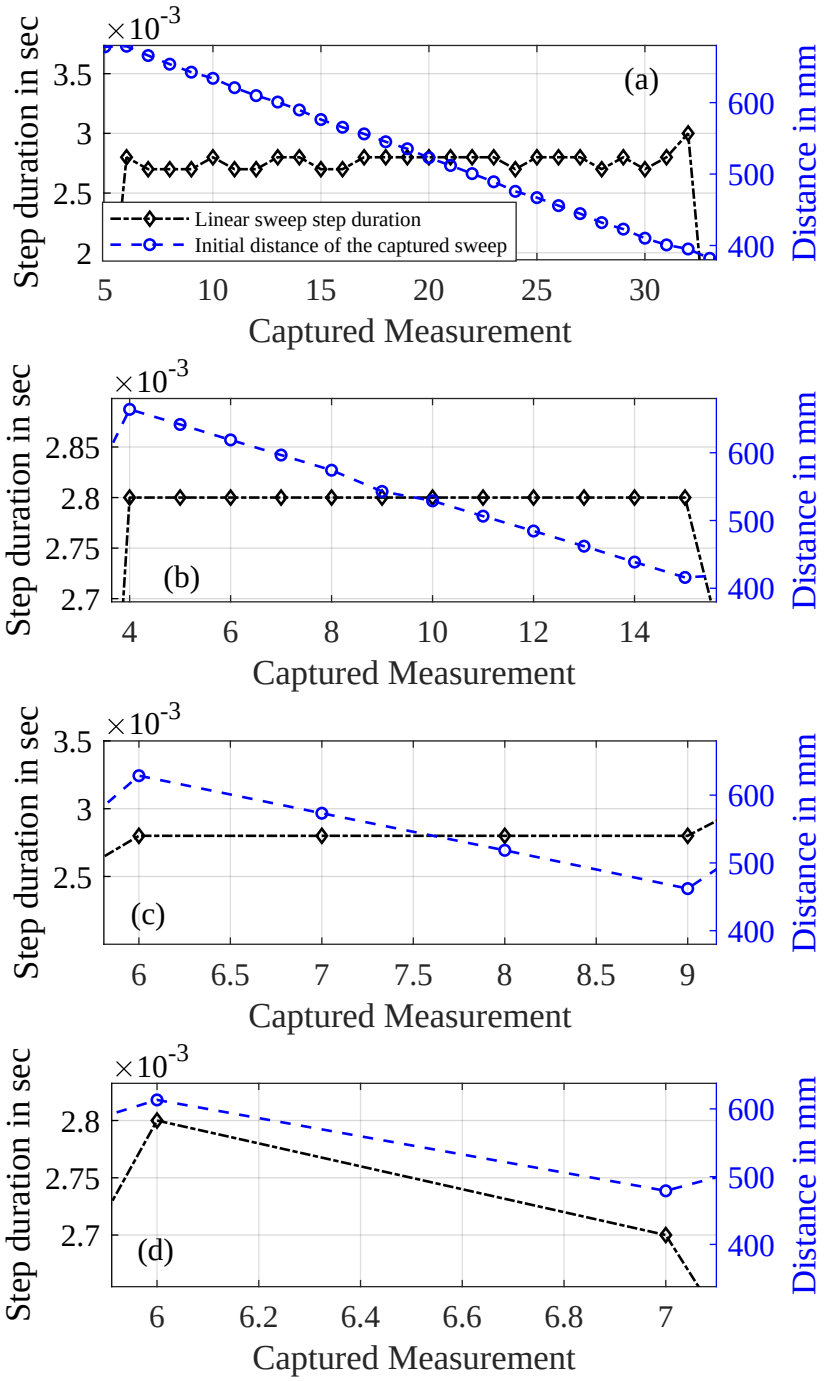

Figure 5.10: Unwrapped phase agreement between the measured and simulated time-varying positions of the LS segments.

The results presented in this investigation highlight the necessity of using directive antennas to ensure sufficient gain, elevating the signal above the noise floor, especially when applying higher IFBWs for faster sweeps. Furthermore, maintaining a stable measurement environment and securing frequency extension modules in fixed positions are crucial to prevent cable movements that could affect measurement accuracy.

Overall, the close agreement between the measured and simulated LS phases across a wide

https://doi.org/10.7795/110.20260421

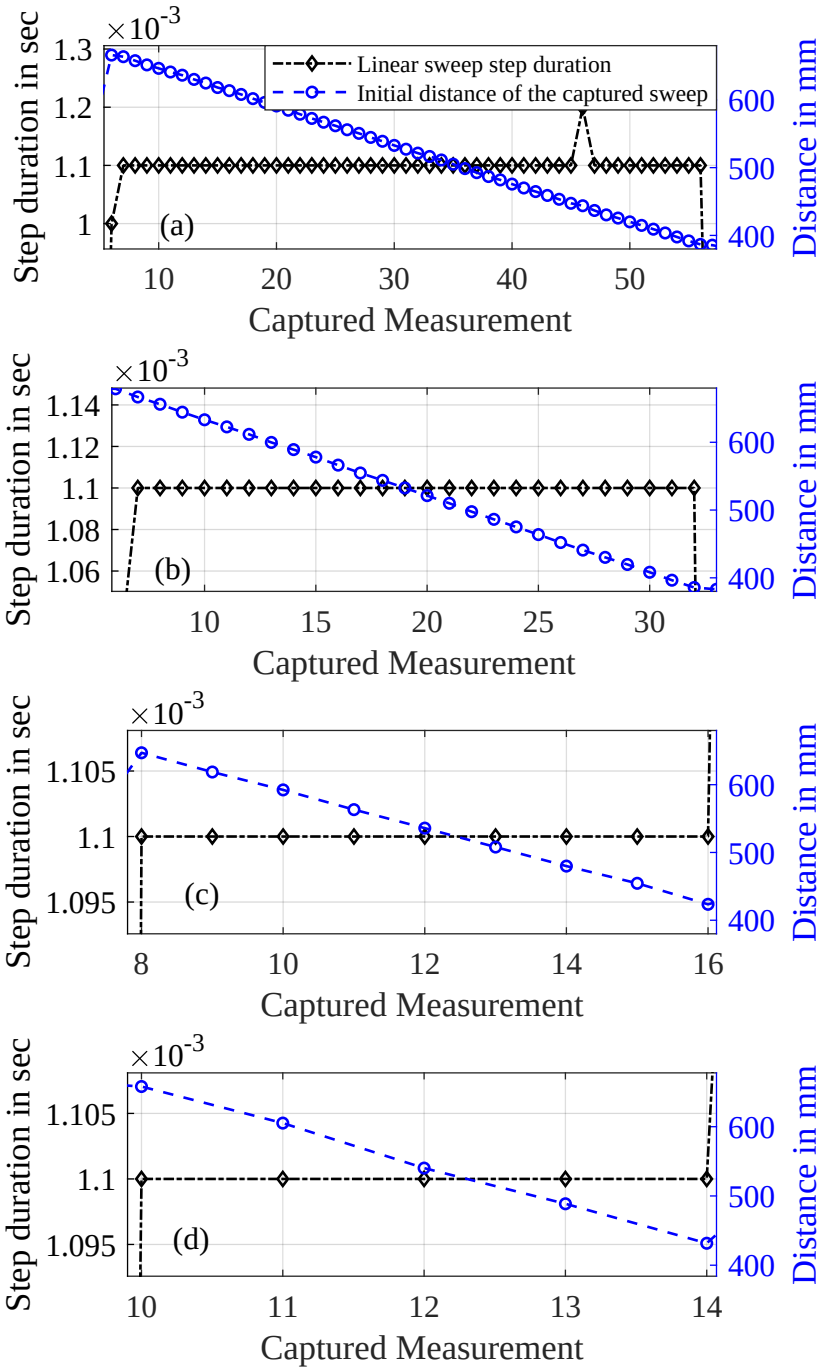

Figure 5.11: Unwrapped phase agreement between the measured and simulated time-varying positions of the LS segments.

range of velocities and IFBW settings confirms the high accuracy of the position and time-offset estimates. The stability of δt_{LS}, particularly at higher velocities, and the consistent d_0 trends demonstrate that the proposed method can reliably track reflector motion with sub-millisecond timing precision and millimeter-level spatial accuracy, even under varying dynamic conditions.

https://doi.org/10.7795/110.20260421

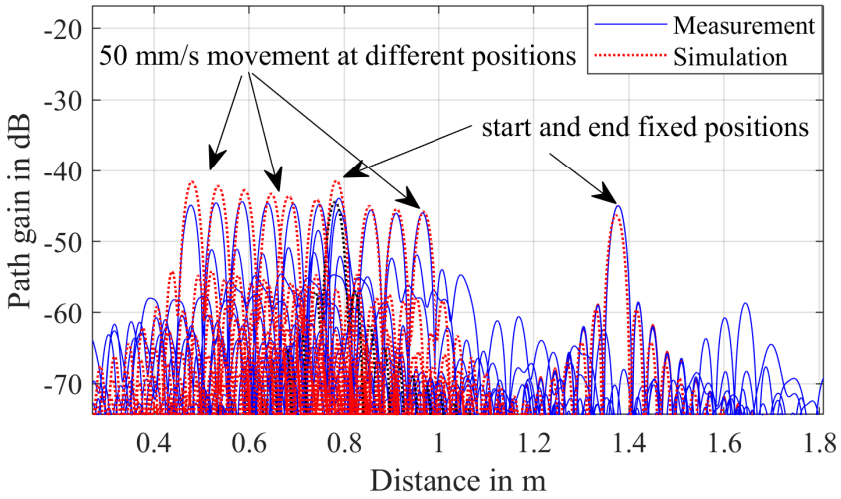

Figure 5.12: The measurement and simulation agreement for the LS segment was analyzed for the frequency band ranging from 280 GHz to 290 GHz. The PDP of the moving reflector was recorded at different positions while maintaining a velocity of 50 mm/s and an IFBW of 10 kHz.

https://doi.org/10.7795/110.20260421

6

Characterizing the Photonic-Assisted Coherent Free-Space Link for Sub-THz Data Transmission

This chapter presents a measurement testbed for a sub-THz OTA measurement. The setup enables wireless signal propagation over a distance of 6 meters. This chapter deviates from the previous chapters by extending the sub-THz investigation with data transmission using photonic-assisted measurement equipment and investigates the EVM of the received signals using different signal modulations and real data transmissions.

The transmission system consisted of a PIN-PD acting as the emitter and a sub-harmonic down-converter at the receiver. The testbed operates across a frequency range of 240 GHz to 300 GHz.

To improve the overall system performance, key transmission parameters were adjusted. These included the optical carrier frequency, frequency hopping configuration, DC bias applied to the transmitter, equalizer settings, and stages of digital signal processing. After optimization, the system successfully transmitted a 25.6 Gbit/s QPSK signal without noticeable errors.

A separate evaluation was carried out using 16-QAM to examine the impact of combining optical power from two branches feeding the PD. Measurements focused on error vector magnitude (EVM), linearity of the in-phase and quadrature amplitude signals, and the probability distribution of the received signal. The optimal performance was achieved with 5 mW input to the optical modulator and 10 mW to the optical carrier source.

To demonstrate practical data transmission, an image was divided into 24 data packets and sent over the link using QPSK at 25 Gbit/s. The image was received without any errors, confirming the system's ability to handle real-world data reliably.

The measurement methodologies, calibration procedures, and propagation analyses presented in Chapters 3 through 5 were primarily focused on system characterization and controlled test environments using a VNA and a PRBS time-domain CS. As a natural extension of this work, Chapter 6 investigates sub-THz measurement techniques within a more complex and application-oriented context: real-data transmission over a photonic-assisted free-space link. The objective is to evaluate how the sub-THz systems and waveform processing strategies perform under higher modulation complexity, using different measurement band-

https://doi.org/10.7795/110.20260421

widths and characterization of transmission quality using the EVM. This chapter bridges the gap between sub-THz fundamentals of laboratory-grade channel sounding and more advanced sub-THz data transmission scenarios.

6.1 Introduction into Photonic-Assisted Sub-THz Data Transmission

Thanks to their technological maturity and cost efficiency, electronic systems have long dominated wireless communication. These systems are widely considered the most reliable option for extending wireless communication into the sub-THz frequency range. Their ability to support compact circuit designs is especially advantageous for integration into end-user devices and other portable applications [107–111]. However, one of the main drawbacks of purely electronic technology lies in its limited component bandwidth. Additionally, achieving broad frequency coverage requires multiple discrete circuits. Electronic systems are also susceptible to noise, waveguide losses, and high power consumption [70, 112].

Due to these limitations and the push toward higher frequencies, optical systems have become a compelling alternative. In the past decade, research efforts have increasingly focused on photonic technologies for wireless transmission, including radio-over-fiber systems. Notably, many high-speed demonstrations have been carried out in frequency bands such as WR-10 (75–110 GHz), WR-06 (110–170 GHz), and more recently, WR03 (220–325 GHz) [113–115].

Photomixers stand out in this context by offering exceptionally wide bandwidths, reaching up to 3 THz—levels that are challenging for purely electronic systems to achieve. However, photomixer devices are costly and difficult to scale down for compact, user-oriented applications. Despite these challenges, photomixers hold significant promise in hybrid architectures, particularly for access points. Their ability to operate across wide frequency ranges enables simultaneous communication with multiple electronic systems operating between 100 GHz and 500 GHz. This makes them suitable for enabling seamless data transmission in sub-THz networks. A notable example of this hybrid approach is using photonic emitters around the 300 GHz range in combination with electronic IQ receivers, as demonstrated in [116].

In this chapter, the characterization of a hybrid sub-THz OTA system that integrates both optical and RF components is presented. The system was evaluated through experiments targeting different aspects of its performance. Multiple sub-THz frequencies within the WR03 band were tested using QPSK modulation. Key performance metrics—such as EVM and received signal strength—were measured using a PIN-PD emitter to generate the sub-THz signals [70].

The initial phase of the evaluation focused on profiling the beam along its transmission path. This was carried out at three distinct locations using the knife-edge technique, with a pyroelectric thin-film (PTF) detector positioned at the receiver's focal point. Analyzing the beam profile is essential for understanding how the signal propagates and whether different frequencies influence the emitter's beam characteristics or alignment. This is particularly important for systems incorporating diffraction optics in their beam path. Parabolic mirrors collimated the beam and successfully delivered the signal across a 6-meter distance. Prior

https://doi.org/10.7795/110.20260421

research has explored the radiation behavior of PIN-PD emitters and how various internal antenna designs can impact their emission characteristics [20, 21, 117].

Next, this chapter studied how the wavelength of the laser source affects the received signal. Since laser sources can vary in output power and stability [118], these variations can directly impact the strength and consistency of the transmitted signal. In this measurements, it examined optical carriers across a 2.5 THz range to observe how changes in carrier frequency and modulated optical signals influence the down-converted output and beam shape [119].

It also investigated the impact of frequency stability and laser frequency hopping on data transmission performance. This was assessed by tracking the IF offset over time and analyzing how these fluctuations affected signal demodulation and reliability. A frequency offset estimation step was implemented as part of the DSP workflow to support robust signal recovery. While cost-effective semiconductor lasers are commonly used in such systems, they are known to exhibit mode hopping, which can lead to performance instability. This issue has been previously discussed in [70, 120].

It then examined if the emitter is operating in the linear regime, by testing how the external bias voltage applied to the emitter influences signal propagation. Measurements were taken at three different DC bias levels to determine whether the output signal strength varies linearly with the bias. The PD bias voltage is critical in controlling the amount of current generated in response to incoming optical signals, which influences the emitter's output power [70]. Prior studies have documented how PIN-PD output power changes with applied bias across frequencies ranging from 100 GHz to 700 GHz [20].

The received baseband signal was then processed using a tailored DSP pipeline with an adaptive equalizer. This equalizer employed the CMA, a well-known blind equalization method first introduced by Godard in 1980 [121]. The CMA is especially effective for minimizing signal distortion in time-varying wireless channels. Additionally, a synchronization mechanism is implemented to align the receiver's LO with the incoming signal, using the method described in [122].

The focus of this investigation is then shifted to evaluating the performance of 16-QAM modulation. This analysis aimed to identify the optimal optical power levels needed at the emitter and the appropriate power distribution between the carrier and modulated branches. Unlike QPSK, 16-QAM offers three distinct IQ amplitude levels, making it easier to observe the impact of optical power variations on symbol magnitude and constellation linearity [70].

These tests were conducted at a sub-THz carrier frequency of 260 GHz. The results demonstrated that the optical modulation path significantly affected the linearity of the received symbols in the constellation diagram. As the power balance between branches was fine-tuned, it observed notable improvements in the quality of the received signal. To support accurate demodulation, a FFT-based algorithm was employed to estimate the frequency offset, following the method outlined in [70, 112, 123].

To validate the stability and practical performance of the system, a real-data transmission test involving image transfer was conducted. This demonstration served to compare the system's handling of actual data streams against standard pseudo-random bit sequences (PRBS).

https://doi.org/10.7795/110.20260421

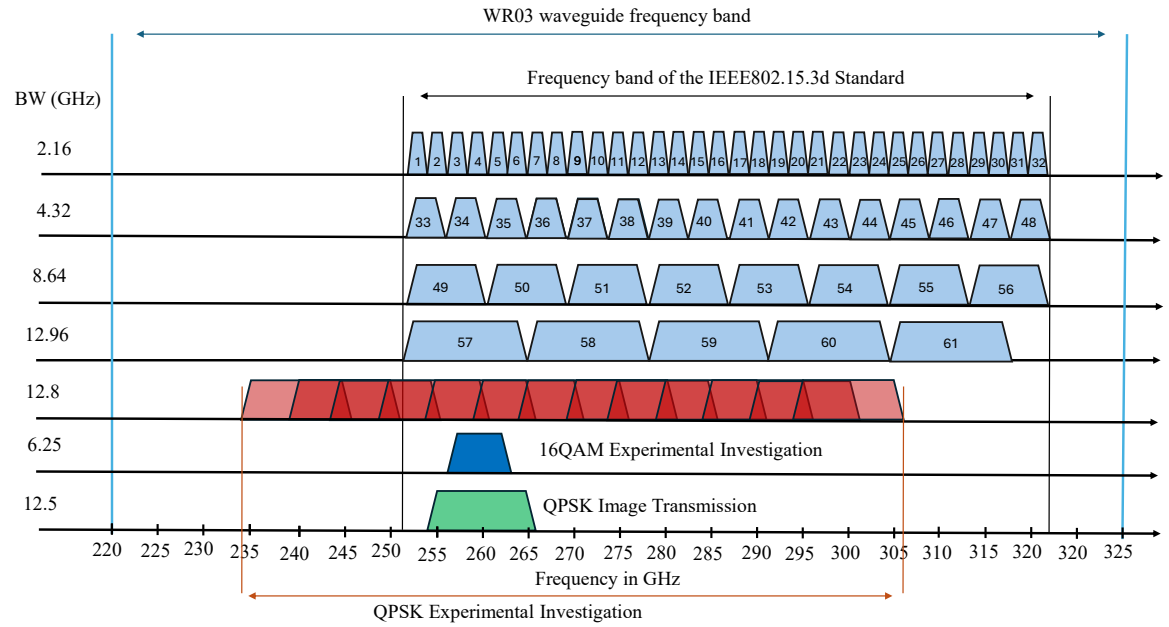

Figure 6.1: Channel allocation proposed by IEEE 802.15.3d, along with the frequency ranges investigated in this chapter. (Adopted from [70]).

Using QPSK modulation at 25 Gb/s, it achieved error-free data reception at a carrier frequency of 260 GHz. The modulated optical frequency was centered at 194.75 THz, with the emitter operating under a DC bias of -1 V [70].

This study specifically targeted the WR03 frequency band, a strong candidate for future 6G applications. The testbed covered frequencies ranging from 252.72 GHz to 321.84 GHz, evaluating how transmission performance and system parameters influenced signal reception. This frequency range has attracted significant attention due to the atmospheric transmission window near 300 GHz [124]. Furthermore, frequencies up to 322 GHz have been standardized under IEEE 802.15.3d [11].

The IEEE 802.15.3d standard supports various channel bandwidths tailored for different applications [111]. Figure 6.1 illustrates the channel allocation proposed in the standard, alongside the specific frequency ranges used in this chapter. The QPSK experiments aligned with channels 57 through 60, while the 16-QAM evaluations fell between channels 49 and 50. The chosen center frequencies and bandwidths were selected based on the modulation scheme and the hardware capabilities, and were further validated by the image transmission tests conducted around 260 GHz.

6.2 Measurement Setup

As illustrated in Fig. 6.2, the measurement setup features a single-channel, heterodyne, photonics-based THz communication link. Signal generation was achieved using two CW, tunable distributed feedback (DFB) laser sources with wavelengths of 1526.05 nm and 1549.75 nm, supplied by the matrIQ-Laser 1000 Series™, which offers a linewidth of 100 kHz and a tun-

https://doi.org/10.7795/110.20260421

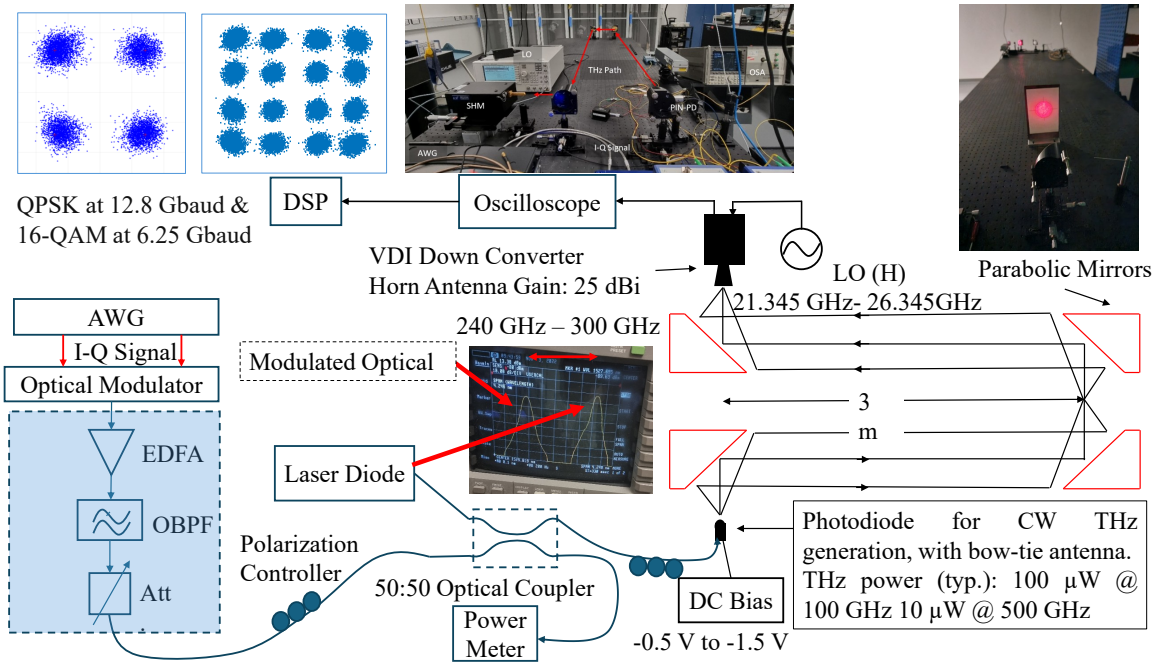

Figure 6.2: Measurement setup illustrating the transmission system, optical spectrum analyser (OSA) trace of the dual-laser output, and received constellation diagrams for QPSK and 16-QAM after 6-meter transmission and DSP.

ing resolution of 0.01 pm, corresponding to 1.27 MHz of frequency resolution. The optical frequency offset between these two lasers resulted in a transmitted sub-THz signal given by $f_{THz} = |f_1 - f_2|$, where f_1 and f_2 are the respective optical frequencies of the lasers. The output sub-THz frequency was selected between 0.24 THz and 0.3 THz to remain within the operational limits of the WR3.4 receiver band [70, 112].

In this setup, one laser served as the optical carrier, while the second was modulated with the I and Q components of a complex signal. These signals were produced using a Coherent Solutions IQ Transmitter-FDP™ complex modulator, driven by electrical signals generated from a Keysight M8194A™ 120 GSa/s AWG. The AWG loaded digitally synthesized waveforms that had been mapped with over-sampled symbols.

The shaded blue section in Fig. 6.2 highlights additional components used during the 16-QAM experiments, which will be discussed in detail later in this chapter.

The output IQ signals from the AWG were applied to drive the optical IQ modulator, which used MZM structures to encode the electrical data onto the optical carrier. Both optical signals were then combined using a 50 % optical coupler before being launched into a TOPTICA Photonics™ PCA-FD-1550-100-TX-3™ InGaAs PIN-PD photomixer. Within the photomixer, the two laser tones were optically mixed, generating a sub-THz signal. This signal was emitted through a bow-tie antenna mounted on a hyper-hemispherical silicon lens, producing a beam with approximately 15° full width at half maximum (FWHM) divergence and an output power near 0 dBm at 0.3 THz. The system achieved a dynamic range of 90 dB at 100 GHz and 70 dB at 500 GHz, as reported in [70].

The resulting sub-THz waveform can be modeled as follows [125]:

https://doi.org/10.7795/110.20260421

$$Y_{\mathrm{THz}}(t) = \eta A_1 A_2 \left[I \cos(\omega_{THz} t + \theta_{\mathrm{THz}}) + Q \sin(\omega_{\mathrm{THz}} t + \theta_{\mathrm{THz}}) \right]. \tag{6.1}$$

Here, η represents the conversion efficiency of the photomixer, influenced by the applied DC bias; A_1 and A_2 denote the optical amplitudes of the carrier and the modulated IQ signal, respectively; and ω_{THz} and θ_{THz} refer to the angular frequency and phase of the generated THz wave, respectively. This architecture enables accurate and distortion-free translation of the modulated signal from the optical to the THz domain. A bandpass filter, defined by the emission and waveguide characteristics, ensured that only the desired frequency was transmitted, suppressing image frequencies.

Due to the LoS nature of sub-THz transmissions, directional beam alignment is essential. To counteract divergence and associated propagation losses, the emitted signal was collimated using four parabolic mirrors arranged in a folded optical path, effectively achieving a total transmission distance of 6 meters. A 25 dBi WR3.4 horn antenna was positioned at the receiver to capture the signal, which was then processed by a VDI WR3.4MixAMC™ SHM. The SHM provided an IF output bandwidth of 40 GHz and was driven by a LO signal multiplied by a factor of 12. The received waveform passed through the horn and the waveguide circuitry for down-conversion.

An external RF synthesizer acted as the LO source. The resulting IF signal fell within the oscilloscope's midband frequency range and can be expressed by:

$$Y_{\mathrm{IF}}(t) = A_{\mathrm{IF}} \left[I \cos(\omega_{\mathrm{IF}} t + \theta_{\mathrm{IF}}) + Q \sin(\omega_{\mathrm{IF}} t + \theta_{IF}) \right]. \tag{6.2}$$

In this expression, A_{IF}, ω_{IF}, and θ_{IF} represent the amplitude, angular frequency, and phase of the intermediate-frequency signal. The captured waveform was post-processed in MATLAB using the Communications Toolbox™. The digital signal processing workflow involved several demodulation stages to accurately reconstruct the original transmitted symbols.

6.3 Digital Signal Processing Techniques

Figure 6.3 shows the signal processing chain that recovers the transmitted constellation from the received waveform.

The signal was recorded using an oscilloscope at a sampling rate f_s close to the one used during transmission. A digital LO at frequency f_{IF} was used to down-convert the signal to baseband, and the IQ components were extracted [70]. With $\omega_{\mathrm{IF}} = 2\pi f_{\mathrm{IF}}$, the digital down-conversion is

$$Y_{\mathrm{BB},I}(nT_p) = -\,Y_{\mathrm{IF}}(nT_p)\,\sin\!\big(\omega_{\mathrm{IF}}\, nT_p\big), \tag{6.3}$$

$$Y_{\mathrm{BB},Q}(nT_p) = \quad Y_{\mathrm{IF}}(nT_p)\,\cos\!\big(\omega_{\mathrm{IF}}\, nT_p\big), \tag{6.4}$$

$$Y_{\mathrm{BB,IQ}}(nT_p) = Y_{\mathrm{BB},I}(nT_p) + j\, Y_{\mathrm{BB},Q}(nT_p). \tag{6.5}$$

Here, n is the sample index ($0 \leq n < N$) and T_p is the sampling period of the digitized waveform.

https://doi.org/10.7795/110.20260421

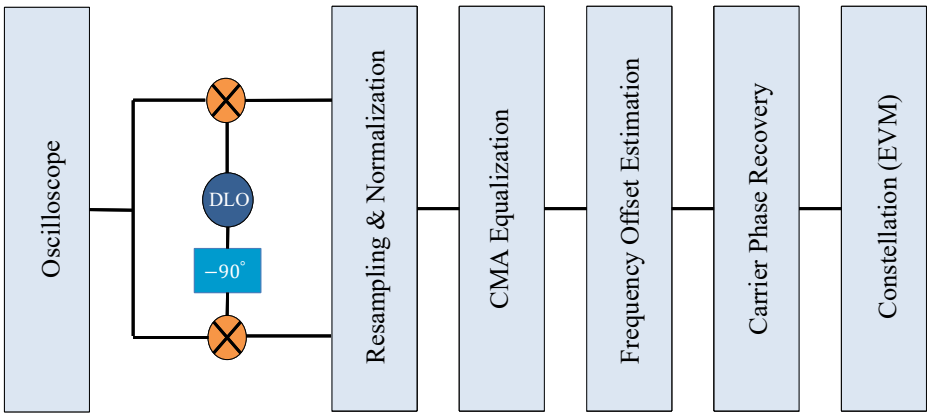

Figure 6.3: DSP blocks used to process and demodulate the received signals. The main steps include resampling, equalization, frequency offset correction, and phase recovery. (Adopted from [70]).

The down-converted complex waveform was filtered, normalized, and downsampled by the oversampling factor L [70]:

$$Y_{\mathrm{DS,IQ}}(nT_p) = \langle Y_{\mathrm{BB,IQ}}(nT_p) \rangle * I_L, \tag{6.6}$$

where $\langle \cdot \rangle$ denotes digital low-pass filtering, I_L is a unity vector for decimation by L, and $*$ denotes convolution.

The complex baseband signal was then passed through a constant-modulus (CMA) equalizer, which does not require training and adapts its weights to minimize dispersion of symbol amplitudes around a target modulus M. The CMA minimizes

$$\varepsilon^2 = E\left[\left(|y(i)|^2 - M^2\right)^2\right], \tag{6.7}$$

$$\varepsilon^2 = E\left[\left(|y(i)|^2 - M^2\right)^2\right]. \tag{6.8}$$

and the equalizer output is:

$$Y_{\mathrm{CMA}}(i) = \sum_{k=0}^{L-1} \omega_i(k)\, Y_{\mathrm{DS,IQ}}(i-k) = \mathbf{W}_i^{\mathsf{T}} \mathbf{Y}_i. \tag{6.9}$$

$$\mathbf{W}(k+1) = \mathbf{W}(k) + \mu\, Y_{\mathrm{DS,IQ}}(k)\, e^*(k), \tag{6.10}$$

where L is the number of equalizer taps (as shown in the figure), μ is the step size, and $e(k)$ is the CMA error term.

After equalization, the carrier frequency offset was estimated using an FFT-based periodogram of the m^{th} power of the equalized signal [70]:

$$Y_{\Delta f} = \underset{f \in \left[-\frac{R_{\mathrm{sym}}}{2}, \frac{R_{\mathrm{sym}}}{2}\right]}{\arg\max} \left| \sum_{n=0}^{N-1} \left(Y_{\mathrm{CMA}}(n)\right)^m e^{-j2\pi f n / f_s} \right|, \tag{6.11}$$

https://doi.org/10.7795/110.20260421

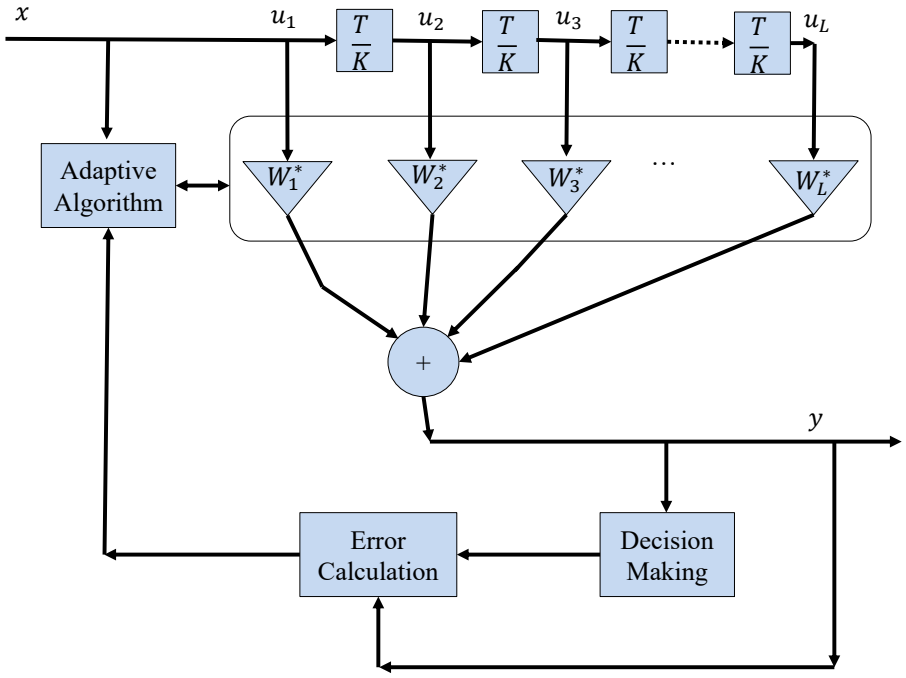

Figure 6.4: CMA equalization block diagram. (Adopted from [70]).

where m is the modulation order, R_{sym} is the symbol rate, and f_s is the sampling rate.

Finally, phase correction was performed using a phase-locked loop (PLL)-based loop (Fig. 6.5). Let $x_n \triangleq Y_{\Delta f}[n]$ denote the input to the phase-recovery block and y_n its output (see Fig. 6.5). The phase error detector is

$$e_n = \text{sgn}\big(\text{Re}\{x_n\}\big)\ \text{Im}\{x_n\} - \text{sgn}\big(\text{Im}\{x_n\}\big)\ \text{Re}\{x_n\}. \tag{6.12}$$

The loop integrator update is

$$\psi_n = g_I e_n + \psi_{n-1}, \qquad g_I = \frac{4(\phi^2/d)}{K_p K_0}, \qquad \phi = \frac{B_n T_p}{\xi + 1/(4\xi)}, \qquad d = 1 + 2\xi\phi + \phi^2, \tag{6.13}$$

where B_n is the normalized loop bandwidth, ξ is the damping factor, K_0 is the phase-recovery gain (samples per symbol), and $K_p = 2$ for QPSK.

The proportional path and direct digital synthesis (DDS) phase accumulator are

$$\lambda_n = (g_p e_{n-1} + \psi_{n-1}) + \lambda_{n-1}, \qquad g_p = \frac{4\xi(\phi/d)}{K_p K_0}. \tag{6.14}$$

Finally, the phase-corrected output (matching the figure's y_n) is

$$y_n = x_n\, e^{j\lambda_n}. \tag{6.15}$$

https://doi.org/10.7795/110.20260421

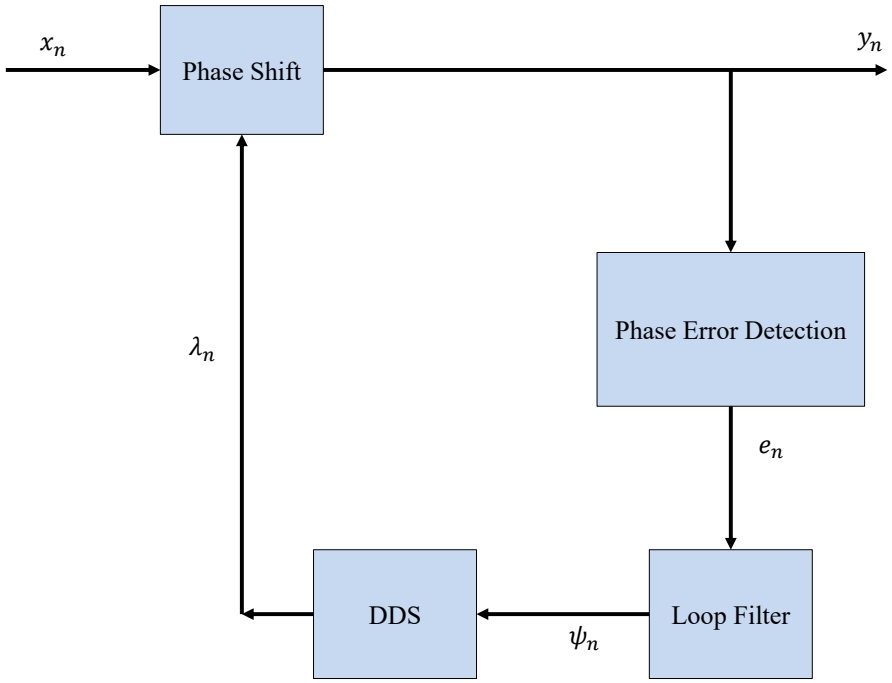

Figure 6.5: Phase recovery using a PLL-based loop [70].

6.4 Beam Profile Analysis

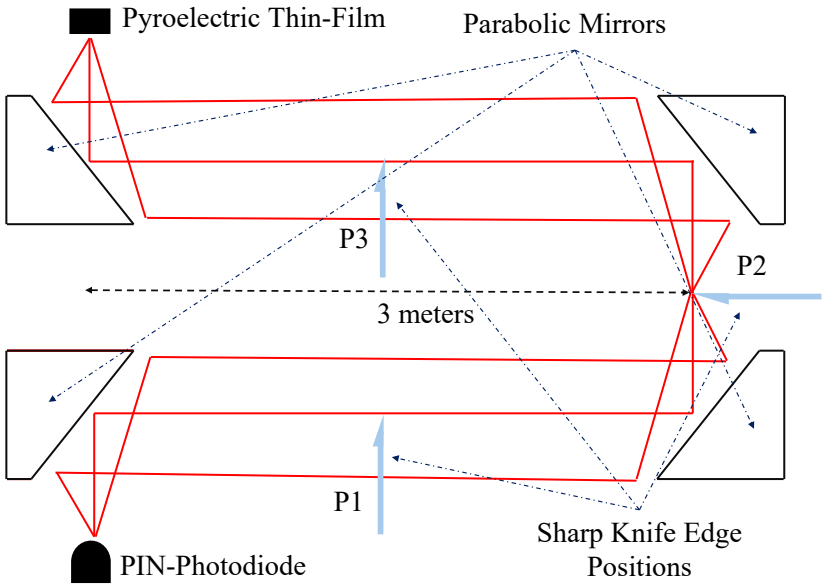

Figure 6.6: Knife-edge measurement positions along the beam path. (Adopted from [70]).

The beam profile played a significant role in this measurement campaign, as no beamforming techniques were used at either the emitter's output or the receiver's horn antenna. Understanding the profile was also important for evaluating the energy density along the propagation path. Figure 6.6 shows the three locations: P_1, P_2, and P_3, where beam measurements were

https://doi.org/10.7795/110.20260421

taken using the knife-edge method. In each case, a rectangular blade was moved laterally across the sub-THz beam to progressively block more of the wavefront. The received power was measured with a PTF detector placed at the focal point of the receiver and connected to a lock-in amplifier [70].

Beam profiles at positions P_1 and P_3, located 1.5 m and 4.5 m from the PIN-PD emitter, respectively, were used to examine the beam collimation. Figure 6.7(a) shows the received power versus blade position, fitted with an error function. The intensity distribution was obtained by taking the derivative of this curve, representing a Gaussian beam profile as shown in Fig. 6.7(b). The results at both positions showed similar beam widths and intensities, confirming that the beam remained well-collimated across the measured distance.

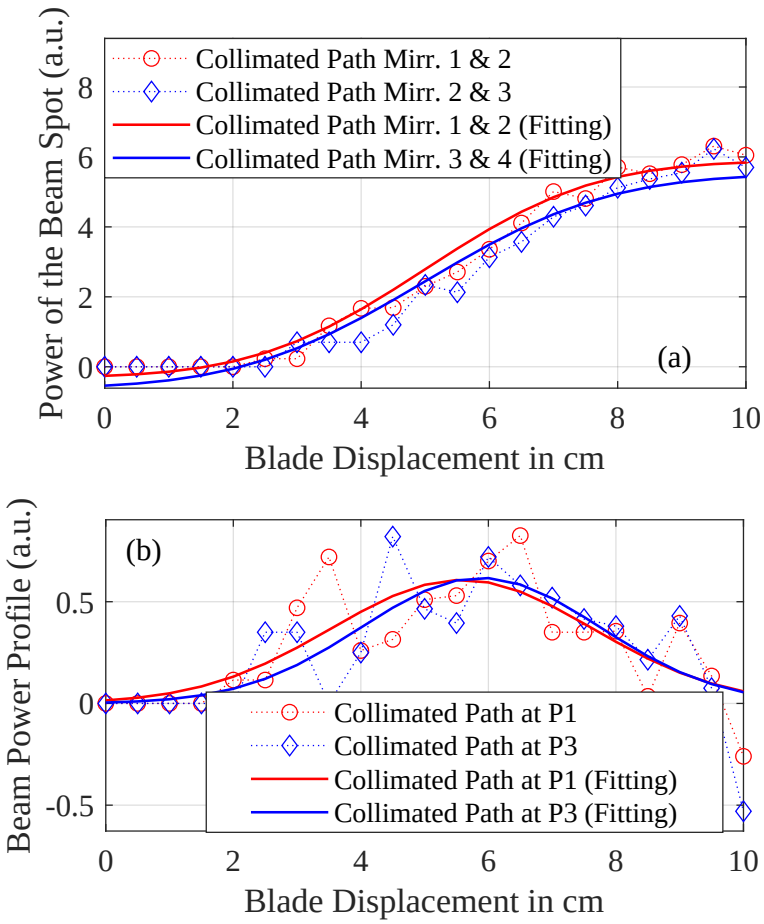

Figure 6.7: Beam profile at 260 GHz measured using the knife-edge method. (a) Received power with error function fit. (b) First derivative showing Gaussian intensity distribution. (Adopted from [70]).

Additional measurements were taken at P_2, close to the focal point at the mid path of the setup. Frequencies from 240 GHz to 300 GHz were tested in 20 GHz steps. The results showed that beam intensity varied with frequency, indicating frequency-dependent propagation behavior. The highest beam intensity was observed at 260 GHz. As shown in Fig. 6.8(a), the power dropped more sharply due to the tighter focus at this point. The corresponding Gaussian intensity profiles derived from the knife-edge data are shown in Fig. 6.8(b).

This point-to-point measurement configuration, demonstrated that the emitted beam re-

https://doi.org/10.7795/110.20260421

mained well-collimated over several meters, ensuring stable energy density along the propagation path. The frequency-dependent variations observed at the focal midpoint highlight the importance of precise alignment and frequency selection in maximizing coupling efficiency in quasi-optical links.

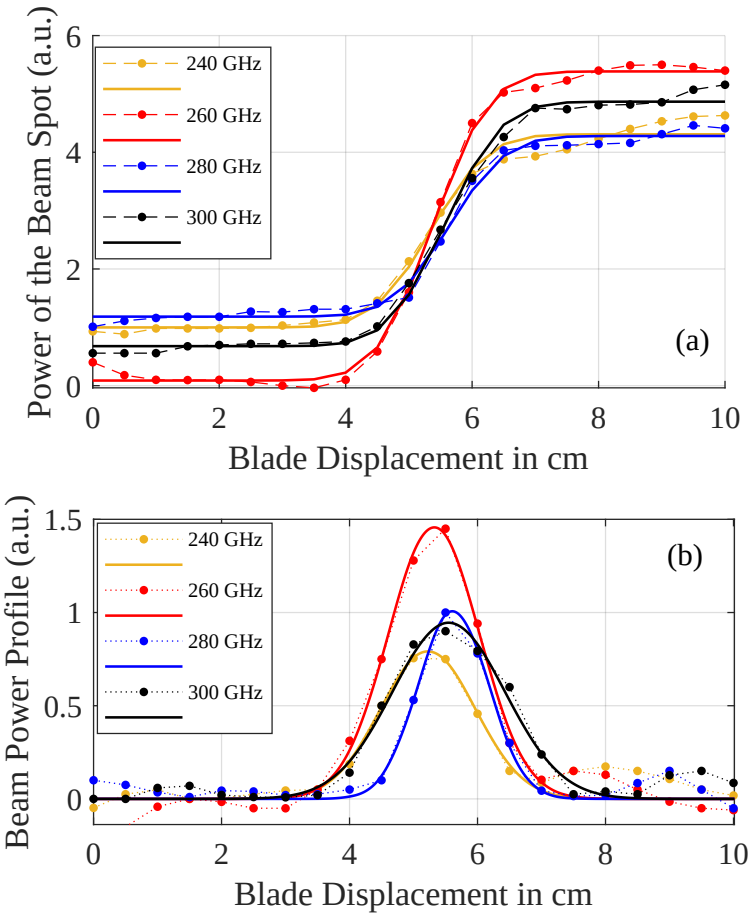

Figure 6.8: Beam profile at position P_2. (a) Power versus blade position for different frequencies. (b) Derivatives showing Gaussian profiles at each frequency. (Adopted from [70]).

6.5 Results and Discussion

6.5.1 QPSK Measurement

For the QPSK measurements, a 2^9 PRBS signal was used at a symbol rate of 12.8 GBaud. The waveform was generated by the IQ output of the AWG operating at 100 GSa/s. A raised cosine (RC) filter with a 0.35 roll-off was used for pulse shaping. The resulting baseband IQ signals were fed into the optical modulator at 500 mV per channel, resulting in a 3 mW modulated optical signal. This was combined with a 16 mW optical carrier before being input to the THz emitter.

To generate the IF, the down-converter LO was tuned between 21.345 GHz and 26.345 GHz, depending on the selected sub-THz frequency, resulting in a consistent 16.5 GHz IF at the receiver. The received waveform was captured using a Keysight UXR0334A™ real-time oscilloscope

https://doi.org/10.7795/110.20260421

(RTO) at 128 GSa/s. Each acquisition contained 2.56 million samples, which were divided into 160,000 sample segments for analysis.

No additional optical amplification was applied to the two optical branches feeding the photomixer. This configuration was used to evaluate the impact of optical and system parameters on the received signal strength and EVM performance [70, 112].

A C-band (1530–1565 nm) optical wavelength was selected to match the optimal operating range of the DFB lasers, optical modulator, and PIN-PD photomixer. This choice aimed to improve the quality of the received signal in terms of signal strength and EVM.

To investigate the optical frequency effect on the measurements, the modulated branch was swept from 193.75 THz to 196.25 THz in 0.5 THz increments. The optical carrier was tuned to produce sub-THz signals from 240 GHz to 300 GHz in 5 GHz steps. Figure 6.9 shows the resulting EVM and signal strength (V_{rms}) across the frequency range. The highest received signal was recorded at 194.75 THz, while the lowest was at 196.25 THz, with a peak-to-peak voltage variation of around 0.4 mV.

Although signal strength showed an explicit dependency on optical frequency, the EVM exhibited less consistent behavior. Figure 6.10 shows the averaged results across all sub-THz frequencies. Overall, 194.75 THz provided the best performance, while 196.25 THz resulted in the weakest signal. The 195.75 THz produced the worst EVM, especially for lower-frequency sub-THz bands [70, 112].

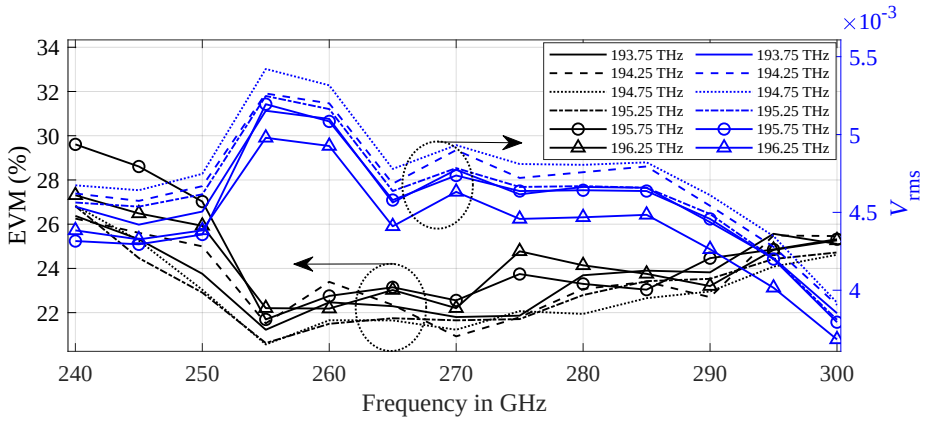

Figure 6.9: Impact of optical frequency on received signal strength and EVM. Combined RMS values are plotted across different optical frequency settings. (Adopted from [70, 112]).

Thermal fluctuations in the laser sources caused wavelength instability during transmission, resulting in frequency hopping. This effect was observed as a 170 MHz drift around the 16.5 GHz down-converted IF [70, 112]. Figure 6.11 shows a persistent spectrum display captured with Keysight PathWave vector signal analysis (VSA) software. The unmodulated photomixed signal centered around 16.5 GHz was used to visualize the hopping behavior. In addition to frequency hopping, a consistent 360 MHz offset was observed due to laser tuning error, corresponding to a 30 MHz error in the IF after down-conversion, which was compensated to realign the signal to the target frequency.

This frequency drift caused variations in the down-converted signal from one measurement to another. To evaluate this, several recorded waveforms were analyzed with respect to EVM

https://doi.org/10.7795/110.20260421

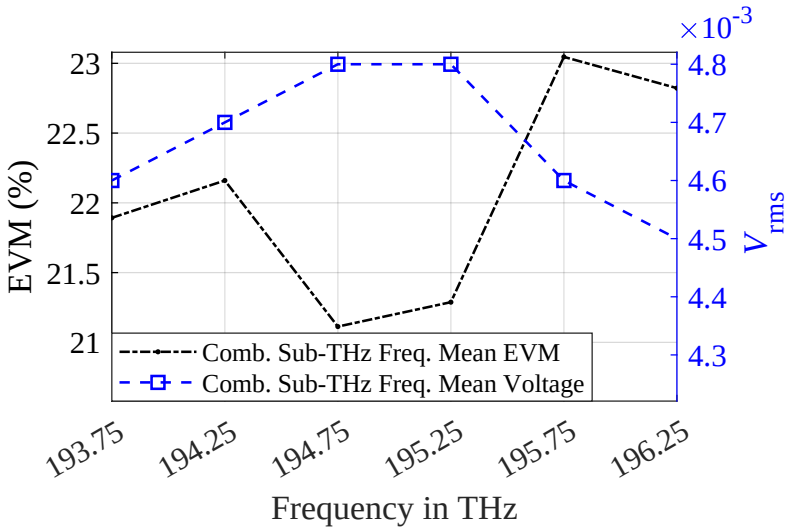

Figure 6.10: Mean V_{rms} and EVM across tested optical frequencies. (Adopted from [70]).

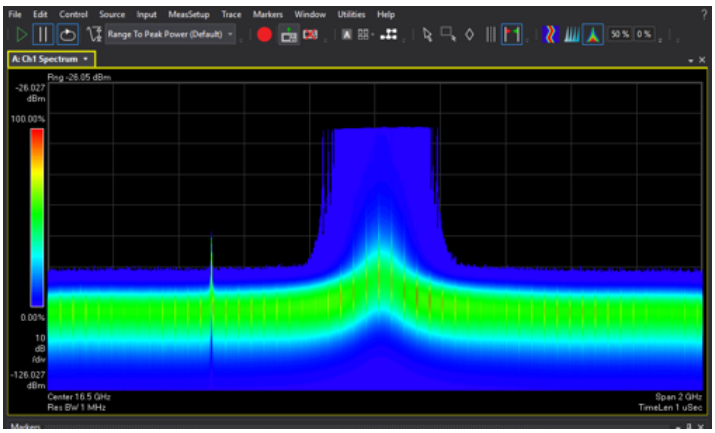

Figure 6.11: Persistence display showing frequency drift of an unmodulated laser signal centered at 16.5 GHz IF. A 2 GHz span is shown. (Adopted from [70, 112]).

under different IF offsets. Figure 6.12 shows the EVM results at 10 MHz IF resolution steps between 16.39 GHz and 16.52 GHz. For a 270 GHz sub-THz signal, the best EVM was 21.22 % when properly aligned. Offsets of 20–80 MHz increased the EVM to values as high as 46.36 %.

To study how the drift varied during the recording, the IF offset was tracked over a 20 µs capture window using a sliding window of 1.25 µs shifted in 0.78 µs steps. Figure 6.13 shows the frequency slope for down-converted 240 GHz and 270 GHz signals. Both signals experienced a total shift of about 4 MHz, corresponding to a drift rate of roughly 200 kHz per microsecond.

The effect of the emitter's DC bias voltage on signal quality was also evaluated. Three reverse bias levels: -0.6 V, -1 V, and -1.5 V were tested. The DC bias affects the PD's output current and response speed. Figure 6.14 shows that a -1 V bias consistently produced the highest received signal strength and lowest EVM across all sub-THz frequencies. This is confirmed in Fig. 6.15, where the average performance of each bias level is compared [70].

Finally, the delay tap length of the CMA equalizer was optimized. Taps ranging from 3 to 50 were tested, and the EVM was calculated across the sub-THz frequency range. As shown

https://doi.org/10.7795/110.20260421

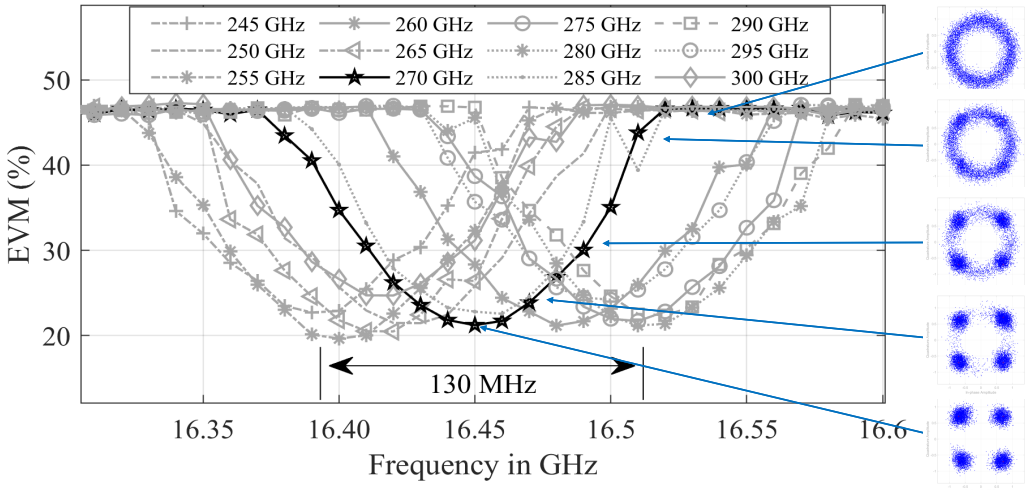

Figure 6.12: Effect of intermediate frequency offset on EVM. The optimal offset reduced distortion compared to misaligned center frequencies. (Adopted from [70]).

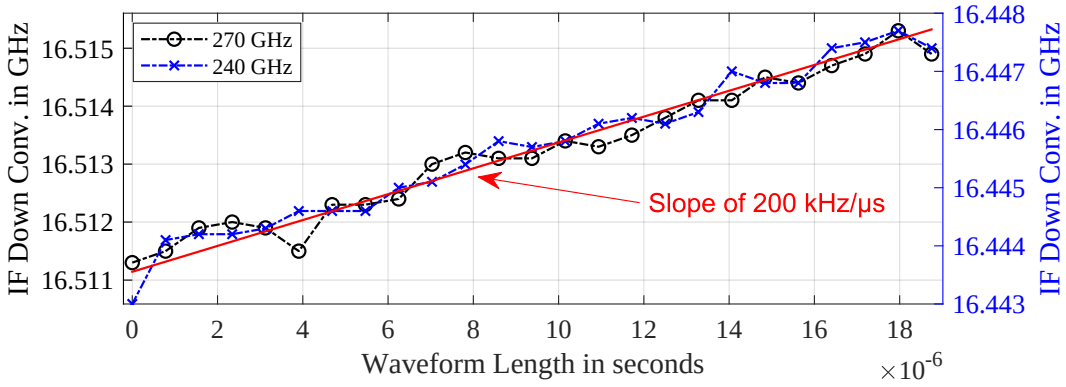

Figure 6.13: Intermediate frequency drift over time for 240 GHz and 270 GHz signals, recorded at 1 kHz resolution. (Adopted from [70]).

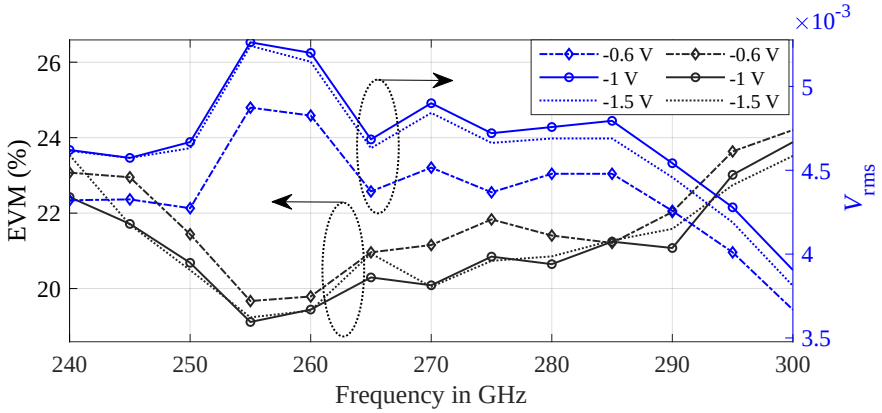

Figure 6.14: Combined EVM and V_{rms} across different DC bias voltages. (Adopted from [70]).

https://doi.org/10.7795/110.20260421

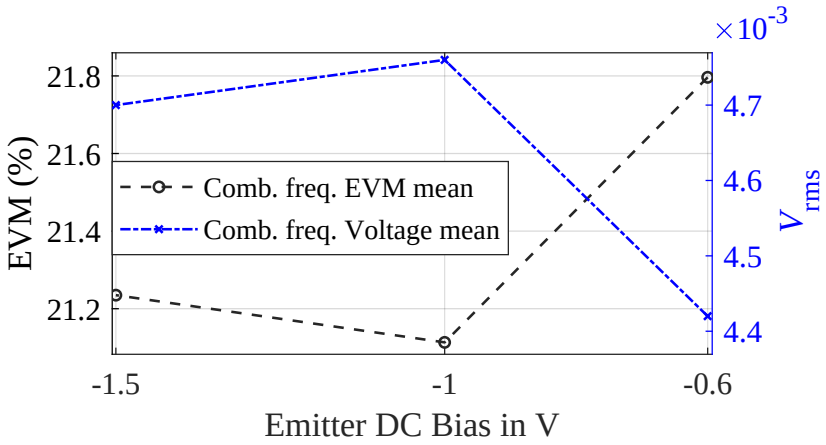

Figure 6.15: Mean EVM and received signal strength across sub-THz frequencies for each DC bias level. (Adopted from [70]).

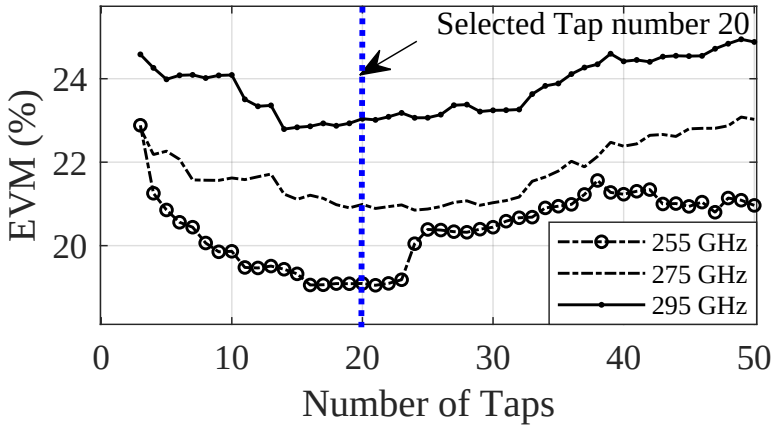

Figure 6.16: Impact of CMA equalizer tap count on EVM for selected sub-THz frequencies. (Adopted from [70]).

in Fig. 6.16, tap length influenced performance differently across the band. Frequencies closer to the center performed better, with optimal tap lengths between 10 and 25. Beyond this range, EVM began to increase again. A tap length of 20 was selected as a balanced value for consistent equalization [70].

6.5.2 16-QAM Measurement

Compared to the QPSK setup, several key modifications were made to support 16-QAM measurements. As shown in Fig. 6.2, the optical signal path was updated to include an EDFA, an optical attenuator, and an optical bandpass filter (OBPF) following the modulator output. These changes provided more control over the signal power and were necessary for evaluating how power levels affect 16-QAM signal quality. The received signals were recorded using a Tektronix DPO72304DX™ oscilloscope operating at 100 GSa/s. Each waveform capture consisted of 2 million samples, with three repetitions recorded per measurement.

The waveforms were generated at 25 GSa/s with 6.25 GHz bandwidth and shaped using a

https://doi.org/10.7795/110.20260421

raised cosine filter with a 0.35 roll-off factor. The optical frequencies selected for this experiment were 194.75 THz (modulated branch) and 194.49 THz (carrier branch), resulting in a transmitted OTA signal at 260 GHz. The demodulation process was performed over multiple time windows of 640 kSa each, sliding in 10 kSa increments across the full waveform.

This measurement focused on identifying the optimal optical power levels for the emitter and the power balance between the modulated and carrier optical branches. Figure 6.17 shows the effect of various total optical power levels, ranging from 10 mW to 25 mW, across different modulator/carrier power splits. These levels were critical for maintaining proper constellation point separation, particularly at the outer levels of the 16-QAM signal [70].

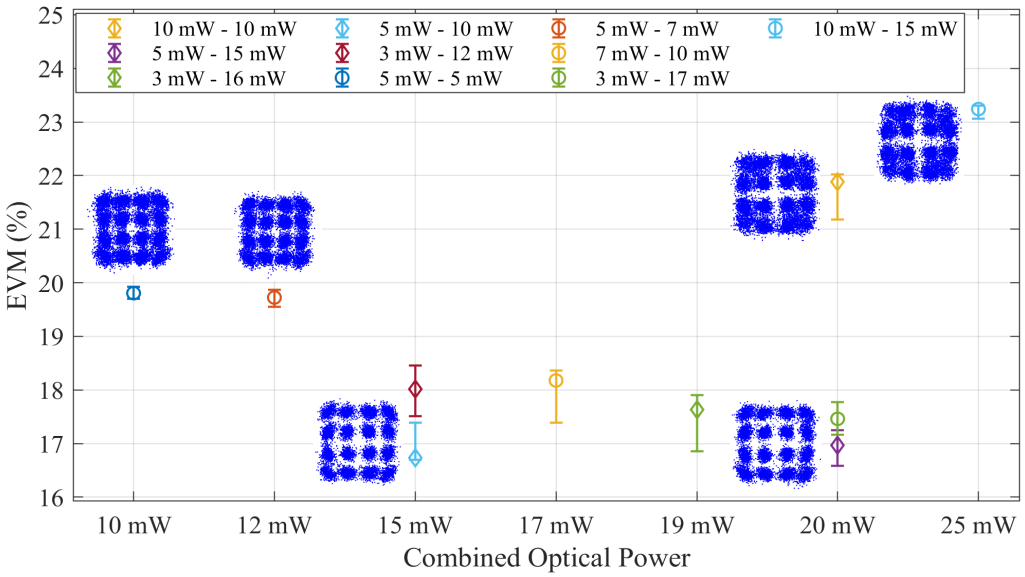

Figure 6.17: Effect of optical power levels on EVM performance. An optimal range was observed; increasing power beyond this point introduced nonlinear distortion. (Adopted from [70]).

As shown in Fig. 6.17, lower power levels (10 mW and 12 mW) resulted in higher EVM, due to limited signal strength. Performance improved at 15 mW, especially with power splits of 5 mW (modulated) and 10 mW (carrier). Error bars represent the variance across three repeated measurements. However, increasing the modulator branch beyond 5 mW led to higher EVM, attributed to nonlinear distortion. This was especially apparent in the 20 mW tests, where the 5 mW–15 mW split outperformed the balanced 10 mW–10 mW configuration by roughly 5 % EVM difference. Further increasing the total optical power to to 25 mW degraded the EVM performance [70].

Figure 6.18 shows the relationship between total optical power and the received signal's RMS voltage. A linear increase in voltage with power was observed, at approximately 0.52 mV/mW. Unlike EVM, different power combinations resulted in similar voltage levels, confirming that power alone does not fully explain constellation distortion.

The influence of power distribution on IQ amplitude and symbol probability was further analyzed using the probability density estimate (PDE) of the 16-QAM signal, shown in Fig. 6.19, which can be defined as a statistical representation of how often signal samples occur within

https://doi.org/10.7795/110.20260421

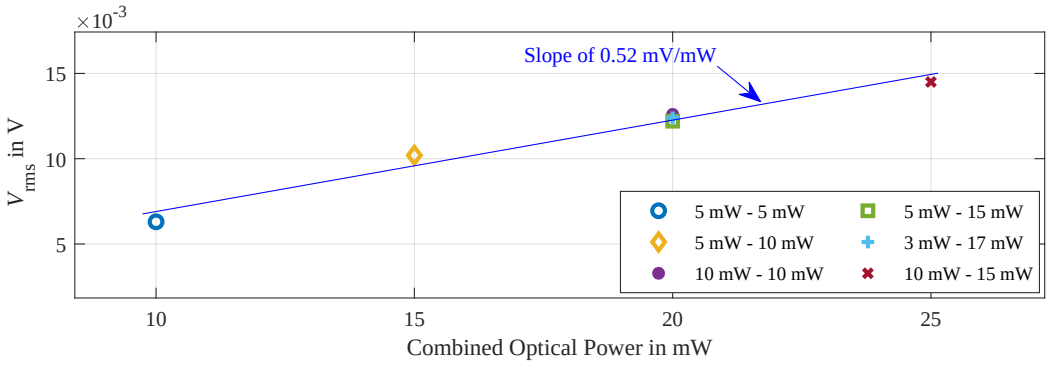

Figure 6.18: Received RMS voltage versus total optical power. Power increased linearly with voltage, but this did not directly correlate with EVM improvement. (Adopted from [70]).

different regions of the IQ plane. The figure highlights how different power levels affect the spacing and symmetry of constellation points. At lower modulated power (e.g., 5 mW), increasing the carrier branch to 15 mW disrupted the balance between inner and outer constellation points. On the other hand, increasing the modulated power to 10 mW affected the IQ amplitude, pushing symbols—especially those in the outer constellation rings—toward nonlinear regions of the PD.

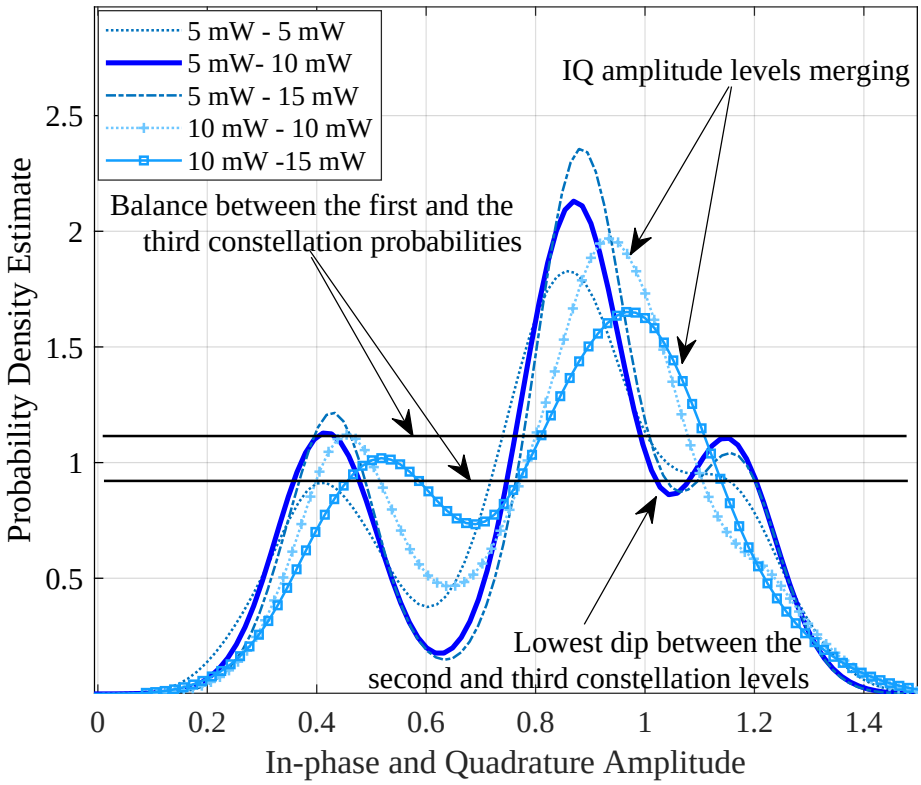

Figure 6.19: IQ amplitude versus probability density for different optical power splits. Higher modulated power led to distortion of outer constellation points. (Adopted from [70]).

The best outer point separation was observed with 5 mW–10 mW and 5 mW–15 mW power

https://doi.org/10.7795/110.20260421

combinations. In contrast, the 10 mW–10 mW and 10 mW–15 mW splits caused amplitude shifts that distorted inner constellation levels and compressed outer ones, leading to symbol overlap [70].

6.5.3 Image transmission

Figure 6.20 shows the setup used for the image transmission test. The image was first converted into digital bits and then mapped to IQ symbols. A QPSK modulation scheme was used at a symbol rate of 12.5 GBaud, centered at 260 GHz. The optical carrier was set at 194.75 THz, and the emitter was biased at -1 V.

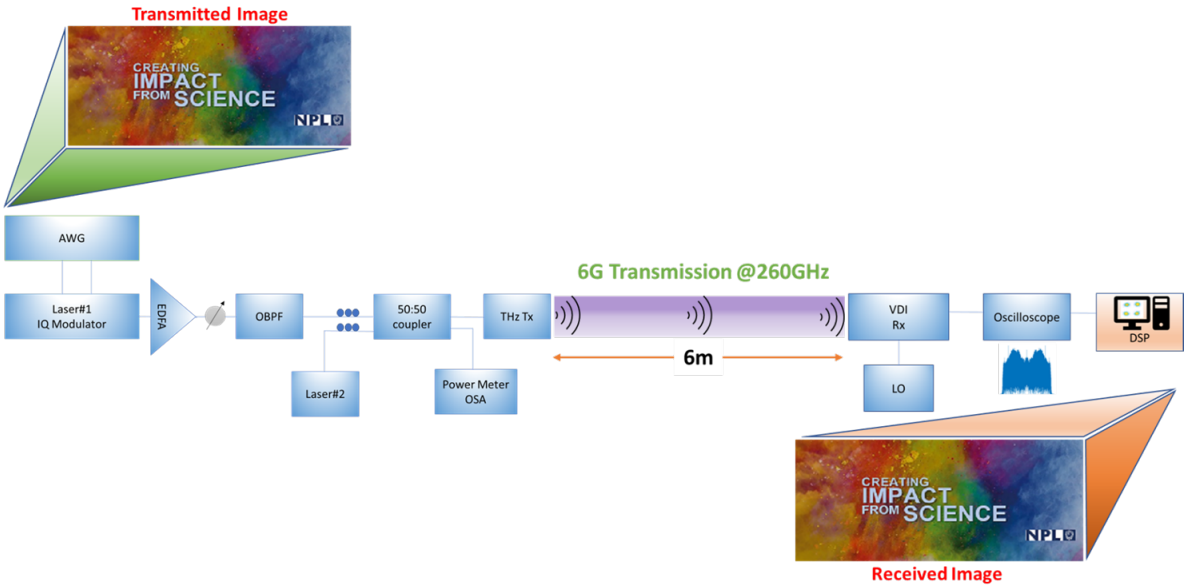

Figure 6.20: Image transmission setup and the image used in the test. (Adopted from [70]).

Due to the memory limitations of the AWG, the full transmission was divided into 24 data packets. Each packet contained 55,296 IQ symbols, oversampled by a factor of 8, resulting in 442,368 samples per packet. This ensured the sample count remained under the AWG's 524,288-sample limit. The chosen value also satisfied the AWG's requirement for sample counts to be a multiple of 128 (3456×128), which avoids the need for padding or truncation during transmission [70].

Figure 6.21 presents the EVM measured for each received packet. No bit errors were detected during reception. The small variations in EVM across packets were linked to the bit distribution within each packet, particularly the ratio of 0s and 1s. Packets with a more balanced bit distribution tend to produce more stable modulation output, resulting in lower EVM. All 24 packets were received correctly, confirming error-free transmission over a 6-meter link at 260 GHz. This result highlights the reliability of the system for high-frequency data transmission and supports the feasibility of using sub-THz links for potential 6G applications [70].

Compared with the PRBS-based transmission tests, the real-image data packets exhibited slightly greater variability in EVM, driven primarily by differences in bit distribution rather

https://doi.org/10.7795/110.20260421

than by channel impairments. While PRBS sequences have a uniform statistical structure that promotes consistent modulation performance, real data contain varying symbol patterns and correlation structures, which can marginally influence the modulation stability. Nonetheless, the absence of bit errors and the consistently low EVM across all 24 packets confirm that the link maintained reliable performance under realistic, non-random data conditions, demonstrating its suitability for practical high-data-rate sub-THz applications.

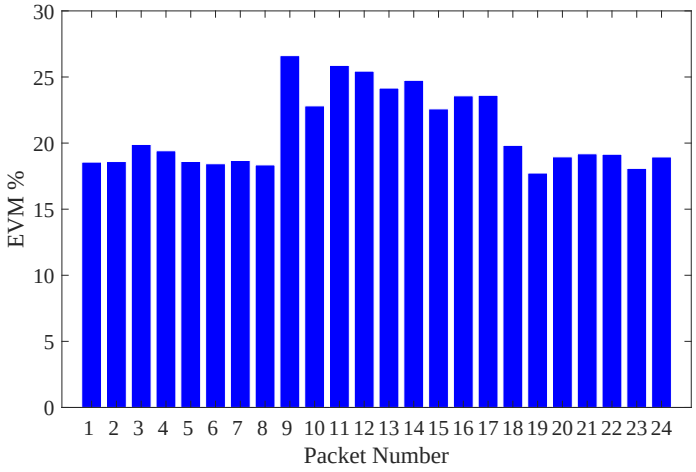

Figure 6.21: Root-mean-square EVM for each received image packet. (Adopted from [70]).

https://doi.org/10.7795/110.20260421

https://doi.org/10.7795/110.20260421

7 Summary and Perspectives

This thesis systematically investigates sub-THz channel sounding by developing advanced measurement techniques and testbeds to ensure traceable and repeatable system characterization. The study follows a structured progression, beginning with measurement fundamentals and calibration procedures, then characterizing correlation-based CS systems, investigating time-varying signal propagation, and implementing a photonic-assisted free-space transmission link.

7.1 Main Achievements

Chapters 3 and 4 provide a comprehensive characterization of correlation-based sub-THz CS systems in OTA measurement scenarios using a VNA at frequencies around 200 GHz and 300 GHz. Initially, system error correction was applied to all measurement setups. Calibration procedures were analyzed using TRL and UOSM methods, demonstrating high precision in both frequency bands. The noise floor and trace noise levels were examined, revealing a noise floor below -80 dB. The highest trace noise recorded for VNA measurements was 3.2×10^{-3} dB in magnitude and 0.042° in phase for WR05, while WR03 exhibited a peak trace noise of 10×10^{-3} dB and a phase variation of 0.075°.

Long-term OTA drift measurements were conducted over 12 hours with a 1 m separation between transmitting and receiving antennas. The primary uncertainty in VNA measurements was found to be PDP path gain drift, reaching 0.2 dB and 0.45 dB for WR05 and WR03, respectively, after interpolation and Hann-windowing. Phase drift influenced PDP delay measurements, shifting the peak delay by 1.5 mm for WR05 and up to 2.3 mm for WR03.

For correlation-based CS systems, zero-time measurement and back-to-back calibration were performed. The impact of DC offset on WR05 CS was investigated, revealing nonlinear path gain variations relative to reference measurements. Additionally, IQ imbalance effects on WR03 CS were examined.

Distance characterization validated VNA-interpolated PDP peaks, showing nonlinear peak-to-peak variations of 0.05 dB for WR05 and 0.22 dB for WR03. Comparison with theoretical Friis loss facilitated the calculation of antenna phase center differences and gain values.

https://doi.org/10.7795/110.20260421

CS measurements at varying distances were used to characterize system frequency steps, feasible bandwidth, and path gain deviations. For WR05, the noise floor affected reference measurements, with path gain deviations increasing from 0.06 dB below 1 m to 0.18 dB beyond 3 m. WR03 showed greater stability, with a peak-to-peak deviation of 0.06 dB across distances.

Uncertainty analysis revealed combined uncertainties of ±0.22 dB for WR05 VNA measurements, with CS standard deviation reducing from 0.39 dB to 0.34 dB after Hann-windowing. For WR03, VNA path gain uncertainties were ±0.51 dB, while CS standard deviation decreased from 1.4 dB to 1 dB after Hann-windowing.

Multipath measurements involved testing different reflectors at various rotational angles between the transmitting and receiving antennas. The wire reflector provided the strongest reflection, with mean path gains of -70.5 dB for WR05 and -62.8 dB for WR03. Smaller reflectors exhibited reduced path gain, with WR05 experiencing greater measurement uncertainties. Using multiple reflectors, PDP components were analyzed under controlled delays at different angles. Results from VNA and CS measurements were comparable across angles.

The measurements demonstrate that CS can deliver link-budget and path-gain characterization at sub-THz with sub-dB repeatability over practical ranges, which is essential for designing quasi-optical, point-to-point backhaul and short-range access links. The validated agreement between VNA-interpolated PDP peaks and CS (peak-to-peak variations of 0.05 dB for WR05 and 0.22 dB for WR03), together with comparable angle-dependent multipath responses across reflectors, indicates that CS reliably captures dominant propagation mechanisms needed for deterministic ray-based design and for calibrating simplified stochastic components in early 6G channel models.

The achieved path-gain stability are sufficient for link-budgeting, antenna phase-center extraction, and validating ray-tracing with realistic gain/phase margins. However, for rich, dynamic, or wideband channels (e.g., mobility, dense multipath, or MIMO with polarization), further improvement is advisable to reduce absolute power uncertainty (e.g., WR03 VNA ±0.51 dB) and to harden the system against front-end impairments (DC offset, IQ imbalance) and noise-floor limitations observed in WR05 at longer ranges.

Chapter 5 investigates segmented waveforms in time-varying CS measurements. Segmented waveforms, comprising discrete frequency steps, offer a trade-off between temporal resolution and frequency coverage. These waveforms are particularly useful when both velocity and position data need to be captured simultaneously. By carefully structuring frequency steps and segment durations, segmented waveforms can record motion details while maintaining high measurement accuracy.

A compact-scale measurement scenario was introduced to examine time-varying signal propagation using a VNA. The proof-of-concept testbed provides a valuable tool for characterizing CS systems operating at sub-THz frequencies, allowing for improved analysis of system responses to motion within the measurement environment.

The results highlight the importance of using directive antennas to enhance the signal-to-noise ratio, especially when applying higher IFBWs for faster sweeps. Additionally, measurement stability and securing frequency extension modules were crucial to preventing cable

https://doi.org/10.7795/110.20260421

movements that could introduce errors.

The single-direction movement simplified the analysis by ensuring known starting and ending positions throughout measurement sequences. The results demonstrated time variations in the VNA sweeps at different IFBWs, highlighting differences between CW and LS segments. Notably, optimization outcomes were particularly pronounced for velocities of 50 mm/s and higher.

The demonstrated time-varying VNA approach offers capabilities beyond those of conventional static measurements or wideband impulse sounders, as it enables high-resolution frequency-domain characterization while capturing temporal changes in the channel. This is particularly advantageous for sub-THz scenarios involving controlled or slow motion, where fine spectral detail and precise phase information are required to analyse Doppler shifts, multipath evolution, and front-end stability under movement. In the context of segmented waveforms, such measurements provide a reference framework for validating sweep designs and quantifying their performance in dynamic environments, thereby supporting the development of accurate time-varying channel models for future wireless systems.

For future wireless measurement systems, these findings indicate that segmented-waveform approaches can extend the applicability of sub-THz channel sounding to dynamic scenarios such as device motion, beam tracking, and environment monitoring. To fully integrate segmented waveforms into standardized channel models, further work should focus on improving sweep synchronization with external motion sensors for precise time–space alignment, enhancing calibration robustness to mitigate drift caused by movement of frequency-extension modules, adapting segment design in real time according to measured velocity or channel coherence time, and validating the approach under multi-directional and multi-velocity motion conditions. Addressing these aspects will strengthen the role of segmented-waveform channel sounding as a reliable tool for modeling and simulating time-varying sub-THz links in next-generation wireless systems.

Chapter 6 presents the design and evaluation of a single-channel heterodyne photonic-based sub-THz testbed. The setup uses four parabolic mirrors arranged in a two-fold configuration to achieve a total transmission distance of 6 m. Several parameters were tested to improve and optimize data transmission efficiency.

The investigation focused on various sub-THz frequencies within the WR03 band. For the QPSK measurement setup, deviations in EVM and received signal strength were observed, with optimal performance found between 255 GHz and 270 GHz. The optical frequency of 194.75 THz yielded the strongest signal performance. Three different emitter bias voltages were examined, with -1 V providing the highest RMS voltage and lowest EVM, outperforming -0.6 V and -1.5 V.

Laser source frequency hopping resulted in a frequency drift of approximately 170 MHz. Analysis of frequency drift across different measurement sessions and within a single 20 µs recording showed that frequency variations of 200 kHz/µs could be detected through EVM readings.

A 16-QAM measurement was conducted to examine the impact of optical power levels

https://doi.org/10.7795/110.20260421

from two optical branches on the received constellation diagram. The best-performing power combinations were found to be 5 mW – 10 mW and 5 mW – 15 mW.

For image transmission, an error-free process was achieved by encoding image data into 24 packets, each containing 55,296 IQ symbols. These were oversampled by a factor of eight, resulting in 442,368 samples per packet.

The developed single-channel heterodyne photonic-based sub-THz testbed successfully demonstrated reliable high-data-rate transmission over a 6 m free-space link within the WR03 band. Performance optimization across modulation formats and operating parameters identified an optimal frequency range of 255–270 GHz, an optical carrier of 194.75 THz, and an emitter bias of -1 V as key settings for minimizing EVM and maximizing received signal strength. The evaluation of laser frequency drift highlighted its measurable impact on signal quality, while 16-QAM experiments confirmed the importance of balanced optical power distribution between branches for maintaining constellation integrity. The error-free image transmission further validated the stability and robustness of the setup, showing its suitability as a flexible platform for sub-THz system characterization and for investigating modulation, alignment, and power optimization strategies relevant to future 6G links.

7.2 Implications and Future Directions

While this research provides a structured methodology for sub-THz channel characterization, several areas warrant further exploration.

1. Extending the measurement bandwidth beyond 330 GHz to investigate ultra-wideband sub-THz communication and its feasibility for higher frequency bands.

2. Integrating signal processing techniques assisted by pattern recognition to enhance calibration accuracy, automate error correction, and improve real-time channel estimation.

3. Conducting measurements in real-world urban and industrial environments to analyze propagation effects under non-ideal conditions.

4. Deeper investigation of measurement systems including the VNA to expand our understanding of system error corrections will build more confidence in our measurements.

5. Improving measurement testbeds for repeatable sub-THz measurement solutions that can be deployed in commercial applications.

6. Investigating higher-order modulation schemes beyond 16-QAM to improve spectral efficiency and data rates.

7. Exploring hybrid optical-RF systems for seamless data transmission in future 6G networks, ensuring reliable and scalable sub-THz communication links.

This thesis establishes a resilient framework for sub-THz measurement and calibration, providing essential insights for future research in high-frequency wireless communication systems.

https://doi.org/10.7795/110.20260421

List of Publications

Journal Articles

- **Mohanad Dawood Al-Dabbagh**, Jessica Smith, Thomas Kleine-Ostmann, Mira Naftaly, and Irshaad Fatadin. "Characterising the photonic-assisted coherent free-space link of sub-THz data transmission." IEEE Access 11 (2023): 128081-128093.

- Fatima Taleb, Mariana Alfaro-Gomez, **Mohanad Dawood Al-Dabbagh**, Jan Ornik, Juan Viana, Alexander Jäckel, Cornelius Mach et al. "Propagation of THz radiation in air over a broad range of atmospheric temperature and humidity conditions." Scientific Reports 13, no. 1 (2023): 20782.

- **Mohanad Dawood Al-Dabbagh**, David Ulm, Tobias Doeker, Diego Dupleich, Alexander Ebert, Reiner S. Thomä, Thomas Kürner, David A. Humphreys, and Thomas Kleine-Ostmann. "Characterization of Sub-THz Channel Sounding Systems in OTA Measurement Scenarios Using a Vector Network Analyzer." IEEE Transactions on Antennas and Propagation (2025).

- **Mohanad Dawood Al-Dabbagh**, David Ulm, David A. Humphreys, and Thomas Kleine-Ostmann. "Time-Varying Signal Propagation at Sub-THz Frequencies Using a Vector Network Analyzer." IEEE Access (2025).

Conference Proceedings

- **Mohanad Dawood Al-Dabbagh**, Thomas Kleine-Ostmann, and David Humphreys. "Radiative Reference Plane Estimation and Uncertainty for THz Path Loss Measurements." In 2021 46th International Conference on Infrared, Millimeter and Terahertz Waves (IRMMW-THz), pp. 1-2. IEEE, 2021.

- Dupleich, Diego, Sebastian Semper, **Mohanad Dawood Al-Dabbagh**, Alexander Ebert, Thomas Kleine-Ostmann, and Reiner Thomä. "Verification of THz channel sounder and delay estimation with over-the-air multipath artifact." In 2022 16th European Conference on Antennas and Propagation (EuCAP), pp. 1-5. IEEE, 2022.

https://doi.org/10.7795/110.20260421

- **Mohanad Dawood Al-Dabbagh**, Tobias Doeker, Thomas Kleine-Ostmann, Thomas Kürner, and David Humphreys. "THz channel sounder and VNA verification measurement based over-the-air multipath artifact." In 2022 47th International Conference on Infrared, Millimeter and Terahertz Waves (IRMMW-THz), pp. 1-2. IEEE, 2022.
- **Mohanad Dawood Al-Dabbagh**, Jess Smith, Thomas Kleine-Ostmann, Mira Naftaly, and Irshaad Fatadin. "Characterization of photonic-assisted free-space Sub-THz data transmission." In 2023 48th International Conference on Infrared, Millimeter, and Terahertz Waves (IRMMW-THz), pp. 1-2. IEEE, 2023.
- **Mohanad Dawood Al-Dabbagh**, David Ulm, Thomas Kleine-Ostmann, and David Humphreys. "Horn Antenna Phase Center Position Influence on Sub-THz Measurements Uncertainties." In 2024 18th European Conference on Antennas and Propagation (EuCAP), pp. 1-5. IEEE, 2024.
- **Mohanad Dawood Al-Dabbagh**, David A. Humphreys, and Thomas Kleine-Ostmann. "Investigating Time-Varying Signal Propagation at Sub-THz Frequencies Using a VNA." In 2025 19th European Conference on Antennas and Propagation (EuCAP), pp. 1-5. IEEE, 2025.

Book Chapters

- **Mohanad Dawood Al-Dabbagh**, and Thomas Kleine-Ostmann. "Vector Network Analysis." Metrology for THz Communications - Findings from DFG FOR 2863 Meteracom. Springer Series in Optical Sciences (2025).
- **Mohanad Dawood Al-Dabbagh**, David A. Humphreys and Thomas Kleine-Ostmann. "Characterising VNA Measurements of Time-Varying Sub-Terahertz Transmissions." Metrology for THz Communications - Findings from DFG FOR 2863 Meteracom. Springer Series in Optical Sciences (2025).
- Jonas Gedschold, Tobias Doeker, **Mohanad Dawood Al-Dabbagh**, Alexander Ebert, Giovanni Del Galdo and Reiner Thomä. "Architecture for Channel Sounding." Metrology for THz Communications - Findings from DFG FOR 2863 Meteracom. Springer Series in Optical Sciences (2025).
- **Mohanad Dawood Al-Dabbagh**, Diego Dupleich, Tobias Doeker, Reiner Thomä, Thomas Kürner, Thomas Kleine-Ostmann and David A. Humphreys. "Artefacts for Channel Sounding Performance Evaluation." Metrology for THz Communications - Findings from DFG FOR 2863 Meteracom. Springer Series in Optical Sciences (2025).
- Carla Reinhardt, **Mohanad Dawood Al-Dabbagh**, Giovanni Del Galdo, Thomas Kleine-Ostmann and Thomas Kürner. "Time-variant Propagation Channel including Metrics and Multi-link Connection." Metrology for THz Communications - Findings from DFG FOR 2863 Meteracom. Springer Series in Optical Sciences (2025).

https://doi.org/10.7795/110.20260421

List of Acronyms

4G	fourth-generation
5G	fifth-generation
6G	sixth-generation
ADC	analogue-to-digital converter
AWG	arbitrary waveform generator
B2B	back-to-back
BRF	band-reject filter
CIR	channel impulse response
CMA	constant-modulus algorithm
CS	channel sounder
CW	continuous wave
DC	direct current
DDS	direct digital synthesis
DFB	distributed feedback
DFT	discrete Fourier transform
DSP	digital signal processing
DUT	device under test
EAM	electro-absorption modulators
EDFA	erbium-doped fibre amplifier
EVM	error vector magnitude
FFT	fast Fourier transform
FSPL	free-space path loss
FWHM	full width at half maximum
HPBW	half-power beamwidth
I	in-phase
IDFT	inverse discrete Fourier transform
IF	intermediate frequency
IFBW	intermediate frequency bandwidth
IFFT	inverse fast Fourier transform

https://doi.org/10.7795/110.20260421

IFT	inverse Fourier transform
IQ	in-phase and quadrature
LO	local oscillator
LoS	line-of-sight
LS	linear sweep
LT	laser tracker
LTE	long term evolution
MIMO	multiple-input and multiple-output
MZM	Mach-Zehnder-Modulator
NMIs	national metrology institutes
NLoS	non-line-of-sight
OBPF	optical bandpass filter
OFDM	orthogonal frequency-division multiplexing
OSA	optical spectrum analyser
OTA	over-the-air
PC	phase center
PD	photodiode
PDP	power delay profile
PIN-PD	positive-intrinsic-negative photodiode
PLL	phase-locked loop
PRBS	pseudorandom binary sequence
PTB	Physikalisch-Technische Bundesanstalt
PTF	pyroelectric thin-film
Q	quadrature
QAM	quadrature amplitude modulation
QPSK	quadrature phase shift keying
RC	raised cosine
RF	radio frequency
RH	relative humidity
RMS	root mean square
RTO	real-time oscilloscope
SHM	sub-harmonic mixer
SI	International System of Units
SNR	signal-to-noise ratio
THz	Terahertz
TRL	through, reflect, line
UOSM	unknown through, offset short, short, match
UTC-PD	uni-traveling carrier photodiode

https://doi.org/10.7795/110.20260421

UWB	ultra-wideband
VNA	vector network analyzer
VSA	vector signal analysis
XAM	cross-absorption modulation

https://doi.org/10.7795/110.20260421

https://doi.org/10.7795/110.20260421

Bibliography

[1] S. Cherry, "Edholm's law of bandwidth," *IEEE spectrum*, 41(7), 58–60, 2004.

[2] Huawei Technologies, "Terahertz Sensing and Communication: The Next Frontier," `https://www.huawei.com/en/huaweitech/future-technologies/terahertz-sensing-communication`, 2025, accessed: 27-Mar-2025.

[3] Y. G. Li and G. L. Stuber, *Orthogonal frequency division multiplexing for wireless communications*, Springer Science & Business Media, 2006.

[4] D. D. Falconer, F. Adachi, and B. Gudmundson, "Time division multiple access methods for wireless personal communications," *IEEE Communications Magazine*, 33(1), 50–57, 1995.

[5] P. J. Winzer, "Making spatial multiplexing a reality," *Nature Photonics*, 8(5), 345–348, 2014.

[6] F. Ferrero, L. Lizzi, R. Staraj, J.-M. Ribero, et al., "Reconfigurable antenna for future spectrum reallocations in 5G communications," *IEEE Antennas and Wireless Propagation Letters*, 15, 1297–1300, 2015.

[7] D.-J. Deng, K.-C. Chen, and R.-S. Cheng, "IEEE 802.11 ax: Next generation wireless local area networks," in *10Th international conference on heterogeneous networking for quality, reliability, security and robustness*, pages 77–82, IEEE, 2014.

[8] C. Cox, *An introduction to LTE: LTE, LTE-Advanced, SAE, VoLTE and 4G mobile communications*, John Wiley & Sons, 2014.

[9] J. Lee and Y. Kwak, "5G standard development: technology and roadmap," *Signal Processing for 5G: Algorithms and Implementations*, pages 561–576, 2016.

[10] T. Nitsche, C. Cordeiro, A. B. Flores, E. W. Knightly, et al., "IEEE 802.11 ad: directional 60 GHz communication for multi-Gigabit-per-second Wi-Fi," *IEEE Communications Magazine*, 52(12), 132–141, 2014.

https://doi.org/10.7795/110.20260421

[11] V. Petrov, T. Kurner, and I. Hosako, "IEEE 802.15. 3d: First standardization efforts for sub-terahertz band communications toward 6G," *IEEE Communications Magazine*, 58(11), 28–33, 2020.

[12] T. Kürner and I. Hosako, "Spectrum and Standardization for THz Communications," in *Handbook of Radio and Optical Networks Convergence*, pages 1141–1163, Springer, 2024.

[13] N. G. Weimann, S. Monayakul, S. Sinha, F.-J. Schmückle, et al., "Manufacturable low-cost flip-chip mounting technology for 300–500-GHz assemblies," *IEEE Transactions on Components, Packaging and Manufacturing Technology*, 7(4), 494–501, 2017.

[14] S.-H. Shin, X. Shang, N. M. Ridler, and S. Lucyszyn, "Polymer-based 3-D printed 140-220 GHz low-cost quasi-optical components and integrated subsystem assembly," *IEEE Access*, 9, 28020–28038, 2021.

[15] K. Kuhlmann, T. Probst, N. Ridler, and J. Watts, "Good Practice Guide on Making Rectangular Waveguide Connections at Frequencies above 100 GHz," *PTB-OAR*, 2019.

[16] V. Seema and S. Anoop, *Fundamentals of microwave engineering: principles, waveguides, microwave amplifiers and applications*, PHI Learning Pvt. Ltd., 2009.

[17] S. Rey, D. Ulm, T. Kleine-Ostmann, and T. Kiirner, "Performance evaluation of a first phased array operating at 300 GHz with horn elements," in *2017 11th European Conference on Antennas and Propagation (EUCAP)*, pages 1629–1633, IEEE, 2017.

[18] T. Merkle, A. Tessmann, M. Kuri, S. Wagner, et al., "Testbed for phased array communications from 275 to 325 GHz," in *2017 IEEE Compound Semiconductor Integrated Circuit Symposium (CSICS)*, pages 1–4, IEEE, 2017.

[19] Y. Fu, X. Zhang, B. Hraimel, T. Liu, et al., "Mach-Zehnder: a review of bias control techniques for Mach-Zehnder modulators in photonic analog links," *IEEE Microwave Magazine*, 14(7), 102–107, 2013.

[20] S. Nellen, T. Ishibashi, A. Deninger, R. Kohlhaas, et al., "Experimental comparison of UTC-and PIN-photodiodes for continuous-wave terahertz generation," *Journal of Infrared, Millimeter, and Terahertz Waves*, 41, 343–354, 2020.

[21] S. Nellen, S. Lauck, G. Schwanke, M. Deumer, et al., "Radiation pattern of planar optoelectronic antennas for broadband continuous-wave terahertz emission," *Optics Express*, 29(6), 8244–8257, 2021.

[22] W. Tong, J. Ding, M. Zhu, B. Hua, et al., "Demonstration of 200-m Wireless Transmission in Photonics-Aided Terahertz 2 × 2 MIMO System Utilizing MRC Technology for OFDM Signals," *IEEE Transactions on Microwave Theory and Techniques*, 2024.

[23] Y. Cai, X. Yang, M. Zhu, B. Hua, et al., "Photonics-aided exceeding 200-Gb/s wireless data transmission over outdoor long-range 2× 2 MIMO THz links at 300 GHz," *Optics Express*, 32(19), 33587–33602, 2024.

https://doi.org/10.7795/110.20260421

[24] "Recommendation ITU-R P.676-10: Attenuation by atmospheric gases," Tech. rep., International Telecommunication Union (ITU), 2013, superseded by later versions.

[25] I. B. of Weights and Measures, *International vocabulary of basic and general terms in metrology*, International organization for standardization, 1993.

[26] M. D. Al-Dabbagh, D. Ulm, T. Kleine-Ostmann, and D. Humphreys, "Horn Antenna Phase Center Position Influence on Sub-THz Measurements Uncertainties," in *2024 18th European Conference on Antennas and Propagation (EuCAP)*, pages 1–5, IEEE, 2024.

[27] M. D. Al-Dabbagh, T. Kleine-Ostmann, and D. Humphreys, "Radiative Reference Plane Estimation and Uncertainty for THz Path Loss Measurements," in *2021 46th International Conference on Infrared, Millimeter and Terahertz Waves (IRMMW-THz)*, pages 1–2, IEEE, 2021.

[28] C. Schulze, W. Heinrich, and O. Bengtsson, "Wideband Calibration Methods on a Modified Vector Network Analyzer System: Wideband VNA Calibration Methods," *IEEE Microwave Magazine*, 26(1), 42–50, 2024.

[29] G. Bonaguide and N. Jarvis, *The VNA Applications Handbook*, Artech House, 2019.

[30] M. Zeier, D. Allal, and R. Judaschke, "Guidelines on the evaluation of vector network analysers (VNA)," *EURAMET Calibration Guide*, 3(12), 507–521, 2018.

[31] M. Hiebel, *Fundamentals of Vector Network Analysis*, Rohde and Schwarz, 2nd ed., 2007.

[32] T. Kürner, D. M. Mittleman, and T. Nagatsuma, "THz Communications: Paving the Way Towards Wireless Tbps," *Springer Series in Optical Sciences*, 234, 2016.

[33] D. Micheli, R. Pastore, A. Vricella, A. Delfini, et al., "Electromagnetic characterization of materials by vector network analyzer experimental setup," in *Spectroscopic methods for nanomaterials characterization*, pages 195–236, Elsevier, 2017.

[34] G. R. MacCartney and T. S. Rappaport, "A flexible millimeter-wave channel sounder with absolute timing," *IEEE Journal on Selected Areas in Communications*, 35(6), 1402–1418, 2017.

[35] M. Landmann, M. Kaske, and R. S. Thoma, "Impact of incomplete and inaccurate data models on high resolution parameter estimation in multidimensional channel sounding," *IEEE Transactions on Antennas and Propagation*, 60(2), 557–573, 2011.

[36] C.-Y. Yeh, C.-P. Lai, M.-C. Tseng, and H.-J. Li, "An OFDM-based channel sounder system," in *2009 IEEE Antennas and Propagation Society International Symposium*, pages 1–4, IEEE, 2009.

[37] A. Hassibi and A. Aziz, "Interference Cancellation in Broadband Wireless Systems Utilizing Phase Aligned Injection-Locked Oscillators," .

https://doi.org/10.7795/110.20260421

[38] P. B. Papazian, C. Gentile, K. A. Remley, J. Senic, et al., "A radio channel sounder for mobile millimeter-wave communications: System implementation and measurement assessment," *IEEE Transactions on Microwave Theory and Techniques*, 64(9), 2924–2932, 2016.

[39] M. D. Al-Dabbagh, D. Ulm, T. Doeker, D. Dupleich, et al., "Characterization of Sub-THz Channel Sounding Systems in OTA Measurement Scenarios Using a Vector Network Analyzer," *IEEE Transactions on Antennas and Propagation*, 2025.

[40] H.-J. Song, K.-H. Oh, N. Shimizu, N. Kukutsu, et al., "Generation of frequency-modulated sub-terahertz signal using microwave photonic technique," *Optics Express*, 18(15), 15936–15941, 2010.

[41] S. D. Saliba and R. E. Scholten, "Linewidths below 100 kHz with external cavity diode lasers," *Applied optics*, 48(36), 6961–6966, 2009.

[42] F. Karimi and S. A. Khorasani, "Optical modulation by conducting interfaces," *IEEE Journal of Quantum Electronics*, 49(7), 607–616, 2013.

[43] S. Kodama and H. Ito, "UTC-PD-based optoelectronic components for high-frequency and high-speed applications," *IEICE transactions on electronics*, 90(2), 429–435, 2007.

[44] M. Ali, L. E. G. Muñoz, G. Carpintero, S. Nellen, et al., "Millimetre-wave photonic emitter integrating a PIN-PD and planar high gain antenna," in *2020 Third International Workshop on Mobile Terahertz Systems (IWMTS)*, pages 1–5, IEEE, 2020.

[45] J. P. Dunsmore, *Handbook of microwave component measurements: with advanced VNA techniques*, John Wiley & Sons, 2020.

[46] E. A. of National Metrology Institutes (Euramet), "Guidelines on the Evaluation of Vector Network Analysers (VNA)," 2018.

[47] M. Wollensack, J. Hoffmann, J. Ruefenacht, and M. Zeier, "VNA Tools II: S-parameter uncertainty calculation," in *79th ARFTG Microwave Measurement Conference*, pages 1–5, IEEE, 2012.

[48] M. Bengtson, Y. Lyu, and W. Fan, "Long-range VNA-based channel sounder: Design and measurement validation at MmWave and sub-THz frequency bands," *China Communications*, 19(11), 47–59, 2022.

[49] L. Carslake, J. Skinner, and T. H. Loh, "Design and Preliminary Indoor Assessment of a Long-Range Sub-THz VNA-Based Channel Sounder between 500 GHz and 750 GHz," in *2024 18th European Conference on Antennas and Propagation (EuCAP)*, pages 1–5, IEEE, 2024.

[50] J. C. for Guides in Metrology (JCGM), "Evaluation of measurement data – Guide to the expression of uncertainty in measurement," 2008, gUM 1995 with minor corrections.

https://doi.org/10.7795/110.20260421

[51] T. Schrader et al., "Verification of scattering parameter measurements in waveguides up to 325 GHz including highly-reflective devices," *Adv. Radio Sci.*, 9, 9–17, 2011.

[52] D. F. Williams, "500 GHz – 750 GHz Rectangular-Waveguide Vector-Network-Analyzer Calibrations," *IEEE Trans. THz Sci. Techn.*, 1, 364–377, 2011.

[53] R. Kibria and M. W. Austin, "All optical signal-processing techniques utilizing four wave mixing," in *Photonics*, vol. 2, pages 200–213, MDPI, 2015.

[54] T. Doeker, J. M. Eckhardt, C. E. Reinhardt, and T. Kürner, "Time-domain channel sounder calibration at low terahertz band," *IEEE Open Journal of Antennas and Propagation*, 2024.

[55] D. S. Baum and H. Bolcskei, "Impact of phase noise on MIMO channel measurement accuracy," in *IEEE 60th Vehicular Technology Conference, 2004. VTC2004-Fall. 2004*, vol. 3, pages 1614–1618, IEEE, 2004.

[56] J. Quimby, J. Quimby, J. A. Jargon, R. Leonhardt, et al., *Channel sounder measurement verification: Conducted tests*, US Department of Commerce, National Institute of Standards and Technology, 2020.

[57] D. Demery, J. Parsons, and A. Turkmani, "Sounding techniques for wideband mobile radio channels: a review," *IEE Proceedings I (Communications, Speech and Vision)*, 138(5), 437–446, 1991.

[58] X. Cai, E. L. Bengtsson, O. Edfors, and F. Tufvesson, "A switched array sounder for dynamic millimeter-wave channel characterization: Design, implementation and measurements," *IEEE Transactions on Antennas and Propagation*, 2024.

[59] W. Y. Yong, A. Vosoogh, A. Bagheri, C. Van de Ven, et al., "An Overview of Recent Development of the Gap-Waveguide Technology for mmWave and sub-THz Applications," *IEEE Access*, 2023.

[60] "IEEE Standard for Rectangular Metallic Waveguides and Their Interfaces for Frequencies of 110 GHz and Above—Part 1: Frequency Bands and Waveguide Dimensions," *IEEE Std 1785.1-2012*, pages 1–22, 2013.

[61] "IEEE Standard for Rectangular Metallic Waveguides and Their Interfaces for Frequencies of 110 GHz and Above—Part 2: Waveguide Interfaces," *IEEE Std 1785.2-2016*, pages 1–22, 2016.

[62] "IEEE Recommended Practice for Rectangular Metallic Waveguides and Their Interfaces for Frequencies of 110 GHz and Above–Part 3: Recommendations for Performance and Uncertainty Specifications," *IEEE Std 1785.3-2016*, pages 1–19, 2016.

[63] N. M. Ridler and R. G. Clarke, "Establishing traceability to the international system of units for scattering parameter measurements from 750 GHz to 1.1 THz," *IEEE Transactions on Terahertz Science and Technology*, 6(1), 2–11, 2015.

https://doi.org/10.7795/110.20260421

[64] N. Ridler, S. Johny, M. Salter, X. Shang, et al., "Establishing waveguide lines as primary standards for scattering parameter measurements at submillimetre wavelengths," *Metrologia*, 58(1), 015015, 2021.

[65] N. Ridler and R. Ginleyt, "A review of the IEEE 1785 standards for rectangular waveguides above 110 GHz," in *2017 89th ARFTG Microwave Measurement Conference (ARFTG)*, pages 1–4, IEEE, 2017.

[66] A. Harvey, "Standard waveguides and couplings for microwave equipment," *Proceedings of the IEE-Part B: Radio and Electronic Engineering*, 102(4), 493–499, 1955.

[67] M. Zhang, J. Hirokawa, and M. Ando, "An E-band partially corporate feed uniform slot array with laminated quasi double-layer waveguide and virtual PMC terminations," *IEEE Transactions on antennas and propagation*, 59(5), 1521–1527, 2011.

[68] Rohde & Schwarz, *R&S ZV-WRxx Waveguide Calibration Kits*, 2020, version 1.00, Application Note.

[69] N. Marcuvitz, *Waveguide handbook*, 21, Iet, 1951.

[70] M. D. Al-Dabbagh, J. Smith, T. Kleine-Ostmann, M. Naftaly, et al., "Characterising the photonic-assisted coherent free-space link of sub-THz data transmission," *IEEE Access*, 11, 128081–128093, 2023.

[71] J. T. Quimby, D. F. Williams, K. A. Remley, D. Ribeiro, et al., "Millimeter-wave channel-sounder performance verification using vector network analyzer in a controlled RF channel," *IEEE transactions on antennas and propagation*, 69(11), 7867–7875, 2021.

[72] J. M. Kast, P. Manurkar, S. Perera, M. K. Hany, et al., "Laboratory-Based Reference Channels for Millimeter-Wave Wireless Device Measurements," in *2024 IEEE Conference on Computational Imaging Using Synthetic Apertures (CISA)*, pages 01–05, IEEE, 2024.

[73] A. Schultze, M. Schmieder, R. Askar, M. Peter, et al., "Comparison of Sub-THz Radio Channel Characteristics at 158 GHz and 300 GHz in a Shopping Mall Scenario," in *2024 18th European Conference on Antennas and Propagation (EuCAP)*, pages 1–5, IEEE, 2024.

[74] A. Schultze, R. Askar, M. Peter, W. Keusgen, et al., "Angle-resolved THz channel measurements at 300 GHz in a shopping mall scenario," in *2023 17th European Conference on Antennas and Propagation (EuCAP)*, pages 1–5, IEEE, 2023.

[75] S. Ju, Y. Xing, O. Kanhere, and T. S. Rappaport, "Sub-terahertz channel measurements and characterization in a factory building," in *ICC 2022-IEEE international conference on communications*, pages 2882–2887, IEEE, 2022.

[76] S. Salous, *Radio propagation measurement and channel modelling*, John Wiley & Sons, 2013.

https://doi.org/10.7795/110.20260421

[77] A. F. Molisch, J. Gomez-Ponce, N. Abbasi, W. Choi, et al., "Properties of Sub-THz Propagation Channels and Their Impact on System Behavior: Channel Measurements and Transmission Experiments," *IEEE Wireless Communications*, 31(1), 18–24, 2024.

[78] J. Fordham, L. Foged, V. Rodriguez, et al., "IEEE Recommended Practice for Antenna Measurements," in *Antennas Propag. Standards Committee IEEE Antennas Propag. Soc.*, vol. 64, pages 143–143, 2022.

[79] C. A. Balanis, *Antenna theory: analysis and design*, John wiley & sons, 2015.

[80] "IEEE Standard Test Procedures for Antennas," *ANSI/IEEE Std 149-1979*, pages 1–144, 1979.

[81] E. Muehldorf, "The phase center of horn antennas," *IEEE transactions on antennas and propagation*, 18(6), 753–760, 1970.

[82] D. Soldani, "6G fundamentals: Vision and enabling technologies," *Journal of Telecommunications and the Digital Economy*, 9(3), 58–86, 2021.

[83] P. Bello, "Characterization of randomly time-variant linear channels," *IEEE transactions on Communications Systems*, 11(4), 360–393, 1963.

[84] A. El Amine and V. Guillet, "Device-free people counting using 5 ghz wi-fi radar in indoor environment with deep learning," in *2020 IEEE Globecom Workshops (GC Wkshps*, pages 1–6, IEEE, 2020.

[85] T. S. Rappaport, G. R. MacCartney, M. K. Samimi, and S. Sun, "Wideband millimeter-wave propagation measurements and channel models for future wireless communication system design," *IEEE transactions on Communications*, 63(9), 3029–3056, 2015.

[86] D. Wütrich, M. Pfister, P. Manso, G. Constantinescu, et al., "Surface turbulence on bores and surges propagating on smooth and rough beds," in *Proceedings of the 6th International Conference on the Application of Physical Modelling in Coastal and Port Engineering and Science (Coastlab16), 10-13 May 2016, Ottawa, Canada*, 10-13 May 2016, 2016.

[87] M. Cerna and A. F. Harvey, "The fundamentals of FFT-based signal analysis and measurement," Tech. rep., Citeseer, 2000.

[88] R. Dubey and D. Agrawal, "Vibration signature analysis using variable Tukey window: A case study on Bearing Fault Data," in *2015 International Conference on Industrial Instrumentation and Control (ICIC)*, pages 540–544, IEEE, 2015.

[89] J. G. Proakis, *Digital signal processing: principles algorithms and applications*, Pearson Education India, 2001.

[90] S. McKinley and M. Levine, "Cubic spline interpolation," *College of the Redwoods*, 45(1), 1049–1060, 1998.

https://doi.org/10.7795/110.20260421

[91] J. Luo, Z. Xie, and M. Xie, "Interpolated DFT algorithms with zero padding for classic windows," *Mechanical Systems and Signal Processing*, 70, 1011–1025, 2016.

[92] J. Campion and J. Oberhammer, "Silicon micromachined waveguide calibration standards for terahertz metrology," *IEEE Transactions on Microwave Theory and Techniques*, 69(8), 3927–3942, 2021.

[93] K. Harima, "Antenna phase center estimation by gain-fitting method," *IEICE Communications Express*, 2(6), 274–279, 2013.

[94] P. Kažimír and D. Kocur, "Display unit for tracking of moving targets based on uwb radar," in *2013 IEEE 11th International Symposium on Applied Machine Intelligence and Informatics (SAMI)*, pages 159–163, IEEE, 2013.

[95] M. D. Al-Dabbagh, T. Doeker, T. Kleine-Ostmann, T. Kürner, et al., "THz channel sounder and VNA verification measurement based over-the-air multipath artifact," in *2022 47th International Conference on Infrared, Millimeter and Terahertz Waves (IRMMW-THz)*, pages 1–2, IEEE, 2022.

[96] A. Mohammadian and C. Tellambura, "RF impairments in wireless transceivers: Phase noise, CFO, and IQ imbalance–A survey," *IEEE access*, 9, 111718–111791, 2021.

[97] F. Liebgott, M. Jandt, M. Eberspächer, A. Liebgott, et al., "Spectrum-based online estimation of IQ imbalance for near field radar distance sensors," in *2021 29th European Signal Processing Conference (EUSIPCO)*, pages 2030–2034, IEEE, 2021.

[98] G. Matz and F. Hlawatsch, "Fundamentals of time-varying communication channels," in *Wireless communications over rapidly time-varying channels*, pages 1–63, Elsevier, 2011.

[99] J. Wu and P. Fan, "A survey on high mobility wireless communications: Challenges, opportunities and solutions," *IEEE Access*, 4, 450–476, 2016.

[100] F. Hlawatsch and G. Matz, *Wireless communications over rapidly time-varying channels*, Academic Press, 2011.

[101] J. Wang, W. Zhang, Y. Chen, Z. Liu, et al., "Time-varying channel estimation scheme for uplink MU-MIMO in 6G systems," *IEEE Transactions on Vehicular Technology*, 71(11), 11820–11831, 2022.

[102] G. P. Sharma et al., "Toward deterministic communications in 6G networks: State of the art, open challenges and the way forward," *IEEE Access*, 11, 106898–106923, 2023.

[103] M. D. Al-Dabbagh, D. A. Humphreys, and T. Kleine-Ostmann, "Investigating Time-Varying Signal Propagation at Sub-THz Frequencies Using a VNA," in *2025 19th European Conference on Antennas and Propagation (EuCAP)*, pages 1–5, IEEE, 2025.

https://doi.org/10.7795/110.20260421

[104] M. Zhao et al., "Measurement of the rotational Doppler frequency shift of a spinning object using a radio frequency orbital angular momentum beam," *Optics Letters*, 41(11), 2549–2552, 2016.

[105] D. Jung et al., "Terahertz Antenna-in-Package Design and Measurement for 6G Communications System," *IEEE Transactions on Antennas and Propagation*, 2023.

[106] M. Wollensack and J. Hoffmann, "METAS VNA Tools - Math Reference V2.8.2," 2024, visited on 30 Aug. 2024.

[107] S. Kim, J. Yun, D. Yoon, M. Kim, et al., "300 GHz integrated heterodyne receiver and transmitter with on-chip fundamental local oscillator and mixers," *IEEE Transactions on Terahertz Science and Technology*, 5(1), 92–101, 2014.

[108] J.-D. Park, S. Kang, S. V. Thyagarajan, E. Alon, et al., "A 260 GHz fully integrated CMOS transceiver for wireless chip-to-chip communication," in *2012 Symposium on VLSI Circuits (VLSIC)*, pages 48–49, IEEE, 2012.

[109] I. Kallfass, F. Boes, T. Messinger, J. Antes, et al., "64 Gbit/s transmission over 850 m fixed wireless link at 240 GHz carrier frequency," *Journal of Infrared, millimeter, and terahertz waves*, 36, 221–233, 2015.

[110] N. Sarmah, J. Grzyb, K. Statnikov, S. Malz, et al., "A fully integrated 240-GHz direct-conversion quadrature transmitter and receiver chipset in SiGe technology," *IEEE Transactions on Microwave Theory and Techniques*, 64(2), 562–574, 2015.

[111] M. Fujishima, "Overview of sub-terahertz communication and 300GHz CMOS transceivers," *IEICE Electronics Express*, 18(8), 20212002–20212002, 2021.

[112] M. D. Al-Dabbagh, J. Smith, T. Kleine-Ostmann, M. Naftaly, et al., "Characterization of photonic-assisted free-space Sub-THz data transmission," in *2023 48th International Conference on Infrared, Millimeter, and Terahertz Waves (IRMMW-THz)*, pages 1–2, IEEE, 2023.

[113] A. Kanno, K. Inagaki, I. Morohashi, T. Sakamoto, et al., "20-Gb/s QPSK W-band (75-110GHz) wireless link in free space using radio-over-fiber technique," *IEICE Electronics Express*, 8(8), 612–617, 2011.

[114] X. Pang, A. Caballero, A. Dogadaev, V. Arlunno, et al., "100 Gbit/s hybrid optical fiber-wireless link in the W-band (75–110 GHz)," *Optics express*, 19(25), 24944–24949, 2011.

[115] Y. Yoshimizu, S. Hisatake, S. Kuwano, J. Terada, et al., "Wireless transmission using coherent terahertz wave with phase stabilization," *IEICE Electronics Express*, 10(18), 20130578–20130578, 2013.

[116] T. Harter, S. Ummethala, M. Blaicher, S. Muehlbrandt, et al., "Wireless THz link with optoelectronic transmitter and receiver," *Optica*, 6(8), 1063–1070, 2019.

https://doi.org/10.7795/110.20260421

[117] R. Müller, W. Bohmeyer, M. Kehrt, K. Lange, et al., "Novel detectors for traceable THz power measurements," *Journal of Infrared, Millimeter, and Terahertz Waves*, 35, 659–670, 2014.

[118] G. Liu, G. Zhao, J. Sun, D. Gao, et al., "Experimental demonstration of DFB lasers with active distributed reflector," *Optics express*, 26(23), 29784–29795, 2018.

[119] J. Smith, M. Naftaly, S. Nellen, and B. Globisch, "Beam profile characterisation of an optoelectronic silicon lens-integrated PIN-PD emitter between 100 GHz and 1 THz," *Applied Sciences*, 11(2), 465, 2021.

[120] T. A. Heumier, "Mode hopping in semiconductor lasers," 1992.

[121] D. Godard, "Self-recovering equalization and carrier tracking in two-dimensional data communication systems," *IEEE transactions on communications*, 28(11), 1867–1875, 1980.

[122] M. Rice, "Digital communications: a discrete-time approach," *(No Title)*, 2009.

[123] Y. Wang, K. Shi, and E. Serpedin, "Non-data-aided feedforward carrier frequency offset estimators for QAM constellations: A nonlinear least-squares approach," *EURASIP journal on advances in signal processing*, 2004, 1–9, 2004.

[124] P. Series, "Attenuation by atmospheric gases and related effects," *Recommendation ITU-R*, 25, 676–12, 2019.

[125] X. Pang, O. Ozolins, S. Jia, L. Zhang, et al., "Bridging the terahertz gap: Photonics-assisted free-space communications from the submillimeter-wave to the mid-infrared," *Journal of Lightwave Technology*, 40(10), 3149–3162, 2022.

https://doi.org/10.7795/110.20260421

Bundesministerium
für Wirtschaft
und Energie

Die Physikalisch-Technische Bundesanstalt, das nationale Metrologieinstitut, ist eine wissenschaftlich-technische Bundesoberbehörde im Geschäftsbereich des Bundesministeriums für Wirtschaft und Energie.

PTB

Physikalisch-Technische Bundesanstalt
Nationales Metrologieinstitut
ISNI: 0000 0001 2186 1887

Bundesallee 100
38116 Braunschweig

Presse- und Öffentlichkeitsarbeit

Telefon: (0531) 592-93 21
Fax: (0531) 592-30 08
E-Mail: presse@ptb.de
www.ptb.de